Wright State University

CORE Scholar

Browse all Theses and Dissertations | Theses and Dissertations

2020

The Hydrostatics and Hydrodynamics of Prominent Heteromorph Ammonoid Morphotypes and the Functional Morphology of Ammonitic Septa

David Joseph Peterman
Wright State University

Follow this and additional works at: https://corescholar.libraries.wright.edu/etd_all

 Part of the Environmental Sciences Commons

Repository Citation

Peterman, David Joseph, "The Hydrostatics and Hydrodynamics of Prominent Heteromorph Ammonoid Morphotypes and the Functional Morphology of Ammonitic Septa" (2020). *Browse all Theses and Dissertations*. 2306.
https://corescholar.libraries.wright.edu/etd_all/2306

This Dissertation is brought to you for free and open access by the Theses and Dissertations at CORE Scholar. It has been accepted for inclusion in Browse all Theses and Dissertations by an authorized administrator of CORE Scholar. For more information, please contact library-corescholar@wright.edu.

THE HYDROSTATICS AND HYDRODYNAMICS OF PROMINENT HETEROMORPH AMMONOID MORPHOTYPES AND THE FUNCTIONAL MORPHOLOGY OF AMMONITIC SEPTA

A dissertation submitted in partial fulfillment of the
requirements for the degree of Doctor of Philosophy

By

DAVID JOSEPH PETERMAN
M.S., Wright State University, 2016
B.S., Wright State University, 2014

2020
Wright State University

WRIGHT STATE UNIVERSITY

GRADUATE SCHOOL

April 17th, 2020

I HEREBY RECOMMEND THAT THE DISSERTATION PREPARED UNDER MY SUPERVISION BY David Joseph Peterman ENTITLED The hydrostatics and hydrodynamics of prominent heteromorph ammonoid morphotypes and the functional morphology of ammonitic septa BE ACCEPTED IN PARTIAL FULFILLMENT OF THE REQUIREMENTS FOR THE DEGREE OF Doctor of Philosophy

Committee on
Final Examination

Christopher Barton, PhD
Dissertation Director

Charles Ciampaglio, PhD

Don Cipollini, PhD
Director, Environmental Sciences PhD program

Margaret Yacobucci, PhD

Barry Milligan, PhD
Interim Dean of the Graduate School

Sarah Tebbens, PhD

Stephen Jacquemin, PhD

ABSTRACT

Peterman, David Joseph. PhD. Environmental Sciences PhD Program, Wright State University, 2020. The hydrostatics and hydrodynamics of prominent heteromorph ammonoid morphotypes and the functional morphology of ammonitic septa.

Ammonoid cephalopods have chambered shells that regulated buoyancy. The morphology of their shells strongly influenced the physical properties acting on these animals during life. Heteromorph ammonoids, which undergo changes in coiling throughout ontogeny, are the focus of this dissertation. The biomechanics of these cephalopods are investigated in a framework involving functional morphology, paleoecology, and possible modes of life.

Constructional constraints were investigated for the marginally-corrugated septal walls within the chambered ammonoid shell. These constraints governed the positive relationship between septal complexity and terminal size. Furthermore, increased septal complexity facilitated liquid retention via surface tension. More complex septa would have increased liquid retention at larger scales, which could have been used as liquid ballasts, reserves for buoyancy adjustment, or to prevent disruptive sloshing of cameral liquid.

New methods for the virtual reconstruction of cephalopod shells are described. The shell constrains the volume and shape of each material of unique density that influenced organismal mass and its distribution. Therefore, these virtual models can be used to compute the conditions for neutral buoyancy, hydrostatic stability, syn vivo orientation, and the directional efficiency of movement. The rigid shell also constrains how the living ammonoid would have interacted with fluids in a dynamic setting. A new

method for the construction of neutrally-buoyant, physical models is described, which can be used to compute hydrodynamic properties such as drag and swimming velocity.

The biomechanics of three heteromorph ammonoid morphotypes from the North American Western Interior Seaway are discussed. These morphotypes represent the families Baculitidae, Nostoceratidae, and Scaphitidae. These investigations provide a better understanding of the hydrostatic and hydrodynamic properties that constrained the modes of life for the majority of prominent ammonoid taxa from the Late Cretaceous of the U.S. Western Interior. Novel modeling techniques provide data that suggests heteromorph ammonoids had selective pressures imposed on them for specific biological functions or life habits, rather than pointless morphological experimentation or liberation from such evolutionary pressures. These syn vivo physical properties also influenced the biogeographic dispersal and paleoecology for these enigmatic creatures that were once vital components of marine ecosystems.

TABLE OF CONTENTS

Page

LIST OF FIGURES

LIST OF TABLES

Table Page

LIST OF INSTITUTIONAL ABBREVIATIONS

AMNH – American Museum of Natural History, Division of Paleontology, New York, New York

BHI – Black Hills Institute of Geological Research, Hill City, South Dakota

USNM – National Museum of Natural History, Washington, D.C.

WSU – Wright State University, Department of Earth and Environmental Sciences, Dayton, Ohio

YPM – Yale Peabody Museum of Natural History (Invertebrate Division), New Haven, Connecticut

PUBLICATION LIST OF THE DISSERTATION

1. **Title:** Power scaling of ammonitic suture patterns from Cretaceous Ancyloceratina: constraints on septal/sutural complexity

   Authors: D.J. Peterman[1], and C.C. Barton[1]

   Published in *Lethaia* (accepted August, 2018); Volume 52; Pages 77–90 (chapter 1 of this dissertation)

   DOI: 10.1111/let.12291

2. **Title:** Mode of life and hydrostatic stability of orthoconic ectocochleate cephalopods: Hydrodynamic analyses of restoring moments from 3D printed, neutrally buoyant models

   Authors: D.J. Peterman[1] C.N. Ciampaglio[2], R.C. Shell[1], and M.M. Yacobucci[3]

   Published in *Acta Palaeontologica Polonica* (accepted April, 2019); Volume 64(3); Pages 441–460 (chapter 2 of this dissertation)

   DOI: 10.4202/app.00595.2019

3. **Title:** A method to the madness: ontogenetic changes in the hydrostatic properties of *Didymoceras* (Nostoceratidae, Ammonoidea)

   Authors: D.J. Peterman[1], M.M. Yacobucci[3], N.L. Larson[4], C.N. Ciampaglio[2], and T. Linn[5]

Published in *Paleobiology* (accepted January, 2020); forthcoming (chapter 3 of this dissertation)

DOI: 10.1017/pab.2020.14

4. **Title:** Syn vivo hydrostatic and hydrodynamic properties of scaphitid ammonoids from the U.S. Western Interior

   Authors: D.J. Peterman[1], N. Hebdon[6], C.N. Ciampaglio[2], M.M. Yacobucci[3], N.H. Landman[7], and T. Linn[5]

   Published in *GeoBios* (accepted April, 2020); forthcoming (chapter 4 of this dissertation)

[1]Department of Earth and Environmental Sciences, Wright State University, Dayton, Ohio

[2]Department of Science, Mathematics, and Engineering, Wright State University Lake Campus, Celina, Ohio

[3]School of Earth, Environment, and Society, Bowling Green State University, Bowling Green, Ohio

[4]Larson Paleontology Unlimited, Keystone, South Dakota

[5]Early Earth Enterprises, LLC, Glendive, Montana

[6]Department of Geology and Geophysics, University of Utah, Salt Lake City, Utah

[7]Division of Paleontology, American Museum of Natural History, New York, New York

AUTHOR CONTRIBUTIONS

D.P. = David Peterman, C.B. = Christopher Barton, C.C. = Charles Ciampaglio, M.Y. = Margaret Yacobucci, N.L.L. = Neal L. Larson, T.L. = Tom Linn, N.H. = Nicholas Hebdon, N.H.L. = Neil H. Landman

First Paper:

D.P. and C.B. conceived the project. D.P. performed the analysis, wrote the manuscript, and created all figures.

Second Paper:

D.P. conceived the project, created all figures and models, and wrote the initial draft. C.C. 3D printed the models for the physical experiments. M.Y. and C.C. provided support with interpretations and the several following drafts of the manuscript.

Third Paper:

D.P. conceived the project, created all figures and models, and wrote the initial draft. M.Y., C.C., T.L. and N.L.L. provided support with interpretations of the results and the several following drafts of the manuscript. T.L. guided the collection of the specimens used to make the virtual models.

Fourth Paper:

D. P. conceived the hydrostatic, hydrodynamic drag, and velocity sections of the project, and wrote the initial draft. N.H. conducted the hydrodynamic lift experiments and drag test, and created the hydrodynamic lift figure. N.H.L. conceived the lift section of

the project. C.C. 3D printed the models for physical experiments. M.Y., C.C., N.H., N.H.L., and T.L. helped with interpreting the results and writing the successive drafts of the manuscript. T.L. guided the collection of the specimens used to make the virtual and physical models.

ACKNOWLEDGEMENTS

I would like to express my gratitude to my dissertation director Christopher Barton and my dissertation committee for their continuing guidance and support. Thanks to Chuck Ciampaglio for assistance with the physical experiments, to Peg Yacobucci for her expertise in ammonoid paleobiology and guidance during publishing, and Chris Barton, Sarah Tebbens, and Stephen Jacquemin for discussions about fluid mechanics and functional morphology.

My sincere thanks to the Licking County (Ohio) Foundation for awarding me the Raymond H. and Beryl Dean Penick Memorial Scholarship in the 2019-2020 academic year, the Columbus Rock and Mineral Society for their 2019 scholarship, the ES PhD program for their travel fund, and the WSU Earth and Environmental Sciences Department for the Benjamin Richard Memorial Fund. These awards allowed me to collect specimens in the field, disseminate my research at conferences, and funded various research materials during my dissertation.

I also thank my brother Ken Peterman and friend/colleague Ryan Shell for keeping me company during countless hours on the road, helping me collect specimens in the badlands and everywhere else, and always being there to talk paleo. Thanks to Tom Linn, Neal Larson, and Don Clements for their help in the field and donation of research specimens.

Finally, I'd like to thank my parents for their support and for fueling my fascination with paleontology and geology at an early age.

1.0 INTRODUCTION

Ectocochleate cephalopods are characterized by their external, chambered shells. Their conchs consist of a body chamber and a phragmocone (Fig. 1). The body chamber houses the living animal while the phragmocone is the chambered portion of the shell used to regulate buoyancy. In conjunction with the growth of the soft body, new shell is accreted at the aperture and new septa (partitioning walls) are formed by the posterior soft body, creating progressively larger camerae (chambers). These camerae are then drained of cameral liquid via osmosis by the siphuncle (a blood-filled organ connecting each camera). Liquid is drained during growth to compensate for an increase in organismal mass in order to produce a condition close to neutral buoyancy (Denton and Gilpin-Brown, 1966).

Ammonoid cephalopods (Fig. 1A) are characterized in part by their complex septa (Fig. 1B) that frill marginally, creating a fractal-like suture line (Fig. 1C). The suture line is an expression of the septa on the inner shell wall, which can be exposed by removing the shell on fossil specimens. The functional morphology of such structures is unclear and many hypotheses have been proposed for why this complex folding may have evolved (described in Chapter 2). Heteromorph ammonoids are the focus of this dissertation. These ammonoids undergo changes in coiling throughout ontogeny that deviate from the morphology of their planispiral counterparts. Chapter 2 of this dissertation focuses on the constraints on heteromorph ammonoid sutures and provides new data for a possible biological function.

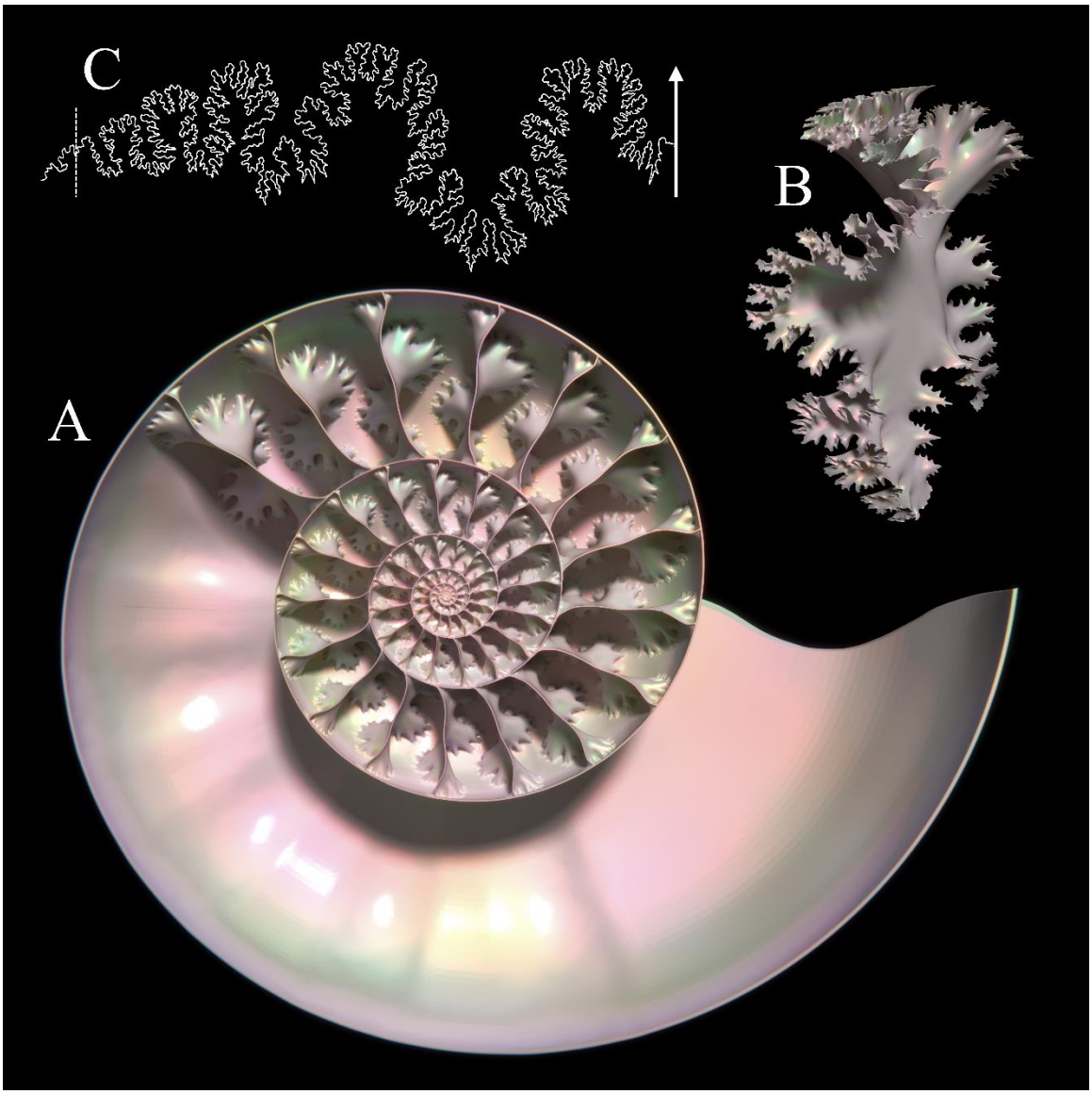

Figure 1: General morphology of a planispiral ammonite shell (*Eopachydiscus marcianus*). A, 3D rendering of a half-cut shell. B, Single septum. C, Suture line.

The following chapters (Chapter 3, 4, and 5) contain biomechanical investigations of common heteromorph ammonoid morphotypes based on specimens from the Western Interior of the United States. These morphotypes include orthocones (straight-shelled; Fig. 2A; Chapter 3), nostocones (tight or loose trochospiral phases, terminating in a U-shaped hook; Fig. 2B; Chapter 4), and scaphiticones (planispiral juvenile whorls followed

by a shaft and U-shaped hook; Fig. 2C; Chapter 5). These morphotypes were abundant in the Late Cretaceous Western Interior Seaway and are represented by many taxa due to the high diversity and remarkably quick turnover rates of these ammonoids (Larson et al., 1997; Cobban et al., 2006). Additionally, ammonoid remains are ubiquitous, which led to their common use as biostratigraphic index fossils in the U. S. Western Interior (Larson et al. 1997; Kennedy et al. 2000; Cobban et al. 2006; Landman et al. 2010; Fig. 3).

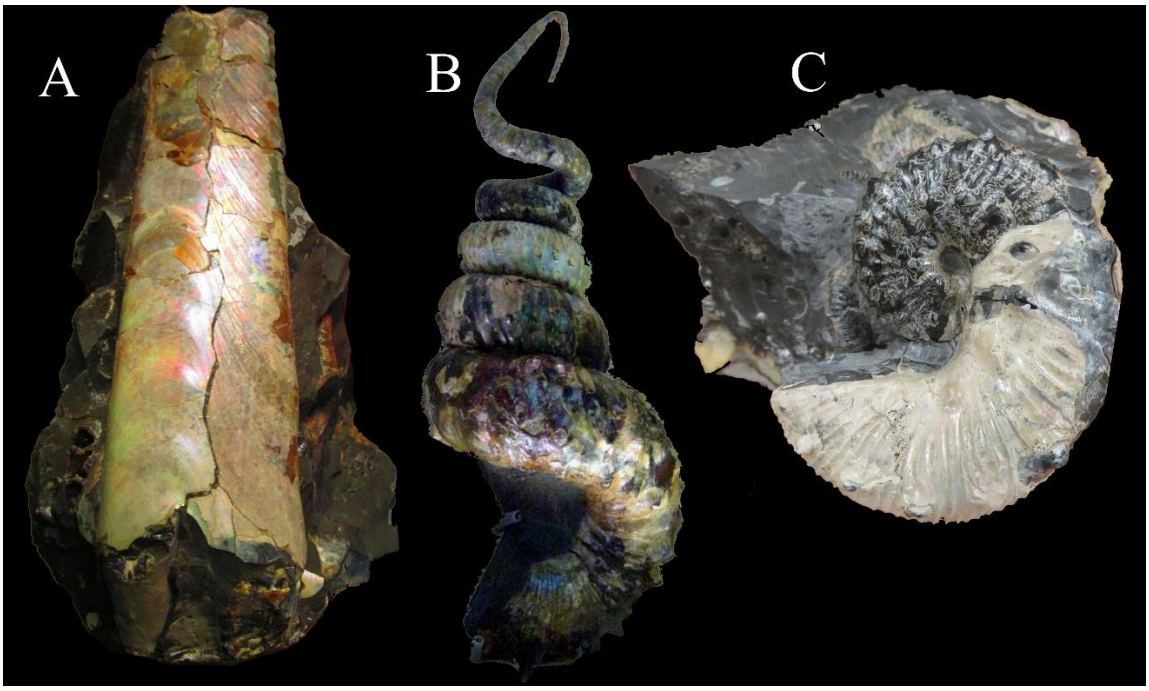

Figure 2: Morphotypes of interest for the aquatic biomechanics sections of the dissertation. **A**, Orthocone (Chapter 3). **B**, Nostocone (Chapter 4). **C**. Scaphiticone (Chapter 5).

While much attention has been paid to biostratigraphy, little is known about the constraints on the modes of life for these ammonoids. New methods for the virtual reconstruction of ectocochleate cephalopods are proposed and refined in each successive chapter. These virtual models allow the computation of hydrostatic properties that would have governed the conditions for neutral buoyancy, life orientation, stability, and the

directional efficiency of movement. Such methods also allow the construction of physical models for experimentation in a chaotic, real-world setting. These hydrodynamic experiments involve computing hydrodynamic efficiency and possible swimming proficiencies.

The three morphotypes of interest comprise about 97% of the U. S. Western Interior biostratigraphic taxa from the mid-Coniacian to the end of the Maastrichtian (88-66 Ma). Additionally, evaluating the *syn vivo* physical properties of the chosen species has implications for expanding the scope of these projects outside of the Western Interior Seaway because they represent morphotypes with much larger paleobiogeographic distributions (Figs. 4, 5, and 6). Therefore, investigating the interaction between fluid mechanics and morphology provides benchmark data on the mode of life, life habit, biogeographic dispersal, and paleoecology of these ubiquitous, widely distributed, and vital components of Mesozoic marine ecosystems.

Period	Stage		Ammonite Zones	Age ($^{40}Ar/^{39}Ar$)	Reference
Upper Cretaceous	Maastrichtian	U	*Hoploscaphites nebrascensis*	66	Cobban et al., 2006
			Hoploscaphites nicolleti		
		L	*Jeletzkytes dorfi*		Larson et al., 1997
			Baculites clinolobatus	69.42 ± 0.37	
			Baculites grandis		
			Baculites baculus		
			Baculites eliasi		
	Campanian	U	*Baculites jenseni*	71.3 ± 0.5	
			Baculites reesidei		
			Baculites cuneatus		
			Baculites compressus	73.35 ± 0.39	
			Didymoceras cheyennense		
			Exiteloceras jenneyi		
			Didymoceras stevensoni		
			Didymoceras nebrascense		
		M	*Baculites scotti*		
			Baculites reduncus		
			Baculites gregoryensis		
			Baculites perplexus		
			Baculites sp. (smooth species)		
			Bacuiltes asperiformis		
			Baculites mclearni		
			Bacuiltes obtusus	80.54 ± 0.55	
		L	*Bacuiltes sp.* (weak flank ribs)		
			Bacuiltes sp. (smooth)		
			Scaphites hippocrepis III		
			Scaphites hippocrepis II	81.71 ± 0.34	
			Scaphites hippocrepis I		
			Scaphites leei III		
	Santonian	U	*Desmoscaphites bassleri*		Cobban et al., 2006
			Desmoscaphites erdmanni		
			Clioscaphites choteauensis		
		M	*Clioscaphites vermiformis*		
		L	*Clioscaphites saxitonianus*		
	Con.	U	*Scaphites depressus*		
			Scaphites ventricosus	88	

Figure 3: Ammonite biostratigraphic zones from the Western Interior of the United States. Each zone is color coded by morphotype. Tan = orthocone, Blue = nostocone, and Red = scaphiticone.

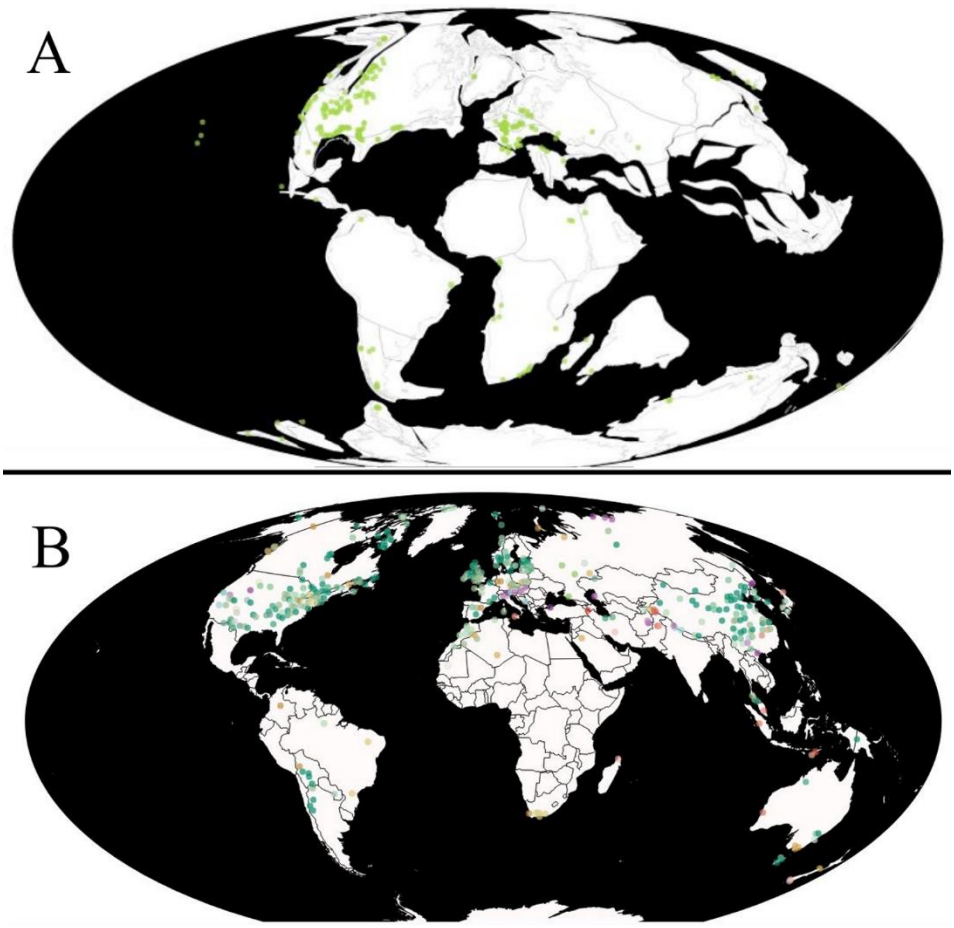

Figure 4: Biogeographic distribution of orthoconic ectocochleate cephalopods. A, Paleobiogeographic distribution of Baculitidae during the Late Cretaceous. B, Distribution of fossil sites containing Orthocerida and Endocerida (note the larger relative abundance and temporal range from the Ordovician to the Jurassic). Images from paleobiodb.org

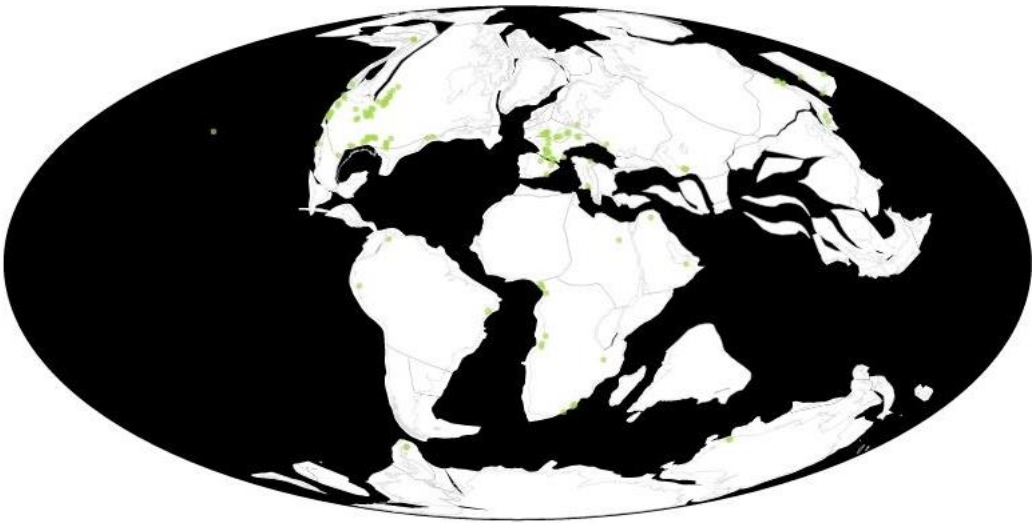

Figure 5: Paleobiogeographic distribution of Nostoceratidae during the Late Cretaceous. Image from paleobiodb.org

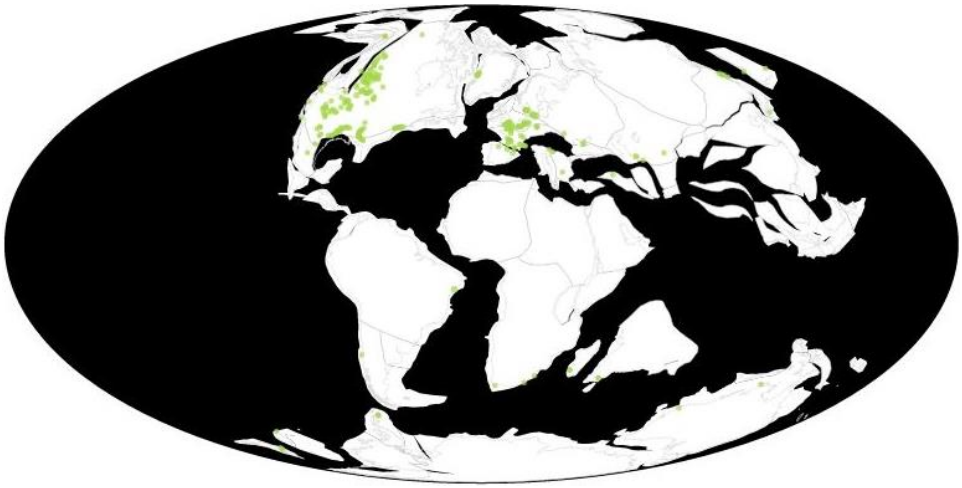

Figure 6: Paleobiogeographic distribution of Scaphitidae during the Late Cretaceous. Image from paleobiodb.org

1.1 REFERENCES

Cobban, W., Walaszczyk, I., Obradovich, J.D., and McKinney, K., 2006, A USGS zonal table for the Upper Cretaceous middle Cenomanian-Maastrichtian of the Western Interior of the United States based on ammonites, inoceramids, and radiometric ages. USGS Open File Report 2006-1250, 47p.

Denton, E.J., and Gilpin-Brown, J.B., 1966, On the buoyancy of the pearly Nautilus. Journal of the Marine Biological Association of the United Kingdom, v. 46, p. 723–759.

Kennedy, W.J., Landman, N.H., Cobban, W.A., and Scott, G.R., 2000, Late Campanian (Cretaceous) heteromorph ammonites from the Western Interior of the United States. Bulletin of the American Museum of Natural History, v. 251, p. 1–88.

Landman, N.H., Kennedy, W.J., Cobban, W.A., and Larson, N.L., 2010, Scaphites of the "nodosus group" from the Upper Cretaceous (Campanian) of the Western Interior of North America. Bulletin of the American Museum of Natural History, v. 342, p. 1–242.

Larson, N.L., Jorgensen, S.D., Farrar, R.A., Larson, P.L., 1997, Ammonites and the other cephalopods of the Pierre Seaway. Geoscience Press, Tucson, Arizona. 148p.

2.0 Power scaling of ammonitic suture patterns from Cretaceous Ancyloceratina (Ammonoidea): constraints on septal/sutural complexity

Peterman, D.J., and Barton, C.C. 2019. Power scaling of ammonitic suture patterns from Cretaceous Ancyloceratina (Ammonoidea): constraints on septal/sutural complexity. *Lethaia*, 52: 77–90.

Abstract

The spatial scaling of 77 hemisutures from 65 species of Cretaceous heteromorphic ammonites was quantified with the fractal box counting method. Fractal dimensions within *Baculites compressus* did not significantly differ between adult hemisutures, however the juvenile suture of this species did exhibit a significantly lower fractal dimension. This suggests that variation in sutural complexity between explicitly adult ontogenetic stages may not contribute to significant noise in comparisons between other species/morphotypes. High spired, three-dimensionally coiled heteromorphs with a larger degree of septal asymmetry exhibit higher fractal dimensions in outer whorl hemisutures than inner whorl hemisutures due to their elongation and improved space occupation over a larger whorl surface. Three-dimensionally coiled ammonites also have higher fractal dimensions on average (mean Db = 1.45) with respect to their 2D coiled counterparts (mean Db = 1.38). All ammonites in this study exhibit a positive trend between sutural complexity and shell size (proxied by whorl height). These relationships

suggest that septal frilling is constrained by shell morphology and whorl section geometry during septal morphogenesis. This, in turn, influences the scaling, space filling properties, and scaling limits of ammonitic suture patterns. Sutural/septal complexity is also found to positively influence the amount of liquid retained in marginal septal recesses. However, as these septa approach larger scales, less cameral liquid is retained per septal mass. This may further explain the positive relationship between sutural complexity and shell size.

2.1 INTRODUCTION

Ectocochleate cephalopod shells consist of a living chamber which house the soft body, and a phragmocone which is divided into a series of progressively larger chambers during life. In Mesozoic ammonoids, septa (walls that partition the phragmocone) frill marginally to create intricately folded structures. Suture patterns are the expression of these structures at the intersection between the septum and shell wall. The practical significance and function of complex septa/sutures has long been a subject of debate and has given rise to several hypotheses (Seilacher 1975; Klug *et al.* 2008; Klug & Hoffmann 2015). Increased sutural complexity (septal frilling) has been hypothesized to increase shell resistance to hydrostatic pressure normal to the shell and the pressure transmitted to the septum through the body (Pfaff 1911; Spath 1919; Westermann 1975; Kennedy & Cobban 1976; Jacobs 1990; Hewitt & Westermann 1997; De Blasio 2008) and thus has commonly been used as a proxy for living depth. Alternatively, Daniel *et al.* (1997) find that septal complexity actually limited depth. Other hypotheses attribute sutural complexity and septal frilling to buoyancy control and modification. The marginal recesses on both sides of each frilled septum could have served as cameral liquid ballasts

that influence the living ammonoid's stability and orientation in the water column (Mutvei & Reyment 1973; Kulicki 1979; Ward 1987; Kulicki & Mutvei 1988; Saunders 1995). Frilled septa could have also influenced the alteration of the living ammonoid's buoyant properties by potentially allowing faster chamber emptying (Mutvei 1967; but see Klug & Hoffmann 2015) or by permitting earlier cameral liquid removal in newly formed chambers due to a more secure incompletely mineralized septum (Klug *et al.* 2008).

The sutural complexity of heteromorphic ammonites has been seldom quantified and many relationships and constraints on their morphology remain poorly understood. Sutures from Cretaceous heteromorphic ammonites (including recoiled forms) are the focus of this study. We recognize the suborder Ancyloceratina to be polyphyletic, however systematic descriptions herein (at family levels and lower) will follow those of Wright *et al.* (1996). The heteromorphic ammonites in this study include the superfamilies Ancyloceratoidea, Douvilleiceratoidea, Deshayesitoidea, Turrilitoidea, and Scaphitoidea. Morphotypes that follow 3D coiling or seemingly aberrant coiling schemes are mostly represented by the turrilitids and nostoceratids (of the Turrilitoidea), while 2D coiled forms are characterized by the douvilleiceratoids, deshayesitoids, scaphitoids, most ancyloceratoids, and some turrilitoids.

Three-dimensionally coiled heteromorphs can exhibit asymmetrical septa/suture patterns about the external lobe (E) and internal lobe (I), which is attributed to the differences in length and radii of curvature between the outer and inner whorl surfaces, and the lateral displacement of the siphuncle (Ward 1979a; Klinger 1980). Ward (1979a) noted that septal asymmetry is more prominent in high spired torticonic forms that

exhibit low apical angles and high whorl translations (such as the turrilitids), contrary to nostoconic shell forms (represented mostly by the nostoceratids) which tend to have a lower degree of septal asymmetry. Septal asymmetry is accompanied with enlarged hemisutures on the outer whorl and reduced hemisutures on the inner whorl, a feature that is independent of coiling direction (Ward 1979a, Seilacher & Gishlick 2015).

Two-dimensionally coiled morphotypes have relatively symmetrical hemisutures, however, all suture patterns are never perfectly symmetric and contain some variability (Yacobucci & Manship 2011). Suture patterns, just as any other morphological feature, display some degree of intraspecific variability as well (Seilacher 1973; Manship 2004; Paul 2011). Polymorphy and sexual dimorphism (between microconchs and macroconchs) also influence sutural morphology within a species (Kakabadze 2004). Sutural complexity throughout ontogeny is not constant and increases to exhibit peak complexity approaching the terminal suture (Schindewolf 1951; Wiedmann & Kullmann 1980; Klug & Hoffman 2015; Hoffmann *et al.* 2018), except for mature modification in some taxa (see Davis *et al*. 1996, Klug *et al.* 2015). All of these aspects of sutural/septal morphology can potentially add noise in the quantitative analyses of suture patterns.

2.1.1 Fractal geometry of ammonitic sutures

While the shape of suture patterns can be quantified in many useful ways (Westermann 1971; Yacobucci & Manship 2011; Ubukata *et al.* 2009, 2014), fractal analysis is chosen herein because it particularly reflects the scaling properties of a pattern. Ammonitic sutures often exhibit intricate corrugations over a range of length scales which can be quantified by a power scaling exponent, or fractal dimension (Fig. 1). A geometric pattern is a fractal if it is scale invariant; i.e., follows a power function over

one or more orders of magnitude in length (Mandelbrot 1983). Two-dimensional suture patterns are planar projections of their three-dimensional frilled septal margins that attach to the shell wall. Therefore, a suture pattern lying in a plane and exhibiting power scaling must have a fractal dimension between one and two. Ammonitic suture patterns can be considered stochastic natural fractals that are scale invariant to some degree (Bayer 1978, 1985). Sutural morphology varies between the lobes and saddles (adoral and adapical elements, respectively) and also between the external lobe (E) and internal lobe (I), causing them to deviate from a mathematically ideal fractal. In the case of a mathematically perfect fractal, the pattern would scale in a self-similar manner, and corrugations would continue to finer scales ad infinitum as the length scale approaches

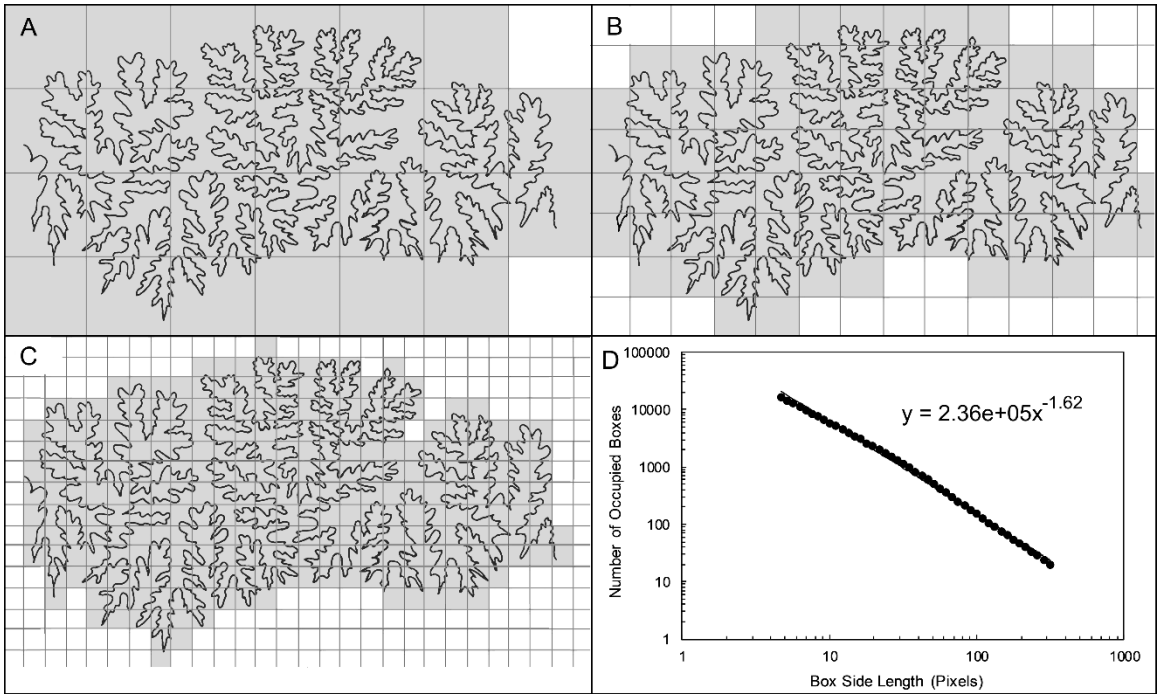

Figure 1: Generalized depiction of the box method of fractal analysis. The suture of *Anisoceras merriami* is overlain by grids of decreasing box side length and the number of occupied boxes are counted for each step size (A-C). The number of occupied boxes are plotted for each step size and the scaling exponent (fractal dimension) is computed from the slope of the power law; where $D_B = 1.62$ for this example (D). The image of the suture pattern is adapted from Packard and Jones, (1962).

The viscous fingering model has been used to partially explain the fractal-like behaviour of complex suture patterns. Perturbations in fluids of differing viscosities move according to the pressure gradient and split into fingers to create fractal patterns (García-Ruiz *et al.* 1990). The crenulated patterns generated by these models qualitatively resemble the lobes and saddles of ammonitic suture patterns and can be invoked to explain some of the constraints on septal morphogenesis. The degree of crenulation depends on the available space and shape, and is known as the "domain effect" (Monnet *et al.* 2011, 2015). According to viscous finger models, areas of larger radii yield fractals with higher fractal dimensions (García-Ruiz *et al.* 1990).

In terms of biologically generated fractals, such patterns can be formed by iterated corrugations of the posterior body. Hammer (1999) suggests these modifications could be driven by morphogens under some genetic control. Similar reaction-diffusion dynamics have been modeled for epithelial folding in kidneys, lungs, teeth, and other organs (Hammer 1999; Hammer & Bucher 1999).

2.1.2 Previous studies of the power scaling of ammonite sutures

Ammonite sutures have been previously described as natural fractals that exhibit approximate self-similarity over a limited range of length scales (Bayer 1985; Seilacher 1988). The Richardson method (also referred to as step-line, divider, or ruler method; Mandelbrot 1983) of fractal analysis has most commonly been used to calculate the fractal dimensions of ammonite sutures (Boyajian & Lutz 1992; Lutz & Boyajian 1995; Olóriz & Palmqvist 1995; Olóriz *et al*. 1997, 1999, 2002; Pérez-Claros *et al.* 2007). This method consists of sequentially measuring the length of a corrugated line, lying in a

plane, with rulers of decreasing length. A fractal line will increase in total length as ruler length decreases, following a power function (Mandelbrot 1983). The box method of fractal analysis (Feder 1988; Barton 1995) consists of counting the number of boxes in a grid that are occupied by an object lying in a plane over a range of step sizes. The relationship between decreasing box side length and an increasing number of occupied boxes also follows a power function. The box method has been used previously to quantify sutural complexity by García-Ruíz *et al*. (1990); García-Ruíz & Checa (1993); Lutz & Boyajian (1995); Checa & García-Ruíz (1996). Mathematically, the ruler and box counting methods should yield the same fractal dimension (Lutz & Boyajian 1995). Lutz & Boyajian (1995) compared the ruler and box counting methods of fractal analysis on ammonitic sutures and found that each method yielded nearly identical fractal dimensions over a relevant range of scales.

Very broadly speaking, ammonoid sutures have become more corrugated throughout geologic time to eventually produce sutures that exhibit fractal scaling (order Ammonitida). Boyajian & Lutz (1992) found that the variance and range of sutural complexity increases after the origination of this order. Because of simple-sutured ammonites persisting, they suggested that increased sutural complexity did not influence taxonomic longevity nor did it allow differential survival of ammonites with more complicated sutures/septa (that is, if such a direct relationship existed).

The relationship between the sutural complexity and shell geometry for Late Jurassic ammonites was explored by Olóriz & Palmqvist (1995); Olóriz *et al*. (1997, 1999, 2002); Pérez-Claros *et al*. (2007). These studies found that sutures belonging to ammonites with planulate (flatter) shell flanks yielded the highest fractal dimensions,

while sutures belonging to ammonites with convex shell flanks had lower fractal dimensions. They also revealed a positive relationship between whorl height and fractal dimension. Olóriz *et al*. (2002) found that ammonites belonging to the neritic domain have more intricate sutures when compared to those of the oceanic domain and suggested that sutural complexity may be more dependent upon shell geometry rather than bathymetric range.

2.2 METHODS

2.2.1 Box-counting method of fractal analysis

The box-counting method measures the scaling of a geometric pattern lying in a plane. The pattern could be comprised of a collection of points, multiple line segments, or intricately crenulated lines such as ammonite sutures. The fractal dimension quantifies how suture patterns scale as a power function of size over some range of lengths. The power scaling exponent, or fractal dimension (D_B), is calculated with Equation 1 (Mandelbrot 1983):

$$N(\delta) \approx C\delta^{-D_B} \quad (1)$$

where N(δ) is the minimum number of boxes occupied by the pattern, δ is the box side length, and C is a constant. D_B is the scaling exponent that quantifies how the pattern scales as a function of size over a range of box side lengths, and also measures the degree of space filling by the pattern. The data pairs δ and N(δ) are plotted on the x and y axes respectively in log-log space and fit with a power function.

2.2.2 Box method as implemented by the fractal analysis software - Benoit 1.3

Seventy-seven hemisutures were analysed from 65 species of Cretaceous heteromorphic ammonites that are classified by Wright *et al.* (1996) as belonging to the

polyphyletic suborder Ancyloceratina. Adult suture patterns and whorl heights (Wh) were gathered from plates in published literature (Wade 1924; Arkell *et al.* 1957; Cobban 1974; Packard & Jones 1962; Jones, 1963; Matsumoto 1977; Klinger & Kennedy 1978; Ward 1979a; Kennedy & Juignet 1983; Kennedy & Cobban 1991; Wright *et al.* 1996; Larson *et al*. 1997; Landman *et al*. 2004; Arkadiev 2008; Shigeta 2014; Larson 2016). The suture patterns of *Baculites compressus* Say 1820 were recorded by the primary author from an adult and juvenile Wright State University specimen (WSU-1400 and WSU-1401). These suture patterns were scanned at 600 dpi from printed plates or screen captured directly from digital resources. Complete patterns between extern lobe (E) and internal lobe (I) were analysed for heteromorphs with open whorls, while sutures of planispiral forms were measured from E to the umbilical seam. Unnecessary portions of the images were removed, including arrows/lines showing the locations of the venter and umbilical seam, and any continuations of the suture past these two points. Because of variation in size of the specimens and the scales at which they were printed, the widths of the suture patterns were variable. A program was written in MATLAB R2016a to normalise suture widths between 3 and 5 pixels and to remove scattered pixels, scanning artifacts, or other imperfections. This program was also used to invert image colours to create a white suture pattern over a black background and to save each file as a bitmap image. Both are required input formats by Benoit 1.3, the fractal analysis software.

Benoit 1.3 was used to implement the box-counting method which superimposed a rotating a grid over each suture pattern (Figure 1A-1C). The grid rotated 360° at 5° increments to remove directional bias and the minimum number of occupied boxes was recorded for that box size. The box side length decreases by a user specified logarithmic

coefficient and the process was repeated. The minimum number of occupied boxes was then plotted for each box side length (in pixels) in log-log space and fit with a power function (Figure 1D). To measure the quality of fit of each power function without weighting smaller step sizes, a linear regression was performed on the log transformed data pairs and standard error was computed for the fractal dimension (scaling exponent). The data points for box side lengths less than 4 pixels (the approximate widths of the suture lines) were excluded from the analysis because they would yield too many occupied boxes for each step size. Whorl heights were consistently recorded at the last septum on the phragmocone for adult specimens in each plate. For the two specimens of *Baculites compressus*, whorl heights were measured with digital calipers by the authors.

2.2.3 Reconstruction of a baculite septum for capillary retention experiments

In order to measure the retention of liquid by frilled septal margins, a 3D shapefile of a fragmentary specimen of *Baculites compressus* (WSU-1400) was created with Autodesk® ReCap photogrammetry software. This produced a tessellated 3D mesh (in .stl format) from a series of 50 photographs taken around the object at varying angles for optimum coverage. The digitized specimen consists of a section of a phragmocone with eight septa. An exposed septum at the adoral edge of the specimen was used as a base to reconstruct the entire septum. The suture line was used as a template to reconstruct the higher order frilling. An array of sculpting tools in Autodesk® Meshmixer Version 11.0.544 was used in order to manually reconstruct the frilled margins. The smoothing tool in Meshmixer was used to approximate the curvature of the septum between the frilled margins and the preserved first order folds. All reconstruction was performed on only half of the model. Meshmixer's mirror utility was used at the end

of processing in order to minimize errors in reconstruction by replicating the reconstructed portion of the model about the sagittal plane. The septum was placed inside a segment of the shell and extruded to a thickness of 0.85 mm. Meshmixer's smoothing function was used to remove the finer scale corrugations of the septum in order to compare the role of sutural complexity on cameral liquid retention. Both models with complex and simple septa were scaled to whorl heights of 60 mm and 90 mm to investigate the role of scaling on cameral liquid retention.

The complex and simple septa shape files were printed at both whorl heights in ABS-P430 filament with a Stratasys Dimension Elite 3D printer. Support material was dissolved with a 10% KOH solution and the models were dried in a fume hood for one day. After dry masses were recorded, each of the four models were submerged in water and allowed to drain by gravity for 10 seconds on the adoral and apical sides. Residual water on the external shell was removed before recording mass. Wet models were dried in the fume hood for at least one day and the trials were repeated for a total of five measurements.

2.3 RESULTS

2.3.1 Distribution in complexity and whorl height

The fractal dimensions for the ammonite hemisutures range from 1.16 to 1.62 (Table 1) out of a possible range of 1 to 2 for any fractal lying in a plane. Of course, ammonitic sutures would never reach either limit because they would have to approach a smooth line or infinitely corrugate to fill a two-dimensional area. The fractal dimensions (D_b) for these hemisutures are normally distributed and have a mean of 1.39 (Figure 2A).

		Min	Max	Mean	Std. Deviation
All Specimens (n=71)	D_b	1.16	1.62	1.394	0.099
	W_h(mm)	3.40	88.90	19.828	16.905
	Log(W_h(mm))	0.53	1.95	1.172	0.326
2D Coiled (n=53)	D_b	1.16	1.62	1.381	0.099
	W_h(mm)	3.50	88.90	21.457	18.665
	Log(W_h(mm))	0.54	1.95	1.193	0.348
3D Coiled (n=18)	D_b	1.29	1.60	1.450	0.086
	W_h(mm)	3.40	28.80	14.328	6.837
	Log(W_h(mm))	0.53	1.46	1.103	0.233

Table 1: Range, mean, and standard deviation of fractal dimensions (D_B), whorl height (W_h) in millimeters, and Log(W_h) for the 71 heteromorphic ammonite specimens of this study.

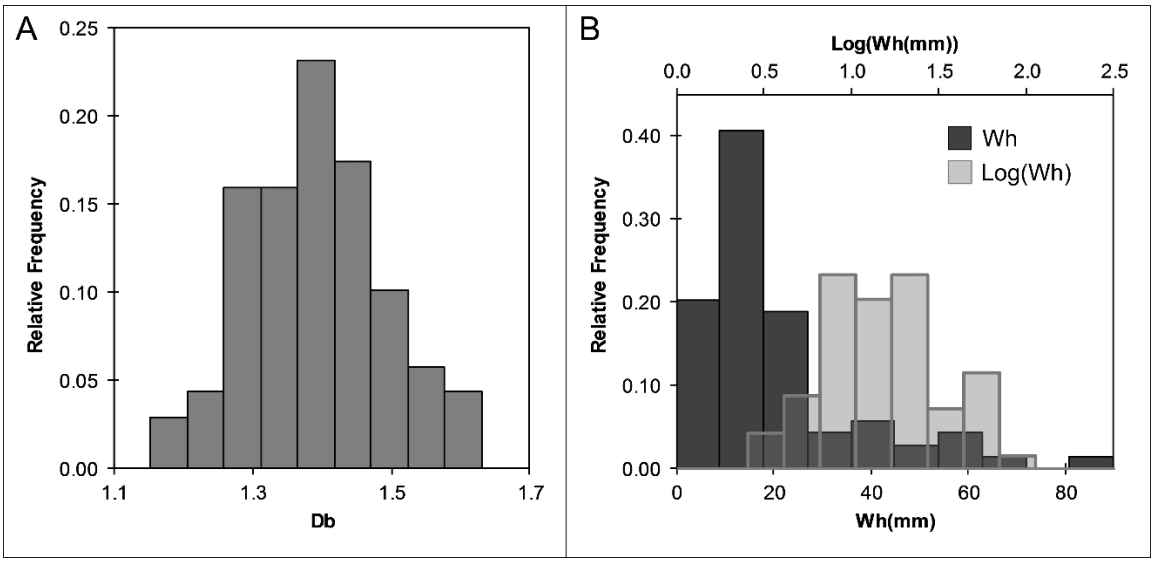

Figure 2: Distribution of fractal dimensions (D_B) for the 71 ammonite hemisutures in this study following a normal distribution (A). The whorl height (W_h) measurements at the terminal septum for these ammonites are lognormally distributed, which promote a logarithmic transform to maintain normality (B).

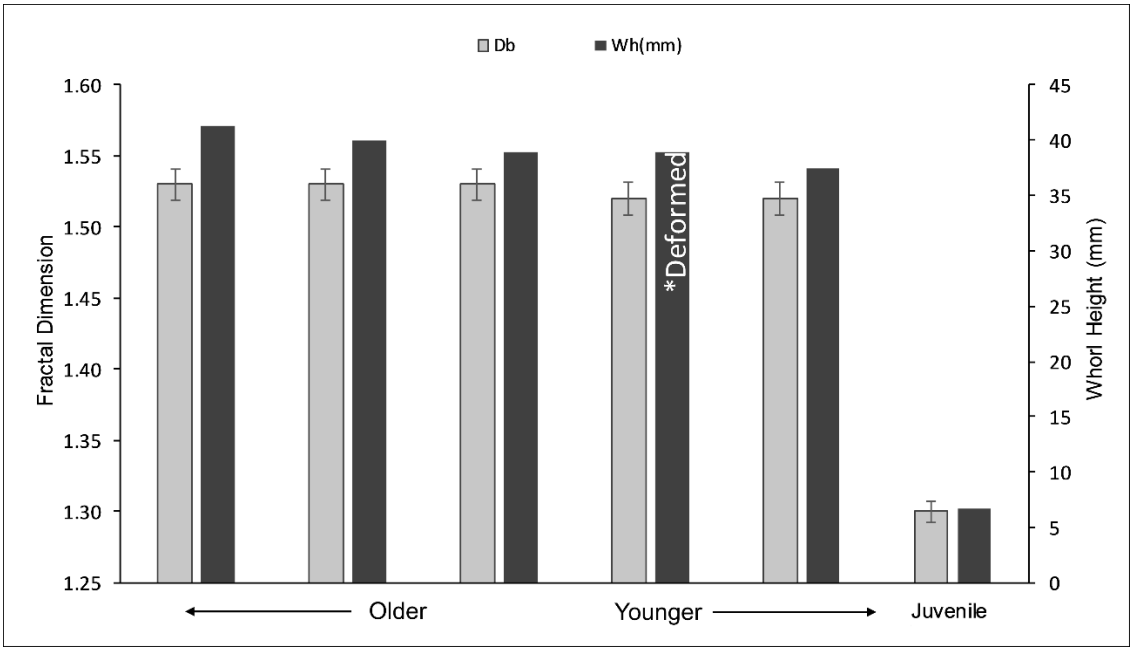

Figure 3: Fractal dimensions (D_B) computed from the right hemisutures of an adult specimen (WSU-1400) and juvenile specimen (WSU-1401) of *Baculites compressus*. Error bars represent standard error, and whorl heights (W_h) are recorded as a proxy for the age of septal formation. The asterisk marks an inaccurate measurement from the taphonomic deformation of the shell.

In contrast, whorl heights (W_h) are lognormally distributed (Figure 2B); a result of the relative abundance of smaller heteromorph specimens in this study.

2.3.2 Sutural ontogeny in *Baculites compressus*

Few suture patterns were reported or recorded at the terminal septum; however, all sutures included in this study have reached their adult stages, and therefore have reached full development of sutural complexity. To assess the significance of variation in complexity throughout ontogeny, hemisutures from an adult specimen (WSU-1400) and a juvenile specimen (WSU-1401) of *Baculites compressus* were analysed. The five hemisutures of the adult specimen have fractal dimensions of 1.53 on average and all fall within their respective standard errors (Figure 3). The insignificant variation in sutural

complexity between adult sutures facilitates the use of any adult suture patterns, and not necessarily the terminal suture. Of course, sutures do gradually degrade in complexity as they approach immature stages. This is made apparent from the much lower fractal dimension (D_B = 1.3) of the hemisuture from the juvenile specimen (Figure 3). A complete adult specimen preserving all sutures would be necessary to fully document the changes in complexity between the juvenile and adult sutures.

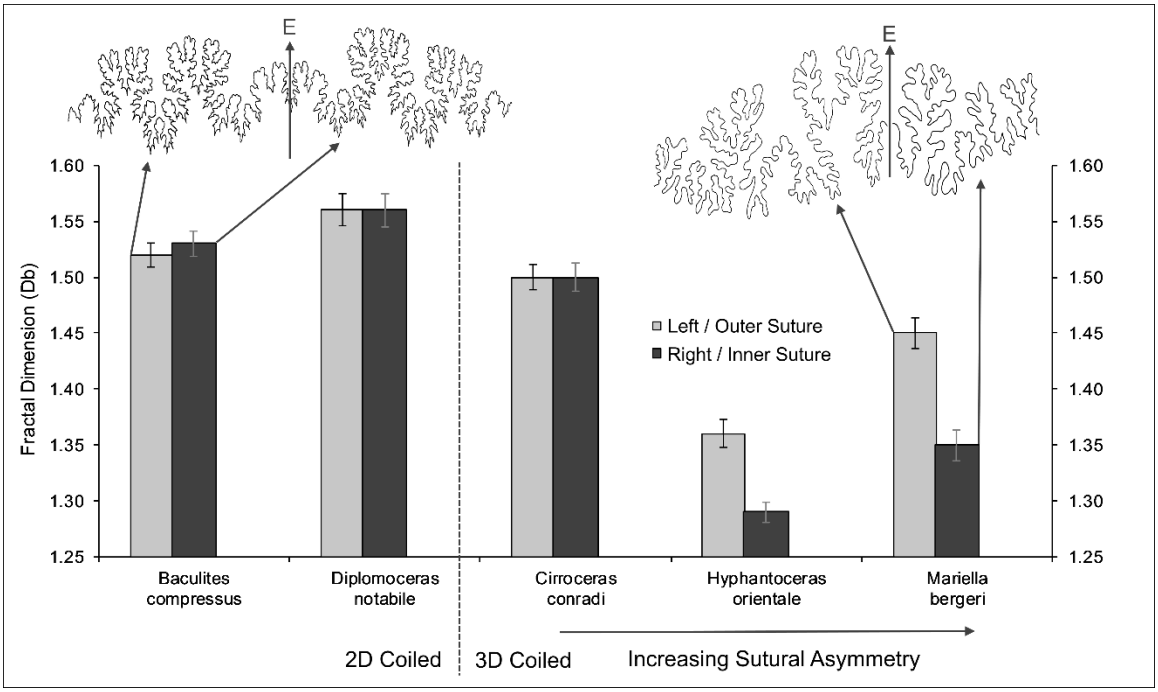

Figure 4: Fractal dimensions (D_B) computed for right and left hemisutures of two 2D coiled heteromorphic ammonites, and the inner and outer hemisutures of three 3D coiled heteromorphic ammonites. Error bars represent standard error. The suture pattern image of *Mariella bergeri* is modified from Ward (1979a).

2.3.4 Sutural symmetry and asymmetry in heteromorphic ammonites

Figure 4 is a comparison of both hemisutures for several 2D and 3D coiled heteromorphic ammonites. The fractal dimensions of hemisutures for the 2D coiled ammonites (*Baculites compressus* Say 1820 and *Diplomoceras notabile* Whiteaves 1903)

are negligibly different (difference of 0.01 and 0.00, respectively) while two out of three of the 3D coiled specimens (*Hyphantoceras orientale* Yabe 1904 and *Mariella bergeri* Brongniart 1822) have markedly different fractal dimensions for each hemisuture (0.07 and 0.10, respectively). The nostoceratid *Cirroceras conradi* Morton 1841 is the only examined 3D coiled heteromorph with no detectable difference in fractal dimensions between hemisutures.

2.3.5 Sutural complexity and whorl height

Tables 2 and 3 organize the 2D coiled and 3D coiled heteromorphic ammonites, respectively. Eleven out of 18 of the 3D coiled specimens had hemisutures on their outer whorls recorded, and only three specimens had both inner and outer hemisutures recorded (see Table 3). The remaining four specimens of the 3D coiled heteromorphs could not be classified as either outer or inner due to complex coiling schemes that deviate from the helical form. Figure 5 shows a positive relationship ($r = 0.69$, $p < 0.0001$) between fractal dimension and logarithm of whorl height for all of the ammonites studied herein. Since whorl heights are lognormally distributed (Figure 2B), log transforms were performed to maintain normality. The mean fractal dimensions for 18 3D coiled and 53 2D coiled hemisutures are 1.45 and 1.38 ($p < 0.01$), respectively (Figure 5). The whorl height means for the 3D coiled specimens appear to be lower than the 2D coiled specimens (14.3 mm and 21.5, respectively), but cannot be deemed significant ($p < 0.25$).

Family	Genus	Species	Age	D_b	W_h(mm)	Log(W_h)	SE of fit	Source
Anisoceratidae	*Algerites*	*sayni*	Cenomanian	1.29	9.0	0.954	0.006	Wright *et al.* 1996
Anisoceratidae	*Allocrioceras*	*angustum*	Upper Turonian	1.33	25.3	1.403	0.005	Wright *et al.* 1996
Anisoceratidae	*Anisoceras*	*merriami*	Late Albian	1.62	63.3	1.801	0.014	Packard & Jones 1962
Anisoceratidae	*Anisoceras*	*plicatile*	Cenomanian	1.39	13.2	1.121	0.010	Kennedy & Juignet 1983
Ancyloceratidae	*Crioceratites*	*nolani*	Upper Hauterivian	1.51	56.0	1.748	0.011	Wright *et al.* 1996
Anisoceratidae	*Idiohamites*	*dorsetensis*	Upper Albian	1.44	22.0	1.342	0.008	Wright *et al.* 1996
Anisoceratidae	*Phlycticrioceras*	*trinodosus*	Coniacian	1.37	29.0	1.462	0.004	Kennedy & Cobban 1991
Astiericeratidae	*Astiericeras*	*astierianum*	Middle Albian	1.30	6.0	0.778	0.012	Wright *et al.* 1996
Baculitidae	*Baculites*	*compressus*	Campanian	1.53	44.3	1.646	0.011	Present Study
Baculitidae	*Baculites*	*grandis*	Maastrichtian	1.44	88.9	1.949	0.009	Larson *et al.* 1997
Baculitidae	*Baculites*	*jenseni*	Upper Campanian	1.51	55.4	1.744	0.011	Larson *et al.* 1997
Baculitidae	*Baculites*	*rugosus*	Upper Campanian	1.58	52.7	1.722	0.013	Larson *et al.* 1997
Baculitidae	*Lechites*	*gaudini*	Upper Albian	1.31	11.0	1.041	0.004	Wright *et al.* 1996
Bochianitidae	*Bochianites*	*levis*	Berriasian	1.23	4.6	0.663	0.006	Arkadiev 2008
Bochianitidae	*Bochianites*	*neocomiensis*	Berriasian	1.27	6.8	0.833	0.005	Arkadiev 2008
Bochianitidae	*Bochianites*	*neocomiensis*	Valanginian	1.23	3.5	0.544	0.006	Arkadiev 2008
Bochianitidae	*Bochianites*	*oosteri*	Valanginian	1.20	4.0	0.602	0.008	Arkadiev 2008
Bochianitidae	*Bochianites*	*oosteri*	Lower Hauterivian	1.29	17.0	1.230	0.005	Arkadiev 2008
Bochianitidae	*Bochianites*	*oosteri*	Lower Barremian	1.36	8.0	0.903	0.006	Arkadiev 2008
Bochianitidae	*Janenschites*	*incisus*	Lower Barremian	1.32	7.7	0.886	0.011	Arkadiev 2008
Bochianitidae	*Janenschites*	*oosteri*	Lower Barremian	1.34	11.0	1.041	0.007	Arkadiev 2008
Bochianitidae	*Umgazaniceras*	*thieuloyi*	Upper Valanginian	1.16	4.2	0.623	0.015	Wright *et al.* 1996
Deshayesitidae	*Deshayesites*	*deshayesi*	Lower Aptian	1.33	14.0	1.146	0.008	Wright *et al.* 1996
Deshayesitidae	*Prodeshayesites*	*fissicostatus*	Lower Aptian	1.38	23.0	1.362	0.008	Wright *et al.* 1996
Diplomoceratidae	*Diplomoceras*	*notabile*	Campanian	1.56	42.0	1.623	0.014	Jones 1964
Diplomoceratidae	*Exiteloceras*	*jenneyi*	Campanian	1.47	24.0	1.380	0.011	Wright *et al.* 1996
Diplomoceratidae	*Exiteloceras*	*oronense*	Maastrichtian	1.51	36.0	1.556	0.012	Cobban 1974
Diplomoceratidae	*Neocrioceras*	*spinigerum*	Campanian	1.47	16.0	1.204	0.012	Wright *et al.* 1996

Diplomoceratidae	*Phylloptychoceras*	*sipho*	Campanian	1.39	6.0	0.778	0.009	Wright *et al.* 1996
Diplomoceratidae	*Rhyoptychoceras*	*mikasaense*	Coniacian	1.37	4.6	0.663	0.018	Matsumoto 1977
Diplomoceratidae	*Ryugasella*	*ryugasensis*	Campanian	1.32	8.0	0.903	0.005	Wright *et al.* 1996
Douvilleiceratidae	*Diadochoceras*	*nodosocostatum*	Upper Aptian	1.26	13.5	1.130	0.008	Wright *et al.* 1996
Douvilleiceratidae	*Douvilleiceras*	*monile*	Lower Albian	1.44	19.5	1.290	0.007	Wright *et al.* 1996
Douvilleiceratidae	*Eodouvilleiceras*	*horridum*	Upper Aptian	1.43	18.0	1.255	0.008	Wright *et al.* 1996
Hamitidae	*Hamites*	*attenuatus*	Middle Albian	1.39	9.5	0.978	0.008	Wright *et al.* 1996
Hamitidae	*Psilohamites*	*bouchardianus*	Upper Albian	1.33	10.0	1.000	0.005	Wright *et al.* 1996
Labeceratidae	*Labeceras*	*plasticum*	Upper Albian	1.31	8.0	0.903	0.006	Wright *et al.* 1996
Parahoplitidae	*Acanthohoplites*	*aschiltaensis*	Upper Aptian	1.29	13.5	1.130	0.007	Wright *et al.* 1996
Parahoplitidae	*Hypacanthoplites*	*plesiotypicus*	Albian	1.40	17.1	1.233	0.010	Wright *et al.* 1996
Parahoplitidae	*Parahoplites*	*melchioris*	Upper Aptian	1.25	13.0	1.114	0.010	Wright *et al.* 1996
Ptychoceratidae	*Ptychoceras*	*adpressum*	Upper Albian	1.37	18.4	1.265	0.014	Wright *et al.* 1996
Scaphitidae	*Acanthoscaphites*	*tridens*	Campanian	1.47	52.0	1.716	0.009	Wright *et al.* 1996
Scaphitidae	*Clioscaphites*	*vermiformis*	Santonian	1.33	18.0	1.255	0.004	Wright *et al.* 1996
Scaphitidae	*Desmoscaphites*	*bassleri*	Upper Santonian	1.46	29.6	1.471	0.012	Wright *et al.* 1996
Scaphitidae	*Discoscaphites*	*cheyennensis*	Maastrichtian	1.50	54.0	1.732	0.008	Wright *et al.* 1996
Scaphitidae	*Discoscaphites*	*iris*	Maastrichtian	1.29	11.5	1.061	0.009	Landman *et al.* 2004
Scaphitidae	*Eoscaphites*	*circularis*	Upper Albian	1.40	10.0	1.000	0.007	Wright *et al.* 1996
Scaphitidae	*Haresiceras*	*placentiforme*	Lower Campanian	1.36	10.1	1.004	0.011	Wright *et al.* 1996
Scaphitidae	*Hoploscaphites*	*constrictus*	Maastrichtian	1.39	17.0	1.230	0.008	Wright *et al.* 1996
Scaphitidae	*Mancosiceras*	*mancosense*	Upper Santonian	1.45	9.9	0.996	0.011	Wright *et al.* 1996
Scaphitidae	*Ponteixites*	*robustus*	Lower Maastrichtian	1.41	14.1	1.149	0.009	Wright *et al.* 1996
Scaphitidae	*Rhaeboceras*	*halli*	Campanian	1.46	44.0	1.643	0.007	Wright *et al.* 1996
Scaphitidae	*Scaphites*	*equalis*	Cenomanian	1.38	10.0	1.000	0.006	Wright *et al.* 1996

Tables 2: Heteromorphic ammonite specimens exhibiting 2D coiling. Taxa are organized alphabetically by family. Fractal dimensions (D_b), respective standard errors of fit (SE), whorl heights (W_h), Log(W_h), and sources are reported.

Family	Genus	species	Stage	D_b	$W_h$mm	LogW_h	SE of fit	Hemisuture	Source
Diplomoceratidae	*Glyptoxoceras*	*indicum*	Campanian	1.41	12.0	1.079	0.009	NA	Wright *et al.* 1996
Nostoceratidae	*Ainoceras*	*kamuy*	Campanian	1.37	10.5	1.021	0.013	Outer	Wright *et al.* 1996
Nostoceratidae	*Cirroceras*	*conradi*	Maastrichtian	1.50	21.7	1.336	0.012	Inner	Wade 1924 - Suture; Larson 2012 - Wh
Nostoceratidae	*Cirroceras*	*conradi*	Maastrichtian	1.50	21.7	1.336	0.012	Outer	
Nostoceratidae	*Hyphantoceras*	*orientale*	Santonian	1.29	10.0	1.000	0.009	Inner	Matsumoto 1977
Nostoceratidae	*Hyphantoceras*	*orientale*	Santonian	1.36	10.0	1.000	0.012	Outer	
Nostoceratidae	*Hyphantoceras*	*reussianum*	Turonian	1.47	21.1	1.324	0.013	Outer	Wright *et al.* 1996
Nostoceratidae	*Morewites*	*sakakibarai*	Campanian	1.31	3.4	0.531	0.007	NA	Shigeta 2014
Nostoceratidae	*Muramotoceras*	*yezoense*	Middle Turonian	1.57	9.5	0.978	0.017	Outer	Wright *et al.* 1996
Nostoceratidae	*Nipponites*	*occidentalis*	Upper Turonian	1.41	10.5	1.021	0.009	NA	Wright *et al.* 1996
Nostoceratidae	*Nostoceras*	*helicinum*	Maastrichtian	1.48	21.5	1.332	0.012	Outer	Cobban 1974
Nostoceratidae	*Nostoceras*	*hayatti*	Maastrichtian	1.45	20.5	1.312	0.012	Outer	Cobban 1974
Nostoceratidae	*Pravitoceras*	*sigmoidale*	Maastichtian	1.53	28.8	1.459	0.011	NA	Wright *et al.* 1996
Turrilitidae	*Mariella*	*bergeri*	Cenomanian	1.35	11.0	1.041	0.014	Inner	Ward 1979a - Suture; Wright *et al.* 1996 - Wh
Turrilitidae	*Mariella*	*bergeri*	Cenomanian	1.45	11.0	1.041	0.013	Outer	
Turrilitidae	*Ostlingoceras*	*rorayense*	Lower Cenomanian	1.40	5.5	0.740	0.007	Outer	Klinger & Kennedy 1978
Turrilitidae	*Pseudohelicoceras*	*robertianum*	Upper Albian	1.60	11.0	1.041	0.011	Outer	Wright *et al.* 1996
Turrilitidae	*Turrilites*	*costatus*	Cenomanian	1.49	18.2	1.260	0.008	Outer	Wright *et al.* 1996

Tables 3: Heteromorphic ammonite specimens exhibiting 3D coiling (nostocones, torticones, vermicones, etc.). Taxa are organized alphabetically by family. Fractal dimensions (D_b), respective standard errors of fit (SE), whorl heights (W_h), Log(W_h), hemisuture position, and sources are reported.

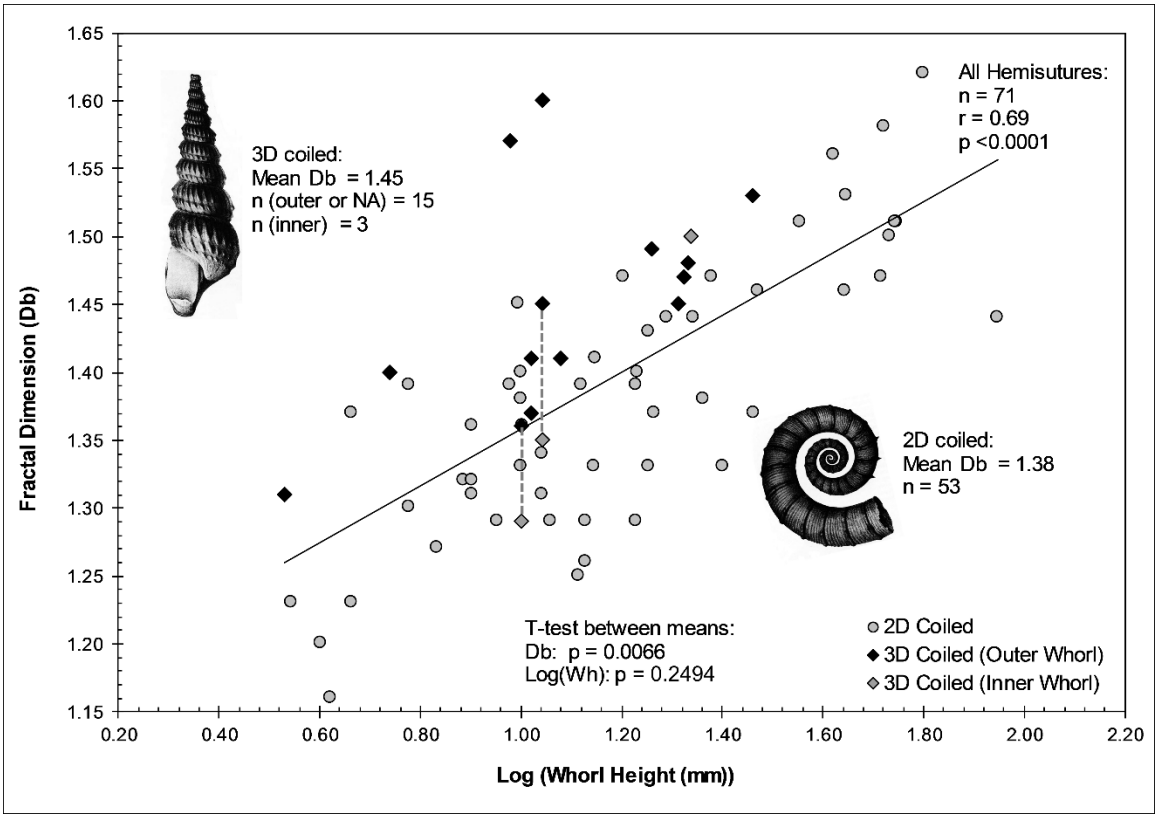

Figure 5: Fractal dimensions (D_B) versus logarithms (Log_{10}) of Whorl height measured in millimeters at the terminal septum. Dashed lines connect inner and outer whorl hemisutures for the same species.

2.3.6 Capillary retention simulated by 3D printed models

In order to investigate the role of scaling on the capillary retention of cameral liquids, a single reconstructed septum of *Baculites compressus* from specimen WSU-1400 was placed in shell segments that were scaled to 60 mm and 90 mm whorl height. The true septum of this species is closely approximated (Figure 6B) by reconstructing finer scale corrugations (lobules and folioles) with the recorded suture pattern (Figure 6A). The smoothed version of this septum (with finer scale corrugations erased; Figure 6D) was used to compare capillary retention between septa with a complex suture line (Figure 6A) and a simple suture line (Figure 6B) within the same whorl sections.

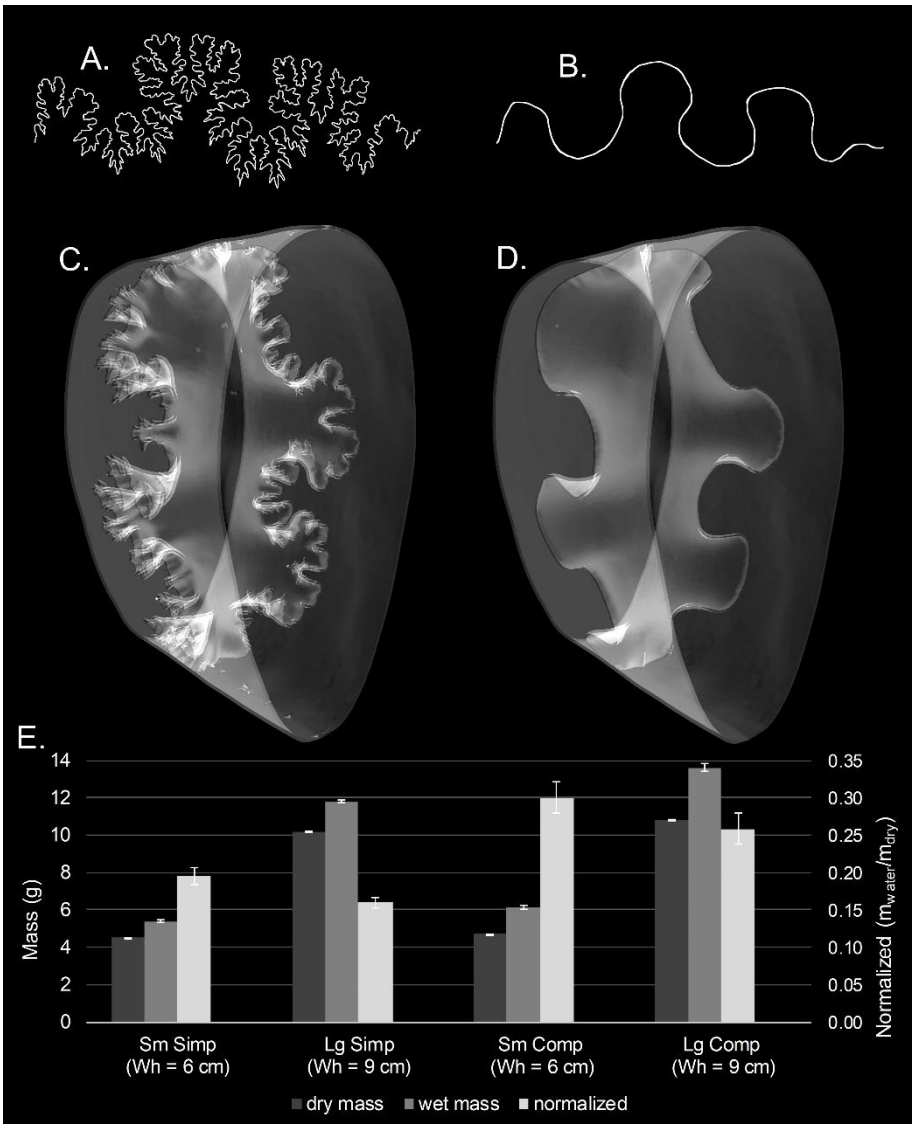

Figure 6: Suture line of *Baculites compressus* (A) recorded from specimen WSU-1400 and reconstructed septum (C). Suture line (B) and septum (D) after smoothing away finer scale corrugations (lobules and folioles). Averaged dry and wet masses (E) over 5 measurements of 3D printed models for small (sm) and large (lg) scaled versions of the simple (simp) and complex (comp) septa. The mass of liquid retained is normalised by the dry mass for each model to understand the mass of liquid retained per mass of septum. The differences in means of normalised masses between the large and small simple septa and the large and small complex septa are significant ($p = 0.0003$ and 0.0064, respectively).

The larger models both retain more liquid than their smaller counterparts. Furthermore, the models with complex septa (Figure 6C) retain a larger mass of liquid than the simple septa for both scales (Figure 6E; Table 4). However, by normalising the mass of liquid retention by the original dry mass of each model, larger models retain a lower mass of liquid per dry mass than the smaller models (Figure 6E; Table 4). Negligible variability in dry measurements resulted from the slow dissolution of residual support material from the surface of the models. Wet measurements were most heavily influenced by variability in capillary retention inside the marginal recesses of the models.

Model	m_{dry}	$\sigma(m_{dry})$	m_{wet}	$\sigma(m_{wet})$	m_{liquid}	$\sigma(m_{liquid})$	normalised	σ(normalised)
Sm Simp	4.516	0.005	5.396	0.048	0.880	0.051	0.195	0.011
Lg Simp	10.180	0.013	11.804	0.063	1.625	0.065	0.160	0.006
Sm Comp	4.720	0.003	6.136	0.099	1.416	0.099	0.300	0.021
Lg Comp	10.824	0.010	13.616	0.238	2.792	0.229	0.258	0.021

Table 4: Averaged dry and wet masses (g) of 3D printed models over 5 measurements with respective standard deviations (σ). The difference between the wet mass and dry mass yields the mass of liquid retention. Mass of liquid retained is normalised by dry mass as a metric for cameral liquid retention per septal mass.

2.4 DISCUSSION

2.4.1 Septal asymmetry in 3D coiled heteromorphs and the scaling properties of their hemisutures

Three-dimensionally coiled heteromorphs commonly exhibit asymmetrical septa. This results in hemisutures from the outer whorl displaying more elongated lobes and saddles than the hemisutures from the inner whorl (Ward 1979a). Figure 4 compares sutural complexity (quantified by fractal dimension) for two 2D coiled heteromorphs and three 3D coiled heteromorphs. The fractal dimensions for the right and left hemisutures

of both 2D coiled species (*Baculites compressus* and *Diplomoceras notabile*) are negligibly different. This suggests that their scaling is uniform on either side of the sagittal plane. Two of the 3D coiled species, *Hyphantoceras orientale* and *Mariella bergeri*, show significant differences in sutural complexity between hemisutures. Whereas the remaining 3D coiled species, *Cirroceras conradi*, does not display any significant difference. Seilacher & Gishlick (2015) suggest that this genus exhibits symmetry between hemisutures because the major septal elements were established early in a straight, juvenile phase. The sutural symmetry of *Cirroceras* is also consistent with the observation of Ward (1979a) who noted that septal asymmetry is more prominent in high-spired shell forms. The behaviour of these heteromorphs suggests that morphotypes with low apical angles and high whorl translations (e.g. the turrilitids) could have a larger difference in scaling between hemisutures than morphotypes with high apical angles and low whorl translations (e.g. the typical nostoceratid phragmocone). However, complete sutural recordings from additional helically coiled morphotypes are needed to fully understand this relationship between shell geometry and sutural complexity. The two-dimensional shape of the whorl section also influences this relationship in some way and should be further explored.

2.4.2 Sutural/septal scaling, shell size, and constructional constraints

While the evolution of frilled septa may have been shaped by their biological function (or functions), they could have also been influenced by phylogenetic overprinting and fabricational/constructional constraints (Seilacher 1973; Seilacher & Gishlick 2015; Klug & Hoffmann 2015; Monnet *et al.* 2015). The poorly understood phylogeny and polyphyly of Ancyloceratina makes it difficult to recognize existing

phylogenetic effects on sutural morphology. The effective environment may have also influenced morphology, which is demonstrated by the possible ecophenotypes of covariate shell forms (Monnet *et al.* 2011). Constraints on septal frilling have been evidenced by the relationship between sutural complexity and whorl height (Olóriz & Palmqvist 1995; Olóriz *et al.* 2002; Pérez-Claros *et al.* 2007) and by compression of the whorl section (Monnet *et al.* 2011, 2015). This behaviour is consistent with models of the viscous fingering of liquids (Checa & García-Ruiz 1996) where areas of larger radii yield fractals of higher fractal dimensions.

The fractal analysis of suture patterns from Cretaceous heteromorphic ammonites reveals a significant positive relationship ($r = 0.69$, $p < 0.0001$) between fractal dimension (D_B) and whorl height (W_h) at the terminal septum in adult specimens (Figure 5). Larger shells (proxied by larger W_h) have more space for lobes and saddles to extend into the longitudinal directions. Larger shells also exhibit an increase in finer scale corrugations (lobules and folioles relative to conch size), which can increase the space-filling of the pattern at finer scales. However, in terms of fractal geometry, a larger number of iterations doesn't necessarily increase the fractal dimension. This difference may be related to the approximation of suture patterns to a self-similar fractal. Suture patterns belonging to smaller shells (with lower W_h) are constrained by a smaller whorl section and are unable to expand to occupy space, resulting in lower fractal dimensions. The relationship between septal complexity and shell geometry for ancyloceratine taxa is consistent with studies of other taxa (Olóriz & Palmqvist 1995; Olóriz *et al.* 2002; Pérez-Claros *et al.* 2007). Although this does not illuminate the function of marginally frilled septa, it shows that their formation is governed by specific constructional constraints

(Seilacher 1973; Seilacher & Gishlick 2015). The size and shape of the whorl section particularly appear to govern the marginal frilling of septa during morphogenesis. As ectocochleate cephalopods grow, they construct a new septum in the posterior of the pre-formed living chamber. This whorl section at the time of septal morphogenesis constrains septal complexity, and therefore sutural scaling. The domain effect invoked in viscous fingering phenomena (Checa & García-Ruiz 1996; Monnet *et al.* 2011, 2015) can be used to explain the positive relationship between septal/sutural complexity and the area over which frilling can occur. Such constraints would similarly apply to reaction-diffusion processes, if the invaginations of the septal walls are controlled genetically by morphogens (Hammer 1999; Hammer & Bucher 1999).

The constraints responsible for the positive relationship between D_B and W_h (proxying shell size) for all ammonites in this study may also explain the sutural asymmetry observed in 3D coiled heteromorphs. The outer whorl hemisutures occupy a larger space, due to their larger whorl surfaces and radii of curvature, which is accompanied with an increase in scaling properties. The inner whorl hemisutures for 3D coiled heteromorphs are more confined, resulting in lower fractal dimensions from less available space (similar to the lower fractal dimensions of sutures with low W_h). This asymmetry is amplified by the adapical migration of the siphuncle (particularly represented throughout the turrilitid lineage; Klinger 1980) which causes the external lobe (E) and internal lobe (I) to become stretched on the outer whorl hemisuture, while compressing the inner whorl hemisuture. This suggests that constraints on septal morphogenesis in the case of sutural asymmetry can also be explained by the domain

effect (Monnet *et al.* 2011, 2015), displaying higher fractal dimensions for hemisutures that occupy larger whorl surfaces.

2.4.3 Functional constraints of septal frilling by capillary retention of cameral liquids

Fabricational constraints appear to be strong factors in the morphology of complex septa in ammonites. These constraints make it difficult to understand whether a functional component for frilled septa exists, and what selective pressures could have shaped them. In the context of a functional purpose, suture patterns with higher fractal dimensions, and more intensely frilled septal margins could have also been shaped by a functional constraint. However, this subject remains a contentious issue (Seilacher 1975; Klug *et al.* 2008; Klug & Hoffmann 2015).

In terms of complex septa acting as buttresses against hydrostatic pressure (Pfaff 1911; Spath 1919; Westermann 1975; Kennedy & Cobban 1976; Jacobs 1990; Hewitt & Westermann 1997; De Blasio 2008; Lemanis *et al.* 2016), increased sutural complexity could have improved support. However, the typical septal morphology is far from ideal to serve this function because of the low angles at which the septal margins meet the shell wall (Seilacher & Gishlick 2015). There is also much variability in the bathymetric zones in which the ammonites of this study resided (Ward 1979a; Klinger 1980; Westermann 1996). Studies of sutures from other taxa (Jurassic specimens of the superfamilies Phylloceratoidea, Lytoceratoidea, Perisphinctoidea, and Haploceratoidea) similarly find variability in bathymetric range and no correlation between habitat depth and sutural complexity (Olóriz & Palmqvist 1995; Olóriz *et al*. 1997, 1999, 2002; Pérez-Claros 2005).

The increased marginal frilling of septa could have influenced the buoyancy of the living ammonite in several ways. Cameral liquid would have been retained in these marginal recesses by surface tension and may have improved stability and living orientation (Kulicki 1979; Ward 1987; Kulicki & Mutvei 1988; Saunders 1995). This may have been a particularly difficult task for 3D coiled heteromorphs throughout ontogeny, which may have required a compensation mechanism. Marginal frilling could also increase the surface area of the septum, and therefore the wettable conchiolin composed pellicle membrane that lined each chamber (Mutvei 1967), possibly increasing the rate of buoyancy exchange (Mutvei & Reyment 1973; Saunders 1995; Klug & Hoffmann 2015). However, several caveats exist with these hypotheses. In the case of septal complexity influencing stability and orientation, retention of cameral liquid would only be useful for emptied camerae. Improving the rate of buoyancy exchange would have also been problematic. The rate of cameral liquid removal is likely insufficient to facilitate vertical migration due to the limitations of osmotic pumping. This would preclude the function of frilled septa allowing faster cameral liquid transport to the siphuncle (Ward 1979b).

Cameral liquid retention, simulated by 3D printed shell segments containing a single septum (Figure 6), provides some insight on a possible function of corrugated septal margins and shell scale. The complex septum retains more liquid via capillarity than the simple septum (Figure 6E; Table 4) for both 60 mm and 90 mm whorl heights. The simple septum with its lobules and folioles erased (Figure 6D), contains minor amounts of liquid on the septal surface and most at the septal margins that meet the shell wall. The complex septum also retains most of the cameral liquid at the margins, but

larger volumes are held in place by adhesion and surface tension. This yields more liquid retention in complex septal margins (i.e. larger perimeter per total length, or larger fractal dimensions; Lutz and Boyajian 1995) at a given scale. When the impact of scaling is considered, the larger model (W_h = 90 mm) retains less liquid per dry mass than the smaller model (W_h = 60 mm). Conceptually, as the shell approaches larger scales (in an isometric shell), the liquid along the septal margins begins to non-optimally fill the lobules and folioles because of changes in the relative capillary action. This suggests that more corrugated septal margins could be necessary in larger shells to retain as much cameral liquid per septal mass as a smaller shell with a simpler septum. This may also be associated with the relationship between sutural complexity (D_B) and shell size (W_h) observed herein (Figure 5). However, it would be essential to compute the amount of cameral liquid required for a neutrally buoyant condition (when appropriate) to fully understand if complex septal margins acted as cameral liquid reserves. Tajika *et al.* (2015) computed the percentage of cameral liquid required to make a 3D model of *Normannites* neutrally buoyant. They found nearly one third of the phragmocone must be filled with cameral liquid to satisfy this condition. This percentage suggests that each camera could require more cameral liquid than the volumes bound by the septal recesses. Therefore, if frilled septa used cameral liquid as ballasts, the dorsally oriented portions of each septum would more heavily influence the total mass distribution (and could actually reduce stability compared to a simple septum because the center of mass would be raised toward the center of buoyancy). The relationship between shell size and sutural complexity, regarding capillary retention of cameral liquids, also has potential ontogenetic implications. While sutural complexity changes from juvenile to adult

ontogenetic stages, a significant portion of the phragmocone retains very similar fractal dimensions (Figure 3). Therefore, these septa at younger ontogenetic stages (smaller scales) will retain more cameral liquid than those of older ontogenetic stages for septa that exhibit the same sutural complexity. This does not necessarily mean that juvenile phragmocones are more negatively buoyant, because a certain amount of cameral liquid may still be unbound from the marginal recesses or pellicle membrane. This raises the question of whether there is a specific biological function for cameral liquid retention in more complex septal margins or the changing relative abundance of cameral liquid throughout ontogeny.

The biological function (or functions) of complex septal margins in ammonites is poorly understood because it is difficult to distinguish this morphological component from others that shape septal morphology (including: fabricational constraints, phylogenetic overprinting, ecophenotypic variation, sexual dimorphism, etc.; Seilacher & Gishlick 2015). The results of this study suggest that septal morphology in terms of sutural complexity and scaling is most strongly influenced by the fabricational (constructional) constraints of whorl section size and shell geometry.

2.5 CONCLUSIONS

Although the number of elements and basic morphology of ammonite sutures/septa are genetically determined, their complexity and scaling are dependent upon whorl section and shell geometries. Septal asymmetry in high-spired 3D coiled morphotypes results in significantly different fractal dimensions between hemisutures. For these shell forms, outer whorl hemisutures exhibit higher fractal dimensions relative to inner whorl hemisutures. Hemisutures for 3D coiled heteromorphs also have higher

fractal dimensions (mean D_B = 1.45) on average than those of 2D coiled heteromorphs (Mean D_B = 1.38). All specimens measured in this study share a significant positive relationship between fractal dimensions and the logarithms of whorl heights ($r = 0.69$, $p < 0.0001$). Generally, larger shells can accommodate septa that marginally frill in such a way that increases the scaling and space-filling properties of their respective suture patterns. This behaviour, as well as the enlargement and increased complexity of outer whorl hemisutures for 3D coiled morphotypes (nostocones, torticones, and vermicones), may be a result of geometrical constraints of shell coiling and shell geometry. Septal/Sutural morphology behaves in a similar manner to viscous fingering models (Checa & García-Ruiz, 1996) in the sense that their morphogenesis is constrained by the size of the whorl section. In both cases, either ammonite septal frilling or viscous fingering, there is a positive relationship between fractal dimension and the available space over which these patterns are generated (García-Ruiz *et al*. 1990; Monnet *et al*. 2011, 2015). Complex septa with intricate marginal corrugations also have a range of scales over which they optimally retain cameral liquid. This may also play a role in the observed relationship between fractal dimension of sutures and shell size.

2.6 ACKNOWLEDGEMENTS

We greatly appreciate the help of Neal Larson with collecting the well-preserved specimens of *Baculites compressus* (WSU-1400 and WSU-1401). Our thanks also go to Mark Johnson at the Wright State Lake Campus Department of Engineering and Technology for 3-D printing the models used in the capillary retention experiments.

2.7 REFERENCES

Arkadiev, V., 2008, Representatives of the Family Bochianitidae (Ammonoidea) From the Lower Cretaceous of the Crimean Mountains. Paleontological Journal, v. 42, p. 468-478.

Arkell, W.J., Furnish, W.J., Kummel, B., Miller, A.K., Moore, R.C., Schindewolf, O.H., and Wright, C.W., 1957, Mollusca 4; Cephalopoda, Ammonoidea, Part L of Treatise on invertebrate paleontology, Moore, R. C., ed. xxii.

Barton, C., 1995, Fractal Analysis of Scaling and Spatial Clustering of Fractures. *In* Barton C.C. and La Pointe, P. R. (eds.), Fractals in the Earth Sciences, Plenum Press, New York. 141-178

Bayer, U, 1978, Constructional morphology of ammonite septa. Neues Jahrbuch fuer Geologie und Palaeontologie. Abhandlungen, v. 157, p. 150-155.

Bayer, U., 1985, Pattern recognition problems in geology and paleontology. Springer-Verlag. New York.

Boyajian, G. and Lutz, T., 1992, Evolution of Biological Complexity and Its Relation to Taxonomic Longevity in the Ammonoidea. Geology [Boulder], v. 20, p. 983-986.

Brongniart, A., 1822, Sur quelques terrains de Craie hors du Basin de Paris. In, Cuvier, G. and Brongniart, A. (eds.), Description geologique des environs de Paris, 3rd edn, 428p. Dufour & d'Ocagne, Paris, p. 80-101.

Checa A.G. and García-Ruiz, J.M., 1996, Morphogenesis of the septum. In Landman N.H., Tanabe K. & Davis R.A. (eds.) Ammonoid Paleobiology. Plenum, New York.

Cobban, W.A., 1974, Ammonites from the Navesink Formation at Atlantic Highlands, New Jersey. U. S. Geological Survey Professional Paper v. 845, p. 1-21.

Daniel, T.L., Helmuth, B.S., Saunders, W.B., and Ward, P.D. 1997: Septal complexity in ammonoid cephalopods increased mechanical risk and limited depth. Paleobiology, v. 23, p. 470-481.

Davis, R.A. Landman, N.H. Dommergues, J. Marchand, D. and Bucher, H., 1996, Mature Modifications and Dimorphism in Ammonoid Cephalopods. In Landman N.H., Tanabe K. and Davis R.A. (eds.) Ammonoid Paleobiology. Plenum, New York.

De Blasio, F.V., 2008, The role of suture complexity in diminishing strain and stress in ammonoid phragmocones. Lethaia, v. 41, p. 15–24.

Feder, J., 1988, Fractals. Plenum (now Springer), New York.

García-Ruiz, J.M. and Checa, A., 1993, A model for the morphogenesis of ammonoid septal sutures. GeoBios, v. 26, p. 157–162.

García-Ruiz, J.M., Checa, A. and Rivas, P., 1990, On the origin of ammonite sutures. Paleobiology, v. 16, p. 349–354.

Hammer, Ø., 1999, The development of ammonoid septa: An epithelial invagination process controlled by morphogens? Historical Biology, v. 13, p. 153-171.

Hammer, Ø. and Bucher H, 1999, Reaction-diffusion processes: Application to the morphogenesis of ammonoid ornamentation. Geobios, v. 32, p. 841-852.

Hassan, M.A., Westermann, G.E.G., Hewitt, R.A. and Dokainish, M.A., 2002, Finite-element analysis of simulated ammonoid septa (extinct Cephalopoda): Septal and sutural complexities do not reduce strength. Paleobiology, v. 28, p. 113-126.

Hewitt, R.A. and Westermann, G., 1997, Mechanical significance of ammonoid septa with complex sutures. Lethaia, v. 30, p. 205–212.

Hoffmann, R., Lemanis, R.E., Falkenberg, J., Schneider, S., Wesendonk, H. and Zachow, S., 2018, Integrating 2D and 3D shell morphology to disentangle the paleobiology of ammonoids: a virtual approach. Palaeontology, v. 61, p. 89–104.

Jacobs, D.K., 1990, Sutural pattern and shell stress in Baculites with implications for other cephalopod shell morphologies. Paleobiology, v. 16, p. 336–348.

Jacobs, D.K, 1996, Chambered Cephalopod Shells, Buoyancy, Structure and Decoupling: History and Red Herrings. PALAIOS, v. 11, p. 610–614.

Jones, D.L, 1963, Upper Cretaceous (Campanian and Maestrichtian) Ammonites from southern Alaska. U. S. Geological Survey Professional Paper, v. 432, p. 1–129.

Kakabadze. M.V., 2004, Intraspecific and intrageneric variabilities and their implication for the systematics of Cretaceous heteromorph ammonites; a review. Scripta Geologica, v. 128, p. 17–37.

Kennedy, W.J. and Cobban, W.A., 1976, Aspects of ammonite biology, biogeography, and biostratigraphy. Special Papers in Palaeontology, v. 17, p. 1–94.

Kennedy, W.J. and Cobban, W.A., 1991, Coniacian ammonite faunas from the United States Western Interior. The Palaeontological Association, Special Papers in Palaeontology, v. 45, p. 1–96.

Kennedy, W.J. and Juignet, P., 1983, A revision of the ammonite faunas of the type Cenomanian. I. Introduction, Ancyloceratina. Cretaceous Research, v. 4, p. 3–83.

Klinger, H. and Kennedy, W.J., 1978, Turrilitidae (Cretaceous Ammonoidea) from South Africa, with a discussion of the evolution and limits of the family. Journal of Molluscan Studies, v. 44, p. 1–48.

Klinger, H.C., 1980, Speculations on Buoyancy Control and Ecology in some Heteromorph Ammonites, p. 337-355. In House, M.R. and Senior, J.R. (eds.), The Ammonoidea, Academic Press Inc., New York.

Klug, C., Meyer, E.P., Richter, U. and Korn, D., 2008, Soft-tissue imprints in fossil and recent cephalopod septa and septum formation. Lethaia, v. 41, p. 477–492.

Klug, C. and Hoffmann, R., 2015, Ammonoid Septa and Sutures. In Klug, C., Korn, D., De Baets, K., Kruta, I. & Mapes, R.H. (eds.): Ammonoid paleobiology, Volume I: from anatomy to ecology. Topics in Geobiology, v. 43, p. 45–90, Springer, Dordrecht.

Klug, C., Zatoń, M., Parent, H., Hostettler, B. and Tajika, A., 2015, Mature Modifications and Sexual Dimorphism. In Klug, C., Korn, D., De Baets, K., Kruta, I. & Mapes, R. H. (eds.): Ammonoid paleobiology, Volume I: from anatomy to ecology. Topics in Geobiology, v. 43, p. 261–328, Springer, Dordrecht.

Kulicki, C., 1979, The ammonite shell, its structure, development and biological significance. Palaeontologia Polonica, v. 39, p. 97–142.

Kulicki, C., and Mutvei, H., 1988, Functional interpretation of ammonoids septa. In Wiedmann, J., Kullmann, J. (eds.) Cephalopods-present and past, Schweitzerbart, Stuttgart.

Larson, N.L., Jorgensen, S.D., Farrar, R.A. and Larson, P.L., 1997, Ammonites and the other cephalopods of the Pierre Seaway; identification guide. Geoscience Press, Tucson, AZ, United States.

Larson, N.L., 2016, The Late Cretaceous (upper Campanian) cephalopod fauna from the Coon Creek Science Center, McNairy County, Tennessee. Bulletin of the Alabama Museum of Natural History, v. 33, p. 1–40.

Landman, N., Johnson, R. and Edwards, L., 2004, Cephalopods from the Cretaceous/Tertiary Boundary Interval on the Atlantic Coastal Plain, With a Description of the Highest Ammonite Zones in North America. New York - American Museum of Natural History, v. 287, p. 1–83.

Lemanis, R., Zachow, S. and Hoffmann, R., 2016, Comparative cephalopod shell strength and the role of septum morphology on stress distribution. PeerJ, v. 4, e2434; DOI 10.7717/peerj.2434.

Lutz, T.M. and Boyajian, G.E., 1995, Fractal geometry of ammonoid sutures. Paleobiology, v. 21, p. 329–342.

Mandelbrot, B.B., 1983, The fractal geometry of nature. Freeman and co., San Francisco.

Manship, L.L., 2004, Pattern matching; classification of ammonitic sutures using GIS. Palaeontologia Electronica, v. 7, p. 1–15.

Monnet C., De Baets K. and Klug C., 2011, Parallel evolution controlled by adaptation and covariation in ammonoid cephalopods. BMC Evolutionary Biology, v. 11, p. 1-115. doi:10.1186/1471-2148-11-115

Monnet, C., De Baets, K. and Yacobucci, M., 2015, Buckman's Rules of Covariation, p. 67-94. In Klug, C., Korn, D., De Baets, K., Kruta, I. and Mapes, R.H. (eds.), Ammonoid Paleobiology: From Macroevolution to Paleogeography. Springer.

Morton, S.G., 1841, Description of several new species of fossil shells from the Cretaceous deposits of the United States. Proceedings of the Academy of Natural Sciences of Philadelphia, v. 1, p. 106–110.

Mutvei, H., 1967, On the microscopic shell structure in some Jurassic ammonoids. Neues Jahrbuch Fuer Geologie Und Palaeontologie. Abhandlungen, v. 129, p. 157–165.

Mutvei, H. and Reyment, R.A., 1973, Buoyancy control and siphuncle function in ammonoids. Palaeontology, v. 16, p. 623–636.

Olóriz, F. and Palmqvist, P., 1995, Sutural complexity and bathymetry in ammonites: fact or artifact? Lethaia, v. 28, p. 167–170.

Olóriz, F., Palmqvist, P. and Perez-Claros, J.A., 1997, Shell features, main colonized environments, and fractal analysis of sutures in Late Jurassic ammonites. Lethaia, v. 30, p. 191–204.

Olóriz F., Palmqvist, P. and Pérez-Claros, A., 1999, Recent advances in morphometric approaches to covariation of shell features and the complexity of suture lines in Late Jurassic ammonites, with reference to the major environments colonized. In Olóriz F. and Rodríguez-Tovar, F.J. (eds), Advancing Research on Living and Fossil Cephalopods. Kluwer Academic, New York.

Olóriz, F., Palmqvist, P. and Pérez-Claros, J., 2002, Morphostructural constraints and phylogenetic overprint on sutural frilling in Late Jurassic ammonites. Lethaia, v. 35, p. 18–168.

Packard, E.L. and Jones, D.L., 1962, A new species of *Anisoceras* from Oregon. Journal of Paleontology, v. 36, p. 1047–1050.

Paul, C.R.C., 2011, Sutural variation in the ammonites Oxynoticeras and Cheltonia from the Lower Jurassic of Bishop's Cleeve, Gloucestershire, England and its significance for ammonite growth. Palaeogeography, Palaeoclimatology, Palaeoecology, v. 309, p. 201–214.

Pérez-Claros, J., 2005, Allometric and Fractal Exponents Indicate a Connection between Metabolism and Complex Septa in Ammonites. Paleobiology, v. 31, p. 221–232.

Perez-Claros, J.A., Oloriz, F. and Palmqvist, P., 2007, Sutural complexity in Late Jurassic ammonites and its relationship with phragmocone size and shape; a multidimensional approach using fractal analysis. Lethaia, v. 40, p. 253–272. doi:10.1111/j.1502-3931.2007.00022.

Pfaff, E., 1911, Über Form und Bau der Ammonitensepten und ihre Beziehung zur Suturlinie. Jahresber. Nieders. geologischen Vereins Hannover, v. 4, p. 207–223.

Saunders, W.B., 1995, The ammonoid suture problem: relationships between shell and septum thickness and suture complexity in Paleozoic ammonoids. Paleobiology, v. 21, p. 343–355.

Say, T., 1820, Observations on some species of zoophytes, shells, etc., principally fossil. American Journal of Science, 1st ser., v. 2, p. 34–45.

Schindewolf. O.H., 1951, Zur Morphogenie und Terminologie der Ammoneen-Lobenlinie. Paläontologische Zeitschrift, v. 25, p. 11–34.

Seilacher, A., 1973, Fabricational noise in adaptive morphology. Systematic Zoology, v. 4, p. 451–465.

Seilacher, A, 1988, Why are nautiloid and ammonite sutures so different? Neues Jahrbuch fur Geologie und Palaontologie Ab-handlungen, v. 177, p. 41–69.

Seilacher, A. and Gishlick, A., 2015, Morphodynamics. Boca Raton, FL.

Shigeta, Y., 2014, *Morewites*, a new Campanian (Late Cretaceous) heteromorph ammonoid genus from Hokkaido, Japan. Paleontological Research, v. 18, p. 1–5.

Spath, L., 1919, Notes on ammonites. Geological Magazine, v. 56, p. 26–255.

Tajika, A., Naglik, C., Morimoto, N., Pascual-Cebrian, E., Hennhofer, D. and Klug, C., 2015, Empirical 3D model of the conch of the Middle Jurassic ammonite microconch *Normannites*: its buoyancy, the physical effects of its mature modifications and speculations on their function. Historical Biology, v. 27, p. 181–191.

Ubukata, T., Tanabe, K., Shigeta, Y., Maeda, H. and Mapes, R.H., 2009, Eigenshape analysis of ammonoid sutures. Lethaia, v. 43, p. 266–277.

Ubukata T., Tanabe, K., Shigeta, Y., Maeda H. and Mapes, R.H., 2014, Wavelet analysis of ammonoid sutures. Palaeontologia Electronica, v. 17, p. 1–17.

Wade, B., 1924, The fauna of the Ripley Formation on Coon Creek, Tennessee. U. S. Geological Survey Professional Paper, v. 137, p. 1–272.

Ward, P. and Westermann, G., 1977, First Occurrence, Systematics, and Functional Morphology of *Nipponites* (Cretaceous Lytoceratina) from the Americas. Journal of Paleontology, v. 51, p. 367–372.

Ward, P.D., 1979a, Functional Morphology of Cretaceous Helically-Coiled Ammonite Shells. Paleobiology, v. 5, p. 415–422.

Ward, P.D., 1979b, Cameral liquid in Nautilus and ammonites. Paleobiology, v. 5, p. 40–49.

Ward, P.D., 1987, The natural history of Nautilus. Allen and Unwin, Boston.

Wiedmann, J., 1969, The heteromorphs and ammonoid extinction. Biological Reviews of The Cambridge Philosophical Society, v. 44, p. 563.

Wiedmann, J. and Kullmann, J., 1980, Ammonoid sutures in ontogeny and phylogeny, In House, M.R. and Senior, J.R. (eds.), The Ammonoidea, Academic Press Inc., New York, p. 215-255.

Westermann, G.E.G., 1971, Form, structure and function of shell and siphuncle in coiled Mesozoic ammonoids. Life sciences contributions. Royal Ontario Museum, v. 78, p. 1–39.

Westermann, G.E.G., 1975, Model for origin, function and fabrication of fluted cephalopod septa. Paläontologische Zeitschrift, v. 49, p. 235–253.

Westermann, G.E.G., 1996, Ammonoid life and habitat. Ammonoid Paleobiology, Topics in Geobiology, v. 13, p. 607–707.

Whiteaves, J.F., 1903, Mesozoic fossils. Canada Geological Survey, Pt. 5, p. 309-416.

Wright, C.W., Callomon, J.H. and Howarth, M.K., 1996, Treatise on invertebrate paleontology, Part L, Mollusca 4 Revised, vol. 4: Cretaceous Ammonoidea. Geological Society America & University Kansas Press, Boulder.

Yabe, H., 1904, Cretaceous Cephalopoda from the Hokkaido, Part 2. Journal of the College of Science, Imperial University of Tokyo, v. 20, p. 1–45.

Yacobucci, M. and Manship, L., 2011, Ammonoid septal formation and suture asymmetry explored with a geographic information systems approach. Palaeontologia Electronica, v. 14, p. 1–17.

3.0 Mode of life and hydrostatic stability of orthoconic ectocochleate cephalopods: hydrodynamic analyses of restoring moments from 3D-printed, neutrally buoyant models

Peterman, D.J., Ciampaglio, C.N., Shell. R.C., and Yacobucci, M.M. 2019. Mode of life and hydrostatic stability of orthoconic ectocochleate cephalopods: hydrodynamic analyses of restoring moments from 3D-printed, neutrally buoyant models. *Acta Palaeontologica Polonica,* 64(3): 441–460.

Abstract

Theoretical 3D models were digitally reconstructed from a phragmocone section of *Baculites compressus* in order to investigate the hydrostatic properties of the orthoconic morphotype. These virtual models all had the capacity for neutral buoyancy (or nearly so) and were highly stable with vertical syn vivo orientations. Body chamber lengths exceeding approximately 40% of the shell length cause buoyancy to become negative with the given modeled proportions. The distribution of cameral liquid within the phragmocone does not change orientation and only slightly influences hydrostatic stability. The mass of cameral liquid required to completely reduce stability, permitting a non-vertical static orientation, would cause the living cephalopod to become negatively buoyant. A concave dorsum does not significantly change the mass distribution and results in a 5° dorsal rotation of the aperture from vertical. The restoring moments acting

to return neutrally buoyant objects to their equilibrium position were investigated using 3D printed models of *Nautilus pompilius* and *B. compressus* with theoretically equal masses and hydrostatic stabilities to their virtual counterparts. The *N. pompilius* behaved as an underdamped harmonic oscillator during restoration due to its low hydrostatic stability and drag relative to the *B. compressus* model. In contrast, the *B. compressus* model more quickly returns to its equilibrium position without oscillating (overdamped system). The thrust required to overcome such a large restoring moment was explored using several extant cephalopod analogues. Significant angles of displacement were only achieved with coleoid-like thrusts, which were unrealistically high despite the probable similarities in their locomotor design. These maximum bursts of thrust may have been too energetically expensive and would preclude a usual form of locomotion in a non-vertical orientation. These results suggest baculitids and other orthocones with similar hydrostatic stabilities probably lived a nektic to quasiplanktic mode of life with a primarily vertical orientation and mobility.

3.1 INTRODUCTION

3.1.1 Function of ectocochleate cephalopod shells and their hydrostatics

The conch of ectocochleate (externally-shelled) cephalopods consists of a body chamber that was inhabited by the living animal and a phragmocone that is divided by septa into a series of progressively larger chambers (camerae) during growth. The soft body and mineralized shell are denser than seawater and are negatively buoyant while the phragmocone is positively buoyant due to some fraction of gas in its chambers. The phragmocone allows the cephalopod to achieve neutral buoyancy and functions as a passive gas float by regulating the weight and bulk density of the cephalopod. Neutral

buoyancy is achieved when the total mass of the organism is equal to the mass of the displaced seawater. The syn vivo static orientation of a neutrally buoyant object occurs when the centers of buoyancy and mass are aligned vertically. Hydrostatic stability is determined by the degree of separation between these two centers (Okamoto 1996). A larger separation between the centers of buoyancy and mass relative to their weight will result in a larger restoring moment: a torque resulting from the downward acceleration of gravity acting on the center of mass and an upward buoyant force acting on the center of buoyancy. After displacing the centers of mass and buoyancy from a vertical alignment, this restoring moment returns the neutrally buoyant cephalopod to its equilibrium position. The rocking behavior of extant nautilids during locomotion reflects this hydrodynamic restoration after each jet pulse (Chamberlain 1981; Jacobs and Landman 1993). The manner in which this restoring moment acted upon extinct taxa during life is largely unknown, especially for non-planispiral morphotypes. Therefore, it is crucial to investigate the hydrostatic and hydrodynamic properties of different ectocochleate cephalopod morphotypes to better understand their specific modes of life and life habits.

We constructed several virtual 3D models of the Late Cretaceous heteromorph ammonoid *Baculites compressus* Say, 1820 to investigate the constraints and sensitivities on the hydrostatic properties of the straight-shelled (orthoconic) morphotype. This approach included calculating the liquid to gas ratio necessary for a neutrally buoyant condition, as well as the volume of the shell, camerae, and soft body. These properties were used to compute the syn vivo orientation and hydrostatic stability of this species, which provide a better understanding of the orthoconic morphotype and baculitid mode of life. The restoring moments acting on a baculite displaced from its equilibrium

position were also experimentally assessed with 3D printed models that have theoretically equal mass distributions and buoyancy to the virtual 3D models.

3.1.2 Previous studies of baculite hydrostatics and mode of life

The study of the geometry, buoyancy, and hydrostatics of ammonoids was pioneered by Moseley (1838) and Trueman (1941) in work that promoted a better understanding of ammonoid modes of life and led to many theoretical and empirical studies on these subjects (Raup and Chamberlain 1967; Saunders and Shapiro 1986; Shigeta 1993; Tanabe et al. 1995; Okamoto 1996; Kröger 2002; Hoffmann et al. 2014, 2015, 2018; Tajika et al. 2015a, 2015b; Lemanis et al. 2015; Naglik et al. 2015b, Peterman and Barton 2017; Peterman et al. 2018; Peterman and Ciampaglio 2018; Peterman et al. 2019). Trueman (1941) suggested that baculitids, as orthoconic heteromorphs would have been stably oriented with their aperture inclined downwards at rest due to the positive buoyancy of earlier chambers. This same orientation is also present in orthoconic nautiloids, endoceratoids, and actinoceratoids (Trueman 1941; Klinger 1980; Tsujita and Westermann 1998; Peterman et al. 2018), which have high hydrostatic stability in groups not possessing significant masses of cameral or endosiphuncular deposits (Peterman et al. 2019). The orthoconic morphotype of ectocochleate cephalopods has high hydrostatic stability relative to other morphotypes because its mass distribution is moved in a beeline fashion away from the center of buoyancy. Thus, a highly-stable, vertical orientation for orthoconic ectocochleates without cameral or endosiphuncular deposits has been commonly accepted (Reyment 1973; Ward 1976; Westermann 1977, 1996, 2013; Klinger 1980; Batt 1989; Peterman et al. 2018; Peterman et al. 2019).

While much evidence suggests that a highly-stable, vertical, static orientation is likely for orthocones, this interpretation is not without its caveats. Westermann (1977, 1996, 2013), Klinger (1980), and Tsujita and Westermann (1998) suggested that orthoconic ammonoids could deviate from this vertical posture by flooding the adapical portion of their phragmocone to act as a liquid counterweight. Westermann (2013) experimented on orthocone hydrostatics by creating several 2D models with neutral buoyancy. These models consist of several regions partitioned into cameral gas, cameral liquid, and the body chamber. Westermann (2013) found that models with adapically placed gas and flooded chambers directly behind the body had stable vertical orientations. However, placing the same proportion of cameral liquid adapically was found to reduce stability enough to permit horizontal swimming. Westermann (2013) also attempted to replicate the concave dorsum similar to *Baculites grandis* Hall and Meek, 1854 by creating a "quadripartite" model with adapical and adoral emptied chambers and a flooded portion in between. According to his model, a somewhat stable horizontal orientation was achieved without rolling (keeping the venter oriented downwards). A physical experiment was performed in his study where *B. grandis* was modeled with Plexiglas, Styrofoam, and various internal iron weights and which experienced a horizontal orientation when neutrally buoyant.

A non-vertical (sub-horizontal) orientation was inferred for the baculitid *Sciponoceras* sp. (Hauschke et al. 2011) by the orientation of a cirripede epizoan on the venter of the shell. The authors also suggested a forward direction of locomotion for this baculitid because the cirripede grew from the venter and slightly rotated the feeding apparatus towards the aperture throughout growth. This epizoan behavior is also recorded

for planispiral ectocochleate cephalopods including other ammonoids and even the extant *Nautilus* (Keupp et al. 1999; Seilacher and Keupp 2000; Hoffmann and Keupp 2015; Seilacher and Gishlick 2015; Naglik et al. 2015a).

The depth range of baculitids (including *B. compressus*) in the Western Interior Seaway of the United States may have been around 50-100 meters based on isotopic analyses (Fatherree et al. 1998; Lukeneder et al. 2010; Landman and Klofak 2012; Henderson and Price 2012; Lukeneder 2015; Landman et al. 2018). Additionally, a demersal habitat is inferred from these analyses due to their isotopic similarity with the benthos (Sessa et al. 2018; Landman et al. 2018), which suggests that these baculitids may have lived within a few meters from the sea bottom. Ontogenetic sampling of baculites from methane seeps reveals they probably did not laterally migrate over long distances and spent the majority of their lives at or nearby these sites (Landman et al. 2018).

Information about the baculitid diet can be inferred by the morphology of the buccal mass. Kruta et al. (2011) reported on a buccal mass of a baculite revealed by synchrotron x-ray microtomography that had remains of possible prey items including pelagic isopods and possibly a larval gastropod. The morphology of the baculitid buccal mass along with the remains of potential prey suggests that they fed on small organisms in the water column (Kruta et al. 2011). This interpretation is reinforced by Klug et al. (2012), who also suggest a planktotrophic feeding habit based on several well-preserved baculitids.

3.1.3 Three-dimensional modeling of ectocochleate cephalopods

Recently, accurate hydrostatic analyses have been improved by tomographic techniques. The application of computed tomography (CT) can yield 3D models with excellent precision to aid in morphometry (Hoffmann et al. 2014; Lemanis et al. 2015; Tajika et al. 2015a) and the approach has been used for hydrostatic calculations, including the conditions for neutral buoyancy (Hoffmann et al. 2014, 2015, 2018; Lemanis et al. 2015). However, low contrasts in physical properties (X-ray attenuation, etc.) between the matrix and/or mineral growth inside chambers and the fossil shell can yield problems in imaging the fossil anatomy, as can averaging of densities of different materials within each voxel (the partial volume effect; see Hoffmann et al. 2014). The ideal scenario involves well-preserved specimens with hollow chambers, or in the case of Inoue and Kondo (2016), chamber casts surrounded by a void after shell dissolution. The reconstruction of ammonites with complex septal frilling is especially difficult where mineral growth covers the internal shell and/or septa and distorts higher-order folds. When the conditions are adequate for ideal 3D reconstructions, these models can be used to compute the hydrostatic properties from the volumes, and therefore mass, of the materials occupying the camerae, soft body, shell, and any other feature with a unique density. These morphometrics can be then used to compute buoyancy, syn vivo orientation, and stability. Serial grinding tomography is also a valuable tool for constructing models to be used in morphometry and hydrostatic calculations (Tajika et al. 2015a, 2015b; Naglik et al. 2015b, 2016). These techniques can produce 3D models from processing many successive slices through an object. Of course, this method is invasive and causes complete destruction of the specimen. It is also susceptible to the partial volume effect and other discrepancies (Hoffmann et al. 2014).

While tomographic techniques can produce accurate 3D models of cephalopod shells, they rely on ideal specimens that are complete, undeformed, and have appropriate contrasts (either optically or by attenuation factor) between the shell and its surroundings. Theoretical 3D models for virtual paleontology are a necessary alternative to tomographic modeling for rare species or specimens that seldom preserve in an adequate manner for 3D imaging. Such models can be generated by imaging and reconstructing multiple fragmentary specimens or replicating real pieces until the whole specimen is virtually reconstructed. Such reconstructions can be performed with the use of photogrammetry in the absence of access to tomographic equipment or expensive surface scanners. Photogrammetry can be used to scan the exterior of a specimen by generating a 3D mesh from a series of overlapping photographs (Sutton et al. 2014). This method has been more recently used in paleontology (Petti et al. 2008; Falkingham 2012; Knauss and Yacobucci 2014; Fau et al. 2016), and can yield 3D models of comparable resolution to high quality surface scanners (Fau et al. 2016). This cheap and portable technique (Cunningham et al. 2014) can be suitable to produce theoretical models of ectocochleate cephalopod shells for the computation of their hydrostatic properties (Peterman and Barton 2017; Peterman and Ciampaglio 2018).

Institutional abbreviations.---WSU, Department of Earth and Environmental Sciences, Wright State University, Dayton, Ohio, USA.

3.2 METHODS

3.2.1 Modeled specimens

Orthoconic (straight-shelled) cephalopods (e.g., nautiloids, baculitids, etc.) are rarely found complete because long, slender, hollow shells are subject to myriad

taphonomic processes that result in disarticulation and alteration. A baculite was chosen for the current study because specimens are common and excellently preserved in concretions within the Upper Cretaceous Pierre Shale in the U.S. Western Interior. Such specimens exhibit largely unaltered shell material that is required to define shell and septum thicknesses and ultimately the volume for theoretical virtual models. Fragmentary specimens of the late Campanian baculite species *Baculites compressus* were used in this study to create the 3D models and measure shell and septal thicknesses. These specimens are currently housed at WSU.

3.2.2 Virtual model generation

The virtual 3D model of the extant *Nautilus pompilius* from Peterman et al. (2019; fig. 2.5) was used in the current study to serve as a reference for the hydrostatic experiments of the orthoconic *Baculites compressus*. This model also served as an assessment of the experimental modeling techniques used in this study. The *Nautilus pompilius* model, although isometric, was found to have very similar hydrostatic properties to a model generated from a CT-scanned specimen (Hoffmann et al. 2014; Lemanis et al. 2015, 2016), especially in terms of hydrostatic stability (Peterman et al. 2019).

Several theoretical 3D models were digitally reconstructed from a fragmentary specimen of *Baculites compressus* (WSU-1400). A 3D shapefile of this specimen was created with 3DF Zephyr (3DFlow 2018) photogrammetry software (Fig. 1A). This produces a tessellated 3D mesh (in .stl format) from a series of photographs taken around the object (~50 for optimum coverage). The digitized specimen consists of a section of a phragmocone with eight septa. An exposed septum at the adoral edge of the specimen

(Fig. 1B) was used as a base to reconstruct the entire septum. The suture line (Fig. 1C) was used as a template to reconstruct the higher order frilling. An array of sculpting tools in Meshmixer (Autodesk Inc. 2017a) was used in order to manually reconstruct the frilled margins (Fig. 1D). The smoothing tool in Meshmixer (Autodesk Inc. 2017a) was used to approximate the curvature of the septum between the frilled margins and preserved first and second order folds. All reconstruction was performed on only half of the model. Meshmixer's mirror utility was used at the end of processing in order to minimize errors in reconstruction by replicating the reconstructed portion of the model about the sagittal plane.

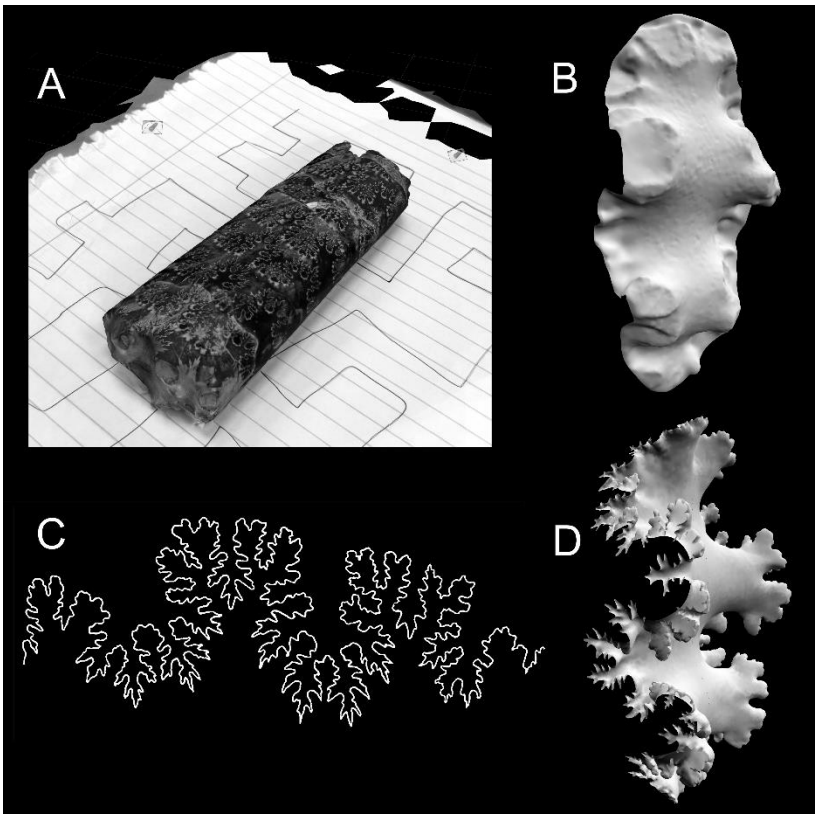

Figure 1: Three-dimensional reconstruction of a fragmentary baculite. **A.** Model of a fragmentary specimen of *Baculites compressus* (WSU-1400) generated by photogrammetry with the software, 3DF Zephyr. **B.** Broken septum isolated from the photogrammetry model of WSU-1400. **C.** Suture pattern of *Baculites compressus* recorded from WSU-1400. **D.** Complete septum created by reconstructing the higher-order frilling with the suture pattern as a template.

After reconstructing a single septum, it was then duplicated and placed inside the segment of shell that was originally scanned. The magnetize tool in Meshmixer (Autodesk Inc. 2017a) was used to seal the space between the septa and the shell while simultaneously smoothing the model. The septal spacing was relatively constant and was achieved by placing the farthest-reaching folioles tangential to the farthest-reaching lobules from the previous (adoral) septum. This yielded a single septate section of shell which was then duplicated in order to recreate the entire phragmocone of the baculite using the degree of taper from the scanned fragment. The living chamber was constructed by using the originally scanned shell fragment with the same degree of taper.

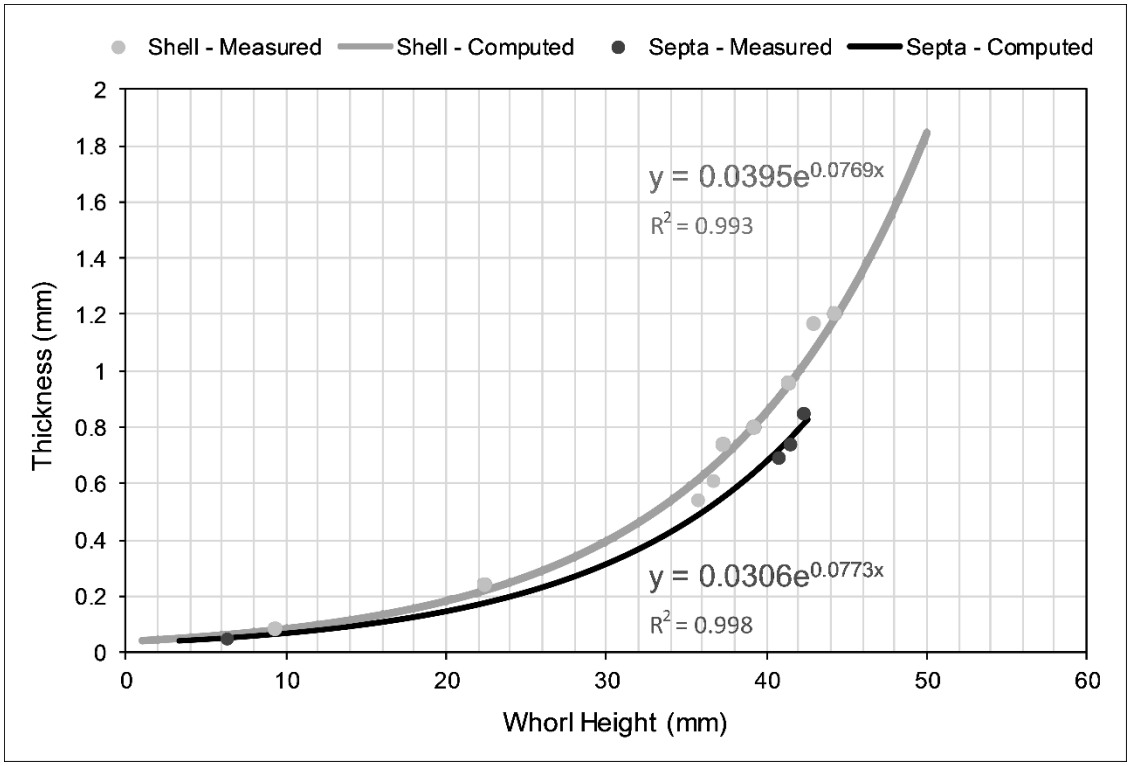

Figure 2: Shell and septum thickness measured from three specimens of *Baculites compressus* (WSU-1400, WSU-1401, and WSU-1405). Exponential curves were fit to these points to define thickness for the full 3D model as a function of whorl height.

Measurements of shell and septum thickness were made using digital calipers on well-preserved specimens (WSU-1400, WSU-1401, and WSU-1450). Exponential curves (Fig. 2) were used to estimate shell and septum thickness in the model corresponding to whorl heights (Wh). The 3D computer graphics software, Blender, was used to define thickness of the model. This process, called extrusion, was performed with positive offset on the external shell segments. These segments were then sealed together and smoothed in Meshmixer (Autodesk Inc. 2017a) in order to recreate an extruded thickness gradient similar to the actual shell of an adult *Baculites compressus* (Fig. 2). The 83 septa were individually extruded in Blender with zero offset and combined with the extruded shell to create a complete shell model (Fig. 3A). The length of the body chamber was reconstructed at 40% and 33% of the total length of the baculite in order to compare the hydrostatics between the upper and lower limits of the "mesodome" body chamber ratio (Westermann 2013).

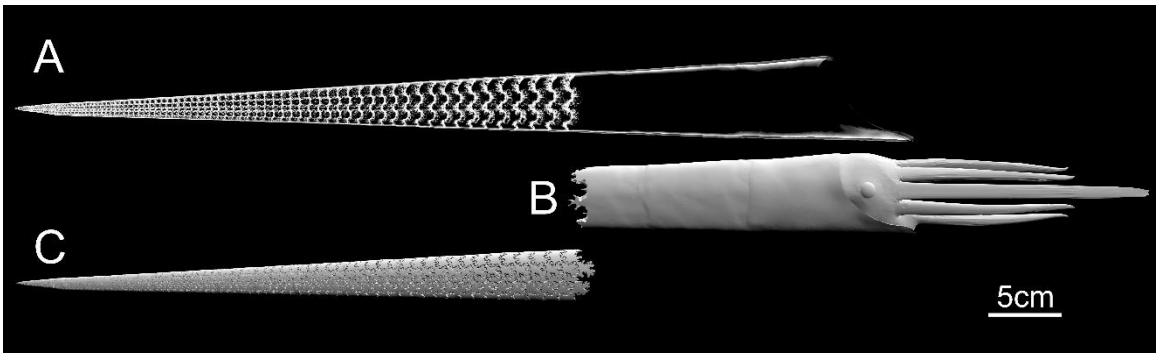

Figure 3: Full 3D model of *Baculites compressus* with model components. **A.** Complete, digitally-reconstructed shell rendered in X-ray view to show internal structure. **B.** Three-dimensional model the soft body. **C.** Three-dimensional model of the cameral volumes within the phragmocone.

The soft body was reconstructed by deleting the external wall of the baculite shell mesh and isolating the living chamber. This represents the interface between mineralized shell and the soft body. The normals of the faces were inverted (which denote the exterior direction of the mesh) to produce a mesh that appropriately has its normals pointing outwards. The soft body, which resembles the baculitid reconstruction of Klug et al. (2012), was then constructed and shaped to fit inside the living chamber (Fig. 3B). Each camera was reconstructed in a similar manner to the soft body. The exterior mesh of the phragmocone was deleted and the internal interfaces were isolated and inverted. This allowed the reconstruction of all camerae (Fig. 3C) and for each of their volumes to be calculated. Each model had to be repaired using Autodesk Netfabb (Autodesk Inc. 2017b) to remove non-manifold elements and other mesh errors in order to calculate geometric measurements. All volumes and centers of mass were then calculated with MeshLab (Cignoni and Ranzuglia 2014).

3.2.3 Hydrostatic calculations

Hydrostatic calculations herein largely follow the methods of Peterman et al. (2019). The proportion of cameral gas and cameral liquid to produce a neutrally buoyant condition was calculated for each model using a modification of Archimedes principle:

$$m_{sb} + m_{sh} + m_{cl} + m_{cg} = m_{wd} \quad (1)$$

Where m_{sb} is the mass of the soft body, m_{sh} is the mass of the shell, m_{cl} is the mass of cameral liquid, m_{cg} is the mass of cameral gas, and m_{wd} is the total mass of water displaced.

The ratio of the volume of cameral gas to total cameral volume (Φ) is found by setting Equation 1 in terms of density and volume then solving for Φ:

$$\Phi = \frac{\left(\frac{V_{wd}\rho_{wd} - V_{sb}\rho_{sb} - V_{sh}\rho_{sh}}{V_{ct}}\right) - (\rho_{cl})}{(\rho_{cg} - \rho_{cl})} \quad (2)$$

Where V_{wd} and ρ_{wd} are the volume and density of the water displaced by the entire model, V_{sb} and ρ_{sb} are the volume and density of the soft body, V_{sh} and ρ_{sh} are the volume and density of the shell, ρ_{cl} is the density of cameral liquid, ρ_{cg} is the density of cameral gas, and V_{ct} is the total volume of all camerae. A soft body density of 1.065 g/cm^3 is adopted from Westermann (2013) and is assumed here to uniformly fill the living chamber (Fig. 3B). A shell density of 2.62 g/cm^3 is also commonly accepted (Reyment 1958; Okamoto 1996; Klug and Hoffmann 2015). The density of cameral liquid is assumed to be equal to that of seawater (1.025 g/cm^3; Greenwald and Ward 1987). The density of cameral gas is negligible, but set here for calculations as 0.001 g/cm^3.

The volumes of cameral gas and liquid necessary for neutral buoyancy were then modeled by splitting the shapefile containing all of the modeled camerae (Fig. 3C) into their appropriate gas and liquid fractions. These models do not include the pellicle or liquid retained via capillary forces. They also do not include the siphuncle, a feature with a probably negligible mass relative to the total organismal mass (Lemanis et al. 2015).

The models of the shell, soft body, cameral gas, and cameral liquid each have a density-weighted influence on the mass distribution of the living baculite due to their differences in density and geometry. The total center of mass from these models of differing densities was calculated with the formula:

$$M = \frac{\sum(L * m_o)}{\sum m_o} \quad (3)$$

Where M is the x, y, or z component of the total center of mass, L is the x, y, or z component of the center of mass of a single object measured with respect to an arbitrary datum, and m_o is mass of any particular object that has a unique density (this includes the shell, soft body, cameral gas, and cameral liquid for the models herein).

The center of buoyancy can be found by computing the center of mass of the water displaced by the baculite (i.e. center of volume). The stability of the model depends on the degree of separation between the centers of buoyancy and mass. Their true separation was found by using the theorem of Pythagoras on the x and z components of the models (ignoring the y components because of model symmetry). In order to apply to heteromorphic ammonoids, Okamoto (1996) redefines the stability index (S_t) of Raup (1967):

$$S_t = \frac{\overline{BM}}{\sqrt[3]{V}} \quad (4)$$

Where S_t is the stability index, $\overline{BM}$ is the distance between the center of buoyancy and mass, and V is the entire volume occupied by the model (equal to V_{wd} defined above).

3.2.4 Restoring moment experiments with 3D-printed models

Physical experimentation to investigate hydrostatics and hydrodynamics is hindered by the difficulty in creating models with the same mass (and distribution of that mass) as the living animal. This is primarily because morphometry and physical reconstruction are rather difficult in fossil shells (especially the ammonoids), and because there are no perfect model analogues for the materials of which the living animal was composed. In the current study, these caveats were addressed by modifying the virtual models (Fig. 4A) so that they had very simple internal geometry (Fig. 4B) while still having the same center of buoyancy as the original virtual models. The differences in

mass and total center of mass were corrected by 3D printing the modified virtual models in PLA (polyactic acid) filament, and then solving for the mass and position of a bismuth counterweight within the model (Figs. 4C and 4D).

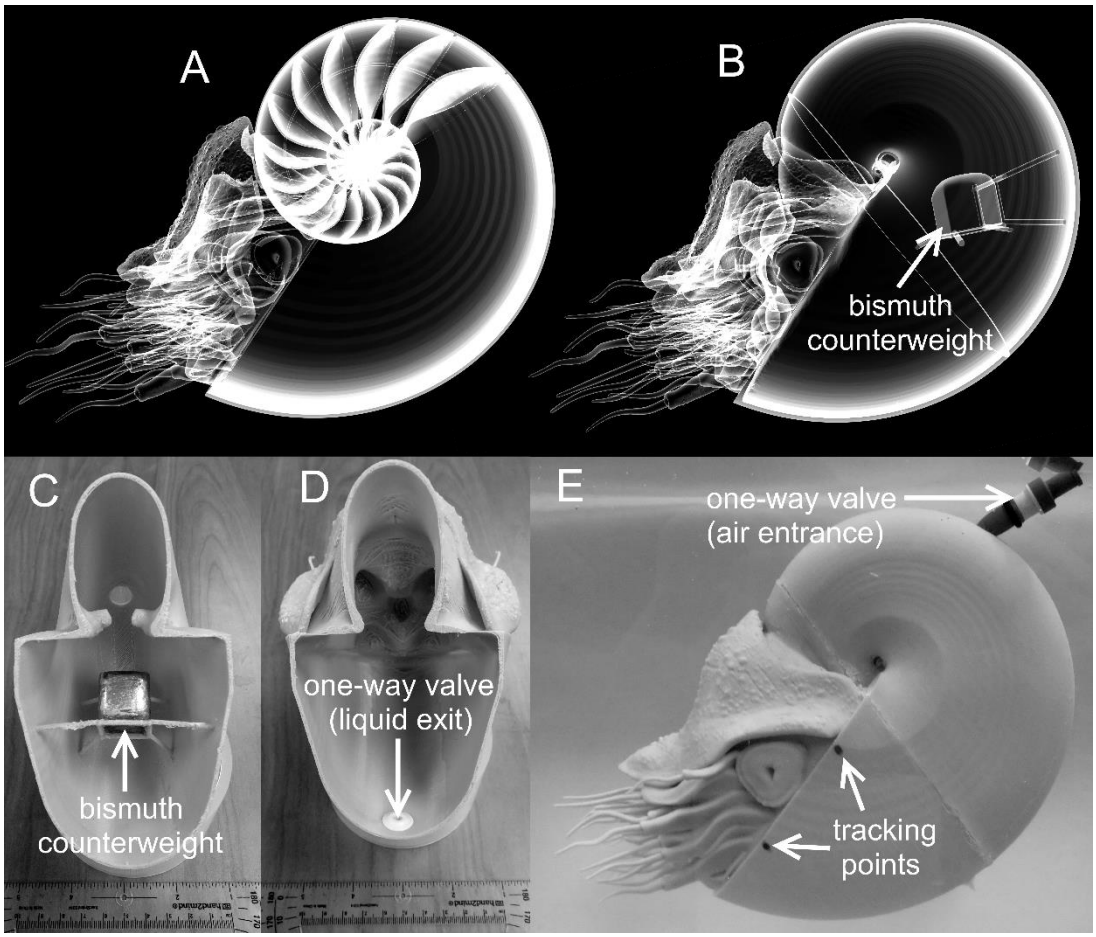

Figure 4: Generation of a 3D-printed model of *Nautilus pompilius* with theoretically equal physical properties to the virtual counterparts. A. Original virtual model from Peterman et al. (2019; fig. 2.5). B. Modified virtual model with simplified internal geometry. The center of buoyancy remains the same because external geometry does not change. The total center of mass, however, is corrected by a bismuth counterweight of known volume, density, and mass. C. 3D-printed posterior half of the physical model with bismuth counterweight in the computed position. D. Anterior half of the physical model showing the one-way valve for liquid to exit upon displacement by an air-filled balloon. E. Neutrally buoyant physical model with the required volume to liquid ratio for neutral buoyancy. This computed volume of air is inserted through a one-way entrance valve into the internal balloon. Tracking points are placed parallel to the aperture in order to analyze movement in a hydrodynamic setting.

The position of the counterweight was solved by modifying Equation 3 as follows:

$$L_{Bi} = \frac{M*\sum(m_o)-\sum(L*m_o)}{m_{Bi}} \quad (5)$$

Where L_{Bi} is the x, y, or z component of the counterweight and m_{Bi} is the mass of the bismuth counterweight. This counterweight allows the models to be constructed with completely different internal geometries and densities to the living animal (Fig. 4E), yet they still have theoretically equal hydrostatic properties (that is, the centers of mass and buoyancy). Since all physical experiments were performed in freshwater, the density of the water displaced (ρ_{wd}) for these models was changed from 1.025 g/cm^3 to 1.000 g/cm^3.

The densities of the PLA (after printing an object) and the bismuth counterweight were measured directly on reference objects that were constructed with simple geometries (2 cm cubes). The bismuth counterweights were casted by creating a positive model of the weight in Blender, surrounded by a base and walls in the horizontal directions. This positive model was then 3D printed and filled with high performance silicone rubber casting material. This process created a mold that could withstand the heat of melted bismuth (~270°C) and with the required dimensions for each model. The 3D printed models required some ratio of gas and liquid so that they could achieve neutral buoyancy. After submerging the models and filling them with water, the computed volume of gas was inserted through a one-way valve into a latex balloon (Fig. 4E), which displaced the internal water through another one-way valve (Fig. 4D) until the desired ratio was achieved. This process was conducted for the *Nautilus pompilius* model and the *Baculites compressus* model. The 3D printed *B. compressus* model was scaled from a length of 86.4 cm to 60.0 cm in order to fit in the 1000 L tank where the restoration

experiments were performed. The neutrally buoyant models of *N. pompilius* and *B. compressus* were rotated approximately 38˚ from their static syn vivo orientations and released. This angle was chosen because it was easy to measure for the *Nautilus* model and equals its syn vivo apertural angle measured from the vertical axis. The movement of each model was digitally recorded and analyzed with the physics modeling software, Tracker 4.11.0 (Brown 2017). Two points, parallel to the transverse plane, were placed on each of the models (Fig. 4E) and their X/Z coordinates were recorded as a function of time (Fig. 5). The angles of the apertures (where horizontally facing = 0˚, downward vertical = -90˚, and upward vertical = +90˚) were then computed from the relative positions of these tracking points.

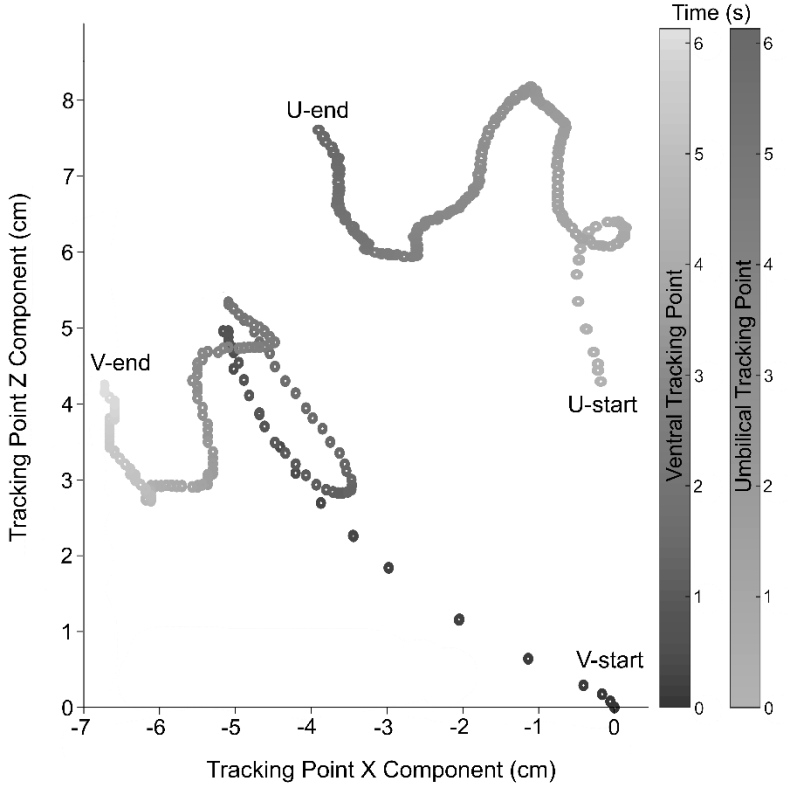

Figure 5: Position of the ventral tracking point (V) and umbilical tracking point (U) as a function of time measured with the physics modeling software, Tracker 4.11.0 (Brown 2017). Note that the rotation of the aperture is coupled with translational motion, resulting in complex movement.

3.2.5 Experiments on active locomotion to overcome hydrostatic stability

The high hydrostatic stability of orthoconic cephalopods relative to other morphotypes was explored in terms of active locomotion to deviate from a stable orientation. A second 3D-printed model of *Baculites compressus* was created following the same procedure as the first model. However, this model included an empty space for an axle located at the pivot point of rotation (i.e., the midpoint between the centers of buoyancy and mass). The axle was suspended by a ring stand clamp and fixed to two ball bearings to minimize friction while the baculite rotated. A 1 m long lightweight segment of silicone tubing with an inner diameter of 6.35 mm was fixed to the baculite perpendicular to the aperture (pointing in the ventral direction) to act as the source of thrust. Because little is known about the soft body of the baculitids (and generally all ammonoids), the amount of thrust they could generate with their mantle cavity and hyponome is highly speculative. Therefore, we use thrust values that fall within the range of extant cephalopod analogues during experimentation (Table 1). Because thrust is dependent upon size (Chamberlain 1990; Thompson and Kier 2002), the thrust efficiency can be quantified by the thrust ratio (maximum propulsive thrust / total weight). This metric of efficiency is generally larger in coleoids, however *Nautilus* is actually more efficient in terms of its metabolic cost of locomotion (Neil and Askew 2018). The thrust ratio for several living cephalopods (see Chamberlain 1990) was multiplied by the weight of the baculite model to yield estimates of thrust that the baculite could produce at several different levels of thrust efficiency. We used three scenarios of thrust generation during experimentation (summarized in Table 1) that fall within the range of the thrust ratios of the extant cephalopods: *Nautilus pompilius*, *Sepia officinalis* (common cuttlefish), and

Loligo vulgaris (European squid). The resultant thrusts were calibrated with a Vernier dual-range force sensor with a sensitivity of 0.01 N during 30 second intervals of recording at a sample interval of 30 samples per second.

	Thrust Ratio	**Thrust (N)**	**Funnel Ratio**	**Hyp. Diameter (mm)**
Nautilus pompilius	0.2	0.30	0.035	?
Sepia officinalis	0.7	1.05	0.037	?
Loligo vulgaris	1.5	2.25	0.030	?
Scenario 1	0.169	0.254 ± 0.020	0.034	5.50
Scenario 2	0.255	0.384 ± 0.021	0.034	5.50
Scenario 3	1.069	1.607 ± 0.144	0.045	6.35

Table 1: Thrust ratio (maximum propulsive thrust / total weight), thrust (N) generated with the weight of the *Baculites compressus* model (Thrust ratio $*$ 9.8 m/s^2 $*$ 0.153 kg), funnel ratio (max cross-sectional area of funnel / $volume^{2/3}$), and hyponome diameter for *Nautilus pompilius*, *Sepia officinalis*, and *Loligo vulgaris* reported in Chamberlain (1990). These metrics are also reported for the three thrust scenarios used during physical experimentation on the *B. compressus* model.

Scenario 1 simulates a thrust at a similar efficiency to a *Nautilus pompilius* with an endless water supply (infinite mantle cavity volume). This was achieved by using a 10.7 LPM pump attached to the silicone tubing and reducing the exit cross-sectional area (reported as diameter in Table 1) until the desired thrust was approximated. Scenario 2 was performed by forcing a fixed volume of water through the tubing with a siphon pump. This fixed volume represents the total mantle cavity volume of the baculite model (estimated to be 20% of the soft body volume; 0.20 * 86.7 cm^3 = 17.3 cm^3). Chamberlain (1990) stated that the effective mantle cavity volume in coleoids is about 70% of the total mantle cavity volume. Therefore, this value is a rather liberal estimate to test the difficulty in rotating from a stable vertical orientation. Scenario 3 was performed with a

larger funnel ratio (Table 1) and larger mantle volume (the entire siphon pump volume of 75 cm^3) to yield a high thrust ratio in between the values for *Sepia officinalis* and *Loligo vulgaris* (Table 1). Each of these thrust experiments provides a scenario to test how difficult it may have been for orthocones to deviate from their equilibrium position using active locomotion, by measuring the angle the baculite could rotate in response to thrust applied from the ventral direction.

3.3 RESULTS

3.3.1 Virtual 3D models of *Baculites compressus*

The conditions for neutral buoyancy Φ, hydrostatic stability (S_t), and orientation are dependent upon the assumed densities for each model component. The hydrostatic influence of using different historical values for soft body and shell densities were computed and are organized in Table 2. High density values of 1.068 g/cm^3 (Denton and Gilpin-Brown 1961) and 2.94 g/cm^3 (Trueman 1941) for the soft body and shell, respectively, yield an 18.6% increase in Φ (now emptying all camerae), and a 17.2% increase in S_t. The very large value for shell density was assumed to have the same density as crystalline aragonite without any organic components. Lower density values of 1.047 g/cm3 (Hoffmann and Zachow 2011) and 2.53 g/cm3 (Collins et al. 1980) for the soft body and shell, respectively, yield a 9.3% decrease in Φ and a 12.3% decrease in S_t. The *Baculites compressus* model is very stable in a vertical orientation for each of these simulations with both high and low density values (Table 2).

	ρ_{sb} (g/cm^3)	ρ_{sh} (g/cm^3)	Φ (%)	S_t	%$\Delta\Phi$	%ΔS_t
High ρ (g/cm^3)	1.068	2.94	100.2	0.592	18.6	17.2
Low ρ (g/cm^3)	1.047	2.53	76.6	0.443	-9.3	-12.3
Averaged ρ (g/cm^3)	1.065	2.62	84.5	0.505		

Table 2**:** Different density values applied to the *Baculites compressus* hydrostatic model with an even distribution of cameral liquid and gas. High and lower density (ρ) values applied to the soft body (sb) and shell (sh) resulting in different percentages of the phragmocone to be emptied (Φ) and different stability indices (S_t). Percent change in hydrostatic parameters is denoted by %Δ.

The averaged bulk density of 1.065 g/cm^3 was adopted from Westermann (2013) because of the unknown volumes of the dense, calcified aptychi and the low-density mantle cavity filled with seawater. However, this value was roughly tested by assuming a mantle cavity of 15-20% soft body volume, and aptychi of similar proportions to *Baculites sp*. reported in Kruta et al. (2009). The average length aptychi of 27 mm were scaled to fit the 58 mm aperture of the current *Baculites compressus* model. Kruta et al. (2009) reported aptychi thicknesses between 600 μm and 1 mm depending on the rugae. Linearly scaling the averaged thickness of 800 μm to the length of the aperture yielded aptychi that were 1.75 mm thick with a mass of 6.22 g (assuming an aptychi density of 2.71 g/cm^3). The bulk density computed from the mass of the soft body with a density of the *Nautilus* (1.06 g/cm^3; Hoffmann et al. 2015), and the masses of the mantle cavity and aptychi was 1.066 g/cm^3 (a 0.1% difference from the value used herein and in Westermann 2013). A 15% mantle cavity would yield a bulk density of 1.069 g/cm^3 (approximately a 0.4% difference). These differences would not considerably influence the total mass distribution of the organism (but compare other morphotypes with larger aptychi; Parent et al. 2014).

The masses and volumes of each virtual model component are listed in Table 3, and their spatial distributions are listed in Table 4. Comparison of the total mass (m_{total}) and mass of the water displaced (m_{wd}) yields the error in buoyancy calculations which should theoretically be equal for neutrally buoyant objects. Each of the neutrally buoyant, virtual models in this study have less than 1% difference between these two metrics. This source of error is most likely due to subtle volume changes in the digital mesh induced by trying to manage the .stl file sizes.

Virtual Model	**V_{sh} (cm^3)**	**m_{sh} (g)**	**V_{sb} (cm^3)**	**m_{sb} (g)**	**V_{cg} (cm^3)**	**m_{cg} (g)**	**V_{cl} (cm^3)**	**m_{cl} (g)**
N. pompilius	53.802	140.961	695.690	740.910	109.053	0.131	21.471	22.008
N. pompilius (Modified)	192.135	214.039	NA	NA	93.601	0.115	587.666	587.666
B. compressus (40% BCL, Emptied)	57.269	150.045	293.384	312.454	96.954	0.117	0.000	0.000
B. compressus (33% BCL, Adoral Liquid)	61.771	161.840	259.099	275.941	107.218	0.129	19.729	20.222
B. compressus (33% BCL, Adapical Liquid)	61.771	161.840	259.099	275.941	107.218	0.129	19.729	20.222
B. compressus (Curved, Adoral Liquid)	66.124	173.246	250.033	266.285	113.511	0.137	10.239	10.495
B. compressus (Curved, Adapical Liquid)	66.124	173.246	250.033	266.285	113.140	0.136	10.610	10.875
B. compressus (33% BCL, Even Gas)	20.661	54.132	86.664	92.297	35.859	0.043	6.603	6.768
B. compressus (33% BCL, Modified 1)	76.244	84.936	NA	NA	54.989	0.067	12.913	12.913
B. compressus (33% BCL, Modified 2)	76.381	85.089	NA	NA	72.332	0.089	0.000	0.000

Virtual Model	V_{Bi} (cm^3)	m_{Bi} (g)	V_{ct} (cm^3)	V_{wd} (cm^3)	m_{wd} (g)	m_{total} (g)	ϕ (%)
N. pompilius	NA	NA	132.735	882.227	904.283	904.010	83.6
N. pompilius (Modified)	8.250	79.332	587.666	882.227	882.227	881.151	13.7
B. compressus (40% BCL, Emptied)	NA	NA	96.954	446.969	458.143	462.615	104.5
B. compressus (33% BCL, Adoral Liquid)	NA	NA	126.946	446.969	458.143	458.120	84.5
B. compressus (33% BCL, Adapical Liquid)	NA	NA	126.946	446.969	458.143	458.132	84.5
B. compressus (Curved, Adoral Liquid)	NA	NA	123.750	439.174	450.153	450.162	91.7
B. compressus (Curved, Adapical Liquid)	NA	NA	123.750	439.174	450.153	450.162	91.7
B. compressus (33% BCL, Even Gas)	NA	NA	42.461	149.503	153.241	153.241	84.5
B. compressus (33% BCL, Modified 1)	5.357	51.496	67.902	149.503	149.503	149.412	80.8
B. compressus (33% BCL, Modified 2)	6.674	64.150	72.332	149.503	149.503	149.327	100

Table 3: (This page and previous page) The volumes (V) and masses (m) of the shell (sh), soft body (sb), cameral gas (cg), cameral liquid (cl), bismuth counterweight (Bi), total camerae (ct), water displaced (wd), and total mass for each virtual model. These metrics were used to compute the percentage of the phragmocone emptied for a neutrally buoyant condition (Φ).

	Center of Buoyancy		Center of Mass (Soft Body)		Center of Mass (Shell or Plastic)		Center of Mass (Cameral Liquid)	
Virtual Model	**x (mm)**	**z (mm)**	**x (mm)**	**z (mm)**	**x (mm)**	**z (mm)**	**x (mm)**	**z (mm)**
N. pompilius	-30.715	-13.577	-22.402	-18.522	-46.349	-15.664	-71.196	9.993
N. pompilius (Modified)	-30.715	-13.577	NA	NA	-11.380	9.818	-28.784	-24.928
B. compressus (40% BCL, Emptied)	-139.751	2.093	-61.237	3.567	-172.157	0.406	NA	NA
B. compressus (33% BCL, Adoral Liquid)	-139.751	2.093	-42.004	3.858	-174.241	0.442	-198.763	1.518
B. compressus (33% BCL, Adapical Liquid)	-139.751	2.093	-42.004	3.858	-174.241	0.442	-510.032	-4.386
B. compressus (Curved, Adoral Liquid)	-67.873	43.649	29.614	47.354	-90.362	38.966	-128.910	29.912
B. compressus (Curved, Adapical Liquid)	-67.873	43.649	29.614	47.354	-90.362	38.966	-460.137	72.862
B. compressus (33% BCL, Even Gas)	-112.702	0.665	-44.807	1.901	-136.618	-0.470	-240.275	-1.291
B. compressus (33% BCL, Modified 1)	-112.702	0.665	NA	NA	-142.672	0.111	-4.419	2.238
B. compressus (33% BCL, Modified 2)	-112.702	0.665	NA	NA	-142.593	0.109	NA	NA

	Center of Mass (Cameral Gas)		Center of Mass (Bi weight)		Center of Mass (Total)			
Virtual Model	**x (mm)**	**z (mm)**	**x (mm)**	**z (mm)**	**x (mm)**	**z (mm)**	**$\overline{BG}$ (mm)**	**S_t**
N. pompilius	-69.245	13.937	NA	NA	-27.331	-17.378	5.090	0.053
N. pompilius (Modified)	-84.834	15.303	-59.514	-34.867	-27.331	-17.378	5.090	0.053
B. compressus (40% BCL, Emptied)	-359.497	-1.407	NA	NA	-97.257	2.515	42.466	0.555
B. compressus (33% BCL, Adoral Liquid)	-346.517	-1.156	NA	NA	-95.721	2.547	44.033	0.576
B. compressus (33% BCL, Adapical Liquid)	-289.257	-0.070	NA	NA	-109.447	2.286	30.305	0.396
B. compressus (Curved, Adoral Liquid)	-264.809	39.369	NA	NA	-20.344	43.717	47.529	0.625
B. compressus (Curved, Adapical Liquid)	-234.193	35.372	NA	NA	-28.421	44.740	39.451	0.519
B. compressus (33% BCL, Even Gas)	-240.275	-1.291	NA	NA	-85.927	0.922	26.776	0.505
B. compressus (33% BCL, Modified 1)	-106.395	1.004	-12.748	1.929	-85.927	0.922	26.776	0.505
B. compressus (33% BCL, Modified 2)	-81.291	1.248	-10.773	2.000	-85.927	0.922	26.776	0.505

Table 4: (This page and previous page) The center of buoyancy and centers of mass (X/Z coordinates) for each model component in the virtual models. These values, along with the metrics in Table 2 were used to compute hydrostatic stability S_t. The y-component is ignored because all models are bilaterally symmetric.

Two 3D baculite models of differing body chamber lengths to total length ratios (40% and 33% BCL/L) were reconstructed with measured shell and septum thicknesses (Fig. 2). These values fall within the upper and lower estimates of the "mesodome" category termed by Westermann (2013). The larger body chamber model (Fig. 6A) requires a cameral gas volume that is 104.5% of the available volume of the phragmocone to be neutrally buoyant. This 40% BCL/L model (Fig. 6A) is completely emptied (filled with 100% cameral gas) in order to compute its hydrostatic stability (St = 0.555) with a slightly negative buoyancy. The 33% BCL/L models require 84.5% of their cameral volumes to be emptied of cameral liquid in order to be neutrally buoyant. Distributing the volume of cameral liquid required for neutral buoyancy in the adoral direction (Fig. 6B) and the adapical direction (Fig. 6C) influences the hydrostatic stability of each of these models (0.576 and 0.396, respectively). However, these values are still rather high and orientation is unchanged from vertical.

The mass distribution and hydrostatic properties for baculitids with a concave dorsum were investigated by modifying the 33% BCL/L *B. compressus* model (Figs. 6D and 6E). A shell with a concave dorsum similar to the younger (early Maastrichtian) species *Baculites grandis* requires slightly less cameral liquid to be neutrally buoyant. The apertural angle at rest is rotated from about 5° from the vertical axis in the dorsal direction when compared to the straight, vertical models.

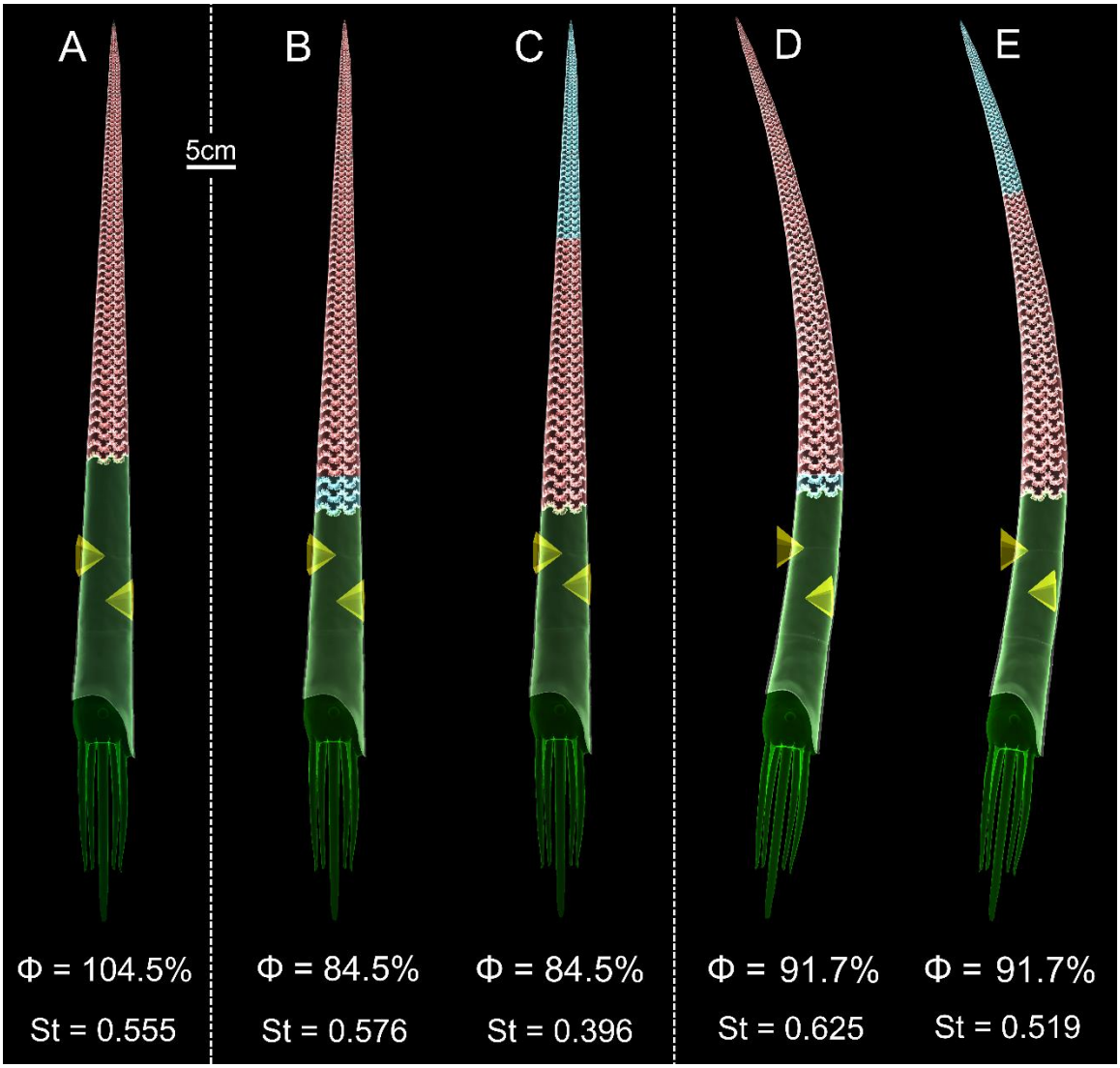

Figure 6: Hydrostatic models of *Baculites compressus* with computed percentage of the phragmocone emptied for neutral buoyancy (Φ) and hydrostatic stability (S_t). All models are oriented dorsum-left. The centers of buoyancy are marked by the tip of the higher pyramid. The total centers of mass are marked by the tip of the lower pyramid. Each material of unique density is designated a color (green = soft body; red = cameral gas; blue = cameral liquid; transparent grey = shell). **A.** Virtual model with 40% body chamber length to total length (BCL/L). **B.** Virtual model with 33% BCL/L and adorally distributed cameral liquid. **C.** Virtual model with 33% BCL/L and adapically distributed cameral liquid. **D.** and **E.** *B. compressus* model with modified with a concave dorsum similar to *B. grandis* and 33% BCL/L. **D.** Adorally distributed cameral liquid. **E.** Adapically distributed cameral liquid.

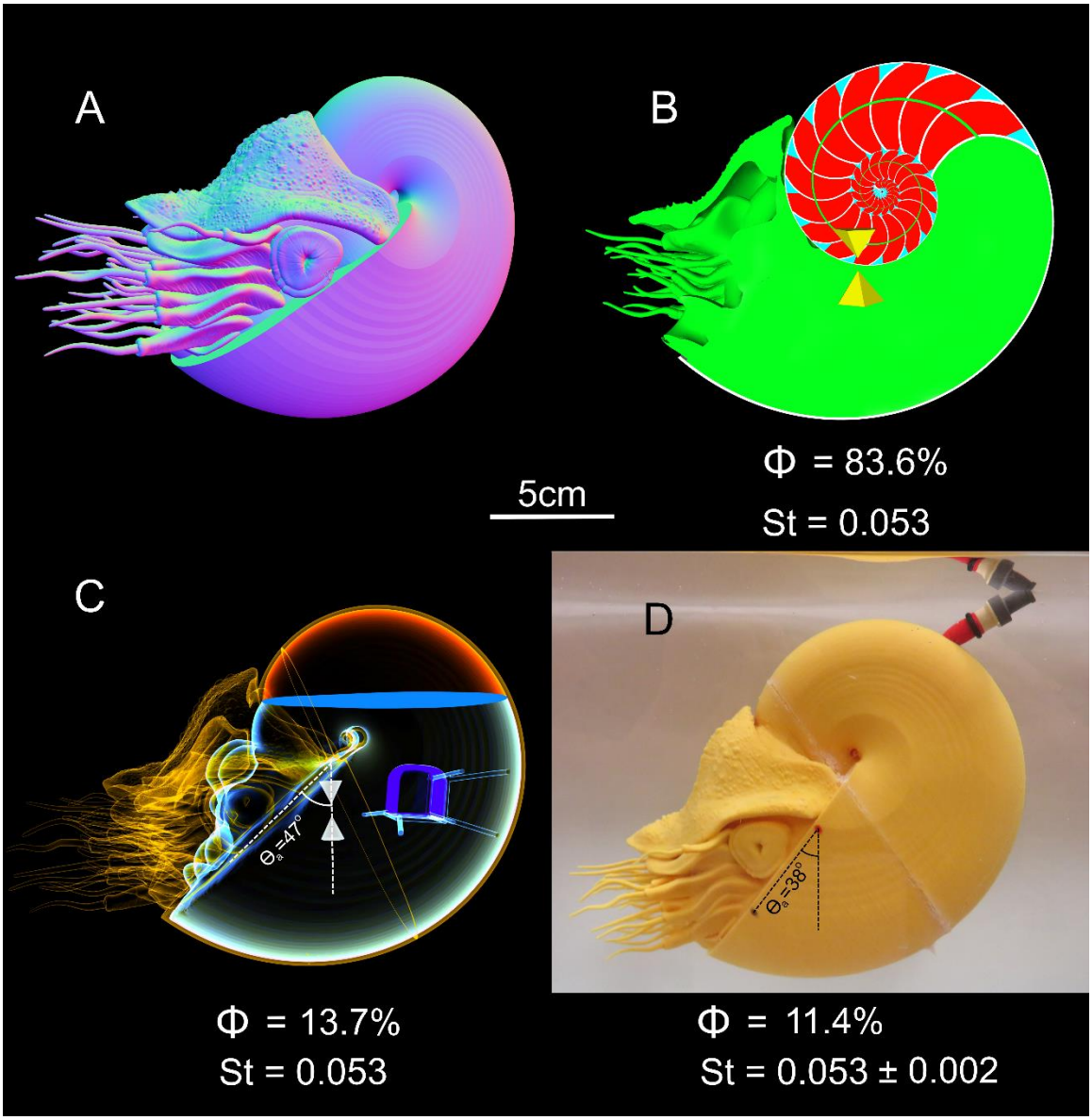

Figure 7: Virtual and physical hydrostatic models of *Nautilus pompilius* with computed percentage of the phragmocone emptied for neutral buoyancy (Φ) and hydrostatic stability (S_t). The tip of the up-side-down pyramid = center of buoyancy. The tip of the right-side-up pyramid = total center of mass. **A.** External view of the virtual model. **B.** Medial section of the virtual model with each component of unique density (green = soft body; red = cameral gas; blue = cameral liquid; grey = shell). **C.** Modified virtual model with simplified internal geometry and bismuth counterweight (yellow = PLA plastic; red = air; blue = liquid; purple = bismuth counterweight). **D.** Neutrally-buoyant, 3D-printed model. The differences in Φ and the apertural angle (θ_a) are a result of the mass discrepancy (Table 5) and irregular geometry of the balloon. The error in S_t was computed assuming that the total mass discrepancy was distributed in the positive or negative z-directions.

3.3.2 Restoring moments of *Nautilus pompilius*

The virtual *Nautilus pompilius* model (Figs. 7A and 7B) is neutrally buoyant when 83.6% of its cameral volume is emptied. The hydrostatic stability of this model (St = 0.053) is about an order of magnitude lower than the virtual baculite models (Fig. 6). The modified virtual *N. pompilius* model (Fig. 7C) requires less cameral gas to be neutrally buoyant because it has a larger cavity volume due to the added mass of the bismuth counterweight (Table 3). The neutrally buoyant, 3D printed *N. pompilius* model (Fig. 7D) has a very similar mass distribution to the virtual models, but is slightly different due to discrepancies in the total masses between the two. Removing support material after 3D printing, and drilling holes in the plastic for the one way valves have resulted in a slightly lower mass in the physical model than the virtual model. This translates to a negative mass discrepancy of 5.340% (Table 5). This lower mass requires less gas in the cavity to be neutrally buoyant (11.4%) and can cause the stability index to vary by 0.002. The variability in the stability index is computed by shifting the deficient mass in the positive and negative z directions. The balloon also becomes convex as it displaces the liquid in the cavity, which contrasts with the flat interface of the virtual model. This difference also subtly influences the mass distribution and is responsible for the differing orientations of the aperture between the virtual and physical models (Figs. 7C and 7D).

The restoring moment of the 3D printed *Nautilus* model was periodic and caused the aperture to oscillate back and forth (Fig. 8) about the equilibrium orientation (θ_a of 38°). This motion is characterized as underdamped harmonic oscillation because each

progression decreases in amplitude and increases in wavelength as a function of time. Each of the 10 trials resulted in very similar paths that took approximately 7 seconds to stabilize.

Object	N. pompilius (Modified)		B. compressus (Modified 1)		B. compressus (Modified 2)	
	Virtual Mass (g)	Actual Mass (g)	Virtual Mass (g)	Actual Mass (g)	Virtual Mass (g)	Actual Mass (g)
PLA Shell	214.040	194.900	84.936	85.450	85.089	79.306
Bismuth Weight	79.332	79.332	51.496	51.496	64.150	64.150
Air Valve	NA	2.113	NA	2.113	NA	2.113
Balloon	NA	0.224	NA	0.224	NA	0.224
Glue	NA	1.171	NA	2.154	NA	1.900
Total (Empty)	293.372	277.740	136.590	141.437	149.503	147.693
Mass Discrepancy (%)		-5.340		3.427		-1.210
St	0.053		0.505		0.505	
St Error	0.002		0.035		0.013	
Virtual Φ	13.7		80.8		100.0	
Actual Φ	11.4		85.0		97.3	

Table 5: Mass discrepancies between the modified virtual models with simple internal geometries and their 3D printed counterparts for each model component. The error in hydrostatic stabilities (S_t) were computed by assuming that the mass surplus or deficit was acting in the positive and negative z-directions only (representing maximum error in S_t).

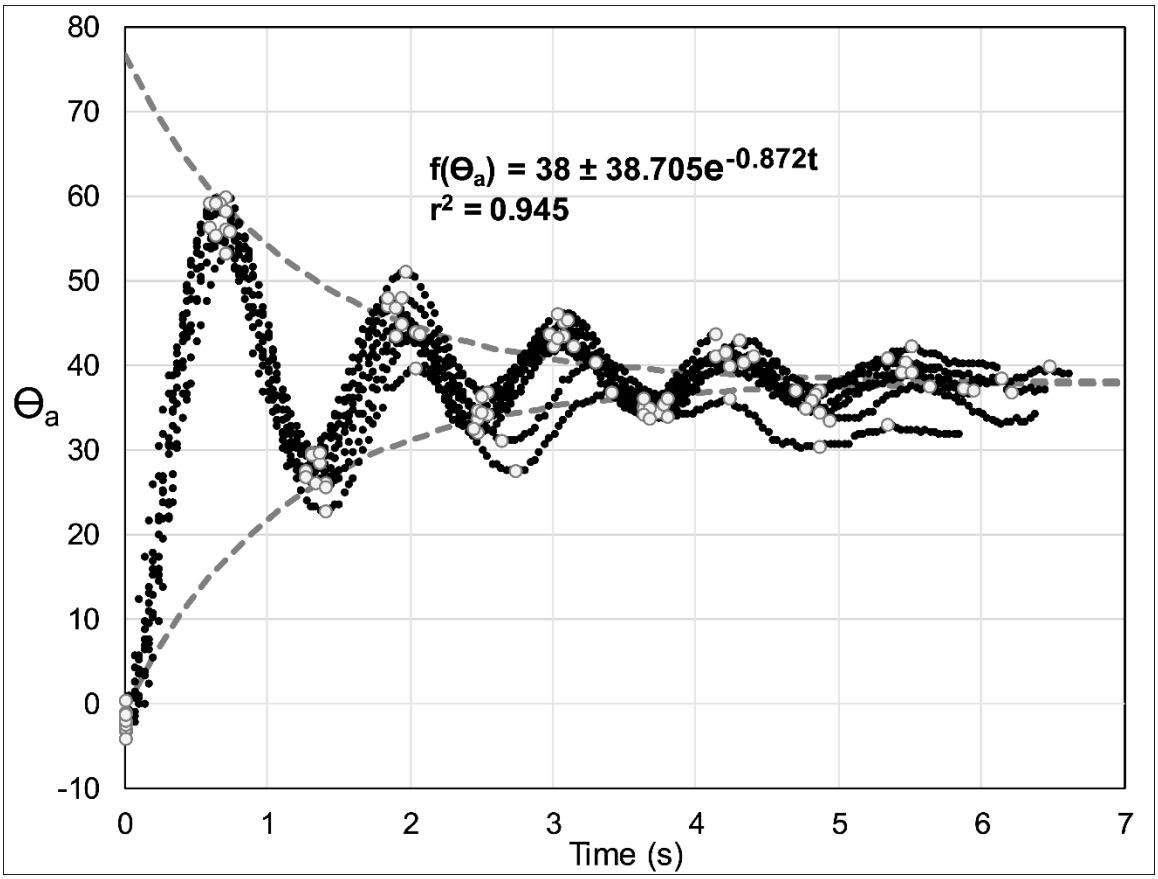

Figure 8: Hydrodynamic restoration of the *Nautilus pompilius* 3D-printed model following underdamped harmonic oscillation. Apertural angle (θ_a) measured in degrees as a function of time after rotating approximately 38° from the equilibrium orientation. An angle of zero represents a condition where the aperture is horizontally oriented. Open dots represent the peaks used to calculate decay in amplitude with time (grey dashed curves).

3.3.3 Restoring moment of *Baculites compressus*

After scaling the original virtual model of *Baculites compressus* to 60.0 cm, it was altered to have a somewhat even distribution of cameral liquid and gas in each camera. This distribution was approximated by setting the individual centers of mass for the cameral liquid and cameral gas equal to the center of volume of all of the camerae (Fig.

9A). This condition resulted in a stability index (0.505) in between the adorally and adapically distributed cameral liquid scenarios (Figs. 6B and 6C). The virtual *B. compressus* model modified to have a simple internal geometry (Fig. 9B) required 80.8% of its cavity to be filled with liquid in order to be neutrally buoyant. After 3D printing this model (Fig. 9C), residual support material and glue resulted in a positive mass discrepancy of 3.427% (Table 5). This increase in mass requires Φ to be increased to 85.0% and translates to a maximum error in St of 0.035.

The 3D printed model of *Baculites compressus* (Fig. 9C) is fundamentally different from the *Nautilus pompilius* model during hydrodynamic restoration from the same angle of displacement (38°). Instead of oscillating around the equilibrium position, the baculite model experiences a quick decay to its stable, vertical orientation (Fig. 10). This type of motion is characterized as overdamped harmonic motion. The seven trials of the *B. compressus* hydrodynamic restoration (Fig. 10) were more chaotic than the *N. pompilius* experiment (Fig. 8), but the original restoring orientation was reached in approximately half the time (just over 3 seconds). It should be noted that there was a significant amount of translation in addition to the rotational movement during hydrodynamic restoration. This was likely due to the differences in drag between the portions of the shell above and below the pivot point (which have different cross sectional areas and probably drag coefficients that both positively influence the force of drag).

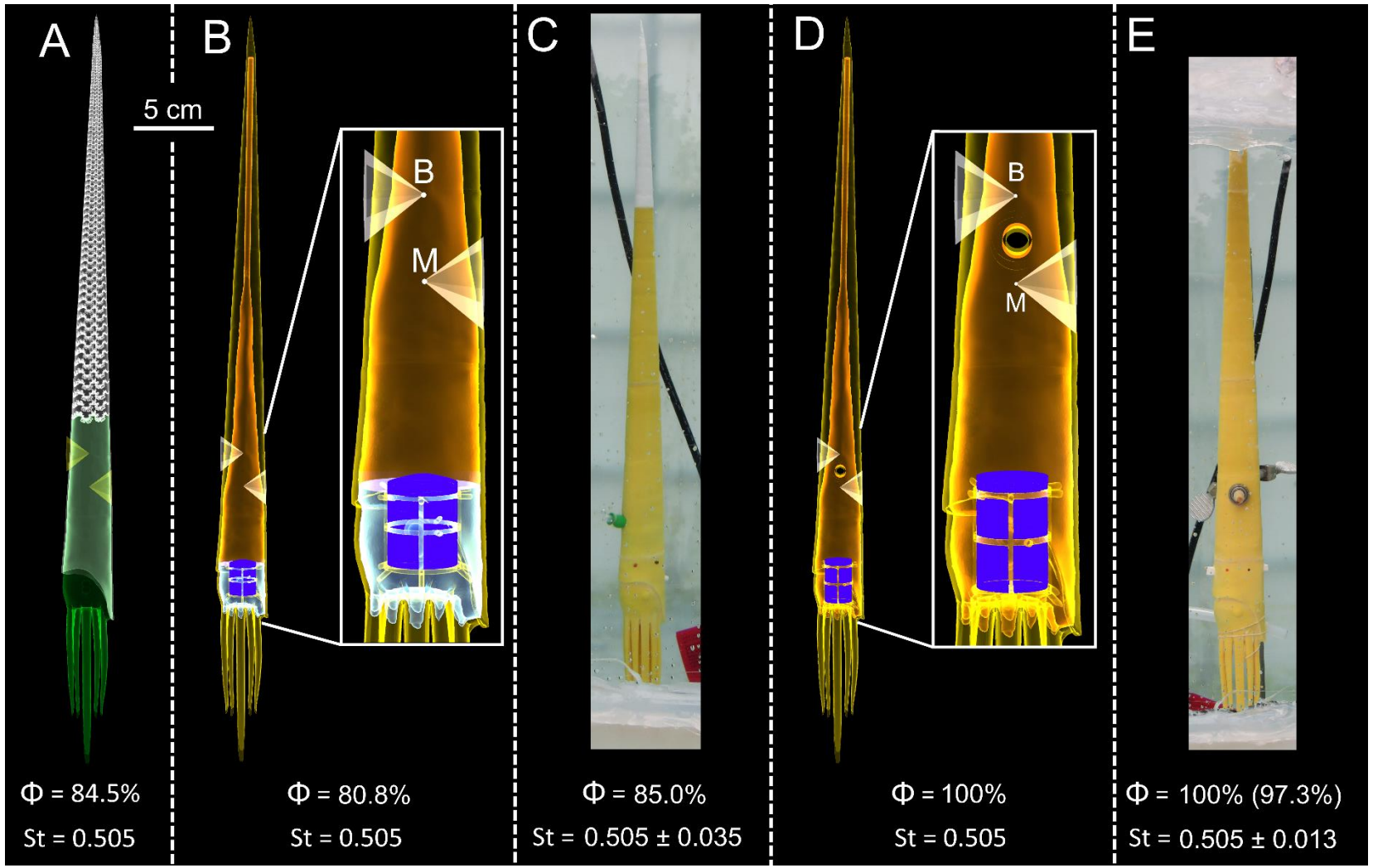
A
B
C
D
E
5 cm
B
M
B
M
Φ = 84.5%
St = 0.505
Φ = 80.8%
St = 0.505
Φ = 85.0%
St = 0.505 ± 0.035
Φ = 100%
St = 0.505
Φ = 100% (97.3%)
St = 0.505 ± 0.013

Figure 9: (Previous page) Virtual and physical hydrostatic models of *Baculites compressus* with computed percentage of the phragmocone emptied for neutral buoyancy (Φ) and hydrostatic stability (S_t). Green = soft body; grey = shell; red = gas; blue = liquid; yellow = PLA plastic; purple = bismuth counterweight; B = center of buoyancy; M = center of mass. **A.** Virtual model with an even distribution of cameral liquid and gas in the phragmocone (center of mass of cameral liquid and gas = center of volume of the phragmocone; cameral liquid and gas not shown). **B.** Modified virtual model with simplified internal geometry (named Modified 1 in Table 3). **C.** Neutrally-buoyant, 3D-printed model. **D.** Modified virtual model with simplified internal geometry and axel hole through pivot point of rotation (named Modified 2 in Table 3). **E.** Neutrally-buoyant, 3D-printed model fixed to an axel and silicone tubing used to supply thrust in the ventral direction. For this model (E), the mass discrepancy (Table 5) resulted in a slightly lower Φ of 97.3%, but was held constant at 100%. All computed errors in S_t were computed assuming that the total mass discrepancy was distributed in the positive or negative z-directions.

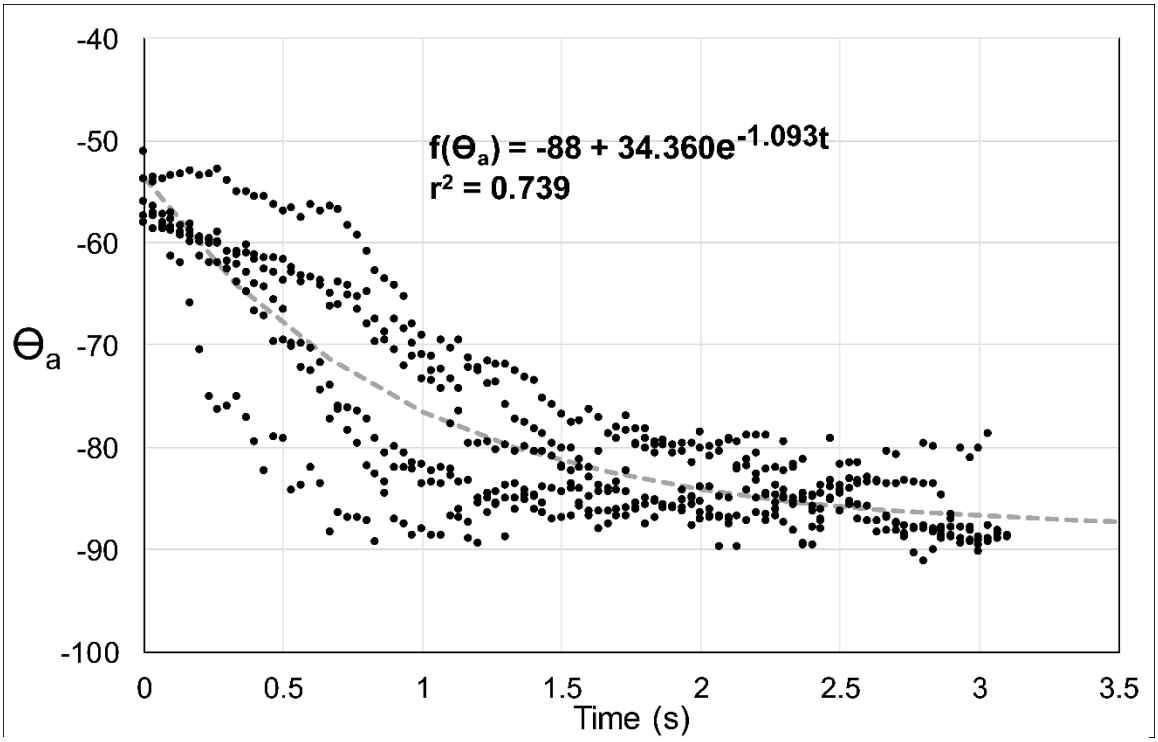

Figure 10: Hydrodynamic restoration of the *Baculites compressus* 3D-printed model following overdamped harmonic motion. Apertural angle (θ_a) measured in degrees as a function of time after rotating approximately 38° from the equilibrium orientation. An angle of -90° represents a condition where the aperture is directed downwards. The function of decay in θ_a with time is represented by the grey dashed curve. Note that this model restores more quickly and does not oscillate about the equilibrium orientation.

3.3.4 Thrust required to overcome the *Baculites compressus* restoring moment

The *B. compressus* model used to test thrust (Modified 2 in Tables 3 and 4; Fig. 9E) had a negative mass discrepancy of 1.210%, which corresponds to a maximum error in stability index of 0.013. This mass discrepancy also influenced the required cameral liquid for neutral buoyancy, but Φ was held at 100% for this experiment because there was no way to verify neutral buoyancy from this stationary model.

Thrust was applied to the venter of the model during three scenarios to generate rotation (see Table 1): (1) a continuous thrust near the value computed from the thrust ratio of *Nautilus pompilius* (Fig. 11A), (2) periodic pulses from the computed mantle cavity volume (17.3 cm^3) and realistic funnel ratio (0.034; Table 1) of the scaled *Baculites compressus* virtual model (Fig. 11B), and (3) larger periodic thrusts between the thrust ratios for *Sepia officinalis* and *Loligo vulgaris* (Fig. 11C). During scenario 1, the thrust produced (0.254 ± 0.020 N) resulted in an average displacement from the vertical resting orientation of 22.7° in the dorsal direction. This thrust value is similar to the value computed from the relatively low thrust ratio of the extant *N. pompilius* (Table 1) and follows the conditions of an infinite mantle cavity (constant thrust). Scenario 2 operates under the condition of a finite mantle cavity volume (17.3 cm^3) that produces 0.384 ± 0.021 N of thrust. This value of thrust corresponds to a slightly larger thrust ratio than *N. pompilius* (Table 1) and results in an average peak rotation of 25.6°. In order to produce larger values of thrust (in between the thrust ratios of the coleoids *Sepia officinalis* and *Loligo vulgaris*; 1.607 ± 0.144 N), a volume of 75 cm^3 was expelled through a larger jet orifice, resulting in an average peak rotation of 72.2° from the resting vertical position.

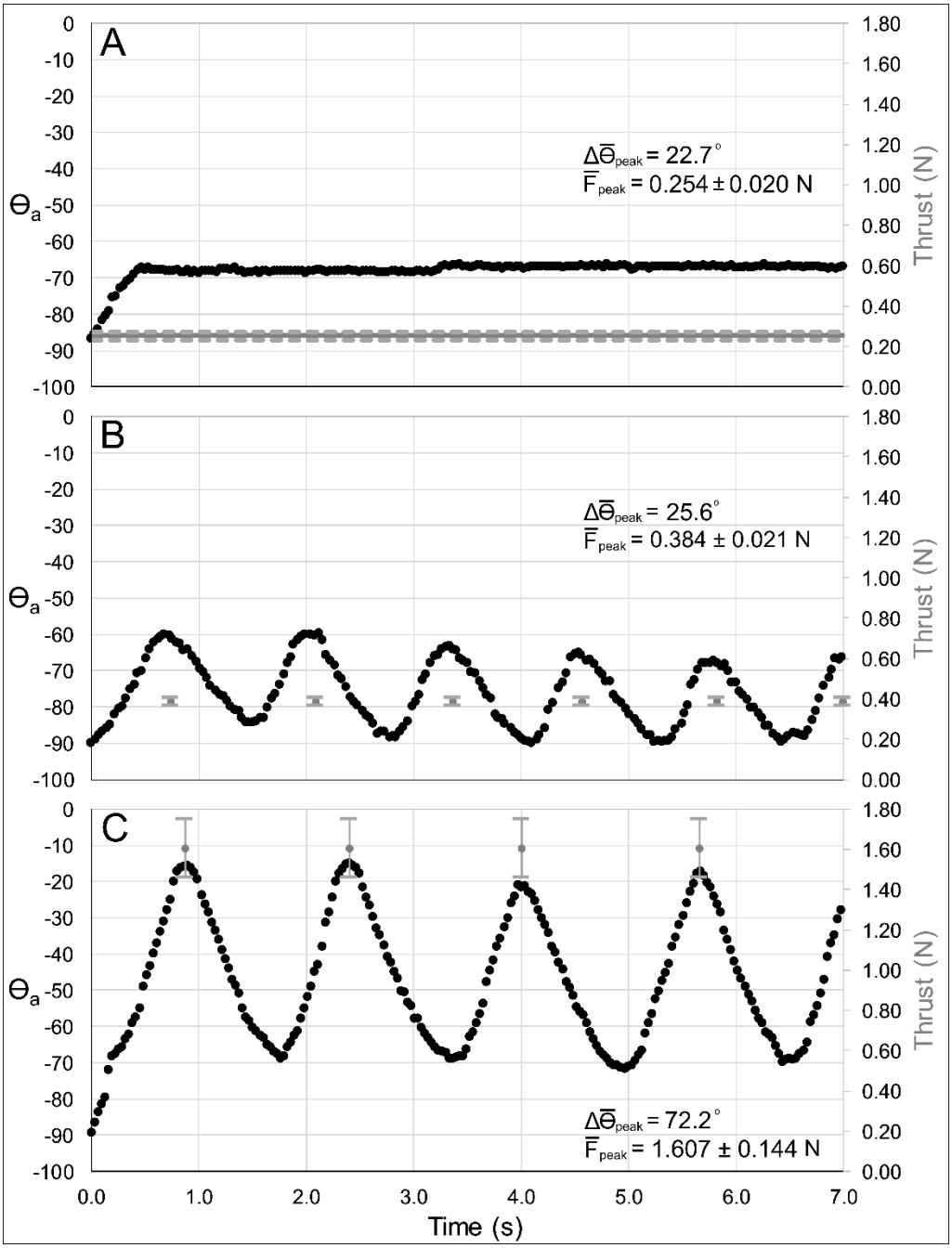

Figure 11: Thrust required to change the *Baculites compressus* model orientation (θ_a). **A.** Thrust Scenario #1: A continuous thrust supplied to the venter with a similar thrust ratio to *Nautilus* (Table 1). The average change from a vertical resting orientation ($\Delta\bar{\theta}_{peak}$) is 22.7°. **B.** Thrust Scenario #2: Periodic pulses from a pump with a simulated mantle cavity of 20% soft body volume of *B. compressus* (Table 1). The average change from a vertical resting orientation ($\Delta\bar{\theta}_{peak}$) is 25.6°. **C.** Thrust Scenario #3: Periodic pulses from a pump with a thrust ratio between *Sepia officinalis* and *Loligo vulgaris* (Table 1). The average change from a vertical resting orientation ($\Delta\bar{\theta}_{peak}$) is 72.2°. Average peak thrust ($\bar{F}_{peak}$) error bars represent one standard deviation calibrated from 30 second intervals of pumping.

It may be important to consider several sources of error during physical experimentation. The bearings were chosen to reduce the friction of rotation along the axle; however, some value of friction must still be present. The silicone tubing that suppled thrust at the venter of the shell also had some weight and drag. Each of these factors could have made it more difficult for the baculite to move through the water.

3.4 DISCUSSION

3.4.1 Hydrostatic properties of *Baculites compressus*

All of the *Baculites compressus* models in the current study have the capacity to be neutrally buoyant (or nearly so). Body chamber length is a limiting factor on neutral buoyancy because larger soft bodies contribute more towards the total organismal mass and result in fewer camerae that can be emptied to regulate the weight of the living cephalopod. As the body chamber ratio decreases for a neutrally buoyant orthocone, it would become positively buoyant unless some volume of cameral liquid filled the phragmocone. Modifying the body chamber ratio in *B. compressus* (Figs. 6A vs. 6B and 6C) shows that syn vivo orientation and hydrostatic stability (S_t) do not change very much between the upper and lower limits of the mesodome category (40% and 33%; Westermann 2013). The largest difference in hydrostatic properties between these two models is the ratio of cameral liquid and gas in the phragmocone for a neutrally buoyant condition (Φ). The model with the larger body chamber ratio is only slightly negatively buoyant, with an effective mass of 4.4 g. A very slight negative buoyancy is easier to manage by the living cephalopod and is commonly observed in the extant *Nautilus* (Ward 1987). This can also be accomplished with more cameral liquid than what is required for

perfect neutral buoyancy. However, as the body chamber ratio increases, this effective mass will become too large to be considered negligible.

The virtual baculite models (Fig. 6) all assume a stable vertical orientation, even when distributing the cameral liquid within the phragmocone in the adapical direction (Fig. 6C). The hydrostatic stability of *Baculites compressus* is around an order of magnitude higher than the *Nautilus pompilius* (St = 0.05; see Peterman et al. 2019; fig. 2.6). Changing the distribution of cameral liquid would not allow the baculite to deviate from a vertical static orientation. Adapically distributed cameral liquid only slightly reduces stability and does not cause the shell to rotate to a dorsum upward orientation. This horizontal orientation would require mass displacement in the ventral direction (to situate the center of mass under the center of buoyancy), which is not practical for the orthoconic morphotype. One feasible way to modify the orientation of these orthoconic models in a neutrally buoyant, static setting is to reduce stability until the centers of buoyancy and mass coincide. Under this scenario, there is no preferred orientation and active locomotion could be used to modify orientation. This has been experimentally demonstrated by Westermann (1977, 2013) by using 2D '*Orthoceras*' models and postulated by Klinger (1980), Westermann (1996), and Tsujita and Westermann (1998). However, the virtual *B. compressus* models in the current study (Fig. 6C) would require much more cameral liquid to reduce hydrostatic stability. As the phragmocone becomes completely filled, stability would approach a value near zero, and buoyancy would decrease significantly (Peterman and Barton 2017). Adapically distributing cameral liquid is much less effective than higher density counterweights such as cameral deposits or endosiphuncular deposits employed by Paleozoic orthocones (Teichert 1964;

Mironenko 2018; Peterman et al. 2019). There is also no evidence that suggests siphunculate cephalopods had the ability to selectively choose which chambers are flooded or emptied (Ward 1979). Also, some portion of cameral liquid would be retained by capillary retention within complex septal recesses (Peterman and Barton 2019) which would partially distribute the center of mass of the cameral liquid toward the center of the phragmocone, rather than adapically or adorally. Therefore, an even distribution of cameral liquid and gas in the phragmocone is more realistic; that is, after the camera behind a newly formed septum is sufficiently emptied.

Westermann (1996, 2013) has suggested that large orthocones with a concave dorsum (such as *B. grandis*) were able to rest horizontally in the water column by situating their center of mass in the ventral direction under the center of buoyancy. As discussed above, the required cameral liquid to move the center of mass close to the center of buoyancy would cause the model to become negatively buoyant. Additionally, a ventrally displaced total center of mass can only be achieved by distributing more mass in the ventral direction (or an absence of mass in the dorsal direction). The *B. compressus* models modified with a concave dorsum similar to *B. grandis* (Figs. 6D and 6E) show that a horizontal orientation is not likely to occur in a static setting. These models have high stability indices even when the cameral liquid is distributed adapically (Fig. 6E). The only significant change is that the aperture is rotated about 5° from the vertical axis in the dorsal direction. This could have improved the field of view in the dorsal direction, which could have been useful in the water column or in a demersal setting. The difference in size between the virtual models and larger orthocones is relative (St is

independent of size) and would only matter in a hydrodynamic setting (from differences in Reynolds numbers).

3.4.2 Restoring moment of the stable, orthoconic morphotype

Since the restoring moment is essentially a torque, it is proportionate to the distance between the centers of mass and buoyancy. Therefore, neutrally buoyant objects with a higher hydrostatic stability (S_t) have a greater restoring moment acting upon them after they are displaced from their static equilibrium position. These properties are fundamentally different between the *Nautilus pompilius* model (Fig. 7D) and the *Baculites compressus* model (Fig. 9C) because the latter has a hydrostatic stability value that is approximately an order of magnitude larger than the former. Hydrodynamic restoration is also dependent upon the force of drag, that is proportionate to the cross-sectional area of the object moving through the liquid and its drag coefficient (a metric inversely proportionate to the degree of streamlining). Underdamped harmonic oscillation, observed in the *N. pompilius* restoration experiment (Fig. 8), is diagnostic for neutrally buoyant objects with low hydrostatic stability relative to the force of drag during restoration. In contrast, the *B. compressus* model has high hydrostatic stability that exerts a larger restoring moment after it is displaced. This rotational movement also experiences much more drag, which prevents oscillation around the vertical equilibrium orientation. These hydrodynamic properties during restoration result in overdamped harmonic motion, causing the *B. compressus* model to reach its resting orientation in about half the time as the *N. pompilius* model (compare Figs. 8 and 10).

3.4.3 Were orthoconic cephalopods able to overcome their restoring moments?

As demonstrated by the virtual *Baculites compressus* models (Fig. 6) and the hydrodynamic restoration experiment (Fig. 10), this species (and generally the orthoconic morphotype) is very stable in a vertical orientation and would rely upon active locomotion in order to significantly alter their position. The thrust efficiency of baculitids is unknown and may be independent of retractor muscle size. Jacobs and Landman (1993) propose a coleoid-like swimming mechanism for ammonoids that differ from the *Nautilus* by contracting the mantle cavity rather than retracting the head complex into the body. However, the constraints of being enclosed within a rigid shell and the ammonoid mechanism for propulsion (effective musculature) are largely unknown. Therefore, the true baculitid thrust ratio is probably not significantly lower than the *N. pompilius* ratio, and probably does not exceed the values of the very efficient, shell-less coleoids.

The magnitude of thrust generated by compressing the mantle cavity is dependent upon the mantle cavity volume, cross sectional area of the jet orifice, and the time over which the mantle liquid is expelled. A constant thrust (simulating an infinite mantle cavity volume) with a thrust ratio near that of the *Nautilus pompilius* does not significantly allow the baculite to alter its orientation (Fig. 11A). This scenario is unrealistic in the sense that a jet pulse is followed by a period of refilling. During this time, the restoring moment acting on the baculite will begin to return it to its vertical equilibrium position (where $\Theta_a = -90^{\circ}$). A finite mantle cavity pulse generated from the computed *B. compressus* mantle cavity (17.3 cm^3) is a more realistic scenario. However, the thrust produced is only slightly larger than the thrust computed from the *N. pompilius* thrust ratio. This similarly does not allow the baculite to significantly alter its orientation (Fig. 11B). Larger angles of offset (Θ_a) yield larger restoring moments and require

sufficient thrusts applied at the aperture to overcome them. A much larger average peak force that corresponds to a thrust ratio in between *Sepia officinalis* and *Loligo vulgaris* is generated by using a larger mantle cavity volume. This volume produces a thrust relative to the weight of *B. compressus* within the coleoid range, but would require the expulsion of a mantle cavity that is 86% of the volume of the entire body chamber. Perhaps these values of thrust could be obtained from the appropriate mantle cavity volume if it was expelled at lower time intervals. However, shortening the pumping intervals in this study caused pump failure, which questions the ability of the living baculite to withstand such pressures in the mantle cavity. If the practicality of generating such thrusts is ignored, it is still unlikely that the living cephalopods would have expended such a large amount of energy. The thrust ratios reported by Chamberlain (1990) and used herein are a measurement of the maximum propulsive burst normalized by the organismal weight. The maximum propulsive burst (as observed in escape jetting) is much different from normal locomotion because the resting mantle cavity volume is increased by hyperinflation (Anderson and Demont 2000); an ability that may have been hindered by being enclosed within a rigid shell. The degrees of rotation induced by the liberal values of thrust used in this study suggest that a horizontal or sub-horizontal form of locomotion is very unlikely in baculitids and other orthoconic cephalopods with similar stability indices (i.e., Paleozoic orthocones without cameral or endosiphuncular deposits; Peterman et al. 2019).

3.4.4 Insights on the mode of life for highly-stable orthoconic cephalopods

The highly-stable, vertical syn vivo orientation of *Baculites compressus* and other orthocones with similar shell geometries makes it difficult to deviate from this

equilibrium position. Traditional methods of active locomotion (jet propulsion) may not have generated enough thrust to overcome the restoring moment acting on the shell at higher angles of offset. The unknown soft body morphology of the baculitids is problematic when interpreting their mode of life and habit. The models in the current study had rigid arms that did not move. During life, a baculitid may have been able to use these arms to aid in locomotion, especially if a webbing connected each of the arms. In this case, the living baculite could have modified its drag by spreading its tentacles to help prevent falling to a vertical position. The position of the arms could also generate lift during movement through the water. However, both of these scenarios remain entirely speculative because there is no unequivocal preservation of ammonoid arms (Klug and Lehmann 2015).

It probably would have been rather cumbersome for the hyponome to bend around the ventral rostrum present on many baculitid shells (as noted by Westermann 2013). This long ventral rostrum, along with lateral sinuses, led Westermann (2013) to revive the concept of a dual hyponome system, with two hyponome openings on either side of the ventral rostrum. This concept was originally proposed by Schmidt (1930) and Frentzen (1937) where jetting could take place from any direction and even promote forward horizontal swimming. There is currently no fossil evidence for this, or any hyponome for that matter (Klug and Lehmann 2015), aside from possible imprints (Summesberger et al. 1999; Landman and Cobban 2007). The lateral sinuses of baculitid shells have been interpreted by Klug et al. (2012) to house large eyes, in contrast to accommodating hypothetical dual hyponomes. The curved ventral rostrum of the baculitid, *Sciponoceras*, has been suggested to allow it to occasionally rest on the

substrate (Crick 1912; Matsumoto and Obata 1962; Klinger 1980). This behavior or demersal behavior could have been possible as long as the living baculitid conformed to its inferred depth of approximately less than 100m (Fatherree et al. 1998; Lukeneder et al. 2010; Klug et al. 2012). In a nektic setting, a mostly-vertical syn vivo orientation, as implied by the hydrostatic and hydrodynamic experiments of the current study, would rule out the need for the application of thrust from the ventral direction. Therefore, the ventral rostrum of baculitid shells may not have been a hindrance.

The influence of conch compression and depression in the baculitids were not investigated in the current study. However, the laterally compressed forms such as *B. compressus* appear to be more streamlined than baculitids with ovate whorl sections. This interpretation has led to the depiction of such compressed forms as having enhanced lateral mobility (Tsujita and Westermann 1998). During the hydrodynamic restoration of the baculite model (Fig. 9C), movement was preferred in the ventral direction after being rotated in the dorsal direction. This preference is due to a much lower hydrodynamic drag (proportionate to cross sectional area) in the dorso-ventral directions relative to the lateral directions in a compressed form. It is therefore possible that lateral compression of the conch was an adaptation to prevent rolling in the longitudinal axis rather than true streamlining. Orthoconic morphotypes with different whorl section geometries should be comparatively investigated in future studies.

The growth direction and orientation of a stalked cirripede attached to the venter of *Sciponoceras* was interpreted by Hauschke et al. (2011) to have occurred in a setting where the living baculitid moved forward in a more or less horizontal orientation. This idea conflicts with the vertical hydrostatic syn vivo orientations and hydrodynamic

capabilities of the baculitid modeled in the current study. Both *Sciponoceras* and *Baculites compressus* probably had similar stability indices based on their similar body chamber lengths (33%; Klug et al. 2012) and degree of shell taper. The position of the adult cirripede on the venter of the shell and the adapical end of the body chamber could have contributed to the total mass distribution toward the apex and venter. A significant change in orientation has been observed for other taxa with epibionts as indicated by changes in the growth of the cephalopod shell (Seilacher and Gishlick 2015). The magnitude of this influence is unknown, however, and would have been less significant during the juvenile stage of the cirripede, when it would have chosen this preferred growth orientation. This specimen reported by Hauschke et al. (2011) is largely enigmatic and warrants further investigation on the baculitid mode of life. It is unknown whether this cirripede orientation is anomalous, or if frequent vertical movement of the *Sciponoceras* could have facilitated this epizoan behavior.

The results of this study suggest that baculitids and similar orthocones assumed a mode of life with very poor mobility in the horizontal directions and rather moderate mobility in the vertical direction, living as a quasiplanktic to nektic vertical migrant (Westermann 1996). Anatomical interpretations of well-preserved specimens support a planktotrophic habit (Kruta et al. 2011; Klug et al. 2012), and oxygen isotope values of aragonitic shells infer the occupation of relatively shallow waters of less than 100 m (Fatherree et al. 1998; Lukeneder et al. 2010; Landman and Klofak 2012; Henderson and Price 2012; Lukeneder 2015; Sessa et al. 2015; Landman et al. 2018). Furthermore, these baculitids were somewhat sedentary and probably lived most of their lives at or near a single location within a few meters from the seafloor (Landman et al. 2018). The

constraints imposed on their life habits agree well with their hydrostatic limitations revealed in the current study. Poor horizontal mobility would preclude extensive lateral migration, in contrast to the portrayal of seemingly streamlined forms (such as *B. compressus*) as swift, mid-water swimmers (Tsujita and Westermann 1998). The hydrostatic and hydrodynamic properties of the baculitids support a lower energy mode of life in a vertical or near vertical condition.

3.5 CONCLUSIONS

Baculitids and other orthocones had the capacity for neutral buoyancy providing that they had sufficient body chamber ratios. The *Baculites compressus* models in the current study demonstrate that orthocones of the mesodome category of body chamber length (Westermann 2013) are neutrally buoyant (or nearly so) and that body chamber lengths of greater than approximately 40% with the modeled geometries will be negatively buoyant. Each of these models exhibit a highly stable, vertical syn vivo orientation in a static setting. These hydrostatic conditions occur in orthoconic cephalopods because they most efficiently separate the total center of mass away from the total center of buoyancy in a linear fashion; by partitioning the shell in to a largely empty section (the phragmocone) and having a higher concentration of mass at the adoral end of the organism (the soft body).

The distribution of cameral liquid in the phragmocone does not alter the syn vivo orientation. Adapically distributing the cameral liquid in a neutrally buoyant baculite model reduces hydrostatic stability, but cannot be used as a counterweight to permit a non-vertical orientation. A concave dorsum similar to *B. grandis* does not shift the mass distribution ventrally or closer to the center of buoyancy. Such a modification would only

rotate the aperture in the dorsal direction. In the modified virtual baculite models (Figs. 6D and 6E) the concave dorsum results in a 5° rotation of the aperture towards the dorsum in a static setting (see Westermann 2013 for alternative findings).

An even distribution of cameral liquid within the phragmocone of the baculite model yields a hydrostatic stability about an order of magnitude larger than the *N. pompilius* model. This difference in hydrostatic stability and differences in hydrodynamic drag are responsible for fundamentally different modes of hydrodynamic restoration between the two models. The *N. pompilius* model behaves as an underdamped harmonic oscillator that wobbles around its equilibrium position before resting. In contrast, the *B. compressus* model experiences overdamped harmonic motion and more quickly returns to its equilibrium position without oscillating.

The large separation between the centers of mass and buoyancy (high stability) of the baculite models result in large restoring moments after the models were rotated from their equilibrium position. Thrust applied to the venter using a continuous water supply and a similar thrust ratio to *N. pompilius* slightly rotated the model (22.7°). The thrust produced from a finite mantle cavity computed for the scaled *B. compressus* similarly rotated the model at small angles (25.6°). An overestimated value of thrust in between the thrust ratios of the extant coleoids, *Sepia officinalis* and *Loligo vulgaris* significantly rotated the model (72.2°), but such values are unlikely to be produced from the computed mantle cavity volume. Each of the experimental thrust ratios are based on the maximum propulsive burst, which probably would have been too energetically expensive for usual locomotion. Therefore, active orientations were likely less than 25° from vertical. The results of the current study support the interpretations of baculitids and orthocones with

similar hydrostatic properties as having lived a nektic to quasiplanktic mode of life with a primarily vertical orientation and mobility.

3.6 ACKNOWLEDGEMENTS

We very much appreciate the help of Neal Larson (Larson Paleontology, Keystone, South Dakota, USA) with collecting the specimens WSU-1400 and WSU-1401 and Don Clements (North Carolina Museum of Natural Sciences, Raleigh, North Carolina, USA) for donating WSU-1450. Each of these specimens were essential in reconstruction of the baculite models. We also thank Peter Minister (Peter Minister Digital Art, Manchester, England) for providing a digital model of the *Nautilus pompilius* soft body. René Hoffmann (Ruhr-Universität Bochum, Bochum, Germany) and Takao Ubukata (Kyoto University, Kyoto, Japan) are thanked for their constructive reviews of our manuscript.

3.7 REFERENCES

3DFlow., 2018, 3DF Zephyr Free Edition [Computer software]. Strada Le Grazie, 15 37134 Verona (VR) – Italy.

Autodesk Inc., 2017a, Meshmixer 3.3. Autodesk Inc., San Rafael, California.

Autodesk Inc., 2017b, Netfabb 2017.3. Autodesk Inc., San Rafael, California.

Anderson, E.J., and Demont, M.E., 2000, The mechanics of locomotion in the squid *Loligo pealei*: locomotory function and unsteady hydrodynamics of the jet and intramantle pressure. The Journal of Experimental Biology, v. 203, p. 2851-2863.

Batt, R.J., 1989, Ammonite shell morphotype distribution in the Western Interior Greenhorn sea and some paleoecological implications. Palaios, v. 4, p. 32–42.

Brown, D., 2017, Tracker 4.11.0 [Computer software]. Retrieved June 21, 2018, from https://physlets.org/tracker/

Chamberlain, J.A., 1981, Hydromechanical design of fossil cephalopods. In House, M.R. and Senior, J.R., (eds.) The Ammonoidea, p. 289-336. Systematics Association, London.

Chamberlain, J.A., 1990, Jet propulsion of *Nautilus*: a surviving example of early Paleozoic cephalopod locomotor design. Canadian Journal of Zoology, v. 68, p. 806-814.

Cignoni, P. and Ranzuglia, G., 2014, MeshLab (Version 1.3.3) [Computer graphics software]. Visual Computing Lab – ISTI – CNR Pisa, Italy. Available from http://meshlab.sourceforge.net/

Crick, G.C., 1912, On the aperture of a baculite from the Lower Chalk of the Chadstock, Somerset. Proceedings of the Malacological Society of London, v. 2, p. 77-80.

Cunningham, J.A., Rahman, I.A., Lautenschlager, S., Rayfield, E.J., and Donoghue, P.C., 2014, A virtual world of paleontology. Trends in Ecology and Evolution, v. 29, p. 347–357.

Falkingham, P.L., 2012, Acquisition of high resolution three-dimensional models using free, open-source, photogrammetric software. Palaeontologia Electronica, v. 15, p. 1-15.

Fatherree, J.W., Harries, P.J., and Quinn, T.M., 1998, Oxygen and carbon isotopic ‘‘dissection’’ of Baculites *compressus* (Mollusca: Cephalopoda) from Pierre Shale (Upper Campanian) of South Dakota: implications for paleoenvironmental reconstructions. Palaios, v. 13, p. 376–385.

Fau, M., Cornette, R., and Houssaye, A., 2016, General Palaeontology, Systematics and Evolution (Vertebrate Palaeontology): Photogrammetry for 3D digitizing bones of mounted skeletons: Potential and limits. General Palaeontology, Systematics and Evolution (Vertebrate Palaeontology), v. 15, p. 968-977. doi:10.1016/j.crpv.2016.08.003

Frentzen, K., 1937, Ontogenie, phylogenie und systematic der Amaltheen des Lias Deta Suedwestdeutschlands. Anhandlungen der Heidelberger Akademie der Wissenschaften, Mathematisch-naturwissenschaftliche Klasse, v. 1937, p. 131-236.

Greenwald, L., and Ward, P.D., 1987, Buoyancy in Nautilus. In: Saunders, B.W., Landman, N.H., (eds.) Nautilus—the biology and paleobiology of a living fossil. Springer, Dordrecht.

Hauschke, N., Schöllmann, L., and Keupp, H., 2011, Oriented attachment of a stalked cirripede on an orthoconic heteromorph ammonite – implications for the swimming position of the latter. Neues Jahrbuch für Geologie und Paläontologie Abhandlungen, v. 202, p. 199–212.

Henderson, R.A., and Price, G.D., 2012, Paleoenvironment and paleoecology inferred from oxygen and carbon isotopes of subtropical mollusks from the late Cretaceous (Cenomanian) of Bathurst Island, Australia. Palaios, v. 27(9), p. 617–626.

Hoffmann, R., Schultz, J.A., Schellhorn, R., Rybacki, E., Keupp, H., Gerden, S.R., Lemanis, R., and Zachow, S., 2014, Non-invasive imaging methods applied to neo-

and paleo-ontological cephalopod research. Biogeosciences, v. 11, p. 2721-2739. DOI 10.5194/bg-11-2721-2014

Hoffmann, R., Lemanis, R., Naglik, C., and Klug, C., 2015, Ammonoid Buoyancy. In: Klug, C., Korn, D., De Baets, K., Kruta, I., Mapes, R.H., (eds.) Ammonoid paleobiology, volume I: from anatomy to ecology. Topics in geobiology, v. 43, p. 611-648. Dordrecht: Springer.

Hoffmann, R., and Keupp, H., 2015, Ammonoid Paleopathology. In: Klug, C., Korn, D., De Baets, K., Kruta, I., Mapes, R.H., (eds.) Ammonoid paleobiology, volume I: from anatomy to ecology. Topics in geobiology, v. 43, p. 876-926. Dordrecht: Springer.

Hoffmann, R., Lemanis, R., Falkenberg, J., Schneider, S., Wesendonk, H., and Zachow, S., 2018, Integrating 2D and 3D shell morphology to disentangle the paleobiology of ammonoids: a virtual approach. Palaeontology, v. 61, p. 89-104.

Inoue, S., and Kondo, S., 2016, Suture pattern formation in ammonites and the unknown rear mantle structure. Scientific Reports, v. 6, p. 33689. DOI 10.1038/srep33689

Jacobs, D.K. and Landman, N.H., 1993, *Nautilus* – a poor model for the function and behavior of ammonoids? Lethaia, v. 26, p. 101-111.

Keupp, H., Röper, M., and Seilacher, A. 1999. Paläobiologische Aspekte von syn vivo-besiedelten Ammonoideen im Plattenkalk des Ober-Kimmeridgiums von Brunn in Ostbayern. Berliner Geowissenschaftliche Abhandlungen Reihe E Palaeobiologie, v. 30, p. 121–145.

Klinger, H.C., 1980, Speculations on buoyancy control and ecology in some heteromorph ammonites. In: House, M.R., Senior, J.R. (eds.) The Ammonoidea. Systematics Association Special Volume 18, Academic Press, London, pp. 337–355.

Klug, C., Riegraf, W., Lehmann, J., 2012, Soft-part preservation in heteromorph ammonites from the Cenomanian-Turonian Boundary Event (OAE 2) in the Teutoburger Wald (Germany). Palaeontology, v. 55, p. 1307-1331.

Klug, C., and Hoffmann, R., 2015, Ammonoid Septa and Sutures. In: Klug, C., Korn, D., De Baets, K., Kruta, I., Mapes, R.H. (eds.) Ammonoid paleobiology, volume I: from anatomy to ecology. Topics in geobiology, v. 43, p. 45-90. Dordrecht: Springer.

Klug, C., and Lehmann, J., 2015, Soft Part Anatomy of Ammonoids: Reconstructing the Animal Based on Exceptionally Preserved Specimens and Actualistic Comparisons. In: Klug, C., Korn, D., De Baets, K., Kruta, I., Mapes, R.H., (eds.) Ammonoid paleobiology, volume I: from anatomy to ecology. Topics in geobiology, v. 43, p. 515-538. Dordrecht: Springer.

Knauss, M.J., and Yacobucci, M.M., 2014, Geographic Information Systems technology as a morphometric tool for quantifying morphological variation in an ammonoid clade. Palaeontologia Electronica, v. 17(1), p. 19A.

Kröger B., 2002, On the efficiency of the buoyancy apparatus in ammonoids: evidences from sublethal shell injuries. Lethaia, v. 35, p. 61–70.

Kruta, I., Rouget, I., Landman, N.H., Tanabe, K., and Cecca, F., 2009, Aptychus microstructure in Late Cretaceous Ancyloceratina (Ammonoidea). Lethaia, v. 42, p. 312-321.

Kruta, I., Landman, N., Rouget, I., Cecca, F., and Tafforeau, P., 2011, The role of ammonites in the Mesozoic marine food web revealed by jaw preservation. Science, v. 331, p. 70–72.

Landman, N.H., and Cobban, W.A., 2007, Ammonite touch marks in upper Cretaceous (Cenomanian-Santonian) deposits of the western interior sea. In: Landman, N.H. Davis, R.A, Mapes, R.H. (eds.) Cephalopods present and past: new insights and fresh perspectives. Springer, Dordrecht.

Landman, N.H., and Klofak, S.M., 2012, Anatomy of a concretion: life, death, and burial in the Western Interior Seaway. Palaios, v. 27, p. 672–693.

Landman, N.H., Cochran, J.K., Slovacek, M., Larson, N.L., Garb, M.P., Brezina, J., and Witts, J.D., 2018, Isotope sclerochronology of ammonites (*Baculites compressus*) from methane seep and non-seep sites in the Late Cretaceous Western Interior Seaway, USA: Implications for ammonite habitat and mode of life. American Journal of Science, v. 318, p. 603-639. DOI 10.2475/06.2018.01.

Lemanis, R., Zachow, S., Fusseis, F., and Hoffmann, R., 2015, A new approach using high-resolution computed tomography to test the buoyant properties of chambered cephalopod shells. Paleobiology, v. 41, p. 313-329. DOI 10.1017/pab.2014.17

Lemanis, R., Korn, D., Zachow, S., Rybacki, E., and Hoffmann, R., 2016, The evolution and development of cephalopod chambers and their shape. PlosOne, v. 11, p. 1-21.

Lukeneder, A., 2015, Ammonoid Habitats and Life History. In: Klug, C., Korn, D., De Baets, K., Kruta, I., Mapes, R.H. (eds.) Ammonoid paleobiology, volume I: from anatomy to ecology. Topics in geobiology, v. 43, p. 689-791. Dordrecht: Springer.

Lukeneder, A., Harzhauser, M., Müllegger, S., and Piller, W.E., 2010, Ontogeny and habitat change in Mesozoic cephalopods revealed by stable isotopes (δ18O, δ13C). Earth and Planetary Science, v. 296, p. 103–114.

Matsumoto, T. and Obata, I., 1962, Notes on baculites facies. Kaseki, v. 3, p. 57-63.

Mironenko, A.A., 2018, Endocerids: suspension feeding nautiloids? Historical Biology DOI: 10.1080/08912963.2018.1491565.

Moseley, H., 1838, On the geometrical form of turbinated and discoid shells. Philosophical Transactions of the Royal Society, v. 1838, p. 351-370.

Naglik, C., Tajika, A., Chamberlain, J., and Klug, C., 2015a, Ammonoid locomotion. In: Klug, C. Korn, D., De Baets, K., Kruta, I., Mapes, R. (eds.) Ammonoid Paleobiology.

From anatomy to ecology, Topics in Geobiology, v. 43, p. 649-688. Springer, Dordrecht.

Naglik, C., Monnet, C., Goetz, S., Kolb, C., De Baets, K., Tajika, A., and Klug, C., 2015b, Growth trajectories of some major ammonoid sub-clades revealed by serial grinding tomography data. Lethaia, v. 48, p. 29-46.

Naglik, C., Rikhtegar, F., and Klug, C., 2016, Buoyancy of some Palaeozoic ammonoids and their hydrostatic properties based on empirical 3D-models. Lethaia, v. 49, p. 3-12.

Neil, T., and Askew, G.N., 2018, Swimming mechanics and propulsive efficiency in the chambered nautilus. Royal Society Open Science, v. 5, p. 170467.

Okamoto, T., 1996, Theoretical modeling of ammonoid morphology. In: Landman, N.H., Tanabe, K., Davis, R.A. (eds) Ammonoid Paleobiology. Topics in Geobiology, v. 13, p. 225-251. Plenum, New York.

Parent, H., Westermann, G.E.G., and Chamberlain Jr., J.A., 2014, Ammonite aptychi: Functions and role in propulsion. Geobios, v. 47, p. 45-55.

Peterman D.J., and Barton, C.C., 2017, Baculite 3D modeling; a new method for computing buoyancy, stability, and orientation with implications for ectocochleate cephalopod hydrostatics. American Geophysical Union Fall Meeting 2017, n. PP11D-1063.

Peterman, D.J., and Barton, C.C., 2019, Power scaling of ammonitic suture patterns from Cretaceous Ancyloceratina: constraints on septal/sutural complexity. Lethaia, v. 52, p. 77-90, doi: 10.1111/let.12291

Peterman, D.J, Ciampaglio, C.N., and Barton. C.C., 2018, The hydrostatics of Paleozoic orthoconic cephalopods (Nautiloidea) with implications for early colonization of the pelagic zone. Geological Society of America, Abstracts with Programs 50: 4.

Peterman, D.J., and Ciampaglio. C.N., 2018, How stable were orthoconic cephalopods? Hydrodynamic analyses of restoring moments from neutrally buoyant, 3D printed models of ectocochleate cephalopods. Geological Society of America, Abstracts with Programs 50: 6, doi: 10.1130/abs/2018AM-317321.

Peterman, D.J., Barton, C.C., and Yacobucci, M.M., 2019, The hydrostatics of Paleozoic ectocochleate cephalopods (Nautiloidea and Endoceratoidea) with implications for modes of life and early colonization of the pelagic zone. Palaeontologia Electronica, doi: 10.26879/884.

Petti, F.M., Avanzini, M., Belvedere, M., De Gasperi, M., Ferretti, P., Girardi, S., Remondino, F., and Tomasoni, R., 2008, Digital 3D modelling of dinosaur footprints by photogrammetry and laser scanning techniques: integrated approach at the Coste dell'Anglone tracksite (Lower Jurassic, southern Alps, northern Italy). Studi Trentini di Scienze Naturali Acta Geologica, v. 83, p. 303–315.

Raup, D.M., 1967, Geometric analysis of shell coiling: coiling in ammonoids. Journal of Paleontology, v. 41, p. 43-65.

Raup, D.M., and Chamberlain, J.A., 1967, Equations for volume and center of gravity in ammonoid shells. Journal of Paleontology, v. 41, p. 566–574.

Reyment, R.A., 1958, Some factors in the distribution of fossil cephalopods. Stockholm Contributions in Geology, v. 1, p. 97-184.

Reyment, R.A., 1973, Factors in the distribution of fossil cephalopods; Part 3, Experiments with exact models of certain shell types. Bulletin of the Geological Institutions of the University of Uppsala, New Series 4, v. 2, p. 7-41.

Say, T., 1820, Observations on some species of zoophytes, shells, etc. principally fossil. American Journal of Science, v. 2, p. 34-45.

Saunders, W.B., and Shapiro, E.A., 1986, Calculation and simulation of ammonoid hydrostatics. Paleobiology, v. 12, p. 64–79.

Schmidt, H., 1930, Ueber die Bewegungsweise der Schalencephalopoden. Palaeontologische Zeitschrift, v. 12, p. 194-208.

Seilacher, A., and Keupp, H., 2000, Wie sind Ammoniten geschwommen? Fossilien, v. 2000, p. 310–313.

Seilacher, A., and Gishlick, A.D., 2015, Morphodynamics. CRC Press Taylor & Francis Group. p. 1-531.

Sessa, J.A., Larina, E., Knoll, K., Garb, M., Cochran, J.K., Huber, B.T., MacLeod, K.G., and Landman, N.H., 2015, Ammonite habitat revealed via isotopic composition and comparisons with co-occurring benthic and planktonic organisms. Proceedings of the National Academy of Sciences of the United States of America, v. 112, p. 15562-15567. https://doi.org/10.1073/pnas.1507554112

Shigeta, Y., 1993, Post-hatching early life history of Cretaceous Ammonoidea. Lethaia, v. 26, p. 133–146.

Summesberger H., Jurkivsek, B., Kolar-Jurkovsek, T., 1999, Rollmarks of soft parts and possible crop content of Late Cretaceous ammonites from the Slovenian karst. In: Olóriz F, Rodríguez-Tovar FJ (eds.) Advancing research on living and fossil cephalopods. Kluwer Academic, New York. p. 335-344.

Sutton, M.D., Rahman, I.A., and Garwood, R.J., 2014, Techniques for virtual palaeontology. Chichester, West Sussex, UK: John Wiley & Sons Inc. p. 1-208.

Tajika, A., Naglik, C., Morimoto, N., Pascual-Cebrian, E., Hennhöfer, D.K., and Klug C., 2015a, Empirical 3D-model of the conch of the Middle Jurassic ammonite microconch *Normannites*, its buoyancy, the physical effects of its mature modifications and speculations on their function. Historical Biology, v. 27, p. 181–191.

Tajika, A., Morimoto, N., Wani, R., Naglik, C., and Klug, C., 2015b, Intraspecific variation of phragmocone chamber volumes throughout ontogeny in the modern nautilid *Nautilus* and the Jurassic ammonite *Normannites*. PeerJ, v. 3, p. 1-28. DOI 10.7717/peerj.1306

Tanabe, K., Shigeta, Y., and Mapes, R.H., 1995, Early life history of Carboniferous ammonoids inferred from analysis of fossil assemblages and shell hydrostatics. Palaios, v. 10, p. 80–86.

Teichert, C., 1964, Morphology of hard parts K12-K53. In Moore, R.C. (ed.), Treatise on Invertebrate Paleontology Part K Mollusca 3. The Geological Society of America, Boulder, Colorado, and the University of Kansas Press, Lawrence, Kansas, 519 pp.

Thompson, J.T., and Kier, W.M., 2002, Ontogeny of squid mantle function: changes in the mechanics of escape-jet locomotion in the oval squid, *Sepioteuthis lessoniana* Lesson, 1830. Biological Bulletin, v. 203, p. 14-26.

Trueman, A.E., 1941, The ammonite body-chamber, with special reference to the buoyancy and mode of life of the living ammonite. Quarterly Journal of the Geological Society, v. 384, p. 339–383.

Tsujita, C.J., and Westermann, G.E.G., 1998, Ammonoid habitats and habits in the Western Interior Seaway: a case study from the Upper Cretaceous Bearpaw Formation of southern Alberta, Canada. Palaeogeography, Palaeoclimatology, Palaeoecology, v. 144, p. 135-160.

Ward, P.D., 1976, Stratigraphy, Paleoecology and Functional Morphology of Heteromorph Ammonites of the Upper Cretaceous Nanaimo Group, British Columbia and Washington. Unpublished Ph.D. dissertation, McMaster University, Department of Geology, Hamilton, Ontario. p. 1-191.

Ward, P.D., 1979, Cameral liquid in *Nautilus* and ammonites. Paleobiology, v. 5, p. 40–49.

Ward, P.D., 1987, The natural history of Nautilus. Allen and Unwin, Boston. 1-267.

Westermann, G.E.G., 1977, Form and function of orthocone cephalopod shells with concave septa. Paleobiology, v. 3, p. 300–321.

Westermann, G.E.G., 1996, Ammonoid life and habitat. In: Landman, N.H., Tanabe, K., Davis, R.A. (eds.) Ammonoid Paleobiology. Plenum, New York. 607-707.

Westermann, G.E.G. 2013. Hydrostatics, propulsion and life-habits of the Cretaceous ammonoid *Baculites*. Revue de Paléobiologie, v. 32, p. 249–265.

4.0 A method to the madness: ontogenetic changes in the hydrostatic properties of *Didymoceras* (Nostoceratidae, Ammonoidea)

Peterman, D.J., Yacobucci, M.M., Larson, N.L., Ciampaglio, C.C., Linn. T. 2020. A method to the madness: ontogenetic changes in the hydrostatic properties of *Didymoceras* (Nostoceratidae, Ammonoidea). *Paleobiology*, forthcoming. DOI: 10.1017/pab.2020.14.

Abstract

The seemingly aberrant coiling of heteromorphic ammonoids suggests that they underwent more significant changes in hydrostatic properties throughout ontogeny than their planispiral counterparts. Such changes may have been responses to different selective pressures at different life stages. The hydrostatic properties of three species of *Didymoceras* (*D. stevensoni*, *D. nebrascense*, and *D. cheyennense*) were investigated by creating virtual 3D models at several stages during growth. These models were used to compute the conditions for neutral buoyancy, hydrostatic stability, orientation during life, and thrust angles (efficiency of directional movement). These properties suggest that *Didymoceras* and similar heteromorphs lived low energy lifestyles with the ability to hover above the seafloor. The resultant static orientations yielded a downward-facing aperture in the hatchling and a horizontally facing aperture throughout most of the juvenile stage, before terminating in an upward direction at maturity. Relatively high hydrostatic stabilities would not have permitted the orientation of *Didymoceras* to be

considerably modified with active locomotion. During the helical phase, *Didymoceras* would have been poorly suited for horizontal movement, yet equipped to pirouette about the vertical axis. Two stages throughout the growth, however, would have enhanced lateral mobility: a juvenile stage just after the formation of the first bend in the shell and the terminal stage after completion of the U-shaped hook. These two more mobile phases in ontogeny may have improved juvenile dispersal potential and mate acquisition during adulthood, respectively. In general, life orientation and hydrostatic stability change more wildly for these aberrantly coiled ammonoids than their planispiral counterparts.

4.1 INTRODUCTION

Didymoceras is a heteromorphic ammonoid that is common to abundant in late Campanian rocks of the Western Interior Seaway (Kennedy et al. 2000). The abundance of this genus has led to the use of several species as biostratigraphic index fossils in the Western Interior of the United States (Larson et al. 1997; Kennedy et al. 2000; Cobban et al. 2006; Landman et al. 2010). While much attention has been paid to biostratigraphy, little is known about the constraints on hydrostatics, locomotion, and mode of life for these aberrantly-coiled ammonoids. *Didymoceras*, along with other genera within Nostoceratidae, can be characterized by irregular helical whorls that terminate in a retroversal U-shaped hook at maturity. Embryonic shells (ammonitellae) of *D. stevensoni* and *D. cheyennense* are characterized by 1.5 to 2.5 loosely coiled whorls, while the ammonitella of *D. nebrascense* is unknown (Larson et al., 1997; Kennedy et al., 2000). The juvenile phase of *Didymoceras* (beyond the ammonitella) is relatively orthoconic (straight-shelled) to slightly curved. This general morphology can vary considerably, and the apical-most portions are poorly known (Kennedy et al., 2000). The profound changes

in coiling schemes during ontogeny are expected to result in changes in the hydrostatic properties acting on these cephalopods during life. This variation contrasts with that in most planispiral ammonoids, which do not undergo such drastic changes in shell morphology or hydrostatics throughout ontogeny (see Klug, 2001 for description of some notable exceptions). Changing hydrostatic properties implies differences in the constraints influencing orientation, locomotion, and mode of life. These are first order questions about ammonoid paleobiology that, once answered, can shed light on the paleoecology of this enigmatic group of cephalopods. Here, syn vivo hydrostatic properties for multiple phases of ontogeny are investigated for three species of *Didymoceras* (*D. stevensoni*, *D. nebrascense*, and *D. cheyennense*). While these species are mostly known from the Western Interior Seaway, their physical properties are more broadly relevant for the cosmopolitan nostoconic morphotype.

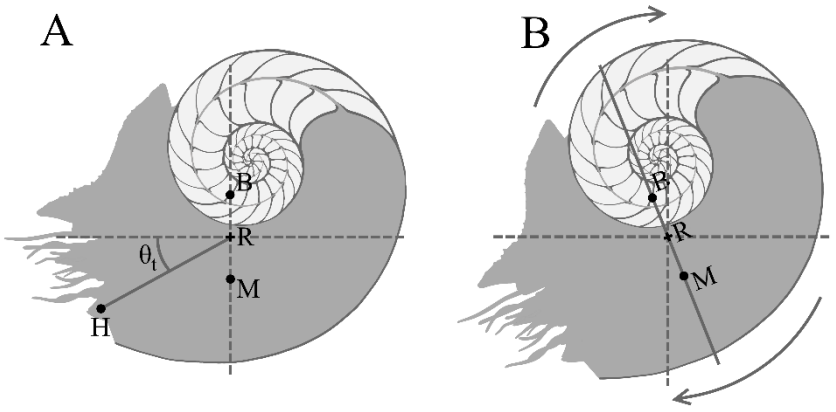

Figure 1: Hypothetical diagram of the hydrostatic metrics used in this study: center of buoyancy (B), center of mass (M), center of rotation (R), location of hyponome (H), thrust angle (θ_t). A, Static setting in equilibrium (i.e., B and M aligned vertically). B, Cephalopod displaced from equilibrium, imparting a restoring moment (arrows). Light gray, phragmocone; dark gray, soft body, based on living *Nautilus*.

4.1.1 Ectocochleate Cephalopod Hydrostatics

Like other ectocochleate (externally-shelled) cephalopods, *Didymoceras* has a shell consisting of a body chamber and a phragmocone. The phragmocone acts as a buoyancy apparatus to reduce organismal weight relative to the weight of the water displaced by the entire animal. A neutrally buoyant condition occurs when these two quantities are equal. The orientation of an ectocochleate during life and its hydrostatic stability can be determined by understanding the relative positions of the centers of buoyancy and mass (Fig. 1). The center of buoyancy is equal to the center of volume of the displaced seawater, while the center of mass depends upon the total 3D distribution of organismal mass (which is influenced by each material of unique density in the living ectocochleate). The equilibrium orientation occurs when the centers of buoyancy and mass are vertically aligned (Fig. 1). Hydrostatic stability is proportionate to the separation between these two centers (Trueman 1941; Raup and Chamberlain 1967; Saunders and Shapiro 1986; Okamoto 1996; Tajika et al. 2015b; Naglik et al. 2016; Peterman et al. 2019a, 2019b). A stability of zero would result in a condition similar to zero-gravity, while higher stabilities would impart larger restoring moments acting to return the living cephalopod to its equilibrium orientation (Okamoto 1996; Peterman et al. 2019b). The thrust angle (Fig. 1) describes the efficiency of locomotion in the direction of movement and the rocking behavior that occurs in response to normal locomotion via jet propulsion. This property is defined as the angle between the center of rotation (midpoint between centers of buoyancy and mass) and the location of the animal's hyponome (source of thrust via expelled jet of water). Idealized horizontal movement without rocking occurs when the location of the hyponome and center of rotation are aligned horizontally (thrust

angle approaches zero). Lower thrust angles where the aperture is facing downwards would result in idealized upward vertical movement. However, this alignment depends on differential drag and lift, which could skew movement direction, especially at higher velocities (Klug and Korn 2004). All of these hydrostatic properties act as constraints on locomotion and therefore have implications for understanding how the living cephalopod could have swam, captured prey, escaped predators, migrated, and mated.

4.1.2 Previous Modeling of Ectocochleate Cephalopods

It is difficult to model heteromorphic ammonoids due to their complex coiling schemes and constantly changing occupation of 3D space throughout ontogeny. The earliest models of ectocochleate hydrostatics were accomplished by finding the approximate centers of buoyancy and mass from two-dimensional medial sections (Moseley 1838; Trueman 1941; Westermann 1977, 2013; Saunders and Shapiro 1986). A 2D approach may approximate the hydrostatics of simple, bilaterally-symmetric shapes, but is not possible for heteromorphs that coil about multiple axes. Morphogenetic models have been created in 3D to investigate the growth of ammonoids and other mollusks (Okamoto 1988b,1996; Checa et al. 2002; Urdy et al. 2010). Heteromorphic ammonoids in particular were generated in 3D with models that simulate a growing tube (Okamoto 1988b,1996) and that accommodate changes in coiling through ontogeny. An alternate method is proposed in the current study, which builds upon these biological growth models, but also accounts for the total 3D distribution of mass and internal morphology to compute various hydrostatic properties. Tomographic techniques have been increasingly used to generate very accurate 3D models of ectocochleate conches. Computed tomography (CT) scanning can be used to image 3D volumes based on X-ray

attenuation factors within a matrix containing fossil ectocochleates (Hoffmann et al. 2014, 2015, 2018; Lemanis et al. 2015, 2016; Inoue and Kondo 2016). Similarly, serial grinding tomography can create 3D models by successively grinding through the fossil and partitioning the objects of interest (Tajika et al. 2015a, 2015b; Naglik et al. 2015a, 2016). However, these methods require significant contrasts in physical properties to distinguish the fossil conch from its surroundings. Tomographic techniques also require relatively complete and undeformed specimens, which is almost impossible for most nostoceratid heteromorphs, especially *Didymoceras* (Kennedy et al. 2000). Such difficult morphotypes can be theoretically modeled with array generation algorithms, similar to the morphospace parameters of Raup (1967), and photogrammetric models of reconstructed specimens (see methods of Peterman et al. 2019a, 2019b; Peterman and Barton 2018). These methods allow the 3D analysis of complicated shapes to determine hydrostatic properties.

4.1.3 Paleobiology of *Didymoceras*

Didymoceras is traditionally thought of as a poor swimmer due to its aberrant shape (Westermann 1996). This shape would have caused considerable hydrodynamic drag, and the cumbersome orientation of the aperture may have further hindered rapid movement and migration over long distances (Landman et al. 2010). Fossils of this genus from the Western Interior Seaway of the United States yield similar isotopic compositions to benthic inoceramids, suggesting they lived very close to the seafloor (He et al. 2005; Slattery et al. 2007). *Didymoceras* is known from methane seeps in the Western Interior Seaway, which may have served as oases in terms of food supply and oxygenation on a seafloor that was otherwise rather poor in prey (Kauffman et al. 1996;

Landman et al. 2012, 2018). However, ammonoids occurring at these seeps are usually common elsewhere in the basin as well. Ammonoid jaws can shed light on their diet and paleoecology within their corresponding habitats (Tanabe and Landman 2002; Kruta et al. 2009, 2010). Kruta et al. (2010) described the jaws of *Didymoceras nebrascense*, reporting a beak-like morphology that may have served a grasping and cutting function. They suggest this morphology corresponds to a macrophagous diet and reject an opercular function due to the very thin calcitic covering of the lower jaw. Other closely related nostoceratids likely had similar jaw morphologies (Tanabe and Landman 2002; Kruta et al. 2010). These lines of evidence support the interpretation of *Didymoceras* as a slow-moving predator that fed on benthic prey, at least in later life stages. However, the exact nature of this ammonoid's orientation and locomotory ability—and how those may have changed through ontogeny—is still unclear. Hence, this investigation of nostoconic hydrostatics presented here provides important insights into the paleobiology of this extraordinary cephalopod.

4.2 METHODS

The virtual reconstruction of three species of *Didymoceras* (*D. stevensoni*, *D. nebrascense*, and *D. cheyennense*) largely follows the methods of Peterman et al. (2019a) and Peterman and Barton (2018) with some improvements described below. Specimens used to create the virtual 3D models of these species are housed in the National Museum of Natural History (USNM), and Wright State University Lake Campus collections (WSU). Final digital models of the three species of *Didymoceras* are stored online at the data sharing website - morphosource.org (Project: *Didymoceras* Theoretical Models).

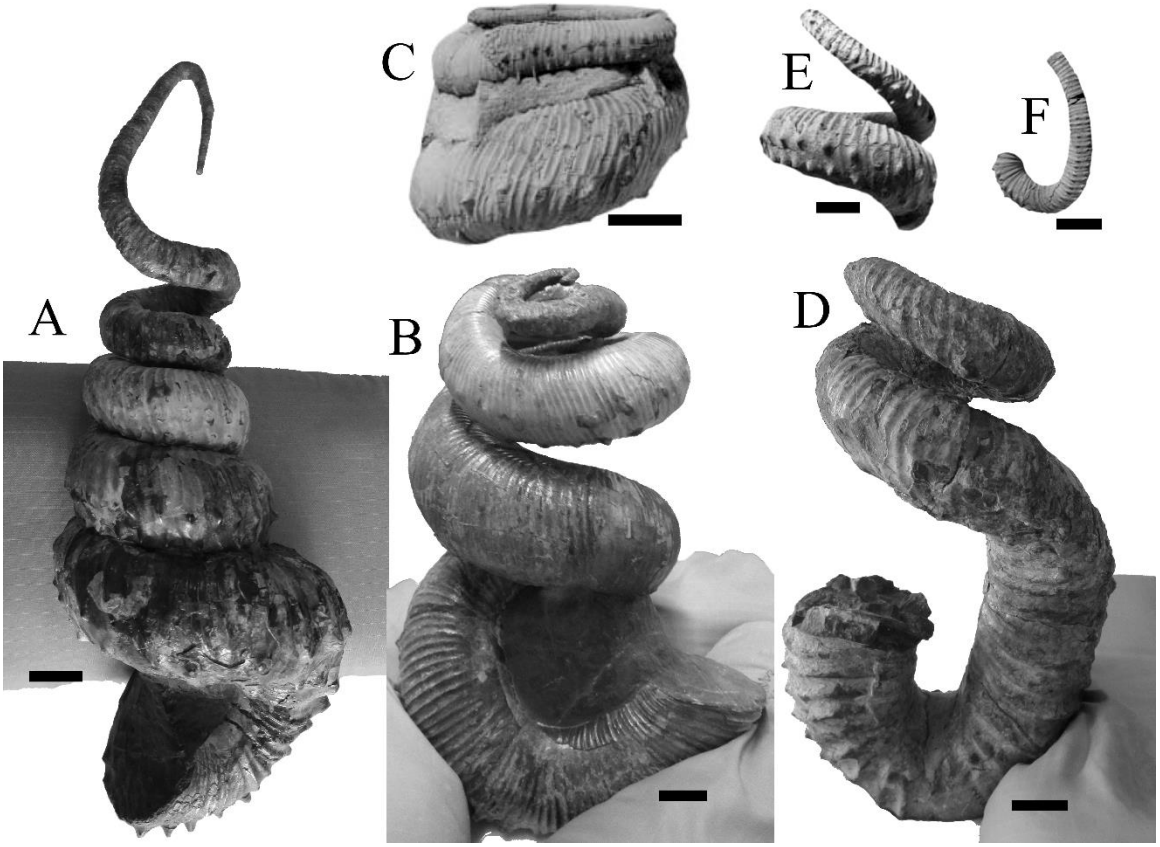

Figure 2: USNM specimens used for model construction. *Didymoceras stevensoni* (A, USNM 430976). Majority of *D. nebrascense* (B, USNM 430977), apical portion of *D. nebrascense* (C, USNM 450333). Majority of *D. cheyennense* (D, USNM 445155), apical portions of *D. cheyennense* (E, USNM 445099; F, 482458). C, E, and F are modified from Kennedy et al. (2000).

4.2.1 Creating Hydrostatic Model Components

Exterior 3D models of *Didymoceras* were created via photogrammetry to serve as stencils for virtual reconstruction. The software 3DF Zephyr (3DFlow 2018) was used to create the initial models, which involved taking ~50 photographs each around the object of interest and using geomatic algorithms to create 3D models of the object's exterior. Well-preserved, remarkably complete, and properly reconstructed specimens of *D. stevensoni* (USNM 430976), *D. nebrascense* (USNM 430977), and *D. cheyennense*

(USNM 445155) served as the initial models to serve as stencils (Fig. 2). Missing apical portions of the models of *D. nebrascense* and *D. cheyennense* were filled-in with the specimens USNM 450333 and USNM 445099 / 482458, respectively. However, the juvenile-most pieces of *Didymoceras* just after the ammonitella are poorly known. Therefore, each apical model extrapolates the juvenile phase to the approximate location of the ammonitella, then terminates. In the current study, we do not investigate the hydrostatic properties at earlier ontogenetic states than the initial uncoiled juvenile shell.

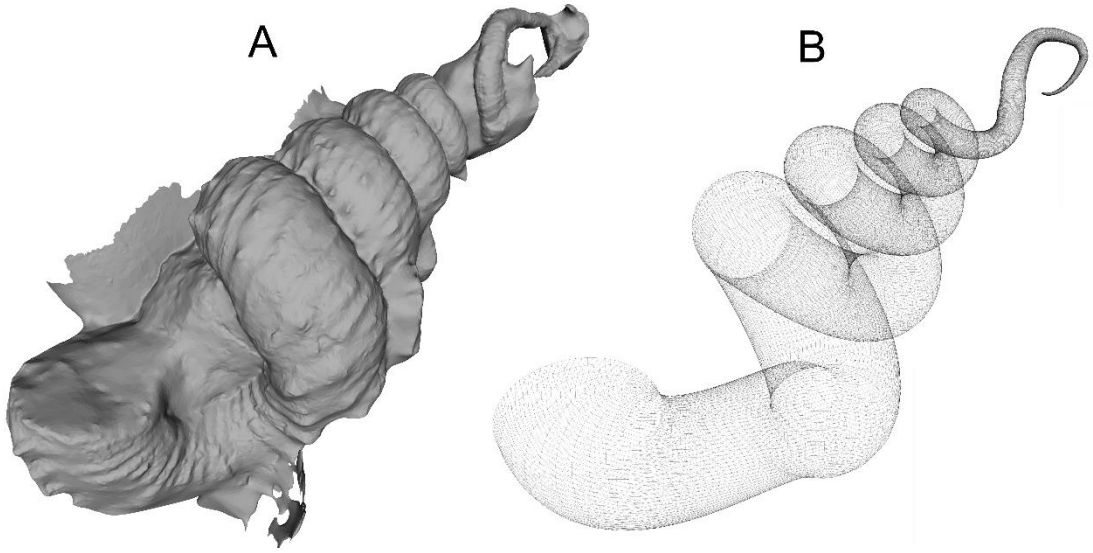

Figure 3: A, Exterior 3D model of *Didymoceras stevensoni* (USNM 430976) created with photogrammetry in 3DF Zephyr. B, Wireframe view of exterior shell created with array instructions in Blender 2.76 after using the photogrammetry model as a stencil (Table 1).

The 3D computer graphics software Blender 2.76 (Blender Online Community, 2017) was used to replicate the whorl section fitted to the terminal aperture on each model with array instructions (Table 1) similar to the parameters of Raup (1967). This process translated, rotated, and scaled the whorl section to match the coiling of the photogrammetry model (Fig. 3). Due to the complex coiling scheme of *Didymoceras*, array instructions were used in a piecewise manner to change shell coiling throughout ontogeny. Towards the apical direction for each model, the origin of the arrays had to be periodically reset in order to make tighter coils (marked with an asterisk on Table 1). Since the models are built from aperture to apex, smaller scaling values represent larger whorl expansion rates throughout ontogeny. The array algorithms create an infinitely thin 3D mesh of the exterior of the shell. Shell thickness can be defined by using the same array instructions on a smaller whorl section, representing the internal interface of the shell. The difference in radii between these two whorl sections is equal to the average ratio of shell thickness to whorl height (0.0314 measured from USNM 445155, USNM 430976, WSU 1459, and WSU 1460; Table 2).

D. stevensoni		Translation (mm)			Rotation (degrees)			Scale
Array #	# Replications	X	Y	Z	X	Y	Z	
1	24	0.8707	0.8878	-4.7199	7.20	3.40	-1.90	0.993
2	20	-0.9100	2.3600	-1.7300	2.00	-9.90	-4.60	0.992
3	142	-1.1600	2.5400	-1.7000	2.00	-6.10	-4.20	0.993
4	55	-0.7900	1.9900	-0.5900	0.80	-2.80	-2.00	0.993
5*	20	-0.1522	149.5444	92.4201	-1.70	-3.60	-4.70	0.992
6	85	-0.8292	150.3931	92.1385	-0.30	-0.50	-0.60	0.992
7*	25	-25.5138	208.5197	110.1478	-4.70	-0.70	-1.20	0.992
8*	100	-19.6526	208.3540	104.8640	-0.65	0.70	-0.10	0.985
D. nebrascense		Translation (mm)			Rotation (degrees)			Scale
Array #	# Replications	X	Y	Z	X	Y	Z	
1	57	-0.1100	-0.1100	-1.4000	-1.50	0.00	0.00	0.998
2	51	0.0500	-0.2100	-0.9900	-1.30	-0.08	-0.18	0.998
3*	30	-11.9500	-88.8700	-11.8500	-2.00	-0.80	-2.70	0.997
4	49	-14.0600	-88.1400	-12.5500	-0.30	0.80	-3.95	1.000
5*	48	18.8300	-54.2700	45.5900	-0.60	0.20	-2.60	0.999
6	66	18.6600	-54.1800	45.4400	-1.00	0.50	-2.40	0.996
7	65	18.4900	-54.6600	45.1000	-1.45	0.80	-2.50	0.997
8	46	18.5200	-55.1899	45.2901	-1.65	-0.65	-2.75	0.991
9*	50	7.9900	-60.4299	110.4001	-0.65	0.20	-0.50	0.990
10*	77	36.1400	-71.9199	100.5601	-0.85	0.35	-1.70	0.996
11*	77	31.6700	-87.5499	101.5501	0.00	0.00	-0.60	0.996
12*	36	9.6718	-79.4678	115.5413	-2.00	0.70	-3.70	0.995
13*	72	13.4018	-72.5678	114.6113	0.00	0.00	-0.35	0.988
D. cheyennense		Translation (mm)			Rotation (degrees)			Scale
Array #	# Replications	X	Y	Z	X	Y	Z	
1	30	-0.1400	-0.3200	-2.0400	1.20	0.25	-0.40	0.998
2	32	-0.9200	-3.2200	-2.6400	4.50	-0.60	-0.40	1.000
3*	60	-7.3920	61.9518	-44.5392	1.00	1.05	-1.20	0.997
4*	40	22.5356	26.5683	50.8891	0.10	0.30	-4.45	0.992
5	100	22.8456	27.5783	50.6791	0.18	0.25	-3.55	0.995
6*	25	-9.7324	3.3336	98.1681	0.30	0.00	-2.20	0.983
7	17	-11.5757	3.3487	98.4267	-0.50	-0.90	-6.40	0.990
8*	50	4.5622	32.0997	112.7608	0.00	0.00	-0.90	0.988
9*	45	19.4348	12.7584	128.3747	0.00	-1.90	-1.90	0.992
10*	150	11.1928	6.3425	129.0736	0.00	0.00	-0.40	0.993

Table1: (Previous page) Array instructions used to build each model of *Didymoceras*. Each array is used in a piecewise manner to replicate the initial whorl section, while simultaneously translating, rotating, and scaling. Asterisks mark the arrays where the origin must be reset to accommodate tighter whorls. Adult apertures were replicated with the following diameters measured or extrapolated from the photogrammetry models: *D. stevensoni* (X 48.600 mm, Y 48.600 mm), *D. nebrascense* (X 43.150 mm, Y 46.660 mm), and *D. cheyennense* (X 40.591 mm, Y 46.619 mm).

The septa were constructed by modeling with photogrammetry (Fig. 4A) an exposed septum of *D. nebrascense* (WSU 1459) that preserved the first and second order folds (see Peterman and Barton 2019). The finer-scale corrugations were constructed for each species by using their respective suture patterns (Figs. 3B, 3C, and 3D; WSU 1461, WSU 1462, WSU 1463, respectively). Each suture pattern was recorded with a digital camera lucida, then wrapped around the whorl section of the phragmocone in the program Meshmixer (Autodesk Inc. 2017a), and extruded inwards. The extruded suture and septal photogram were merged together and smoothed to create a reconstructed septum (Figs. 3E, 3F, and 3G). Thickness was defined for the septum by using the solidify modifier in Blender 2.76. The average septal thickness to whorl height ratio was measured to be 0.0103 from the specimens WSU 1460 and WSU 1461 (Table 2). The extruded septa were replicated with the same array instructions used to build the shell of each corresponding species. Extra septa were deleted until the distal elements of each septum were barely tangential to each other. The external and internal interfaces of the shell, and the replicated septa were repaired and unified together with Netfabb 2017.3 (Autodesk Inc. 2017b) to create a single, manifold 3D mesh capable of volumetry.

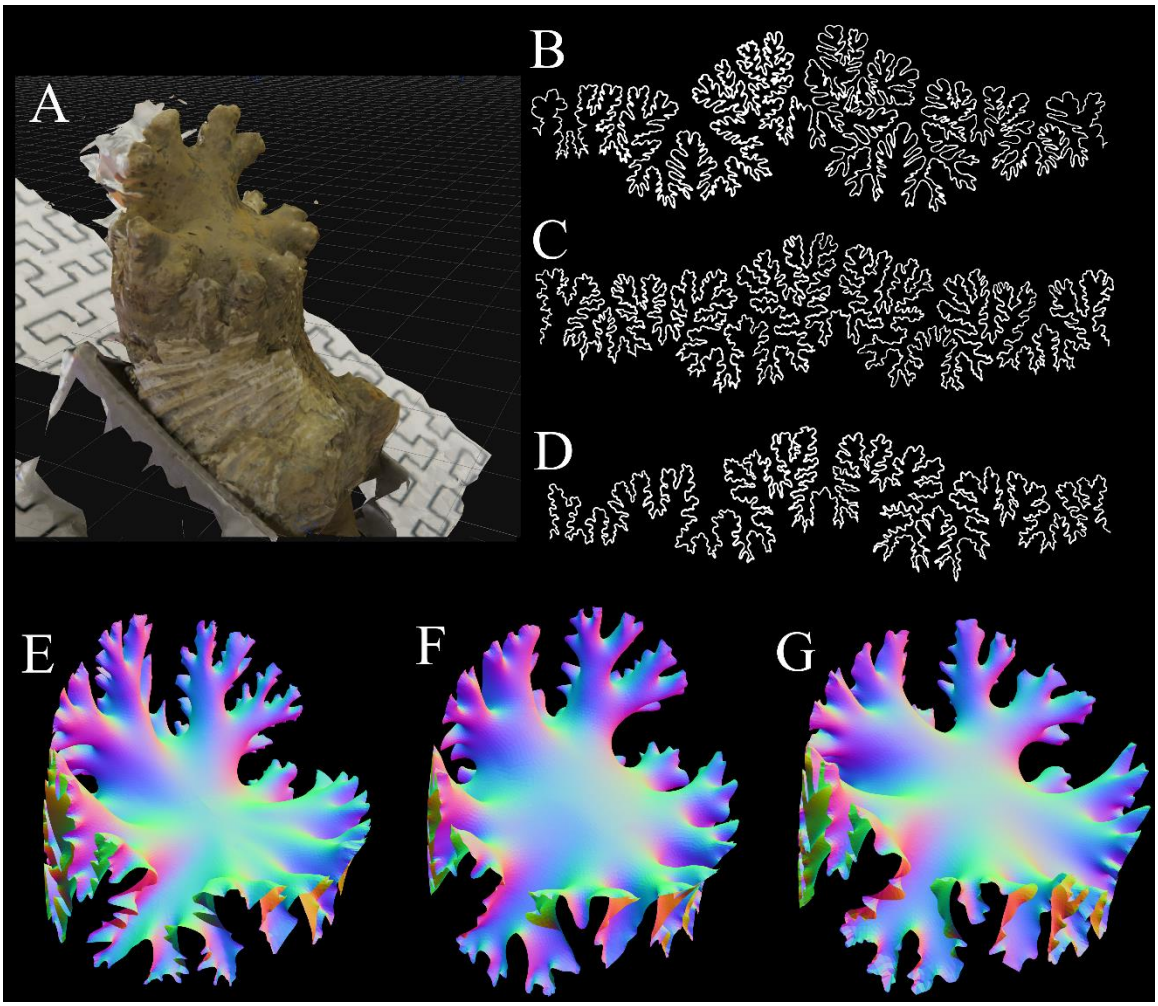

Figure 4: Creation of *Didymoceras* septa. A, Model septum of *D. nebrascense* (WSU 1459) preserving first and second order folds. B, Suture of *D. stevensoni* (WSU 1461). C, Suture of *D. nebrascense* (WSU 1462). D, Suture of *D. cheyennense* (WSU 1463). E, Model septum of *D. stevensoni*. F, Model septum of *D. nebrascense*. G, Model septum of *D. cheyennense*.

Shell Thickness				
Specimen	**Shell (mm)**	**Wh (mm)**	**Shell:Wh**	**Ave. Shell:Wh**
USNM 445155	1.34	41.84	0.0320	0.0314
USNM 445155	1.22	39.86	0.0306	
USNM 445155	0.86	29.33	0.0293	
USNM 430976	0.56	17.23	0.0325	
USNM 430976	1.05	32.23	0.0326	
WSU 1459	0.33	10.20	0.0324	
WSU 1460	0.35	11.45	0.0306	

Septum Thickness				
Specimen	**Septum (mm)**	**Wh (mm)**	**Septum:Wh**	**Ave. Septum:Wh**
WSU 1460	0.24	18.42	0.0130	0.0103
WSU 1460	0.22	24.71	0.0089	
WSU 1460	0.11	11.88	0.0093	
WSU 1461	0.40	39.97	0.0100	

Table 2: Shell thicknesses (Shell) and septum thicknesses (Septum) at respective whorl heights (Wh) measured from specimens of *Didymoceras*. These measurements were used to compute the shell thickness to whorl height (Shell:Wh) and septum thickness to whorl height (Septum:Wh) ratios. The average (ave.) of these two ratios were used to extrude the shell and septum thickness of the *Didymoceras* models of the current study.

The ratio of the body chamber length to total length was measured from an adult *Didymoceras* (USNM 430976) and three progressively more juvenile specimens (USNM 482449, USNM 482445, and USNM 482441). The apical portions of the juvenile specimens were incomplete, so the position of their apertures and terminal septa were marked on the virtual 3D model of a complete *Didymoceras*. The curvilinear distance along the venter between the aperture to terminal septum and between the aperture to apex were recorded from Blender (by summing the spaces between the adjacent replicated whorl sections). The body chamber ratio (length of body chamber to total

length) seems to vary from approximately 1/3 in adults to 1/2 in the earliest juvenile specimen (Fig. 5). It should be noted that the body chamber ratio in nostoceratids has been reported to vary widely during adulthood (Cobban 1974). Body chamber ratios were extrapolated from the recorded relationship to examine several ontogenetic snapshots of each species of the modeled *Didymoceras*. Three-dimensional models of the body chambers were created by isolating the internal interface of the shell from the aperture to terminal septum. The faces of the mesh were inverted so that the exterior was pointing outwards, then the aperture was filled in Meshmixer. A uniform density soft body flush with the aperture was applied similar to Peterman et al. (2019a). Having a similar density to seawater, this has minimal influence in a static setting.

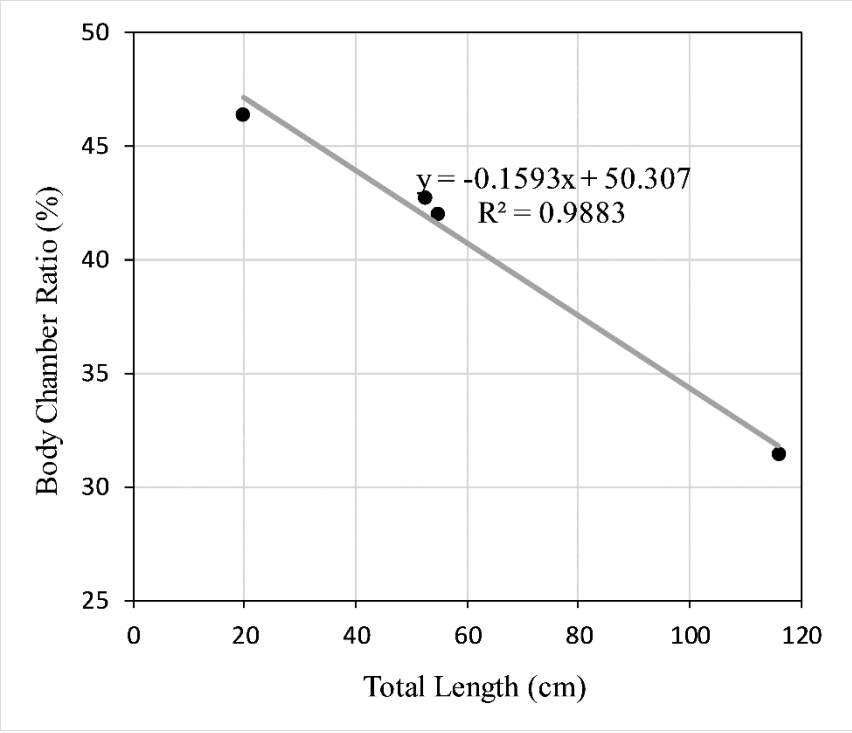

Figure 5: Body chamber ratios as a function of total length recorded from USNM 482411, USNM 482445, USNM 482449, and USNM 430976 (listed from earliest juvenile to adult). These values were used to extrapolate body chamber ratio for the modeled specimens for each ontogenetic stage.

The siphuncle diameter to whorl height ratio was measured at 0.041 from WSU 1461 and WSU 1463. This value allowed a cross section of the siphuncle to be replicated with the corresponding array instructions for each species. The siphuncle 3D model was then unified to the model of the soft body, and subtracted from the model of the shell to create siphuncular foramina in each septum.

A model of the water displaced by each species is required to determine buoyancy and other hydrostatic calculations. This model was created by isolating the external interface of the shell and soft body that come into contact with the surrounding water.

4.2.2 Hydrostatic computations

A neutrally buoyant condition occurs when the sum of the organismal mass is equal to the mass of the water displaced (Archimedes principle):

$$m_{sb} + m_{sh} + m_{cl} + m_{cg} = m_{wd} \quad (1)$$

Where m_{sb} is the mass of the soft body, m_{sh} is the mass of the shell, m_{cl} is the mass of cameral (chamber) liquid, m_{cg} is the mass of cameral gas, and m_{wd} is the mass of water displaced by the cephalopod.

The proportion of the phragmocone volume to be emptied of cameral liquid for neutral buoyancy (Φ) is found by setting Equation 1 in terms of volume and density:

$$\Phi = \frac{\left(\frac{V_{wd}\rho_{wd} - V_{sb}\rho_{sb} - V_{sh}\rho_{sh}}{V_{ct}}\right) - (\rho_{cl})}{(\rho_{cg} - \rho_{cl})} \quad (2)$$

Where V_{wd} and ρ_{wd} are the volume and density of the water displaced, V_{sb} and ρ_{sb} are the volume and density of the soft body, V_{sh} and ρ_{sh} are the volume and density of the shell, ρ_{cl} is the density of cameral liquid, ρ_{cg} is the density of cameral gas, and V_{ct} is the total volume of all camerae. A soft body density of 1.065 g/cm^3 is reported in Westermann (2013) and is assumed to uniformly fill the body chamber of the current

models. A shell density of 2.62 g/cm^3 is commonly accepted (Reyment 1958; Okamoto 1996; Klug et al. 2015). The density of cameral liquid is assumed to be equal to that of seawater (1.025 g/cm^3; Greenwald and Ward 1987). The density of cameral gas is negligible, but fixed at 0.001 g/cm^3 to complete the hydrostatic computations. All volumes were computed in MeshLab 1.3.3 (Cignoni and Ranzuglia 2014).

The volume of cameral gas can be found by multiplying the volume of all camerae by Φ, and conversely, the volume of cameral liquid is found by multiplying the cameral volumes by 1- Φ. After determining these volumes, their spatial distribution in 3D, along with the distribution of the shell and soft body, is required to find the total center of mass:

$$M = \frac{\sum(L * m_o)}{\sum m_o} \quad (3)$$

Where M is the x, y, or z component of the total center of mass, L is the x, y, or z component of the center of mass of each material with unique density (soft body, shell, cameral liquid, and cameral gas) measured with respect to an arbitrary datum, and m_o is the mass of each of these objects of unique density.

The center of buoyancy (B) is equal to the center of volume of the water displaced. The hydrostatic stability of an object is proportional to the separation between the center of buoyancy and the total center of mass (M). Okamoto redefined the stability index of Raup (1967) to apply to heteromorphic ammonoids by dividing the distance between the centers of buoyancy and gravity by the organismal volume (equal to the volume of water displaced):

$$S_t = \frac{\overline{BM}}{\sqrt[3]{V}} \quad (4)$$

It should be noted that the hydrostatic stability in the current study differs from previous studies, which assumed the center of mass was located in the center of the body chamber (Truman 1941; Raup 1967; Raup and Chamberlain 1967; Okamoto 1996).

The syn vivo orientation of each model occurs when the centers of buoyancy and mass are vertically aligned. The apertural angle θ_a was found by appropriately orienting each model then using the protractor function in Blender to measure the angle between the aperture and the vertical plane. Therefore, θ_a equal to -90° corresponds to downward-facing orientations, +90° correspond to upward-facing orientations, and 0° indicates a horizontally facing aperture.

The thrust angle (θ_t) was computed by using the protractor function in Blender to measure the angle between the center of rotation and the location of the hyponome (Fig. 1). The location of the hyponome (along the venter of the aperture) serves as the center of thrust. Therefore, θ_t values of zero would result in optimal horizontal translation with minimal rotation. Note that θ_a herein differs from that of Ebel (1990) and Okamoto (1996). These two studies use the center of mass instead of the center of rotation to measure the thrust angle. Both the organismal weight and buoyancy impact the total restoring moment, therefore the midpoint between the two is the proper pivot point in a hydrostatic setting, as modeled here. However, it should be noted that in a dynamic setting, it is possible to change the pivot point based on rotational drag and differential lift acting on the object.

4.3 RESULTS

4.3.1 Hydrostatic Models of *Didymoceras*

Hydrostatic models of *D. stevensoni* (Figs. 6 and 7), *D. nebrascense* (Figs. 8 and 9), and *D. cheyennense* (Figs. 10 and 11) were examined at several key ontogenetic stages to investigate how their hydrostatic properties changed throughout growth. The progress from an early juvenile stage to the terminal (gerontic) age is proxied by the curvilinear distance from the apex to aperture relative to the total curvilinear length at adulthood for each species (i.e. percentage of their way through life). All of the models at each examined ontogenetic stage have the capacity for neutral buoyancy. The ontogenetic changes of this property, however, are not straightforward. Neutral buoyancy largely depends upon the body chamber ratio and the rate at which the aperture expands during growth. An expansion of the aperture requires a decrease in cameral liquid within the phragmocone for the animal to remain neutrally buoyant. As the shell continues to grow, this region eventually becomes septate and empty, promoting greater buoyancy and allowing Φ to stabilize. Such whorl expansions and changes in Φ are most prominent in juvenile to early intermediate stages of *D. nebrascense* and *D. cheyennense* (Figs. 8 and 10, respectively). It should be noted that the Φ values reported here are dependent upon the arbitrarily chosen life stages, which do not perfectly correlate between each of the chosen species.

Throughout the ontogenetic trajectory of each species, hydrostatic stability (S_t) follows the same general pattern. Each species starts with an orthoconic phase with relatively high stability, then stability gradually decreases throughout ontogeny as the organismal mass is concentrated toward the center of the helical whorls. The helical portion of *D. nebrascense* and *D. cheyennense* has a shorter duration than *D. stevensoni*,

resulting in a slight increase in hydrostatic stability after the formation of the retroversal U-shaped hook (compare Figs. 6-11).

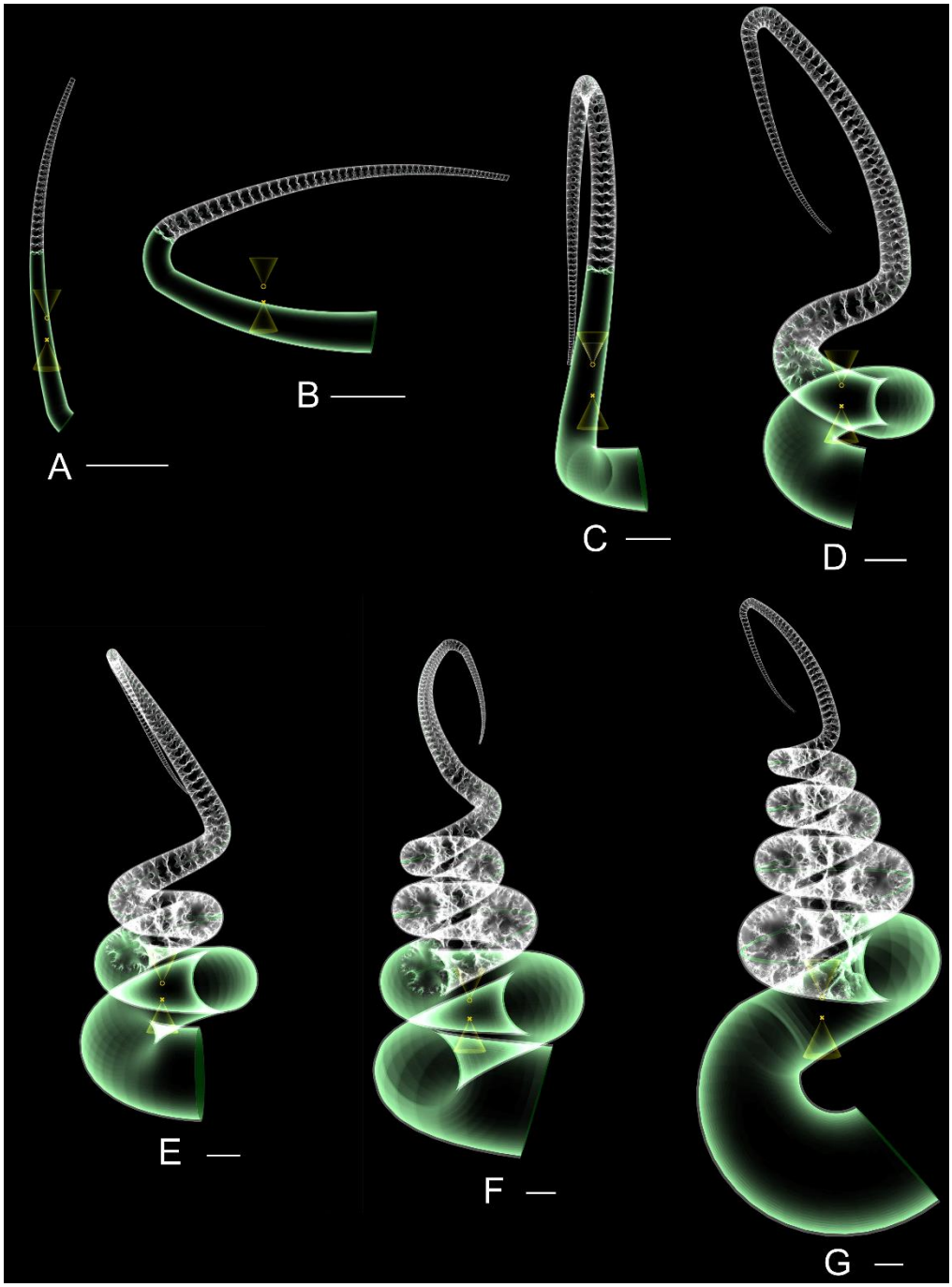

Figure 6: A-G, Hydrostatic models of *Didymoceras stevensoni* throughout ontogeny showing static syn vivo orientations and the locations of the centers of buoyancy (tip of upper cone, circle) and centers of mass (tip of lower cone, x). All scale bars are 1cm.

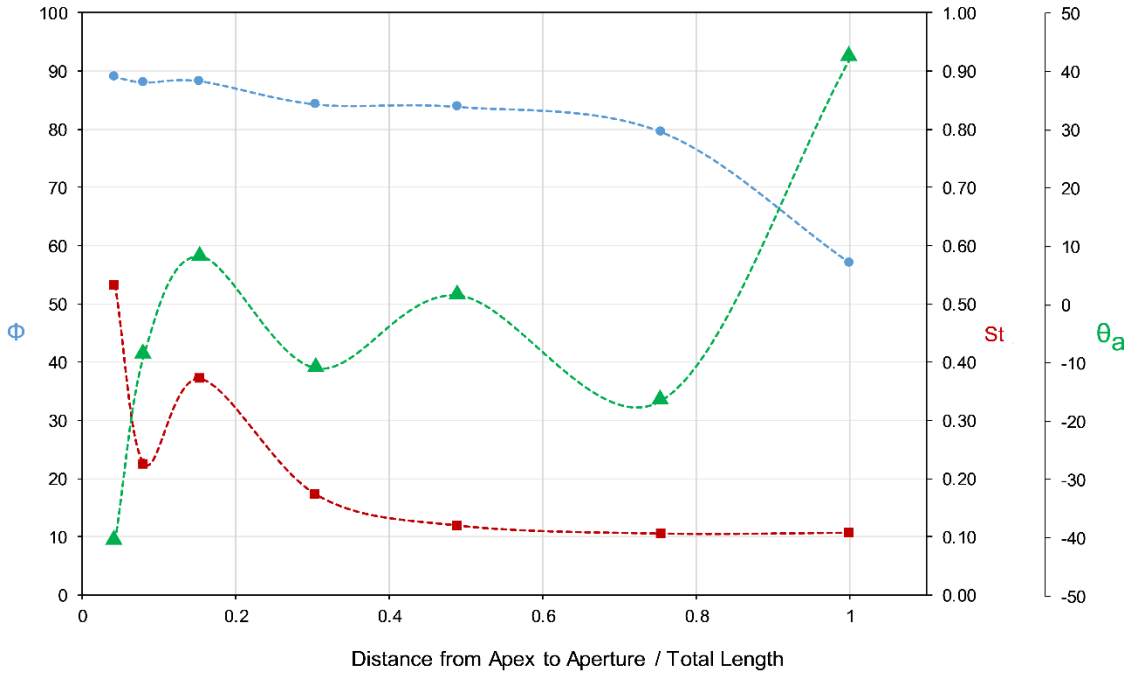

Figure 7: Hydrostatic metrics computed for *Didymoceras stevensoni* for each of the seven ontogenetic stages represented in Figure 6. The percentage of the cameral volumes emptied for neutral buoyancy (Φ; circles), hydrostatic stability index (S_t; Squares), and the angle of the aperture measured from vertical (θ_a; triangles) are reported for each stage. Age is proxied by the curvilinear distance from the apex to aperture at each stage divided by total curvilinear length at adulthood.

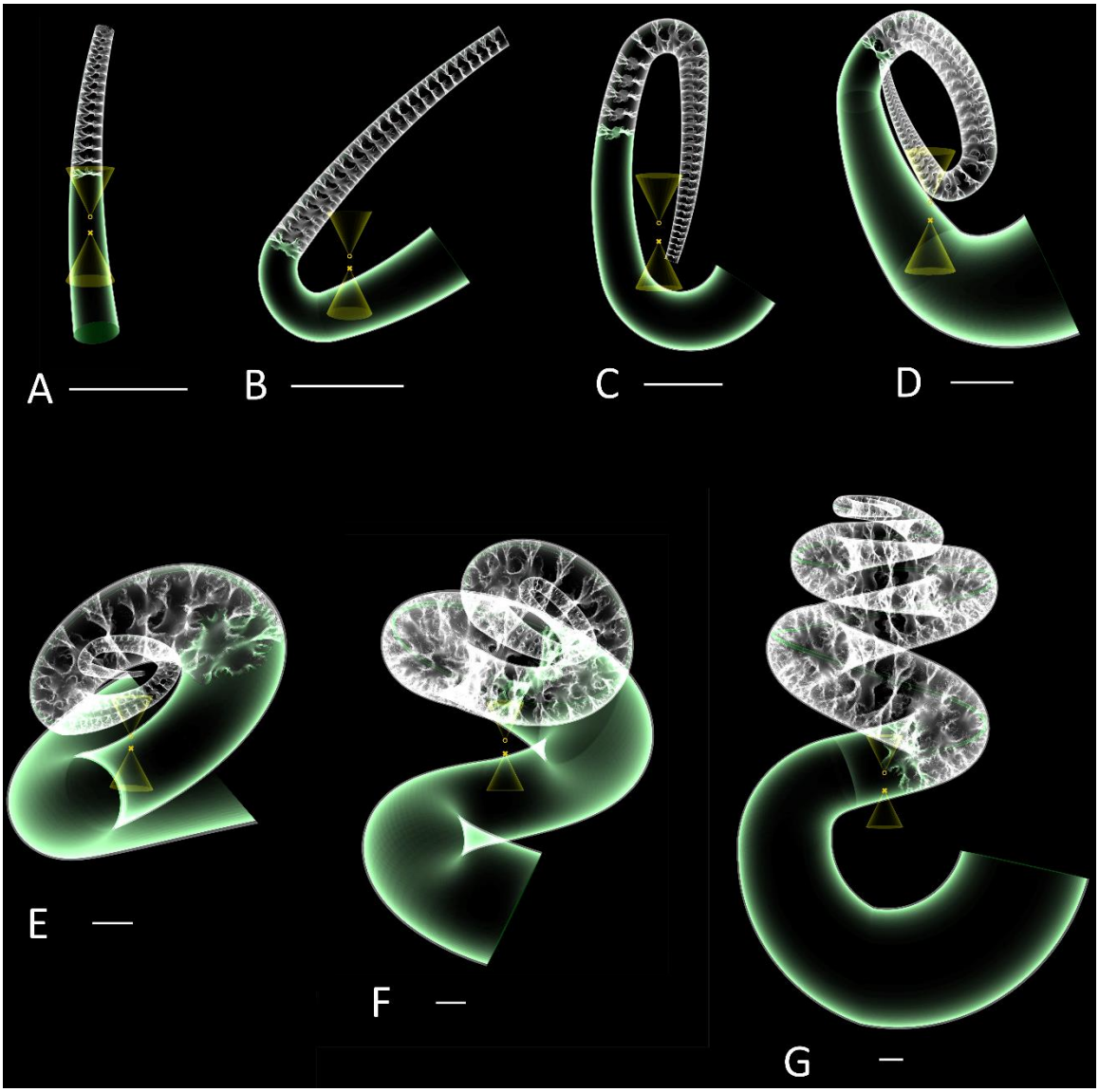

Figure 8: A-G, Hydrostatic models of *Didymoceras nebrascense* throughout ontogeny showing static syn vivo orientations and the locations of the centers of buoyancy (tip of upper cone, circle) and centers of mass (tip of lower cone, x). All scale bars are 1cm.

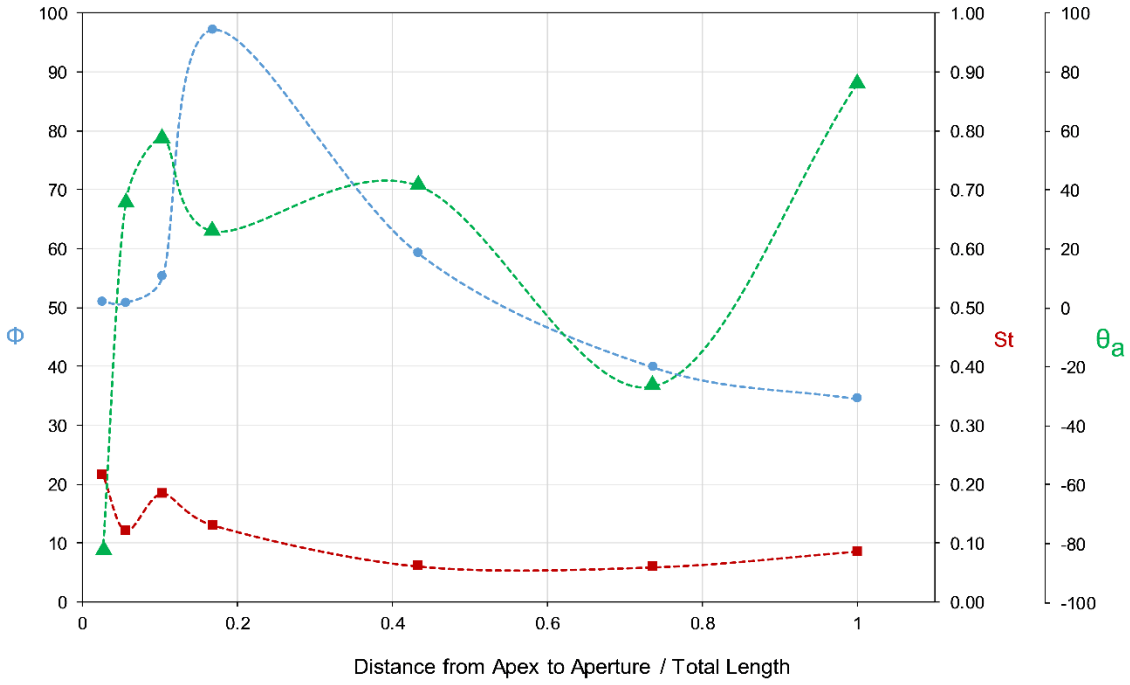

Figure 9: Hydrostatic metrics computed for *Didymoceras nebrascense* for each of the seven ontogenetic stages represented in Figure 8. The percentage of the cameral volumes emptied for neutral buoyancy (Φ; circles), hydrostatic stability index (S_t; squares), and the angle of the aperture measured from vertical (θ_a; triangles) are reported for each stage. Age is proxied by the curvilinear distance from the apex to aperture at each stage divided by total curvilinear length at adulthood.

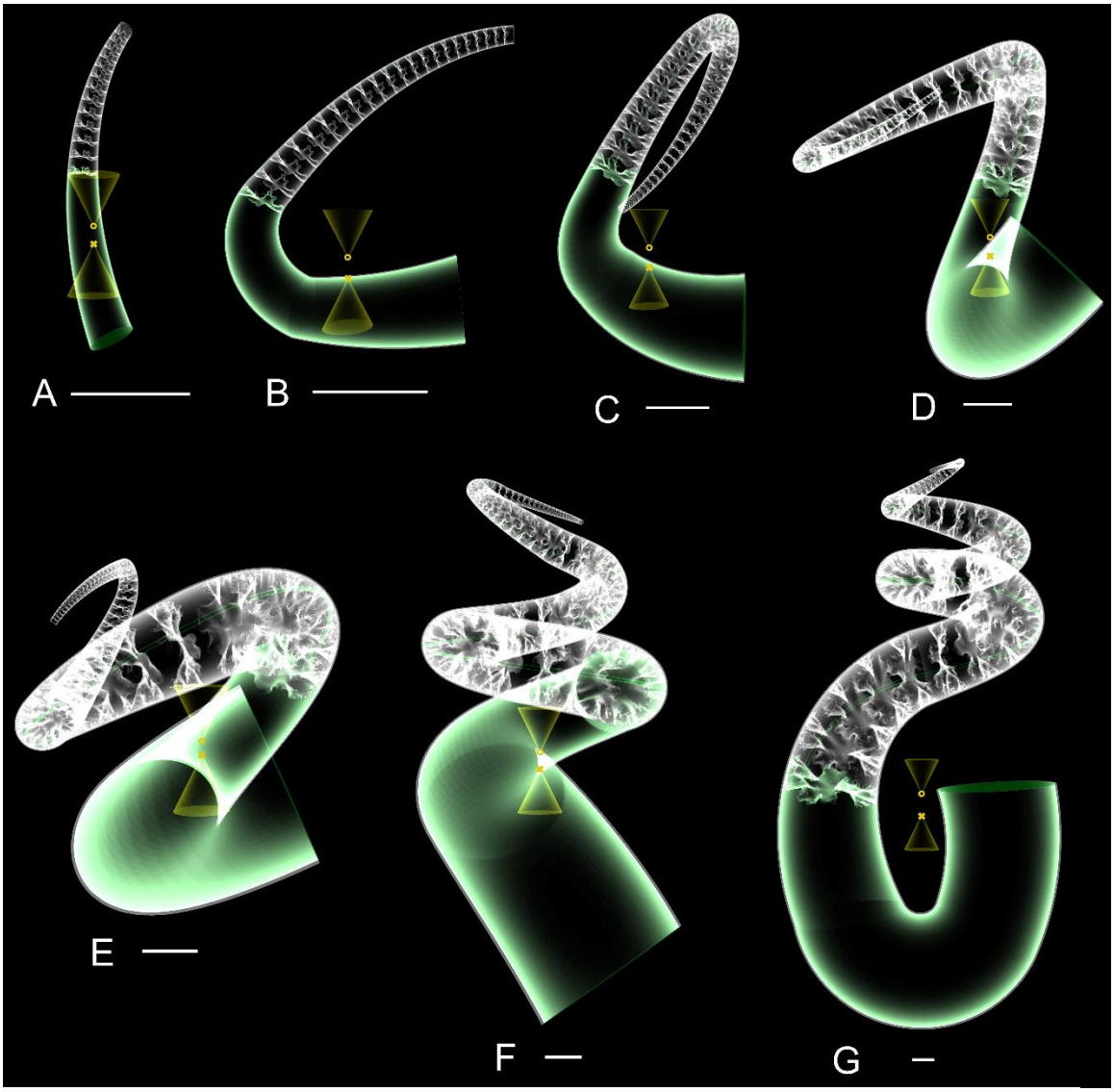

Figure 10: A-G, Hydrostatic models of *Didymoceras cheyennense* throughout ontogeny showing static syn vivo orientations and the locations of the centers of buoyancy (tip of upper cone, circles) and centers of mass (tip of lower cone, x). All scale bars are 1cm.

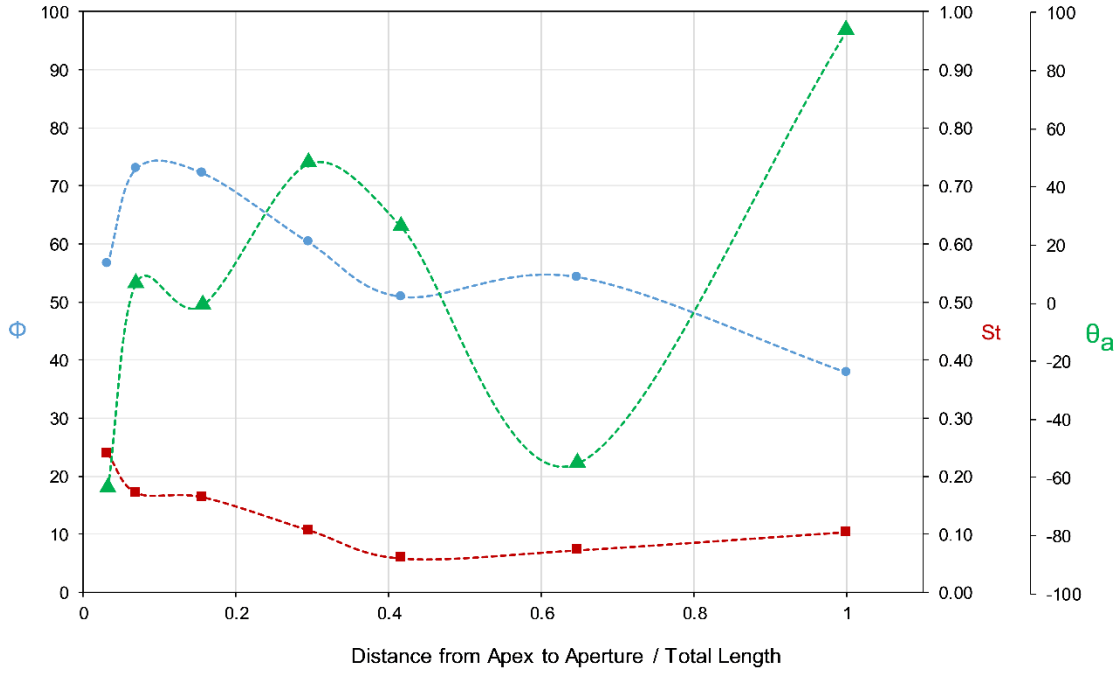

Figure 11: Hydrostatic metrics computed for *Didymoceras cheyennense* for each of the seven ontogenetic stages represented in Fig. 10. The percentage of the cameral volumes emptied for neutral buoyancy (Φ; circles), hydrostatic stability index (S_t; Squares), and the angle of the aperture measured from vertical (θ_a; triangles) are reported for each stage. Age is proxied by the curvilinear distance from the apex to aperture at each stage divided by total curvilinear length at adulthood.

A remarkably similar pattern in syn vivo orientation, based on the computed apertural angle θ_a, occurs throughout ontogeny for all three species of *Didymoceras*. This pattern can be divided into three distinct phases: (1) a juvenile orthoconic phase resulting in a downward facing aperture, (2) a helical phase where the apertural angle oscillates around the horizontal plane, and (3) the formation of the retroversal U-shaped hook yielding an upturned aperture at adulthood.

The thrust angles for each of the three examined species of *Didymoceras* somewhat corresponds to the pattern of syn vivo orientation throughout ontogeny (Fig. 12). Each species starts with low thrust angles, best suited for upward propulsion. After the first deviation from the orthoconic phase (i.e., first elbow bend in the shell), each of

these species are better suited for slow horizontal movement for a relatively short period of time. Afterwards, each of the models have thrust angles suited for diagonal upward thrust. Finally, at adulthood the thrust angle increases to a more horizontal direction of motion for each species, though the shift is modest in *D. stevensoni* compared to the other two species.

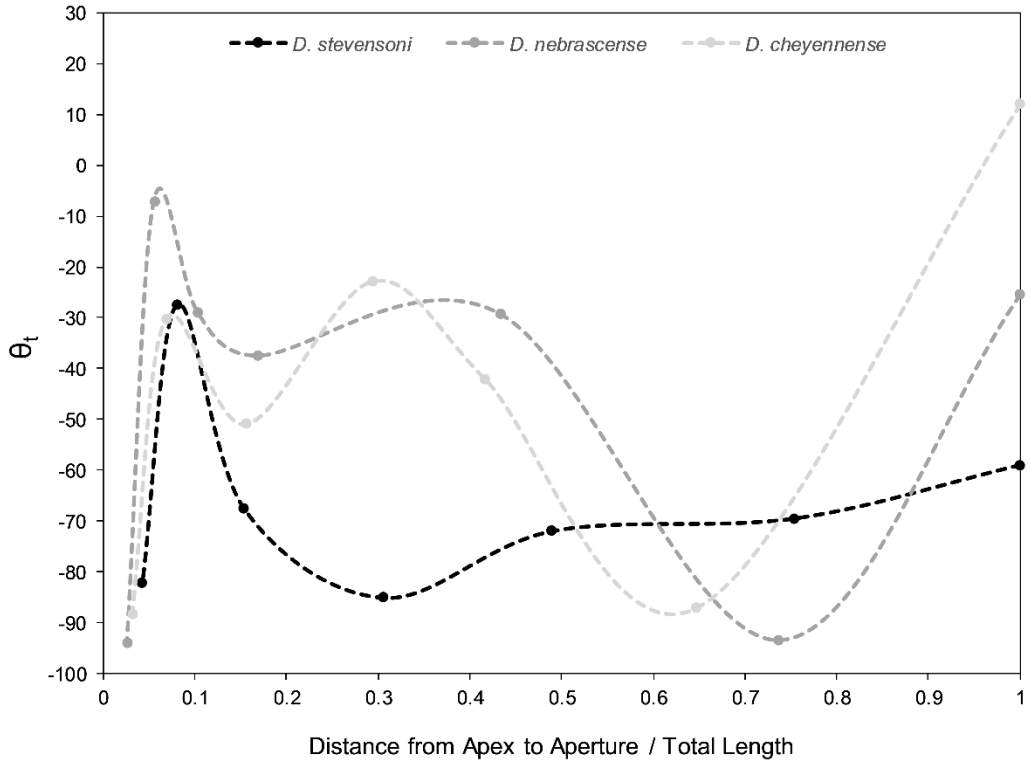

Figure 12: Thrust angle (θ_t) measured from the horizontal vs. age for each of the seven examined ontogenetic stages of *D. stevensoni* (Fig. 6), *D. nebrascense* (Fig. 8), and *D. cheyennense* (Fig. 10). Low thrust angles (-90°) correspond to idealized upward movement, while thrust angles of zero correspond to idealized horizontal-backwards movement.

The Φ values, masses, and volumes of each model component for hydrostatic calculations are organized in Table 3. The centers of mass and buoyancy, their separation, hydrostatic stability, apertural angles, and thrust angles for each model are organized in Table 4. Ideally, the sum of the masses of each model component should be equal to the mass computed from the water displaced. Discrepancies between these values result in a mass surplus or absence that influences all of the hydrostatic calculations. The mass discrepancies for the virtual models are all less than 0.1% (Table 3), suggesting that hydrostatic calculations are not significantly impacted. The absence of ornamentation in the models could cause shell mass to be slightly lower for smooth models compared to actual specimens (potentially raising Φ values). The assumption of isometric shell and septal thicknesses also may contribute some error. However, Peterman et al. (2019a) compared an isometric *Nautilus* shell with a CT scanned specimen from Hoffmann et al. (2014) and found only a 4% difference in mass. The isometric shell thicknesses in the current study likely have a similarly low error. Additionally, the mass of the soft body is much more influential on the hydrostatics and mass distribution than the shell (see Table 3). Other potential sources of error are the discrepancies in septal mass resulting from differences between each of the specimens used to record septa and changes of the models during processing. Sutures were recorded from different positions on each whorl and from differently sized specimens (ranging from whorl heights of 24 mm to 31mm). Suture patterns were also assumed to remain constant through ontogeny. Additionally, some of the finest lobules and folioles were smoothed during the extrusion process (Fig. 4). However, the normalized surface areas of each septum are less than 5% different from

each other and probably do not contribute much to the total error in mass, especially since the shell masses are consistently lower than those of the soft body (Table 4).

Virtual Model	**% life**	**V_{sh} (cm^3)**	**m_{sh} (g)**	**V_{sb} (cm^3)**	**m_{sb} (g)**	**V_{cg} (cm^3)**	**m_{cg} (g)**	**V_{cl} (cm^3)**
D. stevensoni 1	*0.04*	0.01671	0.04378	0.13076	0.13926	0.03069	0.00004	0.00379
D. stevensoni 2	*0.08*	0.07526	0.19717	0.57686	0.61436	0.13981	0.00017	0.01888
D. stevensoni 3	*0.15*	0.35174	0.92156	2.62321	2.79372	0.65131	0.00078	0.08644
D. stevensoni 4	*0.30*	2.06606	5.41309	15.13118	16.11471	3.81731	0.00460	0.71028
D. stevensoni 5	*0.49*	7.14251	18.71338	51.40451	54.74580	13.16473	0.01585	2.52927
D. stevensoni 6	*0.75*	23.44394	61.42313	163.19059	173.79798	42.96273	0.05173	11.05618
D. stevensoni 7	*1.00*	48.19238	126.26402	272.62653	290.34726	85.95270	0.10349	64.87455
D. nebrascense 1	*0.03*	0.01031	0.02700	0.09661	0.10289	0.01987	0.00002	0.01910
D. nebrascense 2	*0.06*	0.03565	0.09341	0.33223	0.35383	0.06867	0.00008	0.06646
D. nebrascense 3	*0.10*	0.11649	0.30521	1.16008	1.23549	0.22731	0.00027	0.18443
D. nebrascense 4	*0.17*	0.54852	1.43712	6.63749	7.06892	1.11668	0.00134	0.03330
D. nebrascense 5	*0.43*	5.83013	15.27494	57.90712	61.67108	11.37083	0.01369	7.82899
D. nebrascense 6	*0.74*	18.09677	47.41355	130.26148	138.72847	33.36715	0.04017	50.42124
D. nebrascense 7	*1.00*	35.67553	93.46989	218.36161	232.55511	64.27713	0.07739	122.21979
D. cheyennense 1	*0.03*	0.00791	0.02071	0.08044	0.08567	0.01549	0.00002	0.01183
D. cheyennense 2	*0.07*	0.04198	0.10999	0.47132	0.50196	0.08403	0.00010	0.03111
D. cheyennense 3	*0.16*	0.37514	0.98286	4.07393	4.33874	0.74541	0.00090	0.28674
D. cheyennense 4	*0.29*	1.70772	4.47422	16.96188	18.06440	3.33190	0.00401	2.19019
D. cheyennense 5	*0.42*	3.68744	9.66108	33.64177	35.82848	7.07983	0.00852	6.81752
D. cheyennense 6	*0.65*	11.23904	29.44630	106.28340	113.19182	21.73059	0.02616	18.25902
D. cheyennense 7	*1.00*	32.25664	84.51239	234.12133	249.33921	59.57845	0.07173	97.86402

Virtual Model	m_{cl} (g)	V_{ct} (cm^3)	V_{wd} (cm^3)	m_{wd} (g)	m_{total} (g)	error (%)	ϕ_{gas} (%)
D. stevensoni 1	0.00389	0.03499	0.18246	0.18702	0.18697	0.031	89.0
D. stevensoni 2	0.01936	0.15866	0.81078	0.83105	0.83106	0.000	88.1
D. stevensoni 3	0.08860	0.73680	3.71175	3.80455	3.80466	-0.003	88.3
D. stevensoni 4	0.72804	4.51887	21.71611	22.25902	22.26043	-0.006	84.3
D. stevensoni 5	2.59250	15.65963	74.20666	76.06182	76.06753	-0.008	83.9
D. stevensoni 6	11.33258	53.93987	240.57441	246.58877	246.60542	-0.007	79.5
D. stevensoni 7	66.49641	150.43966	471.25856	483.04003	483.21117	-0.035	57.0
D. nebrascense 1	0.01957	0.03889	0.14580	0.14945	0.14949	-0.025	51.0
D. nebrascense 2	0.06812	0.13483	0.50272	0.51529	0.51544	-0.029	50.8
D. nebrascense 3	0.18904	0.41084	1.68741	1.72960	1.73001	-0.024	55.2
D. nebrascense 4	0.03414	1.14710	8.33311	8.54143	8.54152	-0.001	97.1
D. nebrascense 5	8.02472	19.15683	82.89408	84.96643	84.98443	-0.021	59.2
D. nebrascense 6	51.68177	83.57661	231.93486	237.73323	237.86396	-0.055	39.8
D. nebrascense 7	125.27528	186.01589	440.05303	451.05436	451.37768	-0.072	34.4
D. cheyennense 1	0.01212	0.02726	0.11561	0.11850	0.11853	-0.021	56.7
D. cheyennense 2	0.03188	0.11484	0.62815	0.64385	0.64393	-0.013	72.9
D. cheyennense 3	0.29391	1.02965	5.47873	5.61570	5.61641	-0.013	72.2
D. cheyennense 4	2.24495	5.50768	24.17728	24.78171	24.78758	-0.024	60.3
D. cheyennense 5	6.98795	13.85675	51.18595	52.46560	52.48604	-0.039	50.1
D. cheyennense 6	18.71550	39.86365	157.38609	161.32075	161.37978	-0.037	54.3
D. cheyennense 7	100.31062	156.97272	423.35069	433.93445	434.23396	-0.069	37.8

Table 3: (This page and previous page) The volumes (V) and masses (m) for each component of the *Didymoceras* models (sh = shell, sb = soft body, cg = cameral gas, cl = cameral liquid, ct = camerae total, wd = water displaced) for each ontogenetic stage (denoted by a number after the species name; 1, earliest juvenile to 7, adult). Age (% life) is proxied by the curvilinear distance between the apex and aperture divided by total curvilinear length at adulthood. The percent error (mass discrepancies between the total model mass and the mass of the water displaced), and the percentage of the cameral volume that must be emptied of liquid to achieve a neutrally buoyant condition (Φ) are listed for each model.

		Center of Buoyancy			Center of Mass (Total)						
Virtual Model	**% life**	**x (mm)**	**y (mm)**	**z (mm)**	**x (mm)**	**y (mm)**	**z (mm)**	$\overline{\mathbf{BM}}$ **(mm)**	$\mathbf{S_t}$	$\boldsymbol{\theta_a}$	$\boldsymbol{\theta_t}$
D. stevensoni 1	0.04	-14.414	198.451	101.181	-15.592	201.107	101.955	3.007	0.530	-40.5	-82.0
D. stevensoni 2	0.08	-22.421	194.523	109.416	-23.823	193.914	110.847	2.094	0.225	-8.5	-27.4
D. stevensoni 3	0.15	-9.647	164.173	100.675	-7.470	159.073	99.180	5.742	0.371	8.2	-67.5
D. stevensoni 4	0.30	-14.382	138.167	77.283	-15.172	134.358	74.514	4.775	0.171	-11.0	-85.0
D. stevensoni 5	0.49	-13.712	116.401	65.097	-13.995	112.196	62.450	4.976	0.118	1.5	-71.9
D. stevensoni 6	0.75	-5.158	88.237	50.340	-4.088	82.383	47.687	6.516	0.105	-16.5	-69.4
D. stevensoni 7	1.00	4.400	65.792	19.545	6.296	59.793	14.198	8.256	0.106	42.3	-58.9
D. nebrascense 1	0.03	20.943	-74.752	110.818	19.983	-74.399	111.312	1.135	0.216	-82.4	-94.0
D. nebrascense 2	0.06	14.955	-78.536	112.878	14.176	-79.036	113.145	0.964	0.121	35.5	-7.1
D. nebrascense 3	0.10	28.212	-81.370	104.475	30.009	-81.840	103.317	2.189	0.184	57.5	-29.0
D. nebrascense 4	0.17	12.576	-67.599	109.142	10.989	-65.532	109.511	2.632	0.130	26.0	-37.5
D. nebrascense 5	0.43	3.223	-65.475	94.014	3.150	-63.377	92.426	2.633	0.060	41.4	-29.3
D. nebrascense 6	0.74	-2.806	-66.282	65.724	-3.198	-66.097	62.131	3.619	0.059	-26.6	-93.5
D. nebrascense 7	1.00	-4.934	-56.910	22.519	-5.659	-55.579	16.188	6.510	0.086	75.8	-25.5
D. cheyennense 1	0.03	4.353	9.329	125.981	5.252	8.745	126.427	1.160	0.238	-64.2	-88.3
D. cheyennense 2	0.07	14.783	14.375	126.121	16.080	15.067	126.105	1.470	0.172	6.5	-30.2
D. cheyennense 3	0.16	-3.559	21.633	108.474	-5.764	21.874	106.621	2.890	0.164	-1.0	-50.9
D. cheyennense 4	0.29	10.122	5.652	96.104	12.041	3.738	94.593	3.103	0.107	47.5	-22.8
D. cheyennense 5	0.42	2.068	14.906	87.885	2.197	16.430	86.343	2.171	0.058	25.7	-42.0
D. cheyennense 6	0.65	8.747	22.342	61.025	9.196	23.209	57.225	3.923	0.073	-55.4	-87.0
D. cheyennense 7	1.00	-0.432	29.806	-1.466	-1.500	30.321	-9.183	7.808	0.104	93.5	12.0

Table 4: The x, y, and z components of the centers of buoyancy and mass are reported with respect to an arbitrary datum (the center of the adult whorl section). Hydrostatic metrics (BM = the distance between the centers of buoyancy and mass, S_t = hydrostatic stability index, θ_a = apertural angle, and θ_t = thrust angle) are reported as a function of age (% life = curvilinear distance from apex to aperture / total curvilinear length).

4.4 DISCUSSION

The three species of *Didymoceras* investigated in the current study can each be divided into three ontogenetic stages based on shell coiling: (1) an early, generally straight phase, (2) a helical intermediate phase, and (3) an adult phase with a retroversal U-shaped hook. This hook probably represents the attainment of sexual maturity, and may have been formed relatively quickly (Bucher et al. 1996). The relative duration of the intermediate helical phase for the examined species increases from *D. cheyennense* to *D. nebrascense* and reaches a maximum in *D. stevensoni*. It is unknown, however, if the extra helical portion of *D. stevensoni* corresponds to a larger amount of time spent building this part of shell. The hydrostatic calculations presented here reveal differences between each of the examined species of *Didymoceras*, and also have implications for the nostoconic morphotype as a whole.

All virtual models of *Didymoceras* have the capacity for neutral buoyancy throughout each ontogenetic stage and must leave some amount of cameral liquid in the phragmocone to maintain this condition. Therefore, while isotopic studies suggest this genus was demersal and lived very close to the benthos (He et al. 2005, 2016), it still retained the ability to hover around, close to the seafloor. This life mode would enable the ammonoid to push up off the seafloor with minimal effort, to evade predators or pounce on prey items. The degree of chamber emptying required for neutral buoyancy would have varied as the ammonoid grew. The largest constraint on neutral buoyancy is the mass of the soft body (Table 3). The soft body mass is directly influenced by the whorl expansion and body chamber ratio, both of which change throughout ontogeny in a very complicated fashion in *Didymoceras.* Interestingly, the whorl expansion of *D.*

stevensoni changes more gradually than that of *D. nebrascense* or *D. cheyennense*. This lower whorl expansion rate results in gradual changes in Φ throughout ontogeny (Fig. 7). Conversely, the amount of cameral liquid in the phragmocone rapidly decreases for *D. nebrascense* (Fig. 9), and *D. cheyennense* (Fig. 11) as they build the "elbow" that starts the intermediate helical phase. It should be noted that the conditions for neutral buoyancy (Φ) must fluctuate during actual growth because each septum is precipitated in water, then emptied of cameral liquid (Ward 1979). Therefore, Φ probably does not change as regularly as the interpolated dashed lines on Figures 7, 9, and 11 depict. Furthermore, decreases in Φ can be compensated by reducing the body chamber ratio (Klug et al. 2004).

While the soft body density is very close to that of water, it is still three orders of magnitude larger than that of the gas filling the camerae. This difference fundamentally weights the distribution of mass toward the body chamber for all ectocochleates and influences the stability index (Peterman et al. 2019a, 2019b). For each model, hydrostatic stability (S_t) is at a maximum during the earliest juvenile, orthoconic phase. Orthocones have very high hydrostatic stability values because they distribute the mass away from the phragmocone and toward the soft body in a linear fashion (see Peterman et al. 2019b). Any deviation from the straight line (coiling of any kind) would consequently reduce stability. Throughout growth, total organismal mass becomes concentrated in response to coiling. The helical whorls in the intermediate growth stages also influence the volume of water displaced and cause the centers of buoyancy and mass to be placed closer together, reducing stability. The formation of the retroversal, U-shaped hook causes hydrostatic stability to slightly increase for all three examined species of *Didymoceras*, though the

increase is quite small in *D. stevensoni*. The adult body chamber deviates from the earlier whorls, distributing mass further from the center of buoyancy. This stability increase is more prominent for *D. nebrascense* and *D. cheyennense* because they devote a smaller portion of their life to coiling during the intermediate stage. Although hydrostatic stability decreases throughout ontogeny for each of the examined species, they all have adult values around twice the stability of the modern *Nautilus* (0.050; Peterman et al. 2019a). While the stability index of *Nautilus* is a seemingly low number, it still imparts a restoring moment large enough so that the living animal does not pinwheel during locomotion (Saunders and Shapiro, 1986; Peterman et al. 2019b). Selective pressures on hydrostatic stability represent a tradeoff in locomotory efficiency: a high stability prevents excessive rocking or pinwheeling during jet propulsion but also makes it more difficult for the animal to move into an orientation other than its hydrostatically defined one. The hydrostatic stability of each of the *Didymoceras* virtual models is large enough that syn vivo orientation is probably unable to be significantly modified with active locomotion, or at least very costly in terms of energy use. This difficulty in movement is especially true in earlier ontogenetic stages. In a dynamic setting, the larger hydrostatic stability values at juvenile stages may be negligible depending on the Reynolds number of the system (the ratio of inertial forces to viscous forces). When moving horizontally at one body width per second, the adult model has a Reynolds number on the order of 10^1 to 10^2, while the early juvenile has a Reynolds number less than 10^0. This lower Reynolds number means that the surrounding seawater would seem more viscous for the early-juvenile ammonoids, hindering movement and possibly the effects of the restoring moment. From the time of an early hatchling, most ammonoids were probably passive

and planktic (Jacobs and Chamberlain 1996; Landman 1988; Mapes and Nützel 2008; Ritterbush et al. 2014; Naglik et al. 2015b; Tajika et al. 2018). If ocean currents within the habitat of *Didymoceras* were not strong enough to facilitate the dispersal of their hatchlings (Tajika and Wani 2010), the hatchlings may have remained close to their hatching sites, as it would be relatively difficult for the early hatchlings to move any distance via active locomotion.

The life orientation of ectocochleates is vital to understanding how the living cephalopods would have swam and interacted with their surroundings (Saunders and Shapiro 1986; Okamoto 1988a; Klug 2001; Naglik et al. 2015b). While the orientation of the aperture (θ_a) may not directly indicate a particular mode of life, it nonetheless imposes some important limitations, especially when the orientation of the aperture cannot be significantly modified with active locomotion due to a high stability index (S_t). Each of the *Didymoceras* models have downward facing apertures during the earliest juvenile orthoconic phase (consistent with the baculite models of Peterman et al., 2019b). A downward orientation in *Didymoceras* hatchlings is consistent with feeding either within the water column or off the bottom. Afterwards, the apertures oscillate around the horizontal, forward-facing plane as the helical intermediate stage progresses. This orientation could have allowed the juvenile ammonoid to feed or scavenge along the seafloor and to catch slow demersal prey items. Each model terminates with an upward apertural orientation after the U-shaped hook is developed. This adult orientation away from the seafloor suggests either a different mode of feeding or possibly the absence of feeding in reproductive adults, which is well-documented in various modern coleoid cephalopod groups (Rocha et al. 2001; Hanlon and Messenger 2018). The duration of the

intermediate helical phase with a generally horizontal apertural orientation is larger for *D. stevensoni* and progressively lower for *D. nebrascense* and *D. cheyennense*. Changes in the duration of each phase indicate that there may have been differences among these species in how long an individual maintained the life habit consistent with that orientation. Alternatively, it may be a consequence of larger whorl expansion rates in *D. nebrascense* and *D. cheyennense* relative to *D. stevensoni*. This is evidenced by the differences in total length along the venter at adulthood (116 cm, 96 cm, and 78 cm for D. stevensoni, *D. nebrascense*, and *D. cheyennense*, respectively). It is unknown whether or not this difference in shell length corresponds to differences in terminal ages or in metabolic growth rates.

The upturned aperture at adulthood is enigmatic for ammonoids that lived close to the seafloor. This orientation may be incompatible with scavenging or searching for prey items in this setting (Klinger 1981; Landman et al. 2012). However, a U-shaped hook is a common adult modification for many taxa of heteromorphic ammonoids within Nostoceratidae, Scaphitidae, Diplomoceratidae, Ancyloceratidae, and Macroscaphitidae among others, spanning multiple higher taxonomic levels (Klug et al. 2015). One adaptive explanation for the prevalence of the adult hook is that, by shifting the aperture to face up, brooding adults could hold their egg masses (assuming they had them) up and away from benthic predators (Walton et al. 2010). Further complicating the interpretation of an upturned aperture, it is unknown how mutable the direction of thrust was for such ammonoids. Were they able to stretch the hyponome over the ventral aperture and direct their jet thrust downwards, enabling them to move in the direction they were facing (like the extant *Nautilus*; Packard et al., 1980)? It is easier for extant ectocochleates (nautilids)

to manage their buoyancy by being very slightly negatively buoyant (Ward 1979). Was this the case for ammonoids with U-shaped body chambers at maturity? If so, were they able to counteract this difference in buoyancy? The largest hurdle in answering these questions is that unequivocal preservation of soft tissues has yet to be discovered (Klug and Lehmann 2015). The functional significance of such an adult modification should be further explored.

The thrust angle (θ_t; Figs. 1, 11) is a useful tool to understand the efficiency and constraints on the direction of locomotion for animals that move via jet propulsion (Okamoto 1996; Klug and Korn 2004; Naglik et al. 2015b). Ideally, the optimal horizontal movement would occur when the thrust angle is zero. This would transmit the energy produced from thrust into more translational movement and less rotational movement. Conceptually, a downward-facing orthocone would have trouble moving horizontally due to its very low thrust angle (around -90^o) and large distance between the center of rotation and location of thrust (in addition to higher drag in this configuration; Peterman et al. 2019b). Similar to the other hydrostatic properties computed in this study, the thrust angle has similar patterns throughout ontogeny for each of the examined species of *Didymoceras*, at least in coarse terms (Fig. 12). The early juvenile orthoconic phase seems to be well adapted for upward vertical movement, however, at smaller sizes, the low Reynolds number may have made locomotion in any direction more difficult. The thrust angle then changes rapidly toward zero (horizontal alignment) just before the helical phase develops for each species. The horizontally oriented aperture and low thrust angles would permit efficient horizontal movement. These properties could have strongly enhanced the dispersal ability of juvenile *Didymoceras*, especially in the absence of a

current near the seafloor. As the helical phase develops, the thrust angles seem more variable, however, they generally do not favor horizontal movement, especially in *D. stevensoni*, even though the apertures are more or less horizontally oriented. This intermediate helical phase resembles the torticonic ammonoids belonging to Turrilitidae. Klinger (1980) suggests that this morphology could have been adept at rotating along the z axis with an improved turning ability compared to monomorphs. For *Didymoceras* the center of mass is displaced laterally outside of the body chamber, in the center of the helical whorls (similar to the probable mass distribution of turrilitids; Figs. 6, 8, 10). A pirouetting mode of life assumed during the helical phase of *Didymoceras* could have allowed them to scan larger portions of the water column for plankton by rotating, while expending less energy compared to lateral movement. At adulthood, thrust angles increase once again, with the increase being much more pronounced in *D. nebrascense* and *D. cheyennense* than in *D. stevensoni*. This increase is due to the U-shaped body chamber raising the aperture with respect to the center of rotation. Therefore, the U-shaped adult modification functions to improve horizontal locomotion by raising the thrust angle relative to the earlier helical stage (as mentioned previously by Klug et al. 2015), even though the aperture faces up in these adult forms. This modification could have been significant during the time of mating, enabling horizontal movements to approach potential mates. The aforementioned differences in the duration of the helical phase between each of the examined species also influence the thrust angle. *D. stevensoni* has more negative thrust angles at adulthood, while *D. nebrascense* and *D. cheyennense* are closer to zero. This is due to *D. stevensoni*'s more helical whorls concentrating the centers of mass and buoyancy in the apical direction. Conversely, fewer helical whorls

result in the centers of buoyancy and mass to be pulled closer to the U-shaped body chamber, causing the thrust angle to approach zero. These differences in adult *Didymoceras* suggest that *D. cheyennense* was best suited for horizontal-backward movement, while *D. nebrascense* was slightly less optimized for this style of locomotion and *D. stevensoni* remained better suited for more vertical-upward movement during the last stage of life. Although subtle differences can result depending upon the position of the terminal aperture, which may be somewhat variable for these species.

D. stevensoni differed somewhat from the other two *Didymoceras* species investigated here in its growth rate and hydrostatic properties through ontogeny, implying differences in the mode of life of this species relative to its congeners, including a longer intermediate juvenile stage and a more vertical component of locomotion through later ontogenetic stages. *D. stevensoni* is intermediate in age between the other two species (Kennedy et al. 2000), so it does not represent an early or late species in a phylogenetic sequence. Rather, the differences seen in *D. stevensoni*'s hydrostatic parameters may indicate an enhanced degree of interspecific variability in modes of life within the genus. More generally, the results presented here indicate that selective pressures varied through ontogeny in these ammonoids, resulting in different shell forms well-adapted to different life habits. Hence, the "aberrant" nostoconic morphotype reflects evolutionary solutions to functional challenges at different stages in the life course of these extraordinary ammonoids.

4.5 CONCLUSIONS

Virtual 3D models of *Didymoceras stevensoni*, *D. nebrascense*, and *D. cheyennense* reveal hydrostatic properties throughout ontogeny that are characteristic of

the nostoconic morphotype, as well as several differences among each of the examined species. All of the models suggest that *Didymoceras* had the capacity for neutral buoyancy and left some amount of cameral liquid in the phragmocone to maintain this condition. Hydrostatic stability was probably too large for the living animal to significantly modify its orientation. The orientation of the aperture for each species starts downward-facing, oscillates around the horizontal plane as the helical whorls develop, and terminates with an upward-facing aperture after formation of the U-shaped adult body chamber. Thrust angles during the helical intermediate phase suggest that thrust energy would most efficiently be transmitted into pirouetting (rotation about the vertical axis). The thrust angles throughout ontogeny do not favor efficient horizontal movement except for two distinct phases: (1) the formation of the first "elbow" before the helical phase develops and (2) after completion of the U-shaped adult body chamber. These hydrostatic properties suggest that the seemingly aberrant coiling of *Didymoceras* and similar heteromorphic ammonoids may reflect a method to their madness. These ammonoids probably exploited a low energy lifestyle near the seafloor, either scavenging or capturing slow demersal prey items. At two life stages, the coiling scheme of *Didymoceras* would enhance lateral movement: for the potential dispersal of juveniles and the location of a mate at adulthood.

4.6 ACKNOWLEDGEMENTS

We thank L. Chang, K. Hollis, H. Little, and M. Florence (Smithsonian National Museum of Natural History) for their help with the specimens of *Didymoceras* used for photogrammetry. We also appreciate the help of D. Clements (North Carolina Museum of Natural Sciences) for donating (WSU 1461) which aided in construction of the virtual

models. We would like to thank M. Hopkins, C. Klug, and an anonymous reviewer for their constructive comments on our manuscript.

4.7 LITERATURE CITED

3DFlow, 2018, 3DF Zephyr. Free Edition. 3DFlow, https://www.3dflow. net/3df-zephyr-free/

Autodesk Inc., 2017a, Meshmixer 3.3. Autodesk Inc., San Rafael.

Autodesk Inc., 2017b, Netfabb 2017.3. Autodesk Inc., San Rafael.

Blender Online Community, 2017, Blender, a 3D modelling and rendering package. Blender Institute, Amsterdam. http://www.blender.org

Bucher, H., Landman, N.H., Klofak, S.M., and Guex, J., 1996, Mode and rate of growth in ammonoids. In: Landman, N. H., K. Tanabe, R. A. Davis (eds.) Ammonoid Paleobiology. Topics in Geobiology, v. 13. Plenum, New York. p. 407–461.

Checa, A., Okamoto, T., and Keupp, H., 2002, Abnormalities as natural experiments: a morphogenetic model for coiling regulation in planispiral ammonites. Paleobiology, v. 28, p. 127–138.

Cobban, W.A., 1974, Ammonites from the Navesink Formation at Atlantic Highlands, New Jersey. Geological Survey Professional Paper 845, 21p.

Cobban, W., Walaszczyk, I., Obradovich, J.D., and McKinney, K., 2006, A USGS zonal table for the Upper Cretaceous middle Cenomanian-Maastrichtian of the Western Interior of the United States based on ammonites, inoceramids, and radiometric ages. USGS Open File Report 2006-1250, 47p.

Cignoni, P., and Ranzuglia, G., 2014, MeshLab (Version 1.3.3) [Computer graphics software]. Visual Computing Lab – ISTI – CNR Pisa, Italy. Available from http://meshlab.sourceforge.net/

Ebel, K., 1990, Swimming abilities in ammonites and limitations. Paläontologische Zeitschrift, v. 64, p. 25–37.

Greenwald, L., and Ward, P.D., 1987, Buoyancy in *Nautilus*. In Saunders, B.W. and N. H. Landman (eds.), *Nautilus*—The Biology and Paleobiology of a Living Fossil. Springer, Dordrecht. p. 547–560.

Hanlon, R.T., and Messenger, J.B., 2018, Cephalopod Behavior, 2nd edition. Cambridge University Press, New York.

He, S., Kyser, T.K., and Caldwell, W.G.E, 2005, Paleoenvironment of the Western Interior Seaway inferred from $\delta^{18}O$ and $\delta^{13}C$ values of molluscs from the Cretaceous Bearpaw marine cyclothem. Palaeogeography, Palaeoclimatology, Palaeoecology, v. 217, p. 67–85.

He, S., Kyser, T.K., and Caldwell, W.G.E., 2016, Redox conditions of the Late Cretaceous Western Interior Seaway recorded by rare earth elements of Bearpaw molluscan fossils. Canadian Journal of Earth Sciences, v. 53, p. 1029–1041. dx.doi.org/10.1139/cjes-2015-0184.

Hoffmann, R., Schultz, J.A., Schellhorn, R., Rybacki, E., Keupp, H., Gerden, S.R., Lemanis, R., and Zachow, S., 2014, Non-invasive imaging methods applied to neo- and paleo-ontological cephalopod research. Biogeosciences, v. 11, p. 2721–2739.

Hoffman, R., Lemanis, R., Naglik, C., and Klug, C., 2015, Ammonoid Buoyancy. In: Klug, C., Korn, D., De Baets, K., Kruta, I., and Mapes, R.H., (eds.), Ammonoid Paleobiology. Volume I: From Anatomy to Ecology. Topics in Geobiology, v. 43, p. 611–648.

Hoffmann, R., Lemanis, R., Falkenberg, J., Schneider, S., Wesendonk, H., and Zachow, S., 2018, Integrating 2D and 3D shell morphology to disentangle the paleobiology of ammonoids: a virtual approach. Palaeontology, v. 61, p. 89–104.

Inoue, S. and Kondo, S., 2016, Suture pattern formation in ammonites and the unknown rear mantle structure. Scientific Reports, v. 6, p. 33689.

Jacobs, D.K., and J. A. Chamberlain, J.A., 1996, Buoyancy and hydrodynamics in ammonoids. In: Landman, N.H., K. Tanabe, and R. A. Davis. (eds.) Ammonoid paleobiology. Topics in Geobiology, v. 13. Plenum, New York.

Kauffman, E.G., Arthur, M.A., Howe, B., and Scholle, P.A., 1996, Widespread venting of methane-rich fluids in Late Cretaceous (Campanian) submarine springs (Tepee Buttes), Western Interior seaway, U.S.A. Geology, v. 24, p. 799–802. https://doi.org/10.1130/0091-7613(1996)024<0799:WVOMRF>2.3.CO;2.

Kennedy, W.J., Landman, N.H., Cobban, W.A., and Scott, G.R., 2000, Late Campanian (Cretaceous) heteromorph ammonites from the Western Interior of the United States. Bulletin of the American Museum of Natural History, v. 251, p. 1–88.

Klug, C., 2001, Life-cycles of some Devonian ammonoids. Lethaia, v. 34, p. 215–233.

Klug, C., and Korn, D., 2004, The origin of ammonoid locomotion. Acta Palaeontologica Polonica, v. 49, p. 235–242.

Klug, C., Korn, D., Richter, U., and Urlichs, M., 2004 The black layer in cephalopods from the German Muschelkalk (Triassic). Palaeontology, v. 47, p. 1407–1425.

Klug, C. and Lehmann, J., 2015, Soft part anatomy of ammonoids: reconstructing the animal based on exceptionally preserved specimens and actualistic comparisons. In: Klug, C., Korn, D., De Baets, K., Kruta, I., and Mapes, R.H. (eds.), Ammonoid Paleobiology. Volume 1: From Anatomy to Ecology. Topics in Geobiology, v. 43, p. 515–538.

Klug, C., Zatoń, M., Parent, H., Hostettler, B., and Tajika, A., 2015, Mature modifications and sexual dimorphism. In: Klug C., Korn, D., De Baets, K., Kruta, I.,

and Mapes, R.H. (eds.), Ammonoid Paleobiology. Volume 1: From Anatomy to Ecology. Topics in Geobiology, v. 43, p. 252–320.

Kruta, I., Rouget, I., Landman, N.H., Tanabe, K., and Cecca, F., 2009, Aptychus microstructure in three genera of Late Cretaceous Ancyloceratina (Ammonoidea). Lethaia, v. 42, p. 312–321.

Kruta, I., Landman, N.H., Rouget, I., Cecca, F., and Larson, N.L., 2010, The jaw apparatus of the Late Cretaceous ammonite *Didymoceras*. Journal of Paleontology, v. 84, p. 556–560.

Landman, N.H., 1988, Early ontogeny of Mesozoic ammonites and nautilids. In: Wiedmann, J., and J. Kullmann, (eds) Cephalopods-present and past. Schweizerbart, Stuttgart. p. 215–228.

Landman, N.H., Kennedy, W.J., Cobban, W.A., and Larson, N.L., 2010. Scaphites of the "nodosus group" from the Upper Cretaceous (Campanian) of the Western Interior of North America. Bulletin of the American Museum of Natural History, v. 342, 242 p.

Landman, N.H., Cochran, J.K., Larson, N.L., Brezina, J., Garb, M.P., and Harries, P.J., 2012, Methane seeps as ammonite habitats in the U.S. Western Interior Seaway revealed by isotopic analyses of well-preserved shell material. Geology, v. 40, p. 507–510. https://doi.org/10.1130/G32782.1.

Landman, N.H., Cochran, J.K., Slovacek, M., Larson, N.L., Garb, M.P., Brezina, J., and Witts, J.D., 2018, Isotope sclerochronology of ammonites (*Baculites compressus*) from methane seep and non-seep sites in the Late Cretaceous Western Interior Seaway, USA: Implications for ammonite habitat and mode of life. American Journal of Science, v. 318, p. 603–639. https://doi.org/10.2475/06.2018.01.

Larson, N.L., Jorgensen, S.D., Farrar, R.A., and Larson, P.L., 1997, Ammonites and the Other Cephalopods of the Pierre Seaway. Geoscience Press, Tucson. 144p.

Lemanis, R., Zachow, S., Fusseis, F., and Hoffmann, R., 2015, A new approach using high-resolution computed tomography to test the buoyant properties of chambered cephalopod shells. Paleobiology, v. 41, p. 313–329.

Lemanis, R., Korn, D., Zachow, S., Rybacki, E., and Hoffmann, R., 2016, The evolution and development of cephalopod chambers and their shape. PLoS ONE, v. 11, p. 1–21.

Mapes, R.H., and Nützel, A., 2008, Late Palaeozoic mollusc reproduction: cephalopod egg-laying behavior and gastropod larval palaeobiology. Lethaia, v. 42, p. 341–356.

Moseley, H., 1838, On the geometrical form of turbinated and discoid shells. Philosophical Transactions of the Royal Society, v. 1838, p. 351–370.

Naglik, C., Monnet, C., Goetz, S., Kolb, C., De Baets, K., Tajika, A., and Klug, C., 2015a, Growth trajectories of some major ammonoid subclades revealed by serial grinding tomography data. Lethaia, v. 48, p. 29–46.

Naglik, C., Tajika, A., Chamberlain, J., and Klug, C., 2015b, Ammonoid locomotion. In: Klug, C., Korn, D., De Baets, K., Kruta, I., and Mapes, R.H. (eds.), Ammonoid Paleobiology. Volume I: From Anatomy to Ecology. Topics in Geobiology, v. 43, p. 649–688.

Naglik, C., Rikhtegar, F., and Klug, C., 2016, Buoyancy of some Palaeozoic ammonoids and their hydrostatic properties based on empirical 3D models. Lethaia, v. 49, p. 3–12.

Okamoto, T., 1988a, Changes in life orientation during the ontogeny of some heteromorph ammonoids. Palaeontology, v. 31, p. 281–294.

Okamoto, T., 1988b, Developmental Regulation and Morphological Saltation in the Heteromorph Ammonite *Nipponites*. Paleobiology, v. 14, p. 272–286.

Okamoto, T., 1996, Theoretical modeling of ammonoid morphology. In*:* Landman, N.H., Tanabe, K., and Davis, R.A. (eds.), Ammonoid Paleobiology. Topics in Geobiology, v. 13, p. 225–251. Plenum, New York.

Packard, A., Bone, Q., and Hignette, M., 2010, Breathing and swimming movements in a captive *Nautilus*. Journal of the Marine Biological Association of the UK, v. 60, p. 313–327.

Peterman, D.J., and Barton, C.C., 2018, Ontogenetic changes in the hydrostatic properties of the heteromorphic ammonite, *Didymoceras*. American Geophysical Union Fall Meeting 2018, Abstract PP13F-1402.

Peterman, D.J., and Barton, C.C., 2019, Power scaling of ammonitic suture patterns from Cretaceous Ancyloceratina: constraints on septal/sutural complexity. Lethaia, v. 52, p. 77–90. https://doi.org/10.1111/let.12291.

Peterman, D.J., Barton, C.C., and Yacobucci, M.M., 2019a, The hydrostatics of Paleozoic ectocochleate cephalopods (Nautiloidea and Endoceratoidea) with implications for modes of life and early colonization of the pelagic zone. Palaeontologia Electronica, v. 22.2.24A, p. 1–29. https://doi.org/10.26879/884.

Peterman, D.J., Ciampaglio, C.N., Shell, R.C., and Yacobucci, M.M., 2019b, Mode of life and hydrostatic stability of orthoconic ectocochleate cephalopods: Hydrodynamic analyses of restoring moments from 3D printed, neutrally buoyant models. Acta Palaeontologica Polonica, v. 64, p. 441–460. https://doi.org/10.4202/app.00595.2019.

Raup, D.M., 1967, Geometric analysis of shell coiling: coiling in ammonoids. Journal of Paleontology, v. 41, p. 43–65.

Raup, D.M., and Chamberlain, J.A., 1967, Equations for volume and center of gravity in ammonoid shells. Journal of Paleontology, v. 41, p. 566–574.

Ritterbush, K., De Baets, K., Hoffmann, R., and Lukeneder, A., 2014, Pelagic Palaeoecology: the importance of recent constraints on ammonoid palaeobiology and life history. Journal of Zoology. doi:10.1111/jzo.12118.

Rocha, F., Guerra, A., and González, A.F., 2001, A review of reproductive strategies in cephalopods. Biological Reviews, v. 76, p. 291–304.

Saunders, B.W., Shapiro, E.A., 1986, Calculation and simulation of ammonoid hydrostatics. Paleobiology, v. 12, p. 64–79.

Slattery, J.S., Clementz, M.T., and Johnson, M.R., 2007, Habitat of the Upper Cretaceous heteromorphic ammonoid *Didymoceras* in the Western Interior Seaway. Geological Society of America Abstracts with Programs, v. 39, p. 398.

Tajika, A., and Wani, R., 2010, Intraspecific variation of hatchling size in Late Cretaceous ammonoids from Hokkaido, Japan: implication for planktic duration at early ontogenetic stage. Lethaia, v. 44, p. 287–298.

Tajika, A., Morimoto, N., Wani, R., Naglik, C., and Klug, C., 2015a, Intraspecific variation of phragmocone chamber volumes throughout ontogeny in the modern nautilid *Nautilus* and the Jurassic ammonite *Normannites*. PeerJ, v. 3, p. 1–28.

Tajika, A., Naglik, C., Morimoto, N., Pascual-Cebrian, E., Hennhöfer, D.K., and Klug, C., 2015b, Empirical 3D-model of the conch of the Middle Jurassic ammonite microconch *Normannites*, its buoyancy, the physical effects of its mature modifications and speculations on their function. Historical Biology, v. 27, p. 181–191.

Tajika, A., Nützel, A., and Klug, C., 2018, The old and the new plankton: ecological replacement of associations of mollusc plankton and giant filter feeders after the Cretaceous? PeerJ, v. 6:e4219. DOI 10.7717/peerj.4219.

Tanabe, K., and Landman, N.H., 2002, Morphological diversity of the jaws of Cretaceous Ammonoidea. In: Summesberger, H., K. Histon, and A. Daurer (eds.), Abhandlungen der Geologischen Bundesanstalt, v. 57, p. 157–165.

Trueman, A. E., 1941, The ammonite body-chamber, with special reference to the buoyancy and mode of life of the living ammonite. Quarterly Journal of the Geological Society, v. 384, p. 339–383.

Urdy, S., Goudemand, N., Bucher, H., and Chirat, R., 2010, Allometries and the morphogenesis of the molluscan shell: a quantitative and theoretical model. Journal of Experimental Zoology, v. 314B, p. 280–302.

Walton, S.A., Korn, D., and Klug, C., 2010, Size distribution of the Late Devonian ammonoids *Prolobites*: indication for possible mass spawning events. Swiss Journal of Geosciences, v. 103, p. 475–494. DOI 10.1007/s00015-010-0036-y.

Ward, P.D., 1979, Cameral liquid in Nautilus and ammonites. Paleobiology, v. 5, p. 40–49.

Westermann, G.E.G., 1977, Form and function of orthocone cephalopod shells with concave septa. Paleobiology, v. 3, p. 300–321.

Westermann, G.E.G., 1996, Ammonoid life and habitat. *In:* Landman, N.H., Tanabe, K., and Davis, R. A. (eds.), Ammonoid Paleobiology. Topics in Geobiology, v. 13, p. 607–707. Plenum, New York.

Westermann, G.E.G., 2013, Hydrostatics, propulsion and life-habits of the Cretaceous ammonoid Baculites. Revue de Paléobiologie, v. 32, p. 249–265.

5.0 Syn vivo hydrostatic and hydrodynamic properties of scaphitid ammonoids from the U.S. Western Interior

Peterman, D.J., Hebdon, N., Ciampaglio, C.N., Yacobucci, M.M., Landman, N.H., and Linn T. 2020. Syn vivo hydrostatic and hydrodynamic properties of scaphitid ammonoids from the U.S. Western Interior. *GEOBIOS*, forthcoming.

Abstract

Scaphitid ammonoids were ubiquitous and significant components of the Western Interior Seaway during the Late Cretaceous. This group is characterized by a recurved hook at maturity that deviates from the juvenile whorls. Such a modification seems counterproductive to active locomotion and to manage a biologically effective orientation that facilitates efficient feeding and swimming. Virtually reconstructed 3D hydrostatic models reveal that the examined mature scaphitids had the capacity for neutral buoyancy while assuming a stable, upward-facing orientation in the water column during life. Models of juvenile *H. nicolletii* suggest that scaphitid apertures were oriented only slightly more horizontal than adults. The hydrostatic influence of sexual dimorphism was explored with the species, *Hoploscaphites crassus*. The inflated macroconch has a lower stability and higher hydrodynamic drag compared to its microconch counterpart. The effect of shell compression was investigated by comparing *H. crassus* and the more compressed *H. nicolletii*. The latter species has a relatively high stability and much less

hydrodynamic drag during movement. The mature U-shaped body chamber distributes organismal mass in a way that increases stability, and simultaneously orients the soft body so that propulsive energy is efficiently transmitted into horizontal backwards movement with minimal rocking. Swimming velocities computed from hydrodynamic drag experiments suggest that scaphitids were relatively slow swimmers with compressed forms attaining slightly higher velocities (when scaled by mass). Hydrodynamic lift was investigated with computational fluid dynamics (CFD) simulations. These experiments revealed that the overall shape of the shell is responsible for significant lift in the upwards direction, which is not heavily influenced by ornamentation. This explains how a reduced soft body can overcome and manage a slightly negatively buoyant condition during life. Therefore, the seemingly cumbersome shape and orientation of the scaphitid morphotype may not have been a hindrance during locomotion.

5.1 INTRODUCTION

Scaphitid ammonoids were diverse and abundant during the Late Cretaceous, and today their fossils are globally distributed (Birkelund, 1965; Skwarko, 1966; Cobban, 1969; Kennedy, 1970; Klinger et al., 1975; Tanabe, 1979; Bengtson, 1983, Medina et al., 1992; Landman and Waage, 1993; Wright, 1996; Larson et al., 1997; Monks, 2000). The ubiquity of this group suggests that they were important components of marine ecosystems during this time. While the morphology, paleobiology, and paleoecology of Scaphitidae is well-studied (Westermann, 1996; Westermann and Tsujita, 1999; Monks, 2000; Sessa et al., 2015; Landman et al., 2012a, 2012b; Naglik et al., 2015a; Tanabe et al., 2015, Klug et al., 2015; Lukeneder, 2015), little is known about their swimming capabilities or other physical properties that constrained their movement during life. The

paleoecology, ethology, and hydrostatic properties of heteromorph ammonoids in general have long been a controversial subject of debate (see e.g., Jacobs et al., 1994; Westermann, 1996; Monks and Young, 1998). These properties are fundamental to reconstruct the position of scaphitids within marine ecosystems during the Late Cretaceous. The current study fills this knowledge gap by virtually reconstructing several scaphitids to investigate their syn vivo physical properties in static and dynamic settings. Variations in these properties due to sexual dimorphism were investigated with macro- and microconchs (females and males, respectively) of *Hoploscaphites crassus* (Coryell and Salmon, 1934). Ontogenetic changes in these properties were explored with *Hoploscaphites nicolletii* (Morton, 1842). Additionally, the relationship between hydrostatic and hydrodynamic properties were investigated. In a dynamic setting, the influence of shell compression on swimming efficiency was compared between these two species. The functional morphology of asymmetrical ventrolateral tubercles (a common feature within Scaphitidae; Landman and Waage, 1993) was also evaluated for a *H. crassus* microconch.

5.1.1 Syn vivo physical properties of fossil cephalopods

The morphology of the living cephalopod and its shell directly influenced its hydrostatic and hydrodynamic physical properties. Like other ectocochleate (externally-shelled) cephalopods, ammonoids had a chambered shell that was used as a buoyancy apparatus. The phragmocone (chambered portion) allowed the living animal to reduce its organismal weight relative to its buoyancy to attain a neutrally buoyant (or nearly neutral) condition (Hoffmann et al., 2015). The body chamber housed the soft body, and its shape was a first-order factor on the distribution of organismal mass (Peterman et al.,

2019a, 2019b). The static orientation of the living cephalopod occurs when the centers of buoyancy and mass are vertically aligned (Fig. 1). This syn vivo (occurring during life) orientation heavily influences locomotion and the living cephalopod's interaction with its surroundings.

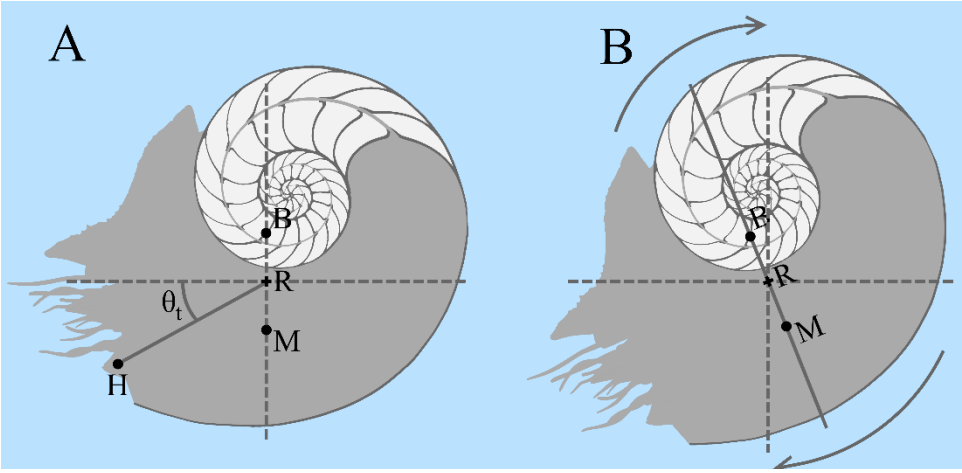

Figure 1: Hypothetical diagram of hydrostatic properties in a static setting (A), and hydrodynamic restoration (B). B – center of buoyancy, M – center of mass, R – point of rotation, H – location of hyponome, θ_t – thrust angle, Arrows – rotation after displacement from the equilibrium orientation.

The separation between the centers of buoyancy and mass is proportionate to hydrostatic stability (Okamoto, 1996; Peterman et al., 2019a, 2019b). This property influences the resistance to rotation away from the static orientation during locomotion and the resistance to external forms of energy (e.g., wave action). The thrust angle is another important property that influenced movement. This angle is measured between the center of thrust (location of the hyponome) and the midpoint between the centers of buoyancy and mass (Fig. 1). A horizontal thrust angle suggests idealized horizontal backward movement because thrust is more efficiently transmitted into translational movement

rather than rotation. The external shape of the rigid shell effects the ease or difficulty in moving through the water (Jacobs, 1992; Jacobs et al., 1994). The resistance of a given shape to movement in a fluid is quantified herein with the drag coefficient; a dimensionless quantity that is proportionate to the force of hydrodynamic drag. Similarly, an object's shape also influences lift – the upward component of force resulting from movement through a fluid.

5.1.2 Scaphitid paleobiology and paleoecology

Scaphitid habitat—Scaphitid ammonoids were basic components of the Western Interior Seaway of North America (Landman and Waage, 1993). Faunal associations with benthic elements in this seaway suggest that scaphitids lived close to the benthos. For example, Tsujita and Westermann (1998) noted that periodic oxygenation events simultaneously allowed the proliferation of scaphitids and the benthic community. The scaphitids and benthic elements are otherwise absent in deposits with other ammonoids not always associated with the benthos (e.g., baculites). Methane seeps also served as oases for scaphitids in terms of planktic food abundance and their potential elevation above dysoxic waters (Kauffman et al., 1996; Landman et al., 2012b). Additionally, ammonoids of various ontogenetic stages are found at methane seeps, and their isotopically-light, methane derived $\delta^{13}C$ values both suggest that it was common for an individual to spend its entire life at the seep (Landman et al., 2012b). Similar to the aforementioned lines of evidence, isotopic comparisons with planktic and benthic organisms suggest that scaphitids lived relatively close to the seafloor (He et al., 2005; Cochran et al., 2010; Sessa et al., 2015) without considerable migration during their lives (Ferguson et al., 2019). An ontogenetic study of oxygen isotopes from *Hoploscaphites* by Linzmeier et al.

(2018) reveals that eggs were laid on the sea bottom. They found that early hatchlings briefly move to somewhat shallower waters before assuming demersal lifestyles from around one whorl after postembryonic growth. Some scaphitids have a small gap between the phragmocone and U-shaped body chamber (e.g., *Hoploscaphites* and some *Scaphites*) leading to the speculation that their hook-like morphology could have facilitated stationary attachment to kelp (Arkhipkin, 2014). While the biological function of this hook-like morphology is still largely unknown, it is unlikely that they performed such a function (see the counter-response by Landman et al., 2016b). The current study aims to better understand this morphology by investigating its consequences in terms of hydrostatics and hydrodynamics as possible evolutionary pressures.

Heteromorph shell form and shell compression— While morphologically diverse, scaphitid shells are generally characterized by relatively involute juvenile whorls, followed by a shaft and recurved hook at adulthood (Wright, 1996). Shell compression is a first-order constraint on swimming ability with more compressed shells resulting in lower hydrodynamic drag (Jacobs, 1992; Westermann and Tsujita, 1999; Naglik et al., 2015a). Jacobs et al. (1994) report variation in shell compression for Turonian scaphitids that covaries with habitat. They note that more compressed shells occur in nearshore sandy facies, whereas more depressed shells occur in offshore muds. Additionally, the more compressed morphs were found to swim more efficiently at higher velocities while the more inflated morphs were more efficient at lower velocities.

Shell compression was investigated in the current study by examining the differences in hydrodynamics between the inflated *Hoploscaphites crassus* and the compressed *Hoploscaphites nicolletii*. The former occurs within the lower Maastrichtian

Baculites baculus Biozone of the Pierre Shale (Bishop, 1973), while the latter occurs in the lower part of the Upper Maastrichtian *H. nicolletii* Biozone of the more nearshore Fox Hills Formation (Landman and Waage, 1993, Landman et al., 2013). These two species follow a similar pattern to the morphs of the Turonian scaphitids of Jacobs et al. (1994) occurring in more distal and proximal paleoenvironments, respectively.

Sexual dimorphism—Similar to other ammonoids, scaphitids are dimorphic, with larger shells presumed to belong to females and smaller shells to belong to males (termed macro- and microconchs, respectively; Lehman, 1981; Klug et al., 2015). In addition to their differences in size, macroconchs are generally more inflated around the umbilicus, resulting in an umbilical bulge (Landman et al., 2010, 2012a). Furthermore, the umbilical shoulder is generally straight in macroconchs, and curved in microconchs. These differences in shell shape fundamentally influenced the swimming efficiency of scaphitids and intuitively suggest that females were poorer swimmers. *Hoploscaphites crassus* is of particular interest because the aforementioned differences in morphology between dimorphs are especially apparent for this species.

Ornamentation—The ornamentation of *Hoploscaphites crassus* consists of closely-spaced ventrolateral tubercles with bifurcated, prominent ribs and nodes on the umbilical shoulder of the phragmocone. These ventrolateral tubercles are very prominent on the microconchs of this species, especially on the body chamber. These tubercles are also asymmetrical in a similar manner to an airfoil. Therefore, the hydrodynamic lift generated by ornamentation in this species is of interest in the current study. Conversely, the ornamentation of *Hoploscaphites nicolletii* is much more reduced and streamlined, suggesting selective pressure acted to reduce hydrodynamic drag in this species.

Soft body characteristics and buccal apparatus—There are currently no unequivocally preserved remains of any ammonoid soft body (Klug and Lehmann, 2015), other than the buccal mass, which is important for the paleobiology of these animals because it sheds light on their feeding habits (Tanabe et al., 1980, 2015; Kruta et al., 2011, 2013). Scaphitids have very thin calcareous aptychi (analogous to the lower jaws) with a blunt apex and narrow muscle attachment sites, which suggest that they were not able to crush or slice large prey (Landman and Waage, 1993; Landman et al., 2012a; Kruta et al., 2009, 2013). While other aspects of the ammonoid soft body are undocumented in the fossil record, the morphology of the scaphitid shell can constrain its possible shape and function in this group. At maturity, the aperture of the shell is restricted, then terminates into a thin and fragile flared lip (Landman et al., 2012a, 2016a). While the restriction may have offered protection from predators (Vermeij, 1993), it possibly obstructed the soft body from protruding from the aperture (Landman et al., 2012a). Additionally, the inhabitation of inarticulate brachiopods within the groove made by this restriction also supports a relatively reduced soft body that did not cover this external portion of the shell (Landman et al., 2016a). The thin, flared lip and absence of a hyponomic sinus suggest that the living scaphitid was not able to extend its hyponome over the aperture and downward, and may have constrained its swimming direction to backwards or downwards at adulthood (Landman et al., 2012a). Muscle scars on the inside of the living chamber also constrain soft body morphology (Jordan, 1968). In scaphitids, the muscle scars are reduced, or absent in some places, suggesting that they were weak swimmers (Landman and Waage, 1993; Landman et al., 2010, 2012a). Jacobs and Landman (1993), however, propose an alternative model based on a coleoid-like swimming mechanism

that is independent of retractor muscle size. Therefore, we used several analogues for propulsive abilities in this study to gauge possible swimming capabilities of scaphitids, ranging from *Nautilus*-like to coleoid-like. Based on the aforementioned lines of evidence, we used the hypothetical reconstruction of *Hoploscaphites nodosus* from Landman et al., (2012a) as a basis for the soft body of the scaphitids investigated in the current study.

5.1.3 Institutional abbreviations

WSU—Wright State University, Department of Earth and Environmental Sciences, Dayton, Ohio, USA.

AMNH—American Museum of Natural History, Division of Paleontology, New York, New York, USA.

BHI—Black Hills Institute of Geological Research, Hill City, South Dakota, USA.

YPM—Yale Peabody Museum of Natural History (Invertebrate Division), New Haven, Connecticut, USA.

5.2 METHODS

The methods for virtual reconstruction of the scaphitids largely follow those of Peterman et al. (2019a) which have been further modified to add ornamentation to the shell (Peterman et al., 2019c). The septa were virtually reconstructed with the methods of Peterman et al. (2019b, 2019c) and Peterman and Barton (2019). These methods serve as alternatives to tomographic techniques like CT (computed tomography) scanning (Hoffmann et al., 2014, 2015, 2018; Lemanis et al., 2015, 2016; Tajika et al., 2015a; Inoue and Kondo, 2016) and serial grinding tomography (Tajika et al., 2015a, 2015b; Naglik et al., 2015b, 2016) with the advantage that they can be used with partial

specimens or those that do not preserve in an adequate manner for 3D imaging (i.e., low contrasts in X-ray attenuation factors or optical properties).

5.2.1 Virtual 3D modeling

The virtual model of the extant *Nautilus pompilius* from Peterman et al. (2019a: fig. 2.5) is used in the current study as a reference for the scaphitids because the behavior and swimming ability of this species is observable and well documented (Ward, 1979; Greenwald and Ward, 1987; Chamberlain, 1987, Shapiro and Saunders, 1987; O'Dor et al., 1990; Wells and O'Dor, 1991; Neil and Askew, 2018).

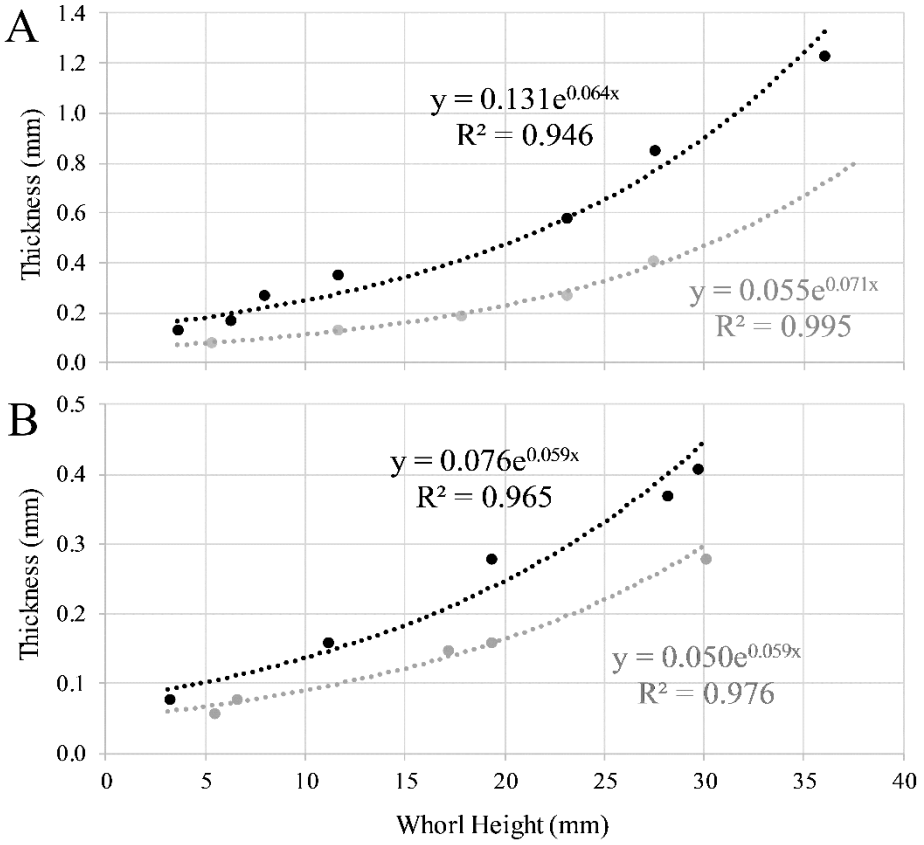

Figure 2: Shell thickness (black) and septum thickness (grey) versus whorl height measured from *Hoploscaphites crassus* (A; WSU 1470, WSU 1473, WSU 1478, WSU 1479), and *Hoploscaphites nicolletii* (B, WSU 1476).

Photogrammetry was used to create a virtual model of the exterior of each scaphitid specimen to serve as a stencil for later reconstruction of the shell (*Hoploscaphites crassus* macroconch – WSU 1470; *H. crassus* macroconch upper mouthparts – WSU 1471; *H. crassus* macroconch aptychi – WSU 1472; *H. crassus* microconch – WSU 1473; *H. crassus* microconch with excellent tubercles – AMNH 76342; *H. nicolletii* macroconch – BHI 7174). This process consists of taking a series of overlapping photographs (~50) around an object to produce a 3D mesh that is on par with high quality surface scanners (Fau et al., 2016). Photogrammetry was performed in the current study with the program 3DF Zephyr (3DFlow, 2018).

The photogrammetry models were scaled to the corresponding sizes of their real-world counterparts, then positioned at the origin of the workspace and oriented so that they approximated the life position of the living animal. These specimens were partially attached to the matrix, so the exposed sides were mirrored about the plane of symmetry in Meshmixer 3.3 (Autodesk Inc., 2017a). Tubercles, nodes, and ribs were reconstructed by mirroring or copying the neighboring well-preserved ornament. Afterwards, the models were imported into Blender (Blender Online Community, 2017) to reconstruct the coiled phragmocones with array algorithms (see Peterman et al., 2019a). These array algorithms (Table 1) are a set of instructions implemented by the array modifier in Blender, which was used to duplicate, rotate, translate, and scale the whorl sections of the mature phragmocones to reconstruct the internal whorls. Each array was fitted by eye; however, Blender was utilized to zoom into the submillimeter scale to perform this function. Transverse cross sections (*H. crassus* macroconch – WSU 1474; *H. crassus* microconch – WSU 1475; *H. nicolletii* macroconch – WSU 1476) were imported into the Blender

workspace to serve as stencils which accommodate changes in whorl section shape throughout ontogeny (allometry). This produced a smooth model of the phragmocone, which was later partitioned into segments containing the ornamentation from the photogrammetry model. The initial segment with ornamentation was replicated with the same array algorithms used to build the smooth shell. This process created extra segments that were later deleted (listed on Table1). Each ornamented segment of the phragmocone and the photogram of the living chamber were then extruded according to the thickness recorded from the shells of real-world specimens with digital calipers (WSU 1470, WSU 1473, WSU 1476, WSU 1478, WSU 1479, Fig. 2). Similarly, the apertural restriction and flared lip were created by measuring their thicknesses and extruding the apertures on the photogrammetry models. Fragmented, juvenile portions of *H. crassus* could not be distinguished by sex, so their measurements were combined into one function (Fig. 2A). *H. nicolletii*, however, was extruded according to its own function (Fig. 2B). Afterwards, each extruded, ornamented shell segment was sutured together using the "zipper" tool in Meshmixer (Autodesk Inc., 2017a), then repaired in the program Netfabb (Autodesk Inc., 2017b) to produce a manifold mesh denoting the shell without septa.

Exposed ammonoid septa rarely preserve completely due to their intricately-frilled margins. The methods of Peterman and Barton (2019) and Peterman et al. (2019b) were used to reconstruct the septa by using photogrammetry on specimens preserving the first and second order folds (*H. crassus* macroconch – WSU 1477; *H. crassus* microconch – WSU 1475, *H. nicolletii* – WSU 1476), then using the suture pattern to reconstruct the detailed periphery from another specimen of the corresponding species (*H. crassus* macroconch – WSU 1470; *H. crassus* microconch – WSU 1473; *H. nicolletii*

adopted from Landman and Waage, 1993; Fig. 3). Suture patterns were recorded with a digital camera lucida, then imported into Blender as 3D objects. Afterwards, these sutures lying in a plane were wrapped around the whorl section of their respective models. The missing portions of the modeled septa were supplemented with the 3D sutures, which were extruded inwards and smoothed to approximate a minimum curvature surface. These septa were then placed at the location of the terminal septum, denoting the proper adult body chamber length, then replicated with the same array algorithms used to build the shell (Table 1). Thickness was defined for the septa by extruding them in Blender according to the measured thickness function (Fig. 2). The 3D models of the septa were then combined with the 3D models of the shells by performing a Boolean unification in Netfabb (Autodesk Inc., 2017b). This process created final 3D models of the shells with defined thickness and internal anatomy.

***H. crassus* Macroconch**			**Translation (mm)**		**Rotation (degrees)**	**Scale**		
Array #	**# Replications**	**# Deletions**	**Y**	**Z**	**X**	**X**	**Y**	**Z**
1	124	10	-0.450	0.000	-2.170	0.995	0.997	0.993
2	540	8	-0.515	0.730	-2.550	0.993	0.995	0.994
***H. crassus* Microconch**			**Translation (mm)**		**Rotation (degrees)**	**Scale**		
Array #	**# Replications**	**# Deletions**	**Y**	**Z**	**X**	**X**	**Y**	**Z**
1	743	9	-0.590	0.020	-2.890	0.993	0.994	0.992
***H. nicolletii* Macroconch**			**Translation (mm)**		**Rotation (degrees)**	**Scale**		
Array #	**# Replications**	**# Deletions**	**Y**	**Z**	**X**	**X**	**Y**	**Z**
1	633	10	-0.808	0.472	-2.100	0.996	0.997	0.994

Table1: Array algorithms used to build the phragmocones of the scaphitid virtual models. The whorl section was replicated, translated, rotated, and scaled in order to build coiled shells. After ornamentation was added extra segments had to be deleted for every replication (denoted # deletions).

In order to perform hydrostatic calculations, a 3D mesh must be created for each material of unique density. Fortunately, the shell of the ammonoid constrains its soft body and cameral volumes. These internal interfaces can be isolated from the 3D mesh of the shell. The normals (vectors denoting the outside direction of the 3D mesh) must then be flipped so that the models are right-side-out. The portion of the soft body protruding from the apertures were fabricated based on the hypothetical reconstruction of Landman et al. (2012a). Cameral liquid and gas occupying the phragmocone must be partitioned according to the proper ratio for a neutrally buoyant condition (following Equation 1 defined below).

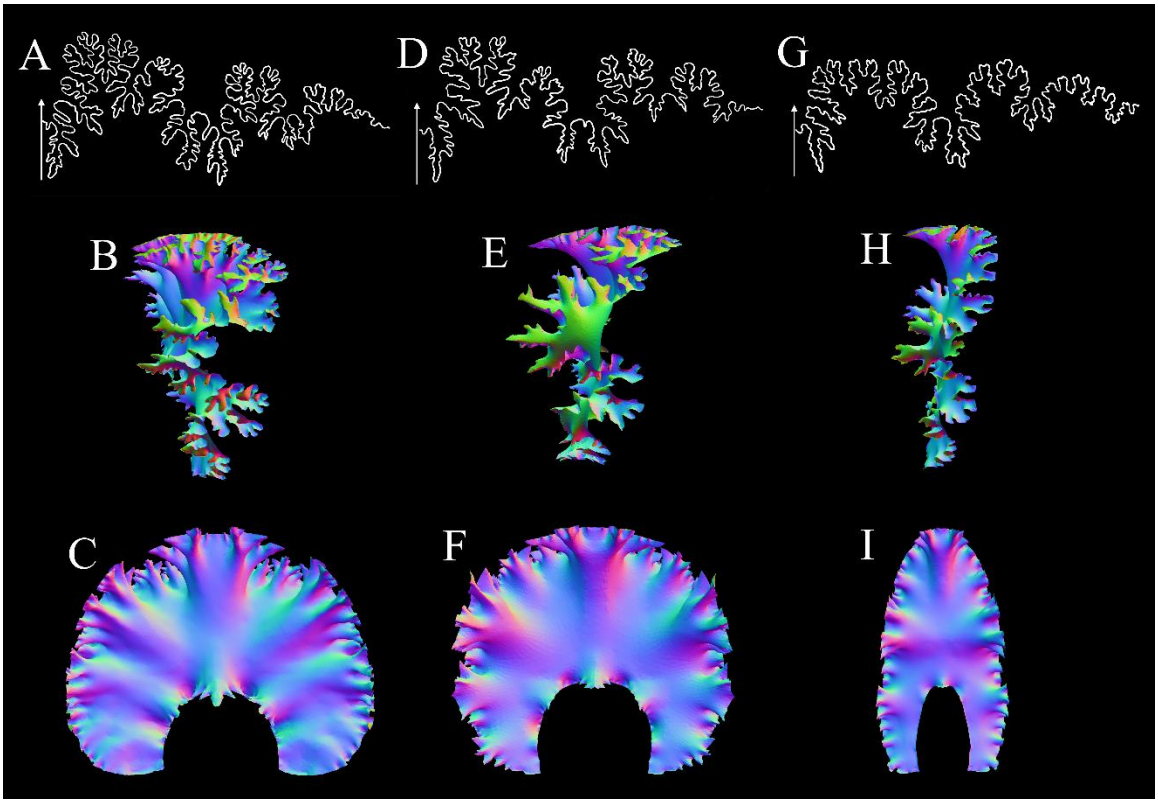

Figure 3: Virtual 3D reconstruction of septa for hydrostatic models. *Hoploscaphites crassus* macroconch suture (WSU 1470, A) and septum (B – side view; C – posterior view). *Hoploscaphites crassus* microconch suture (WSU 1473, D) and septum (E – side view; F – posterior view). *Hoploscaphites nicolletii* macroconch suture (Landman and Waage, 1993; G) and septum (H – side view; I - posterior view).

Lastly, a 3D model that represents the water displaced by the living animal must be created for the hydrostatic calculations described later. This was accomplished by isolating the external interfaces of the shell and soft body and unifying them with Netfabb (Autodesk Inc., 2017b).

5.2.2 Non-uniform soft body components

It is assumed that a uniform-density soft body fills the body chamber for the hydrostatic models in the current study. However, the higher density mouthparts, siphuncle, and lower density mantle cavity filled with seawater all influence the bulk density and total distribution of mass. These differences in hydrostatics were assessed by creating a detailed model of *H. crassus* with each of these aforementioned features. The mouthparts consist of very thin chitin, and calcareous aptychi that cover the lower chitiniferous jaws. The upper and lower jaws were first modeled with photogrammetry (WSU 1471 and WSU 1472, respectively). The chitin components of these specimens were diagenetically altered and the calcareous aptychi were dissolved, which precluded thickness measurements. To circumvent this, these thicknesses were recorded from other scaphitids, then linearly scaled. A specimen of *Hoploscaphites spedeni* (YPM 23223) figured in Kruta et al. (2009, fig. 4) was used to approximate the thicknesses of the lower jaws of *H. crassus*. The center of the aptychus was measured as 0.33 mm, although, this changes from about 0.26 mm to 0.48 mm on the figured specimen. The center thickness was scaled by aptychus length (a ratio of 0.85) to yield an aptychus thickness of 0.28 mm for the modeled *H. crassus*. The altered chitin layer was also figured on this specimen with a thickness of approximately 0.054 mm, which translates to a thickness of 0.046 mm after scaling to the size of the *H. crassus* aptychi. The aptychi cast of the photogrammetry

model was isolated, then copied. The first copy was extruded with positive offset to model the calcareous aptychi, and the second copy was extruded with negative offset to model the chitiniferous lower jaws. A specimen of *Rhaeboceras halli* (AMNH 51334)

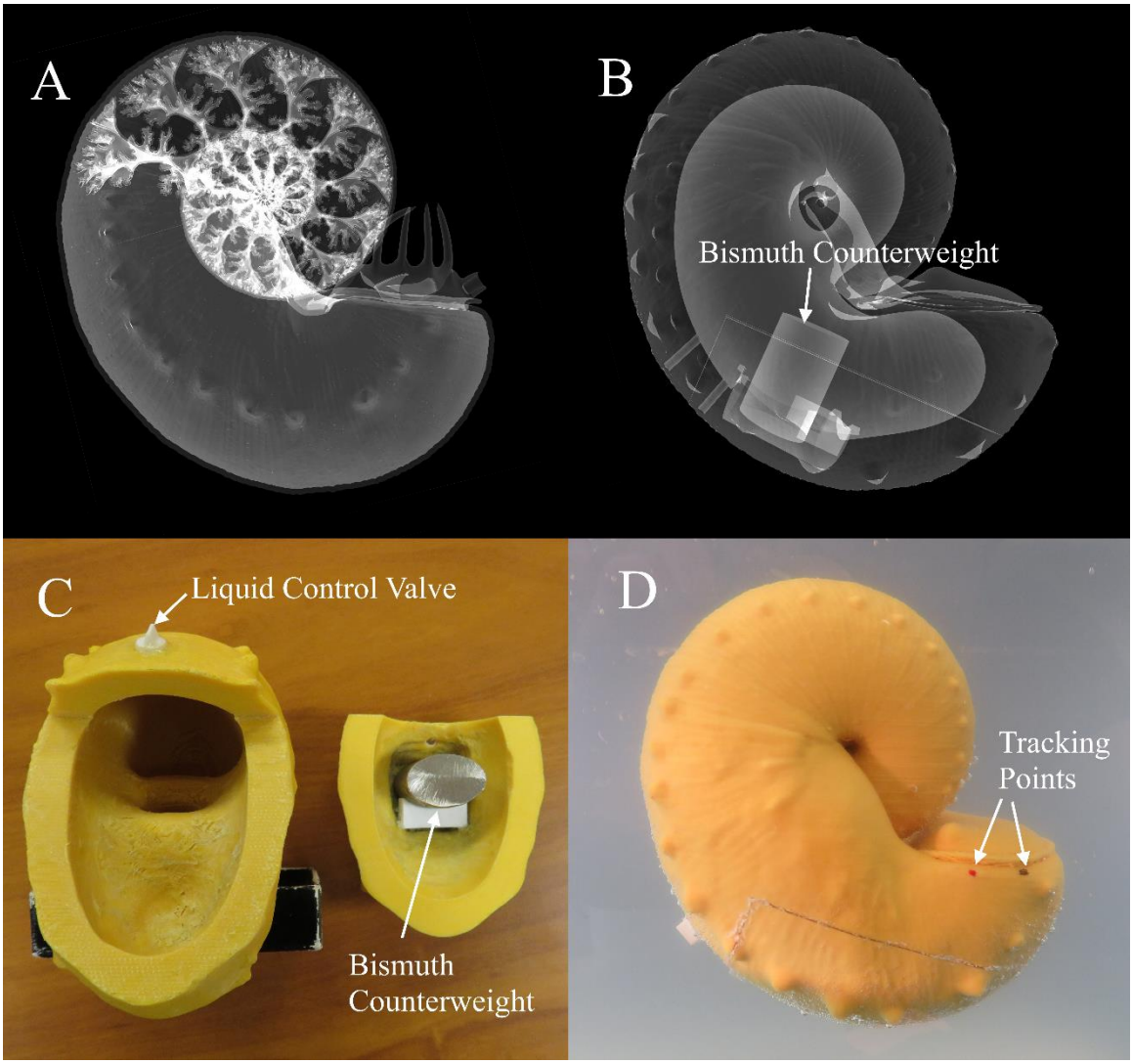

Figure 4: Development of neutrally buoyant physical model from virtual models. A – Original virtual model of *Hoploscaphites crassus* showing complex internal geometry. B – Virtual model of internally simplified shell, and bismuth counterweight at the computed location to emulate the total mass distribution of the original virtual model. C – 3D printed physical model with simple internal cavity, correctly positioned counterweight, and a one-way valve to drain the model in the event of leakage. D – Completely assembled physical model floating neutrally in the test tank, with tracking points parallel to the aperture to monitor hydrodynamics.

The siphuncle was reconstructed by making a circle within the initial phragmocone whorl section of *H. crassus* denoting the siphuncular foramen. The siphuncular diameter was measured at 6.4 % of whorl height from WSU 1474. This circle was later replicated with the same array instructions used to build the shell of the *H. crassus* macroconch (Table 1). The replicated circles were connected in Blender to make a 3D mesh of the siphuncle that was later unified to the soft body 3D mesh, and subtracted from the shell, creating a siphuncular foramen.

A mantle cavity volume of 17.5% of the soft body was used for this model (averaged from previous estimates of 15%-20%; Chamberlain, 1987; Peterman et al., 2019b). This 3D mesh was fabricated so that it did not overlap with the mouthparts or supposed position of the digestive tract (see reconstruction of Klug and Lehmann, 2015). The 3D meshes of the mouthparts and mantle cavity were subtracted from the soft body 3D mesh using Netfabb to prevent overlapping objects.

5.2.3 Juvenile scaphitid models

Juvenile models of *Hoploscaphites nicolletii* were constructed by deleting the portions of the shell and septa of the adult model to yield body chamber ratios reported by Landman and Waage (1993). They measured angular body chamber lengths for this species ranging from 220° to 264° and averaging 237°. Each of the three values were used to make hydrostatic models representing juveniles with variation in body chamber lengths.

5.2.4 Hydrostatic calculations

The conditions for neutral buoyancy were found by solving for the proportion of the phragmocone to be emptied of cameral liquid so that the organismal mass equals the

mass of the water displaced by the living animal. This volume of cameral gas relative to the available cameral volume (Φ) was computed with the following equation from Peterman et al. (2019a, 2019b).

$$\Phi = \frac{\left(\frac{V_{wd}\rho_{wd} - V_{sb}\rho_{sb} - V_{sh}\rho_{sh}}{V_{ct}}\right) - (\rho_{cl})}{(\rho_{cg} - \rho_{cl})} \quad (1)$$

Where V_{wd} and ρ_{wd} are the volume and density of the water displaced, V_{sb} and ρ_{sb} are the volume and density of the soft body, V_{sh} and ρ_{sh} are the volume and density of the shell, ρ_{cl} is the density of cameral liquid, ρ_{cg} is the density of cameral gas, and V_{ct} is the total available cameral volume within the phragmocone. Various soft body densities have been previously reported due to the estimated influences of the aptychi, mantle cavity, and other materials of differing densities (see Hoffmann et al., 2015 for a summary). A new bulk density of 1.049 g/cm^3 is used in this study based on the later described hydrostatic simulations. The shell density of 2.54 g/cm^3 measured with a pycnometer by Hoffman and Zachow (2011) is used here. The density of cameral liquid is assumed to be equal to that of seawater (1.025 g/cm^3; Greenwald and Ward 1987). The density of cameral gas is set here for calculations as 0.001 g/cm^3.

Equation 1 was modified to accommodate the *H. crassus* macroconch model with heterogeneous soft body components (mantle cavity, siphuncle, and chitiniferous and calcareous mouthparts).

$$\Phi = \frac{\left(\frac{V_{wd}\rho_{wd} - V_{sb}\rho_{sb} - V_{sh}\rho_{sh} - V_{mc}\rho_{mc} - V_{ch}\rho_{ch} - V_{ap}\rho_{ap}}{V_{ct}}\right) - (\rho_{cl})}{(\rho_{cg} - \rho_{cl})} \quad (2)$$

Where V_{mc} and ρ_{cm} are the volume and density of the mantle cavity (equal to that of seawater; 1.025 g/cm^3). V_{ch} and ρ_{ch} are the volume and density of the chitiniferous mouthparts. A chitin density of 1.35 g/cm^3 was adopted from Lucia and Rojas (2009). V_{ap}

and ρ_{ap} are the volume and density of the calcareous aptychi. A density of crystalline calcite was used for the aptychi at 2.71 g/cm^3. The latter value is probably slightly higher than the unknown true density based on the heterogeneity of the aptychus microstructure (Kruta et al., 2009). The siphuncle was unified to the soft body and assumed to have the same density, because it is composed of tissue containing blood.

The total center of mass (M) depends upon each material of unique density and is weighted by density according to the spatial distribution of these materials. For a uniform object, the center of volume equals the center of mass. These centers were computed in the program MeshLab (Cignoni and Ranzuglia, 2014) for each model component.

$$M = \frac{\sum(L * m_o)}{\sum m_o} \quad (3)$$

Where M is the total center of mass in a principal direction, L is the center of mass of a single object measured with respect to an arbitrary datum in each principal direction, and m_o is mass of any particular object that has a unique density. Equation 3 was used in the x, y, and z, directions to compute the coordinate position of the center of mass.

The center of buoyancy (B) is equal to the center of mass of the water displaced by each model. The syn vivo orientation in a static setting occurs when B and M are aligned vertically. The hydrostatic stability index can then be computed from these two centers.

$$S_t = \frac{\overline{BM}}{\sqrt[3]{V}} \quad (4)$$

5.2.5 Hydrodynamic restoration and stability

Physical experiments on the restoring moments imparted by hydrostatic stability were performed following the methods of Peterman et al. (2019b). However, the models in the current study were modified to have a smooth, soft body protruding from the

apertures due to more nuanced comparisons than Peterman et al. (2019b). Rigid arms protruding from the soft body do not significantly influence hydrostatics when volume is unchanged, but they would impose some amount of unrealistic drag in a dynamic setting. The internal geometries of these models were then simplified to allow printing in PLA (polylactic acid) filament (Figs. 4A and 4B). The physical models were modified to have the same mass and distribution of mass (and therefore hydrostatic stability) as their virtual counterparts by solving for the position and mass of a counterweight (cast from bismuth; Figs. 4B and 4C). This allows for a neutrally buoyant model that can be monitored with the motion tracking software Tracker 4.11.0 (Brown, 2017). Two tracking points parallel to the aperture were employed to compute the apertural angle θ_a as a function of time; this metric was used to monitor hydrodynamic restoration. This experiment was performed for the models of *Nautilus pompilius*, *H. crassus* (macro- and microconchs), and the adult *H. nicolletii* macroconch. The juvenile *H. nicolletii* models were simply too small to use this method, and scaling would unrealistically increase Reynolds numbers (and therefore the effect of inertial forces relative to viscous forces).

5.2.6 Hydrodynamic efficiency: physical experiments

A new method for the determination of hydrodynamic drag and the drag coefficient is proposed in this study. This approach involved programming a robot with an Arduino microcontroller circuit board and a motor driver connected to a NEMA 17 stepper motor (Fig. 5). The stepper motor controls a series of six identical gears that are connected to a linear gear rack (rack and pinion system). All parts were 3D printed in PLA, and are all housed in an enclosed platform. This configuration allows the stepper motor to remain above water, and push the submerged, neutrally buoyant cephalopod

models at specific velocities. The linear velocity of the gear rack is equal to the rotational velocity of the motor times the effective circumference of the gear. After pushing at a certain velocity, the models would remain at that velocity if not for the force of drag (see equation below):

$$F_d = 0.5A\rho C_d V^2 \quad (5)$$

Where F_d is the drag force, A is the effective area of the object, ρ is the density of the fluid, C_d is the coefficient of drag, and V is the velocity of the object. After pushing the models, their positions were measured with Tracker 4.11.0 (Brown, 2017), which showed that they experienced a nonlinear movement that was closely approximated with a parabolic equation (Fig. 6A). The derivative of this equation yields velocity, which linearly decreased for all models (Fig. 6B). The drag coefficient was found using MATLAB to create a modeled velocity equation with its slope depending upon C_d. The appropriate drag coefficient was found by reducing the sum of squared error (SSE) between the measured velocity and modeled velocity functions (Fig. 6B), both following the equation:

$$V_{t-1} - a_{t-1}\Delta t \quad (6)$$

Where V_{t-1} is the velocity at the previous time step, a_{t-1} is acceleration at the previous time step, and Δt is the change in time. The modeled acceleration is equal to the drag force (a function of C_d; Equation 5) divided by the mass of the neutrally buoyant model. Therefore, manipulating C_d changes the slope of the modeled function and the SSE between the modeled and measured functions. The fitted models were chosen because of their simplicity and the low resultant R^2 values (Fig. 6). The position and velocity

functions could be modeled as logarithmic and hyperbolic, respectively in order to maintain their relationship to Equation 5.

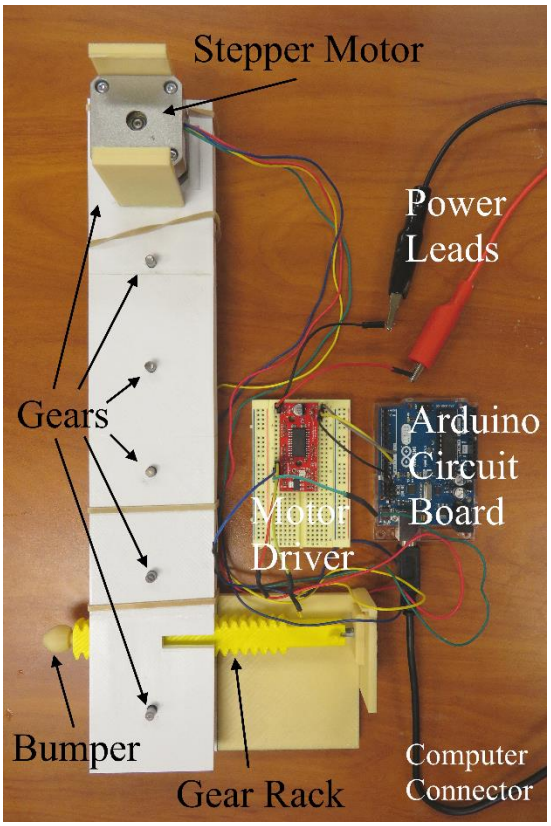

Figure 5: Device used to push the neutrally buoyant physical models at specified velocities. A 3D printed, rack-and-pinon gear system is mounted to a stepper motor that is controlled with Arduino. The spinning motor causes the gear rack to push a model at the approximate location of its hyponome.

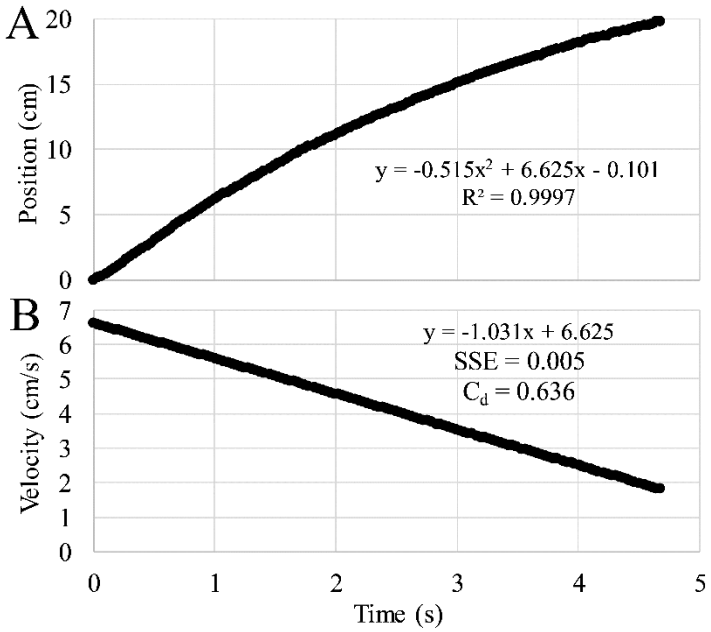

Figure 6: Trial of motion tracking experiments on the physical model of the *Hoploscaphites crassus* macroconch. A – Position of the model monitored as a function of time, well-approximated by a quadratic equation. B – Time derivative of position to compute velocity as a function of time. The model linearly decreases in velocity with time and the sum of squared error (SSE) between this function and the modeled velocity function is minimized to compute the proper drag coefficient (C_d).

5.2.7 Determination of possible swimming velocities

The soft body morphology and swimming potential of ammonoids is largely unknown (Klug and Lehmann, 2015). However, the swimming efficiency and velocity depends upon the drag coefficient and propulsive abilities. We used the methods of Jacobs (1992) to compute possible maximum sustainable velocity (MSV) based on power and hydrodynamic drag. Maximum sustainable velocity was computed in his study based on oxygen consumption rates in modern cephalopods, yielding a power (P) estimate of 660 ergs/s/cm^3. This power value was then scaled according to the ratio of the soft body volume to total volume (because only the soft body is responsible for generating this power). Power is equal to the drag force times velocity, therefore Equation 5 can be modified to solve for the maximum sustainable velocity:

$$\text{MSV} = \sqrt[3]{\frac{2P}{C_d \rho A}} \tag{7}$$

Alternatively, we propose a new method to compute maximum velocity based on shape and propulsive thrust. The propulsive ability and thrust produced by ammonoids is unknown, which requires the use of modern cephalopod analogues. The maximum swimming speed of the *Nautilus* is approximately 25 cm/s (Chamberlain, 1987, 1990; Wells and O'Dor, 1991). The force of thrust required to overcome the force of drag at this velocity is approximately 0.12 N for a 1.616 kg *Nautilus* (Chamberlain, 1987). This value however is instantaneous and does not correspond to peak thrust in a time dependent setting. A peak thrust of 0.22 N yields a maximum velocity of 25 cm/s with Equation 8. Therefore, this value represents the maximum thrust for sustained maximum velocity in a setting where the instantaneous thrust oscillates with time. For the *Nautilus*, thrust is linearly dependent upon size (i.e., mass; Chamberlain, 1987). This relationship is

the basis for scaling the *Nautilus* thrust value by the mass computed for the scaphitids in the current study. The propulsive pulse frequency also influences maximum velocity. This value intuitively seems to scale with size, however, Chamberlain (1987) shows that this relationship is very weak and the slope is not distinguishable from zero. Nonetheless, we chose a propulsive thrust period of 0.9 s for all models based on his measurements of smaller sized *Nautilus*. The periodic nature of thrust can be modeled as a simple harmonic oscillator. This translates into instantaneous velocity with the following equation:

$$V_i = \frac{\int_{t_{i-1}}^{t_i} \left(\frac{-F_{peak} \cos\left(\frac{2\pi}{p} t_i\right)}{2} + \frac{F_{peak}}{2} - \frac{A \rho C_d {V_{i-1}}^2}{2} \right) dt}{m} + V_{i-1} \quad (8)$$

Where V_i is the instantaneous velocity at the current time step, V_{i-1} is the instantaneous velocity at the previous time step, t is time, F_{peak} is the maximum propulsive thrust, p is the propulsive thrust period, and m is mass. Peak thrust values from the *Nautilus* analogue were further scaled based on the available mantle cavity volume. These ratios with respect to total volume, 0.15, 0.25, 0.5, were used to compute several possible maximum velocities based on the propulsive efficiencies of the *Nautilus pompilius*, *Sepia officinalis*, and *Loligo vulgaris*, respectively. Additionally, ventilation thrust (i.e., force generated by contraction of the hyponome to produce water flow over the gills) computed as 0.8 mN for the *Nautilus* (based on ventilation speeds of ~2 cm/s; Wells and O'Dor, 1991), was used as a proxy for velocity during ventilation for the scaphitids.

5.2.8 Hydrodynamic lift: computational fluid dynamics

Assessment of hydrodynamic lift produced from the ornamentation of *Hoploscaphites* was performed with computational fluid dynamics (CFD) simulations in the software, ANSYS Fluent. A 3D scan of an ornate *Hoploscaphites crassus* microconch

(AMNH 76342) was compared with a smooth version. The ornate specimen was well-preserved with most of its ornament intact. Broken ornament was mirrored from its respective neighbor to reconstruct all missing pieces. For the smooth version, the ornate model was smoothed in Meshmixer to produce a model representing the general shell shape only (without ribs, tubercles, or subspinose clavi). The chosen orientation matches that of the *H. crassus* hydrostatic model. Lift and drag coefficients were computed in ANSYS Fluent by simulating flow at 10 cm/s in the horizontal backwards direction. The forces produced at the shell in the direction parallel, and perpendicular to the incident flow were used to compute the drag coefficients and lift coefficients, respectively. Drag coefficients were computed by rearranging Equation 5 and lift coefficients (C_l) were computed with the following equation:

$$C_l = \frac{2F_l}{A_s \rho V^2} \tag{9}$$

Where F_l is the force of lift, and A_s is the surface area of the model. Vertical velocity (i.e., rate of climb) was computed from modeling the hydrodynamic lift based on geometry, the lift coefficient, and horizontal velocity computed from Equation (8).

$$Vz_i = \frac{\int_{t_{i-1}}^{t_i} \left(\frac{A_S \rho C_l {V_{i-1}}^2}{2} - \frac{A \rho C_d {Vz_{i-1}}^2}{2} \right) dt}{m} + Vz_{i-1} \tag{10}$$

Where Vz_i is the vertical velocity (i.e., rate of climb) at the current timestep, and Vz_{i-1} is the vertical velocity at the previous timestep. It should be noted that this upwards velocity is an approximation. These values are influenced by the incident flow, which changes direction based on the rate of climb. Equation 10 is reasonable for objects with drag coefficients that do not significantly depend upon the orientation of an object.

5.3 RESULTS

5.3.1 Testing the assumption of a uniform soft body

Previous hydrostatic experiments showed that the bulk density applied to a uniform soft body that fully occupies the body chamber can potentially cause errors in the computation of buoyancy and mass distribution (Peterman et al., 2019a, 2019b). The differences between a uniform bulk density soft body and a heterogeneous soft body (including a seawater-filled mantle cavity, chitiniferous and calcareous mouthparts, and the siphuncle) were investigated with virtual models of a *Hoploscaphites crassus* macroconch (Figs. 7D and 7E). A soft body density without these components was measured for *Nautilus* at 1.047 g/cm^3 by Hoffmann and Zachow (2011). The higher density mouthparts and lower density mantle cavity yielded a bulk density of 1.049 g/cm^3 for a uniform soft body. For scaphitids, this value is preferred over the previously used, higher estimates for baculitids (Westermann, 2013; Peterman et al., 2019b). These density differences between the current study and previous studies, however, do not cause significant differences in the computed hydrostatic properties (Table 2). The uniform bulk density was computed from the heterogeneous soft body, therefore, the percentages of the phragmocone emptied for a neutrally buoyant condition (Φ) are the same. The distribution of mass is not heavily influenced by heterogeneous soft body components (Fig. 7E) when compared to the uniform soft body model (Fig. 7D). This is because the higher density mouthparts occupy very low volumes (Figs. 7B and 7E; Table 3), and the density difference between the seawater-filled mantle cavity and the soft body is only 0.024 g/cm^3. The historical value of density of chitin can vary (1.655 g/cm^3; Hewitt, 1993). Due to the very low volume of these mouthparts, this value results in differences less than 0.1% in Φ and S_t.

H. crassus macroconch	$\rho_{soft\ body}$ (g/cm^3)	ρ_{shell} (g/cm^3)	Φ (%)	S_t	%diffΦ	%diffS_t
Lower ρ (g/cm^3)	1.049	2.54	93.4	0.086	-9.1	1.2
Higher ρ (g/cm^3)	1.065	2.62	102.8	0.085		

Table 2: Density dependency of hydrostatic properties. The percentage of the phragmocone emptied for neutral buoyancy (Φ) and hydrostatic stability index (S_t) differ depending upon the assumed densities (ρ) of the soft body and shell. The lower bulk density of the soft body was computed from Hoffmann and Zachow (2011) and the volumes and densities of the mantle cavity and mouthparts. Higher bulk densities reported by Westermann (2013), result in minor differences in hydrostatic properties (%diff).

5.3.2 Hydrostatic properties of *H. crassus* and the influences of sexual dimorphism

The body chamber to phragmocone ratios of the *H. crassus* dimorphs allow for neutral buoyancy (Φ < 100%; Figs. 7D and 7F; Table 4). The volume of cameral liquid during this condition (1- Φ) is assumed to reside at the center of each camera (a reasonable assumption due to the capillary properties of ammonitic septa; Peterman and Barton, 2019). The static, syn vivo orientations for both adult dimorphs result in upturned apertures (θ_a around 90° from vertical). The body chamber of the adult microconch is less inflated compared to the macroconch, and also deviates farther from its previous whorls. This difference in shell and soft body morphology distributes the organismal mass farther from the center of buoyancy, resulting in a higher hydrostatic stability index (~42% larger; Table 4). Each model has similar thrust angles (θ_t) near zero degrees, suggesting that energy transmitted during locomotion would efficiently allow for horizontal-backward swimming with minimal rocking.

Virtual Model	V_{sh} (cm^3)	m_{sh} (g)	V_{sb} (cm^3)	m_{sb} (g)	V_{ap} (cm^3)	m_{ap} (g)	V_{ch} (cm^3)	m_{ch} (g)	V_{mc} (cm^3)
***H. crassus* Macro**	33.405	84.848	180.108	188.934	NA	NA	NA	NA	NA
***H. crassus* Macro (heterogeneous)**	33.405	84.848	153.280	160.484	0.225	0.610	0.124	0.167	26.998
***H. crassus* Micro**	10.270	26.085	46.942	49.242	NA	NA	NA	NA	NA
***H. nicolletii* Macro**	6.189	15.720	41.822	43.872	NA	NA	NA	NA	NA
***H. nicolletii* Juvenile 220º**	0.860	2.185	6.758	7.089	NA	NA	NA	NA	NA
***H. nicolletii* Juvenile 237º**	0.921	2.339	7.837	8.221	NA	NA	NA	NA	NA
***H. nicolletii* Juvenile 264º**	1.161	2.950	9.916	10.402	NA	NA	NA	NA	NA

Virtual Model	m_{mc} (g)	V_{cg} (cm^3)	m_{cg} (g)	V_{cl} (cm^3)	m_{cl} (g)	V_{ct} (cm^3)	V_{wd} (cm^3)	m_{wd} (g)	m_{total} (g)	diff (%)
***H. crassus* Macro**	NA	53.631	0.065	3.805	3.900	57.436	270.971	277.746	277.746	0.000
***H. crassus* Macro (heterogeneous)**	27.673	57.436	0.069	0.000	0.000	57.436	270.971	277.746	277.851	0.038
***H. crassus* Micro**	NA	16.305	0.020	0.985	1.009	17.290	74.494	76.356	76.356	0.000
***H. nicolletii* Macro**	NA	9.723	0.012	1.095	1.122	10.818	59.245	60.726	60.726	0.000
***H. nicolletii* Juvenile 220º**	NA	1.347	0.002	0.000	0.000	1.347	8.969	9.193	9.276	0.892
***H. nicolletii* Juvenile 237º**	NA	1.347	0.002	0.000	0.000	1.347	10.149	10.403	10.562	1.503
***H. nicolletii* Juvenile 264º**	NA	1.347	0.002	0.000	0.000	1.347	12.423	12.733	13.354	4.644

Table 3: Volumes (V) and masses (m) of the components of each *Hoploscaphites* hydrostatic model. sh = shell, sb = soft body, ap = aptychi, ch = chitin, mc = mantle cavity, cg = cameral gas, cl = cameral liquid, ct = camerae total, wd = water displaced, %diff = percent difference in m_{total} and m_{wd}. Heterogeneous refers to the *H. crassus* macroconch model containing a mantle cavity, mouthparts, and a siphuncle. The juvenile *H. nicolletii* models are characterized by their body chamber angles.

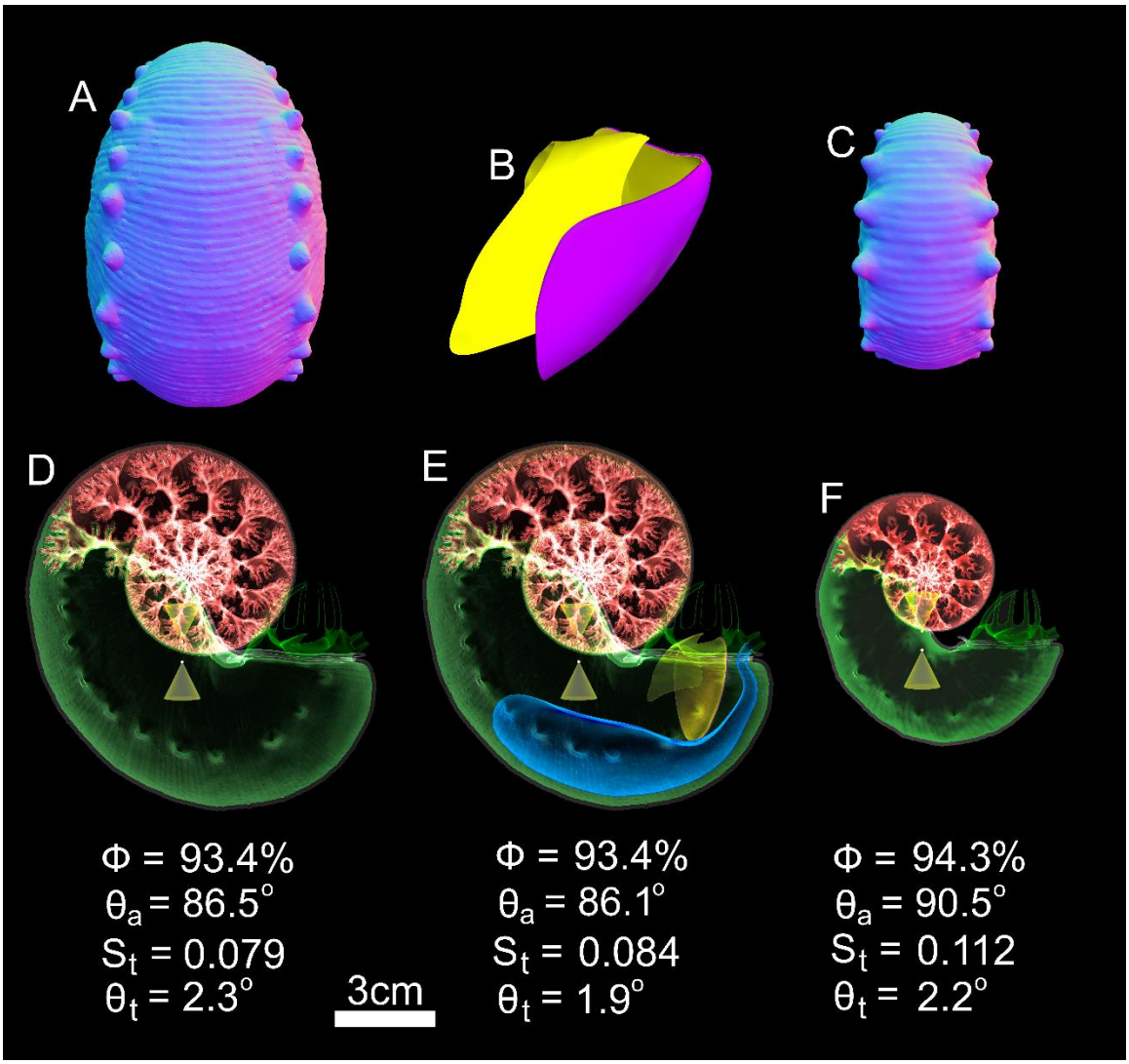

Figure 7: Hydrostatic models of *Hoploscaphites crassus*. *H. crassus* macroconch (A – ventral view; D – transparent view with uniform soft body; B – close view of mouthparts; E – heterogeneous soft body with mantle cavity, mouthparts, and siphuncle). *H. crassus* microconch (C – ventral view; F – transparent view with uniform soft body). Green – soft body, Red – cameral gas, Grey – shell, Blue – mantle cavity filled with seawater, Yellow – chitiniferous jaws, Purple – calcareous aptychi, Tip of upper cone – center of buoyancy, Tip of lower cone – center of mass, Φ – percentage of the camerae to be emptied of liquid for neutral buoyancy, θ_a – angle of the aperture measured from vertical, S_t – hydrostatic stability index, θ_t – thrust angle.

5.3.3 Hydrostatic properties of *H. nicolletii* and ontogeny

The adult *H. nicolletii* macroconch has the capacity for neutral buoyancy (Φ < 100%; Fig. 8A; Table 4) due to its similar body chamber ratio to *H. crassus* (despite the extreme differences in shell compression). The hydrostatic properties of the juvenile models of this species vary depending upon body chamber ratios. The minimum, average, and maximum angular body chamber lengths of 220°, 237°, and 264° (Figs 8C, 8D, and 8E, respectively) measured from Landman and Waage (1993) were modeled in the current study. In a neutrally buoyant condition, 100% of the cephalopod's weight would be relieved by the force of buoyancy. The modeled juveniles are slightly to moderately negatively buoyant, depending on their body chamber ratios. The extant *Nautilus* is very slightly negatively buoyant (~0.6% of its weight is not relieved by its buoyancy; Ward, 1979). This value is close to the minimum body chamber model with a difference between these two forces of 0.89% (Table 3). The averaged body chamber model (Figs. 8D) has approximately twice the percent difference (1.5%) in buoyancy and weight than the *Nautilus* and the maximum body chamber model is over seven times the difference (4.6%; Table 3). This variation in body chamber lengths in the real-world can be explained by differences in morphology that would influence buoyancy (slight shell inflation, shell thickness variation, and variable soft body occupation of the body chamber). Additionally, the shell and septum thickness values for the modeled specimens were based on extrapolation from simple equations (Fig. 2), which could have slightly overpredicted shell volume for the earlier whorls. Larger body chamber ratios would cause the aperture to further rotate upwards.

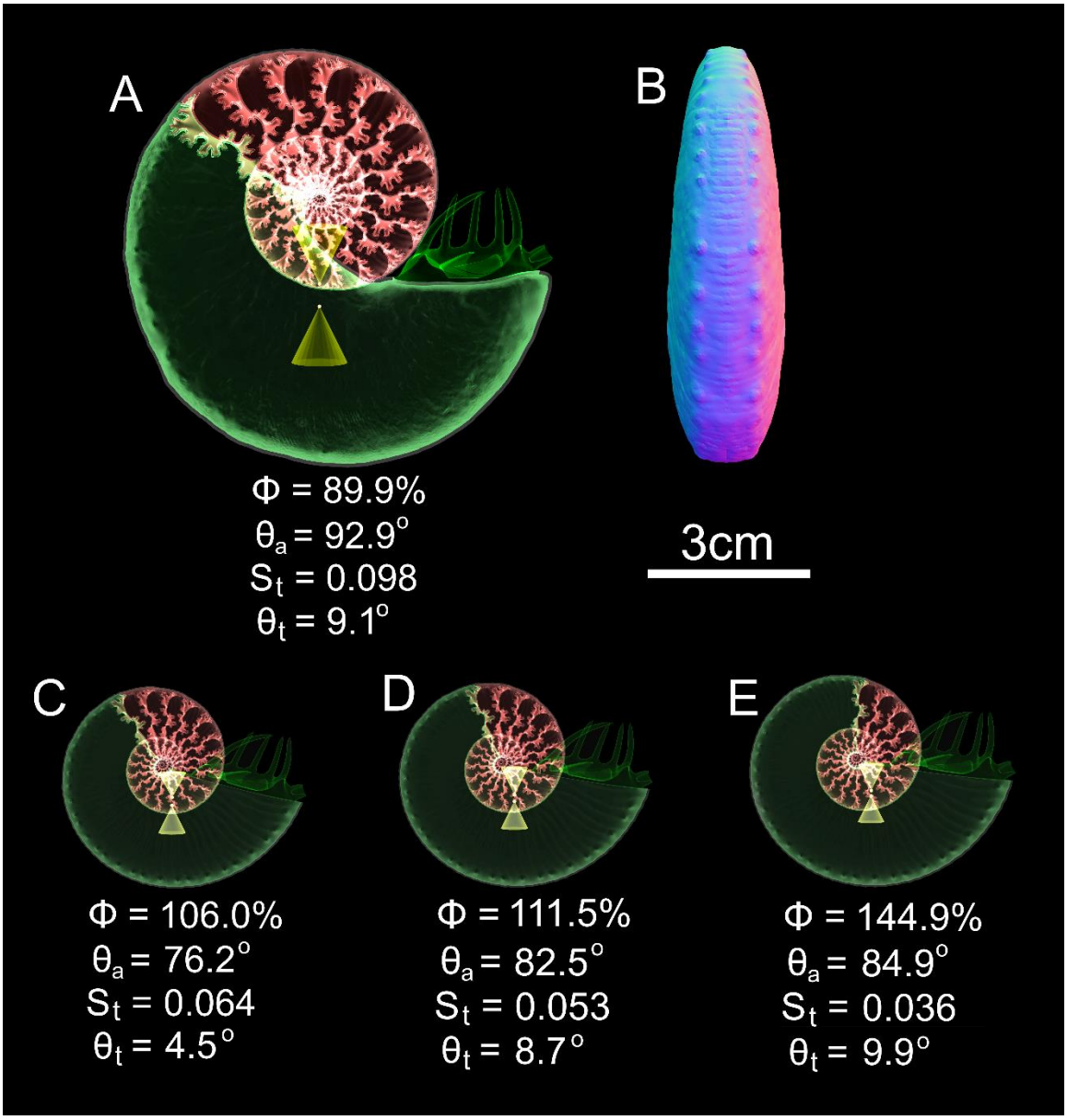

Figure 8: Hydrostatic models of *Hoploscaphites nicolletii*. Adult macroconch (A – transparent view; B – side view). Juveniles with minimum, average, and maximum angular body chamber lengths (C – 220°; D – 237°; E – 264°) reported by Landman and Waage (1993). Green – soft body, Red – cameral gas, Grey – shell, Tip of upper cone – center of buoyancy, Tip of lower cone – center of mass, Φ – percentage of the camerae to be emptied of liquid for neutral buoyancy, θ_a – angle of the aperture measured from vertical, S_t – hydrostatic stability index, θ_t – thrust angle.

Virtual Model	ϕ (%)	$\overline{BM}$ (mm)	S_t	θ_a	θ_t
***H. crassus* Macro**	93.4	5.099	0.079	86.5	2.3
***H. crassus* Macro (heterogeneous)**	93.4	5.461	0.084	86.1	1.9
***H. crassus* Micro**	94.3	4.695	0.112	90.5	2.2
***H. nicolletii* Macro**	89.9	3.804	0.098	92.9	9.1
***H. nicolletii* Juvenile 220º**	106.0	1.329	0.064	76.2	4.5
***H. nicolletii* Juvenile 237º**	111.5	1.140	0.053	82.5	8.7
***H. nicolletii* Juvenile 264º**	144.9	0.828	0.036	84.9	9.9

Table 4: Hydrostatic properties of the *Hoploscaphites* virtual models. Φ = percentage of the camerae to be emptied for neutral buoyancy, BM = separation between the centers of buoyancy and mass, S_t = hydrostatic stability index, θ_a = apertural angle in a static setting, θ_t = thrust angle. Heterogeneous refers to the *H. crassus* macroconch model containing a mantle cavity, mouthparts, and a siphuncle. The juvenile *H. nicolletii* models are characterized by their body chamber angles.

However, each of the juvenile models suggest apertural orientations (θ_a) are similar to the upturned posture of the adult model (all differences < 14°; Table 4). Hydrostatic stability is at a maximum during adulthood at 0.098 (Fig. 8A; Table 4) because the body chamber distributes mass away from the center of buoyancy. Larger body chambers for the juveniles significantly reduce hydrostatic stability by having a larger portion of mass that is positioned above the center of buoyancy (Table 4).

5.3.4 Hydrodynamic restoration and stability

The apertural orientation (θ_a) of each neutrally buoyant, 3D printed cephalopod model (Fig. 9) was recorded for 12 seconds after releasing it from a rotation of 40° in an aperture-forward (black points; Fig. 10) and aperture-backward (grey points; Fig. 10)

direction. A model of the extant *Nautilus pompilius* (Fig. 10A) served as a reference for the other models. The *Nautilus* model was modified from Peterman et al. (2019b) so that it has the same volume and hydrostatic properties as its previous version, but the rigid arms were smoothed away. This caused the previous version from Peterman et al. (2019b) to restore more quickly than the ideal model due to increased rotational drag. The physical modeling technique was further improved in the current study by using smaller valves that minimize external drag and not incorporating a large fraction of water inside the models to regulate buoyancy. The differences in stability in the current study are more nuanced and such error had to be minimized for proper comparisons. The error in hydrostatic stability was computed by assuming the differences in mass between the physical models and virtual models were distributed in the positive and negative z directions. These mass discrepancies for all models were under 3% (Table 4), which yielded less than 2% errors in stability index between the virtual and physical models (Fig. 9; Table 4).

Each model in the current study behaves as an underdamped harmonic oscillator during restoration. The exponential decay coefficients from the exponential functions fit to the peaks and troughs are used to relatively assess how hydrostatic stability relates to hydrodynamic restoration. A larger stability index generally corresponds to quicker restoration for each of the models. The model of the *H. crassus* macroconch (Fig. 10B), however, doesn't follow this trend. While it restores more slowly than the *H. crassus* microconch (Fig. 10C) and *H. nicolletii* macroconch (Fig. 10D) as expected, it is also slightly slower than the *Nautilus* model. This is likely due to difference in size, and therefore Reynolds number. Furthermore, the effect of shape (rotational drag) was not

quantified in the current study because each of the models exhibited a complex trajectory during restoration (translation superimposed on rotational oscillation), but this property, nonetheless, influences hydrodynamic restoration as well.

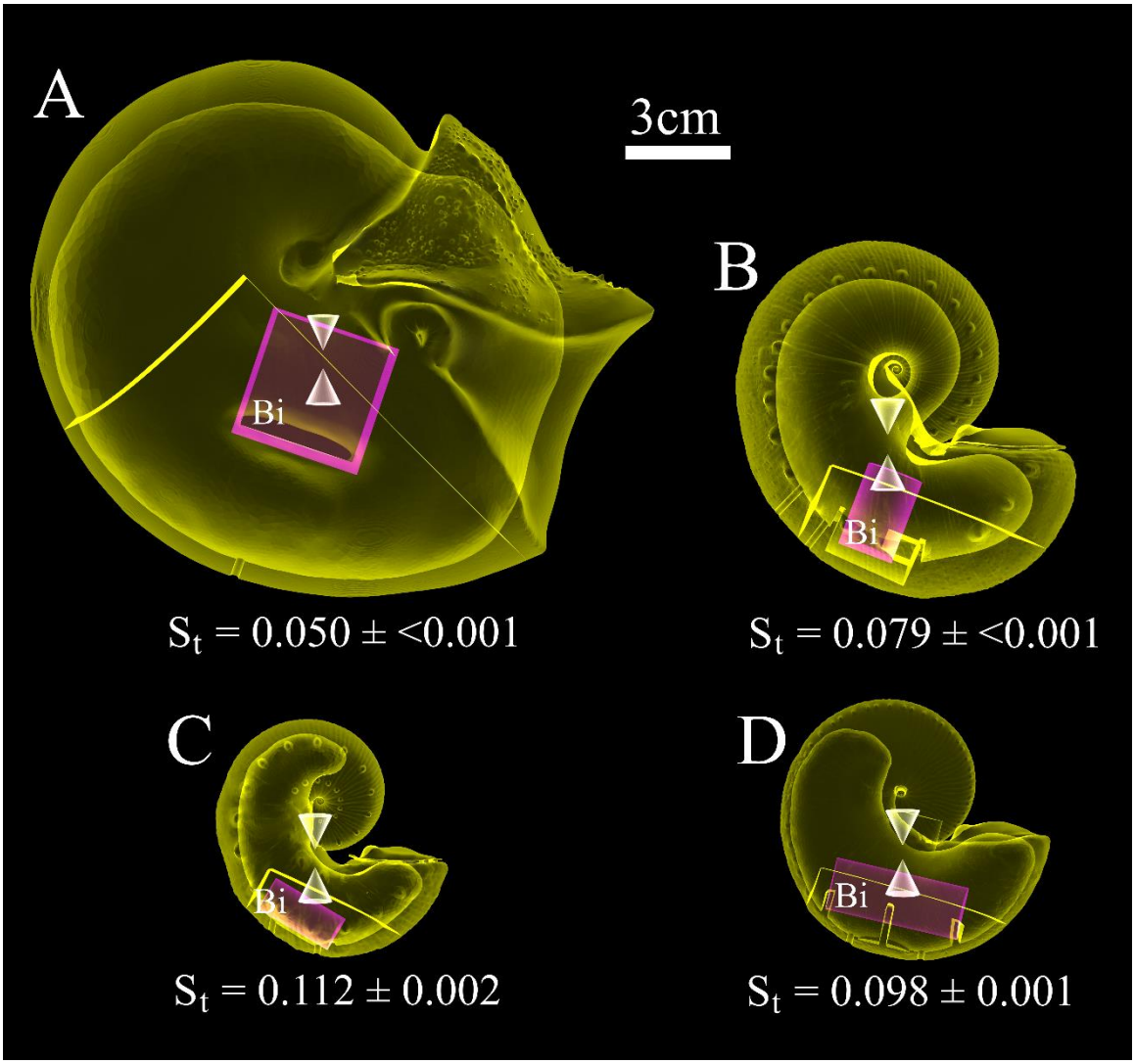

Figure 9: Modified virtual models with simplified internal geometry that were later 3D printed. Errors in stability computed from mass discrepancies between the virtual and physical models and distributing the differences in the positive and negative Z directions. Yellow – PLA plastic filament, Purple – Bismuth counterweight, Tip of upper cone – center of buoyancy, Tip of lower cone – center of mass, S_t – hydrostatic stability index.

Object	*N. pompilius* Model		*H. crassus* Macroconch Model		*H. crassus* Microconch Model		*H. nicolletii* Macroconch Model	
	Virtual Mass (g)	Actual Mass (g)	Virtual Mass (g)	Actual Mass (g)	Virtual Mass (g)	Actual Mass (g)	Virtual Mass (g)	Actual Mass (g)
PLA Shell	475.63	482.43	195.24	195.56	53.90	55.92	32.65	33.98
Bismuth Weight	498.82	494.66	73.30	73.30	18.47	18.47	25.57	25.57
Total	974.45	977.09	268.54	268.86	72.37	74.39	58.22	59.55
Mass Discrepancy (%)	0.27		0.12		2.79		2.28	
S_t	0.050		0.079		0.112		0.098	
S_t Error	<0.001		<0.001		0.002		0.001	

Table 5: Mass discrepancies between the virtual and 3D printed model components and error in hydrostatic stability index (S_t).

3.5 Hydrodynamic drag

The physical models of the *H. crassus* macroconch, *H. crassus* microconch, and *H. nicolletii* macroconch (Figs. 9B, 9C, and 9D) were propelled over several trials ranging between approximately 5 to 35 cm/s (Table 6). Actual initial velocities varied from the Arduino-programmed velocities based on stress imposed on the robot used to propel each model (stepper motor stress and gear stress). For calculations, the true initial velocities of each model were used my monitoring the moment they left contact with the robot. Each model decelerated from these initial velocities due to hydrodynamic drag, allowing the computation of drag coefficients (Fig. 11). T-tests were performed to assess statistical significance between the averaged drag coefficients for each model. The differences in drag coefficients between the *H. crassus* macroconch (average $C_d = 0.691$) and microconch (average $C_d = 0.610$) is not significant (p-value of 0.118). However, the p-values between *H. nicolletii* and both *H. crassus* models suggest that the lower drag coefficient of *H. nicolletii* (average $C_d = 0.423$) is significant (p-values less than 0.002;

Fig. 11). The large mass and absolute drag force imparted on the *Nautilus* model precluded the computation of its drag coefficient due to motor and gear stress. Therefore, a drag coefficient of 0.43 was adopted from Chamberlain (1987) for later comparisons and velocity calculations.

The computation of drag coefficients with neutrally buoyant, physical models was compared with CFD (computational fluid dynamics) analysis in a virtual setting using the *H. crassus* microconch model. CFD simulations yield a drag coefficient of 0.59, which is very close to the average drag coefficient computed from physical experiments (0.61; Table 6).

	V_0 (cm/s)	**C_d**	**SSE**	**Avg. C_d**	**C_d SD**
***H. crassus* Macroconch**	5.999	0.846	0.0021	0.691	0.079
	6.625	0.636	0.0008		
	18.551	0.639	0.0083		
	15.060	0.720	0.0127		
	17.755	0.693	0.0097		
	21.892	0.610	0.0151		
***H. crassus* Microconch**	7.676	0.624	0.0033	0.610	0.062
	7.335	0.670	0.0029		
	16.204	0.643	0.0090		
	17.874	0.492	0.0112		
	35.850	0.621	0.0197		
***H. nicolletii* Macroconch**	6.262	0.696	0.0031	0.423	0.058
	6.068	0.394	0.0054		
	18.896	0.404	0.0175		
	14.372	0.534	0.0092		
	21.201	0.460	0.0162		
	33.075	0.384	0.0269		
	30.989	0.361	0.0300		

Table 6: Drag coefficients (C_d) computed from physical experimentation on 3D printed models during several trials of differing initial velocity (V_0). Drag coefficients

5.3.6 Velocity calculations

Maximum sustainable velocity (MSV) was computed with the power estimate of Jacobs (1992) and the drag coefficients computed in the current study. The MSV is inversely proportionate to the drag coefficient (Equation 7), but also depends upon power (scaled by mass) and the effective cross-sectional area. This method yields the highest MSV for *H. nicolletii* (21.69 cm/s) with both dimorphs of *H. crassus* falling just behind (17.17 cm/s for the microconch, 19.12 cm/s for the macroconch; Table 7). MSV values were computed for a 1.6 kg *Nautilus* at 30 cm/s, which is slightly larger than the maximum velocity reported by Chamberlain (1987, 1990) of approximately 25 cm/s. The modeled scaphitids are much smaller by mass (Table 3) yet have comparable velocities to the larger *Nautilus* when scaled by mass (Table 7). The power estimate of 660 ergs/s/cm^3 from Jacobs (1992) is responsible for this relative increase in possible swimming velocity.

	$T_{Nautilus}$ (dyn)	**T_{Sepia} (dyn)**	**T_{Loligo} (dyn)**	**$V_{Nautilus}$ (cm/s)**	**V_{Sepia} (cm/s)**	**V_{Loligo} (cm/s)**	**MSV (cm/s)**	**Ventilation (cm/s)**
***H. crassus* Macroconch**	3688	6147	12293	11.14 ± 0.59	14.72 ± 0.76	21.62 ± 1.10	19.12 ± 0.68	0.84
***H. crassus* Microconch**	1014	1690	3381	9.84 ± 0.45	13.04 ± 0.59	19.18 ± 0.86	17.17 ± 0.55	0.74
***H. nicolletii* Macroconch**	809	1348	2697	12.91 ± 0.83	17.01 ± 1.08	24.91 ± 1.55	21.69 ± 0.91	0.99
****H. crassus* Macroconch**	1361	2269	4538	4.11	5.43	7.98	7.06	0.30
****H. crassus* Microconch**	1361	2269	4538	13.21	17.50	25.75	23.05	0.98
****H. nicolletii* Macroconch**	1361	2269	4538	21.72	28.62	41.92	36.50	1.62

Table 7: Velocities (V) computed from drag coefficients and various values of thrust (T) for jet propulsive swimming and ventilation of gills. Thrust was assumed for each model by using the extant *Nautilus pompilius*, *Sepia officinalis*, and *Loligo vulgaris* as analogues for thrust, resulting in differing velocity values. Maximum sustainable velocities (MSV) were computed from the methods of Jacobs (1992). Asterisks denote the models scaled to 100 g to compare relative velocities (note that these are not the actual velocities expected from 100 g specimens).

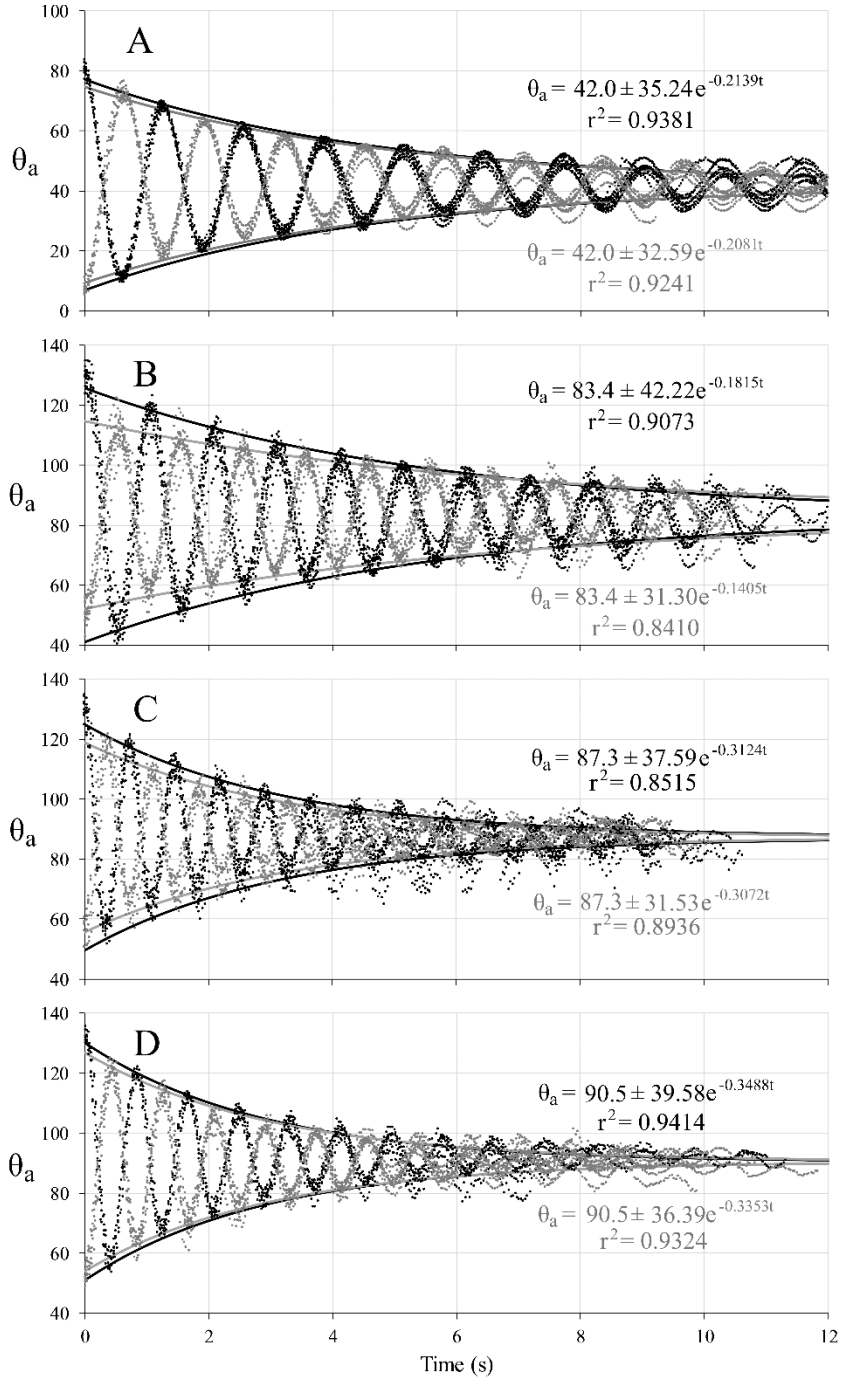

Figure 10: Hydrodynamic restoration of physical models after rotating them approximately 40° from their static equilibrium orientations. The apertural angle (θ_a; in degrees) as a function of time follows underdamped harmonic oscillation. A – *Nautilus pompilius*, B – *Hoploscaphites crassus* macroconch, C – *H. crassus* microconch, D – *H. nicolletii* macroconch, Black – released after aperture is rotated forward, Grey – release after aperture is rotated backwards. Exponential decay functions are fit to peaks and troughs to quantify their decay with time.

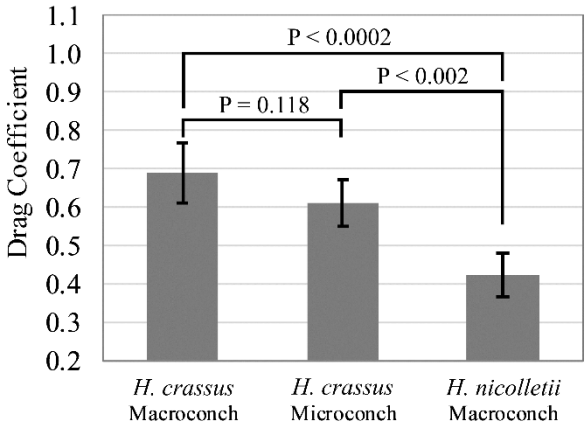

Figure 11: Drag coefficients (C_d) computed after multiple initial velocity trials (Table 6) for the *Hoploscaphites crassus* macroconch, *H. crassus* microconch, and *H. nicolletii* macroconch. Error bars represent one standard deviation. Brackets show comparative P-values computed from t-tests to assess whether or not the difference between mean drag coefficients are statistically significant. The mean drag coefficient of *H. nicolletii* is significantly lower than the *H. crassus* macroconch and microconch. The difference between the *H. crassus* dimorphs is only weakly significant.

Velocity was computed with an alternative method (Equation 8) using the mantle cavity ratios (Chamberlain, 1990) of several extant cephalopods as analogues for potential thrust (*Nautilus pompilius*, *Sepia officinalis*, and *Loligo vulgaris* – ordered by increasing thrust; Table 7). The oscillatory pulses of thrust (Figs. 12A-C) cause each of the models to asymptotically reach their maximum velocities after approximately 5 seconds (Figs. 12E-F; Table 7). Velocity is dependent upon thrust (scaled by mass), effective cross sectional area, and the drag coefficient. The lower drag coefficient and cross-sectional area of *H. nicolletii* allows for larger possible swimming velocities when compared to the other scaphitids.

The period of each jet pulse influences the duration of thrust values at each time step and therefore velocity. The influence of this variable was tested by doubling, and halving the period for the *H. nicolletii* macroconch model then recomputing velocity with

the *Nautilus*-like thrust efficiency. This method yielded velocities of 12.55 and 13.1 cm/s (each are less than 5% different than the original value of 12.91 cm/s; Table 7). However, modeling the thrust equation as a simple harmonic oscillator must deviate from the *Nautilus* thrust profiles of Chamberlain (1987) as the pulse period increases or decreases beyond a reasonable value.

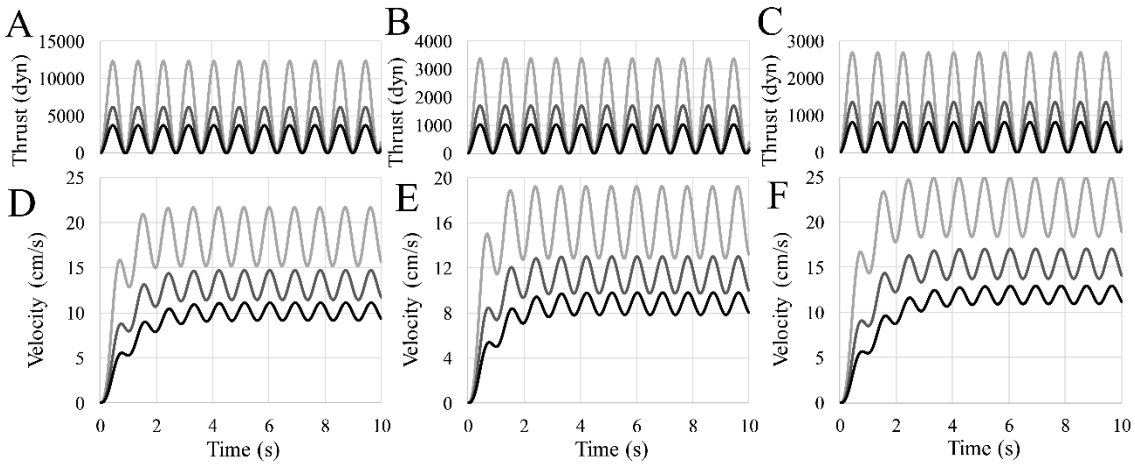

Figure 12: Thrust (A-C) and velocity (D-F) computed for the *Hoploscaphites crassus* macroconch (A, D), *H. crassus* microconch (B, E), and *H. nicolletii* macroconch (C, F). Extant cephalopods were used as analogues for these ammonoids: *Nautilus pompilius* (Black), *Sepia officinalis* (Dark Grey), and *Loligo vulgaris* (Light Grey). Note differences in vertical scales between the plots.

Equation 8 computes velocity, but requires velocity to compute drag. This circular logic was circumvented by computing the array at very small time steps (0.05 s) and using the velocity of the previous time step to compute drag. The chosen time step was tested by reducing it to 0.01 s and computing a change in maximum velocity, which was less than 0.1%. Using the velocity of the previous time step to compute drag is therefore reasonable because the change in thrust at this scale is very small, and changing the resolution yields little difference.

Movement during ventilation of the gills by contraction of the hyponome was investigated for the scaphitids by scaling the thrust produced during *Nautilus* ventilation (enough to move 2 cm/s; Wells and O'Dor, 1991). After approximately 1.5 minutes of ventilation at a pulse period of 0.9 s, each of the models stabilize and reach velocities lower than 1 cm/s. However, the accuracies of these values are questionable due to the assumptions of simple scaling relationships and unknown soft body characteristics in terms of locomotion.

5.3.7 Hydrodynamic lift

The possible function of ventrolateral tubercles (common within Scaphitidae) to produce hydrodynamic lift was explored with a well-preserved *H. crassus* microconch (AMNH 76342). Lift could not be observed in the physical experiments due to the short horizontal distance of the experiment, decaying velocity, and slight differences in buoyancy due to mass discrepancy. Therefore, CFD analyses were used to assess lift (Fig. 13). Simulations reveal that horizontal backwards movement results in positive lift (in the upward vertical direction). The incident streamlines are directed downwards after interacting with the models. Additionally, there is a rather large vortex on the reverse side of the models that is quickly directed downwards after the incident flow passes them (Fig. 13). This is due to the shape of the recurved hook of these mature scaphitids, which causes a change in the velocity field that produces pressure differentials above and below the models, and ultimately produces positive lift. A velocity of 10 cm/s yields a lift force of 156 dynes for the ornate model and 149 dynes for the smooth model (Table 8). These values were used to compute lift coefficients of 0.033 and 0.035, respectively. The rate of climb during movement is influenced by constantly changing drag opposite of the

movement direction. Equation 10 is rooted in the assumption that the drag coefficient does not change based on orientation. The drag coefficient was doubled and halved to test the influence of this assumption. These tests result in up to 27% differences in the computed rates of climb (Table 8). It is unlikely that the drag coefficients in the current study change by a factor of two based on orientation, but even so, lift would remain significant. The horizontal velocity oscillates similarly to the previous experiments (Fig. 14A), yielding an asymptotic maximum velocity between 10 and 11 cm/s for both models and very similar drag coefficients (Table 8). This velocity value is slightly larger than that of the previous *H. crassus* microconch model due to differences in mass and drag coefficients, and therefore thrust (Tables 3, 7, and 8). Rate of climb also oscillates very subtly then asymptotically approaches a maximum value when drag and hydrodynamic lift forces are equal (Fig. 14B). The vertical and horizontal position computed from the corresponding velocities show that lift is significant during backwards locomotion and raises the model upwards (Fig. 14C). The small differences in hydrodynamic lift, rate of climb, and position during locomotion between the ornate and smooth models suggest that the overall shell shape is responsible for lift rather than the ornamentation.

	***H. crassus* Microconch**	
	Ornamented	**Smooth**
Mass (g)	52.33	50.54
Max Thrust (dyn)	712.39	688.10
Lift Force (dyn) @ 10 cm/s	155.89	149.35
Drag Force (dyn) @ 10 cm/s	410.19	360.11
Lift Coefficient	0.033	0.035
Drag Coefficient	0.482	0.445
Max. Horizontal Velocity (cm/s)	10.28	10.74
Max. Rate of Climb (cm/s)	4.36	4.8

Table 8: Results of computational fluid dynamics (CFD) simulations using the ornamented and smoothed *Hoploscaphites crassus* microconch models (AMNH 76342).

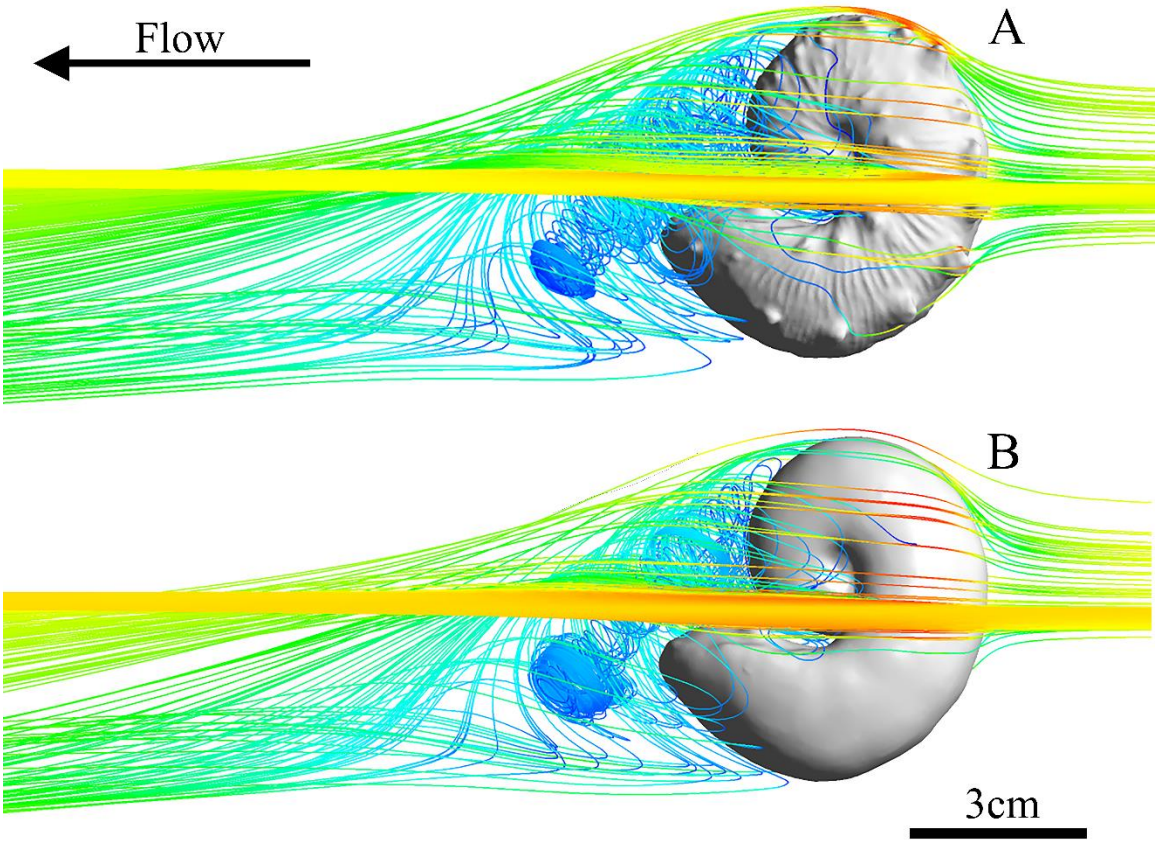

Figure 13: ANSYS Fluent Computational Fluid Dynamics (CFD) simulation. Incident flow occurs from the right to left representing horizontal backwards movement. A) Ornate 3D reconstruction of a well-preserved *Hoploscaphites crassus* microconch (AMNH 76342). B) Smoothed version of AMNH 76342 with ornamentation erased.

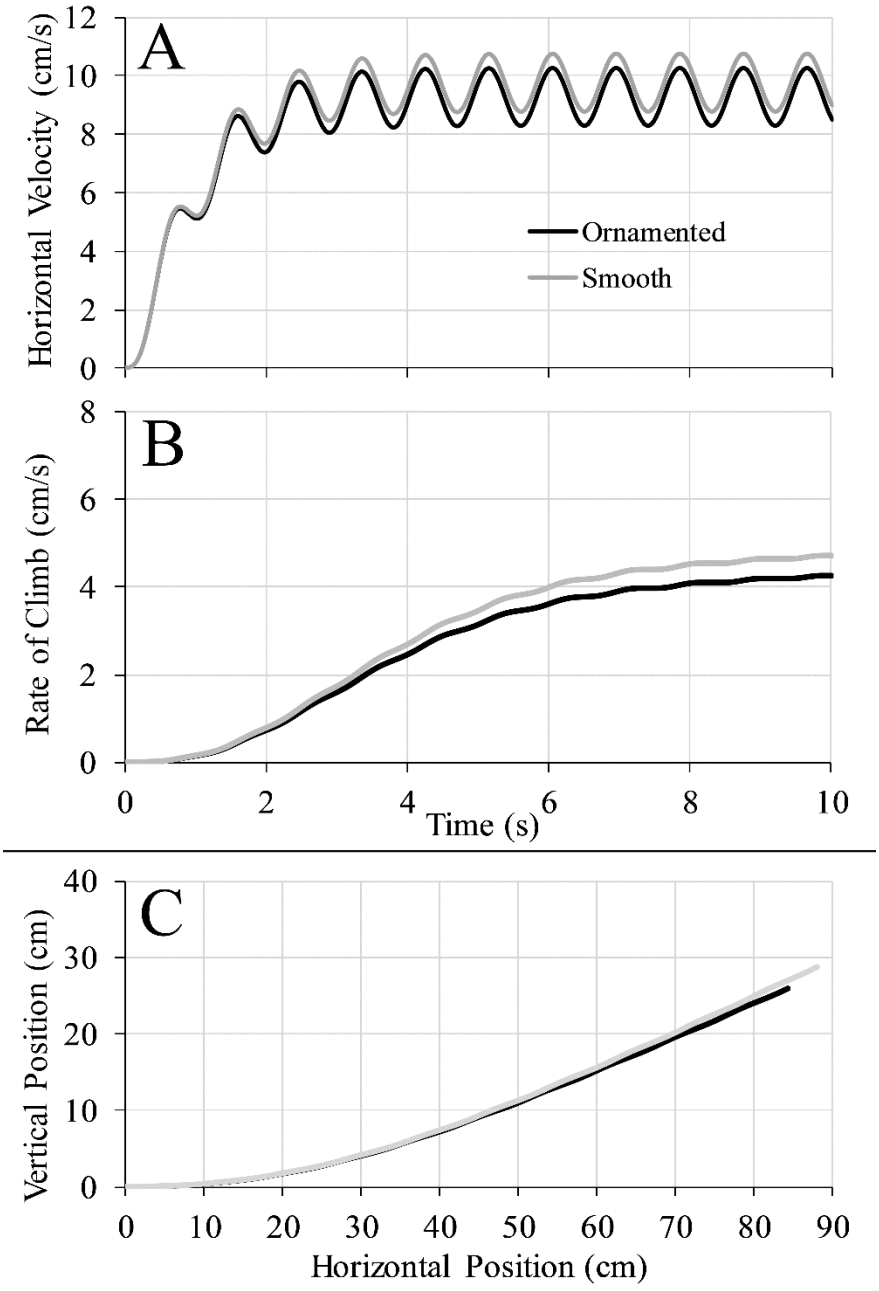

Figure 14: Locomotion computations from the computational fluid dynamics (CFD) simulations for *Hoploscaphites crassus* microconch. A) Horizontal velocity with *Nautilus*-like thrust. B) Rate of climb (upward vertical component of velocity). C) Vertical and horizontal position from a starting point at rest.

5.4 DISCUSSION

5.4.1 Scaphitid hydrostatics

All adult scaphitids in the current study have the capacity for neutral buoyancy with nearly all of their phragmocones emptied of cameral liquid (Figs. 7 and 8). This is due to sufficiently low body chamber to phragmocone ratios that manage the total organismal mass relative to the mass of water displaced by the living cephalopods. However, the juvenile *H. nicolletii* models are slightly negatively buoyant depending on body chamber ratio. Models with the average angular body chamber length (237°; Fig 8D) and lower have residual masses that are less than 2% of the mass relieved by buoyancy. This is on par with the mass difference observed in extant *Nautilus* (Ward, 1979; Ward and Greenwald, 1982). Individuals with the largest observed body chamber for this species (264°; Landman and Waage, 1993) may have struggled to achieve neutral buoyancy unless such a specimen had different proportions than the modeled specimen (e.g., more depressed phragmocone, differences in shell thickness). The results of the current study suggest that scaphitids were able to actively swim or passively drift as neutrally buoyant objects in the water column, possibly near the seafloor (as suggested by Tsujita and Westermann, 1998; He et al., 2005; Cochran et al., 2010; Sessa et al., 2015) while exploiting low energy lifestyles (Landman and Waage, 1993; Landman et al., 2010, 2012a). Scaphitid touch marks on the seafloor likely represent post-mortem bouncing or rolling and do not indicate a completely demersal or benthic mode of life (Seilacher, 1963; Landman and Cobban, 2007; Lukeneder, 2015). The buoyancy results of the current study also support the existing view that extinct ectocochleate cephalopods were largely neutrally buoyant by either adding fluid to a positively buoyant shell or

counteracting slight negative buoyancy with active swimming (Denton and Gilpin-Brown, 1966; Ward and Westermann, 1977; Klinger, 1981; Shigeta, 1993; Tajika et al., 2015a; Lemanis et al., 2015; Hoffmann et al., 2015; Peterman et al., 2019a, 2019b).

The heterogeneity within the soft body (buccal mass, seawater-filled, mantle cavity; Fig. 7E) does not significantly influence the hydrostatics of the modeled scaphitids and suggest that lower densities should be used for studies of similar taxa and/or similar morphologies. The density values measured by Hoffmann and Zachow (2011) are preferred over the density estimates of Westermann (2013) in the current study because of the low volumes of the calcareous aptychi and chitiniferous jaws (Table 3). The opposite influence on hydrostatics has been suggested for ammonoids with larger aptychi (e.g., Laevaptychi, and Lamellaptychi), which may have influenced the distribution of mass and active locomotion (Parent et al., 2014). Lemanis et al. (2015) also report minimal hydrostatic influences for organismal components other than the shell and soft body.

Each of the scaphitids in the current study had upward-facing apertures at adulthood (Figs. 7 and 8). These syn vivo orientations would preclude significant interaction with the benthos at maturity, which is reinforced by their most likely reduced soft body (Landman et al., 2012a, 2016a). The models of the juvenile *H. nicolletii* all have slightly less upturned apertures when compared to the adult, but would still have also been challenged to interact with the benthos (Fig. 8). Therefore, there seems to be a strong preference for upward-facing apertures within Scaphitidae throughout ontogeny. The exception to this pattern is when the straight shaft of the shell is formed, with a presumably lower apertural angle. The shafts of the adult body chambers within *H.*

nicolletii commonly exhibit stretch pathologies – a decrease in whorl width and height, the slight thinning of the shell, and attenuation of ornamentation (Landman and Waage, 1993). These changes in morphology may reflect a period of rapid growth just before the completion of the upturned U-shaped hook (Landman and Waage, 1986; Bucher et al., 1996), such that the duration of life with a downward-facing aperture was minimized. Accelerated growth during this stage would also explain the rarity of individuals with half-formed shaft and hook portions of the shell in the fossil record (Landman and Waage, 1993).

The U-shaped hook at maturity distributes the organismal mass away from the phragmocone and significantly increases stability, which supports earlier studies of similar morphotypes (Trueman, 1940; Klinger, 1981; Westermann, 1996). Higher stability is especially apparent for the *H. crassus* microconch (Fig. 7F) and *H. nicolletii* models (Fig. 7A). In contrast, the *H. crassus* macroconch has lower stability due to the lateral inflation of the shaft of the body chamber. Its overall inflation also partially closes the gap between the recurved hook and phragmocone. Both of these characteristics cause the total mass distribution to remain closer to the center of buoyancy. These features are also apparent in other scaphitid macroconchs (e.g., *H. nodosus*, *H. plenus*, and *H. criptonodosus*; Landman et al., 2010), which likely have similar hydrostatic properties to the modeled *H. crassus*. These inflated scaphitids with large degrees of dimorphism generally correspond to distal, low-energy paleoenvironments. Aside from these differences, all of the modeled adult scaphitids are more stable than the extant *Nautilus* (compare Peterman et al., 2019a, 2019b). The juvenile *H. nicolletii* models, however,

suggest that juvenile planispiral scaphitids were very similar to the *Nautilus* in terms of hydrostatic stability (Figure 7; Table 3).

All of the modeled scaphitids have thrust angles close to zero (Table 4), suggesting that thrust generated by these living cephalopods would be efficiently translated into horizontal-backwards movement with minimal energy lost due to rocking. This horizontal alignment of the hyponome and center of rotation has been suggested to be a possible selective force for similar heteromorphs, yielding recurved hooks at maturity that may have had some significance during the time of mating (Korn and Klug, 2003; Klug and Korn, 2004; Tajika et al., 2015a; Klug et al., 2015). While the current study supports this idea for adult scaphitids, the juvenile models yield similar thrust angles as well (Fig. 8; Table 4), suggesting that this mode of locomotion was not only associated with maturity and mating. The primary difference during ontogeny (at least for *H. nicolletii*) seems to be an increase in stability, while maintaining these ideal thrust angles. Alternatively, stability could be considerably increased by deviating from the planispiral whorls without recurving the body chamber (as in the Paleozoic nautiloids – Lituitidae; Furnish and Glenister, 1964). The absence of the hook, however, would cause the thrust angle to be poorly suited for horizontal swimming.

5.4.2 Scaphitid stability and hydrodynamic restoration

The hydrostatic stability of extant *Nautilus* is regarded as rather high (Okamoto, 1996) due to its low body chamber ratio, yet the stability values of each of the adult scaphitids are much larger (compare the *Nautilus* stability of 0.05 with the current values; Table 4). The *Nautilus* is unable to pinwheel as it moves, or significantly modify its orientation with thrust (aside from its normal rocking movement; Chamberlain, 1981;

Jacobs and Landman, 1993). This relationship suggests that the investigated scaphitids are also unable to significantly modify their orientation. The hydrodynamic restoration experiments suggest that higher hydrostatic stability does impart larger restoring moments, resulting in quicker restoration for these particular species after they rotated away from their equilibrium orientations. This relationship is complicated, however, and depends on size (therefore mass and Reynolds number) and shape (therefore rotational drag, which is influenced by direction) of the shell. Objects of larger mass and nonzero stability will oscillate more slowly and will increase the influence of inertial forces with respect to viscous forces acting upon the ammonoid. During hydrodynamic restoration, each model behaves as an underdamped harmonic oscillator (like a pendulum interacting with drag and gravity; Fig. 10). While the scaphitids of the current study have rather high hydrostatic stability, none of them are so high that they are critically damped. This behavior contrasts the baculite model of Peterman et al. (2019b), which serves as the endmember of a highly-stable ectocochleate cephalopod due to its high hydrostatic stability index (~0.5) and rotational drag. The stable *H. crassus* microconch and *H. nicolletii* macroconch restore themselves more quickly than the *Nautilus* and *H. crassus* macroconch. Both hydrostatic stability and hydrodynamic restoration constrain the ability of the living scaphitids to modify their orientation, but also prevent unwanted rotation during movement or from external forces (turbulence caused by predators, current energy, etc.). These results suggest that highly-stable scaphitids could not modify their orientation with active locomotion enough to directly scavenge the benthos. Similarly, Kaplan (2002) demonstrates that this general morphology could not significantly access the benthos by localizing cameral liquid, or adjusting the position of their soft body

(Kakabadzé and Sharikadzé, 1993; Monks and Young, 1998). These constraints on scaphitid hydrostatics are consistent with their jaw morphology, which would only allow feeding on small prey in the water column (Landman and Waage, 1993; Landman et al., 2012a; Kruta et al., 2009, 2013). It is likely that ancylocone heteromorphs (with a larger degree of uncoiled, U-shaped, mature body chambers) had similar hydrostatic properties to these investigated scaphitids.

5.4.3 Hydrodynamic efficiency and drag

The near-zero thrust angles in the examined scaphitids suggest that energy produced by thrust would have been efficiently transmitted into backwards movement. Previous studies also interpret this mode of movement for the scaphiticone morphotype based on shell shape (Westermann, 1996; Westermann and Tsujita, 1999), although vertical upwards movement probably would have been severely limited by a reduced hyponome. In a horizontal backwards direction of movement, the computed drag coefficients quantify the degree of resistance to movement based on overall shape (Fig. 11). The more streamlined shape of *Hoploscaphites nicolletii* results in drag coefficients that are significantly lower than those of both dimorphs of *H. crassus* (Fig. 11). The *H. crassus* microconch seems more streamlined than the macroconch at first glance, however, the larger gap between the recurved body chamber and phragmocone, and the more prominent tubercles on the ventral body chamber at maturity, both disrupt flow around the entire shell. The shape of the microconch results in a drag coefficient that is only slightly lower than the macroconch (with weak statistical significance; Fig. 11). After periodically applying thrust with a *Nautilus*-like rhythm, higher drag coefficients cause the cephalopods to asymptotically approach their maximum velocity (Fig. 12).

However, these velocities highly depend upon the thrust potential of the living ammonoids. If they had the high efficiency and large mantle cavity ratios of decapodiform coleoids, the computed velocities are approximately twice those of simulations with a *Nautilus*-like thrust. The *Loligo*-like efficiencies are probably too large because they assume thrusts produced from mantle cavity volumes that are 50% of the soft body volume. This estimate is too large for ammonoids which have ratios of approximately 15%-20% (Chamberlain, 1987). Therefore, *Sepia*-like and *Nautilus*-like thrusts probably yield more realistic estimates of maximum velocity for ammonoids. The available power estimate of ammonoids from Jacobs (1992) yields maximum sustainable velocities (MSV) that are consistently higher than the computed velocities with time-dependent thrusts. Both methods depend upon the drag coefficient, however, time-dependency results in a differential amount of drag experienced on the cephalopod as it moves thought the water, which lowers the computed velocity.

Lower drag coefficients let organisms swim faster for their given sizes (mass). Jacobs et al. (1994) demonstrated that the scaphitid *Scaphites whitfieldi* exhibits compressed and inflated morphs that occur in sandy and silty facies, respectively. Furthermore, the compressed morphs were found to require less power at velocities higher than 12 cm/s while the inflated morphs require less power at lower velocities. The variability in shape and power requirements of these ecophenotypes parallels the two species of *Hoploscaphites* investigated in the current study. The inflated *H. crassus* occupies the distal, low energy paleoenvironment of the Pierre Shale, while the compressed *H. nicolletii* is known from the more proximal Fox Hills Formation. Shell compression and higher swimming speeds would have been favorable to survival in

higher energy settings. Conversely, the inflated morphs were either more efficient at lower velocities in lower-energy facies or did not face selective pressures for increased velocities.

5.4.4 Scaphitid ornamentation and lift

An upwards force of lift is imparted on the scaphitid models during horizontal backwards movement, ultimately resulting in an upward component of movement (Fig. 14; Table 8). An ornate *H. crassus* microconch and smoothed version were compared to assess the influence of the ornamentation during hydrodynamic movement. There are few differences in the horizontal velocities, rates of climb (vertical velocity), and position between these two models, suggesting that shell shape is mostly responsible for generating lift during movement, rather than ornamentation. This positive lift may have been able to compensate for the cumbersome orientation of the aperture at maturity. If scaphitids were slightly negatively buoyant, similar to the extant *Nautilus* (Ward, 1979), sinking could have been counteracted by simply aligning the hyponome with the horizontal plane, rather than directing it over the ventral edge of the body chamber. Such behavior is consistent with the probable difficulty in upwards locomotion at maturity, which would have been impeded by the upturned aperture and reduced soft body, prohibiting downward positioning of the hyponome (Landman et al., 2012a, 2016a).

If the asymmetrical shape of the ornamentation on mature *Hoploscaphites* does not significantly influence hydrodynamics, it may have had another functional significance. Lethal injuries have been well reported from the apical body chamber of *Hoploscaphites* (Larson, 2003; Klompmaker et al., 2009; Landman et al., 2012a). At this portion of the body chamber, the ventrolateral tubercles are modified into subspinose

clavi for several species (Landman et al., 2012a; Landman and Waage, 1993), suggesting they could have acted to defend against predators. The spines of ammonoid shells have also been suggested to serve as stabilizers against rocking or as sensory devices (Ifrim, et al., 2018). These functions cannot be ruled out for the examined scaphitids. The asymmetrical shape of these features may be an artifact of construction since they were once protrusions around the premature aperture, which were later filled during shell growth.

5.5 CONCLUSIONS

Hydrostatic and hydrodynamic simulations reveal important physical properties that constrained the mode of life and behavior for scaphitid ammonoids. Each of the adult models have the capacity for neutral buoyancy which suggests that scaphitids with similar morphologies were not restricted to the benthos, despite their isotopic similarities with benthic organisms, but rather were capable of occupying the water column as slow swimmers or passive floaters. The adult body chamber increases stability by distributing mass downwards, while simultaneously raising the aperture and hyponome to efficiently transmit thrust into horizontal backwards movement. High hydrostatic stabilities would have decreased rocking during movement and interaction with external forms of energy (currents, predator wake, etc.), but would also make it difficult for the living scaphitid to modify its own orientation. The upturned aperture and high stability would have also precluded significant interaction with the benthos (e.g., scavenging). Between planispiral juveniles and adults, the orientation of the aperture and thrust angle did not significantly change, therefore hydrostatic stability seems to be the primary influence of the scaphitid mature modification. More inflated shells (especially macroconchs) have poorer stability

and larger drag, resulting in more rocking during locomotion and lower swimming speeds. Shell compression and drag reduction would have been favored in high energy (proximal) paleoenvironments, while inflated morphs are released from such constraints within more distal, low energy habitats. Hydrodynamic lift is significant for morphs with a well-developed U-shaped hook at adulthood (represented in the current study by the microconch of *Hoploscaphites crassus*). The ventrolateral ornamentation does not significantly influence lift, and may have instead served as a defense against predation, stabilization, or as sensory devices. Even though mature scaphitids have a seemingly bizarre shape and orientation, this morphotype has functional significance in terms of hydrostatics and hydrodynamics that does not considerably impede locomotion or behavior as a nektobenthic ammonoid.

5.6 ACKNOWLEDGEMENTS

We thank Mateen Rizki (Wright State University, Ohio) for his guidance with MATLAB to program the velocity integral equation (Equation 8). We also appreciate the help of Robert Farrar (BHI) for help imaging BHI 7174. NHL thanks Carolyn Merril (AMNH) for surface scanning the scaphitid specimen - AMNH 76342.

5.7 REFERENCES

3DFlow, 2018, 3DF Zephyr Free Edition [Computer software]. Strada Le Grazie, 15 37134 Verona (VR) – Italy.

Arkhipkin, A.I., 2014, Getting hooked: the role of a U-shaped body chamber in the shell of adult heteromorph ammonites. Journal of Molluscan Studies, v. 80, p. 354–364.

Autodesk Inc., 2017a, Meshmixer 3.3. Autodesk Inc., San Rafael, California.

Autodesk Inc., 2017b, Netfabb 2017.3. Autodesk Inc., San Rafael, California.

Bengtson, P., 1983, The Cenomanian-Coniacian of Sergipe Basin, Brazil. Fossil and Strata, v. 12, p. 1–78.

Birkelund, T., 1965, Ammonites from the Upper Cretaceous of West Greenland. Grønlands Geologiske Undersøgelse Bulletin, v. 56, 192p.

Bishop, G.A., 1973, Geology, stratigraphy, and biostratigraphy of the north end of the Cedar Creek Anticline, Dawson County, Montana. Montana Bureau of Mines and Geology Special Publication, v. 61, p. 1–2.

Blender Online Community, 2017, Blender, a 3D modelling and rendering package. Blender Institute, Amsterdam. http://www.blender.org

Brown, D., 2017, Tracker 4.11.0 [Computer software]. Retrieved June 21, 2018, from https://physlets.org/tracker/

Bucher, H., Landman, N.H., Klofak, S.M., and Guex, J., 1996, Mode and Rate of Growth in Ammonoids. in: Landman, N.H., Tanabe, K., Davis, R.A. (eds) Ammonoid Paleobiology. Topics in Geobiology, v. 13. Plenum, New York. p. 407–461.

Chamberlain, J.A., 1981, Hydromechanical design of fossil cephalopods. In House, M.R., and Senior, J.R., (eds.), The Ammonoidea, 289-336. Systematics Association, London.

Chamberlain, J.A., 1987, Locomotion of *Nautilus*. In: Saunders, B.W., Landman, N.H., (eds.) *Nautilus*—the biology and paleobiology of a living fossil. Springer, Dordrecht. p. 489–525.

Chamberlain, J.A., 1990, Jet propulsion of *Nautilus*: a surviving example of early Paleozoic cephalopod locomotor design. Canadian Journal of Zoology, v. 68, p. 806–814.

Cignoni, P. and Ranzuglia, G., 2014, MeshLab (Version 1.3.3) [Computer graphics software]. Visual Computing Lab – ISTI – CNR Pisa, Italy. Available from http://meshlab.sourceforge.net/

Cobban, W.A., 1969, The Late Cretaceous ammonites *Scaphites leei* Reeside and *Scaphites hippocrepis* (DeKay) in the Western Interior of the United States. U.S. Geological Survey Professional Paper, v. 619, p. 1–27.

Cochran, J.K., Kallenberg, K., Landman, N.H., Harries, P.J., Weinreb, D., Turekian, K.K., Beck, A.J., Cobban, W.A., 2010, Effect of diagenesis on the Sr, O, and C isotopic composition of Late Cretaceous mollusks from the Western Interior of North America. American Journal of Science, v. 310, p. 69–88.

Coryell, H.N. and Salmon, E.S., 1934, A molluscan faunule from the Pierre Formation in eastern Montana. American Museum Novitates, v. 746, p. 1–18.

Denton, E.J., and Gilpin-Brown, J.B., 1966, On the buoyancy of the pearly *Nautilus*. Journal of the Marine Biological Association of the United Kingdom, v. 46, p. 723–759.

Fau, M., Cornette, R., and Houssaye, A. 2016. Photogrammetry for 3D digitizing bones of mounted skeletons: Potential and limits. Comptes Rendus Palevol, v. 15, p. 968–977. doi:10.1016/j.crpv.2016.08.003

Ferguson, K., Macleod, K.G., Landman, N.H., and Sessa, J.A., 2019, Evaluating growth and ecology in baculitid and scaphitid ammonites using stable isotope sclerochronology. PALAIOS, v. 34(6), p. 317–329. https://doi.org/10.2110/palo.2019.005

Furnish, W.M., and Glenister, B.F., 1964, Nautiloidea – Tarphycerida. In: Moore, R.C. (ed.), Treatise on Invertebrate Paleontology, Vol. K, Mollusca, Part 3. Geological Society of America and University of Kansas Press, Boulder, Colorado and Lawrence, Kansas. p. K343–K368.

Greenwald, L., and Ward, P.D., 1987, Buoyancy in *Nautilus*. In: Saunders, B.W., Landman, N.H., (eds.) *Nautilus*—the biology and paleobiology of a living fossil. Springer, Dordrecht. p. 547–559.

He, S., Kyser, T.K., Caldwell, W.G.E., 2005, Paleoenvironment of the Western Interior Seaway inferred from d18O and d13C values of molluscs from the Cretaceous Bearpaw marine cyclothem. Palaeogeography Palaeoclimatology Palaeoecology, v. 217, p. 67–85.

Hewitt, R.A., 1993, Relation of shell strength to evolution. In: House, M.R. (ed), The Ammonoidea: Environment, Ecology, and Evolutionary Change, Systematics Association, special vol. 47, Clarendon Press, Oxford.

Hoffmann, R., and Zachow, S., 2011, Non-invasive approach to shed new light on the buoyancy business of chambered cephalopods (Mollusca). IAMG 2011 publication, Salzburg. doi:10.5242/iamg.2011.0163:506-516

Hoffmann, R., Schultz, J.A., Schellhorn, R., Rybacki, E., Keupp, H., Gerden, S.R., Lemanis, R., and Zachow, S., 2014, Non-invasive imaging methods applied to neo-

and paleo-ontological cephalopod research. Biogeosciences, v. 11, p. 2721–2739. DOI 10.5194/bg-11-2721-2014

Hoffmann, R., Lemanis, R., Naglik, C., and Klug, C., 2015, Ammonoid Buoyancy. in: Klug, C., Korn, D., De Baets, K., Kruta, I., Mapes, R.H., (eds.) Ammonoid paleobiology, volume I: from anatomy to ecology. Topics in geobiology, v. 43, p. 611–648. Dordrecht: Springer.

Hoffmann, R., Lemanis, R., Falkenberg, J., Schneider, S., Wesendonk, H., and Zachow, S., 2018, Integrating 2D and 3D shell morphology to disentangle the paleobiology of ammonoids: a virtual approach. Palaeontology, 61, p. 89–104.

Ifrim, C., Bengston, P., and Schweigart, G., 2018, Growth and function of spines in Jurassic and Cretaceous ammonites. Cretaceous Research, v. 88, p. 62-78.

Inoue, S., and Kondo, S., 2016, Suture pattern formation in ammonites and the unknown rear mantle structure. Scientific Reports, v. 6, p. 33689. DOI 10.1038/srep33689.

Jacobs, D.K., and Landman, N.H., 1993, Nautilus – a poor model for the function and behavior of ammonoids? Lethaia, v. 26, p. 1–12.

Jacobs, D.K., 1992, Shape, drag, and power in ammonoid swimming. Paleobiology, v. 18(2), p. 203–220.

Jacobs, D.K., Landman, N.H., Chamberlain Jr., J.A., 1994, Ammonite shell shape covaries with facies and hydrodynamics: iterative evolution as a response to changes in basinal environment. Geology, v. 22, p. 905–908.

Jordan, R., 1968, Zur Anatomie mesozoischer Ammoniten nach den Struk turelementen der Gehäuse-Innenwand. Beihefte zum Geologischen Jahrbuch, v. 77, p. 1–64.

Kakabadzé, M.V., and Sharikadzé, M.Z., 1993, On the mode of life of heteromorph ammonites (heterocone, ancylocone, ptychocone). Geobios, v. 15, p. 209–215.

Kauffman, E.G., Arthur, M.A., Howe, B., and Scholle, P.A., 1996, Widespread venting of methane-rich fluids in Late Cretaceous (Campanian) submarine springs (Tepee Buttes), Western Interior seaway, U.S.A. Geology, v. 24, p. 799–802. doi:10.1130/0091-7613(1996)024<0799:WVOMRF>2.3.CO;2.

Kennedy, W.J., 1970, A correlation of the uppermost Albian and the Cenomanian of South-West England. Proceedings of the Geologist's Association, v. 81(4), p. 613–677.

Klinger, H.C., 1981, Speculations on buoyancy control and ecology in some heteromorph ammonites. In: House, M.R., and Senior, J.R., (eds.) The Ammonoidea. The Systematics Association, Special Volume No. 18, p. 337–355.

Klinger, H.C., Wiedmann, J., and Kennedy, W.J., 1975, A new carinate phylloceratid ammonite from the early Albian (Cretaceous) of Zululand, South Africa. Palaeontology, v. 18(3), p. 657–664.

Klompmaker, A.A., Waljaard, N.A., and Fraaije, R.H.B., 2009, Ventral bite marks in Mesozoic ammonites. Palaeogeography, Palaeoclimatology, and Palaeoecology v. 280, p. 245–257.

Klug, C., and Korn, D., 2004, The origin of ammonoid locomotion. Acta Palaeontologica Polonica, v. 49, p. 235–242.

Klug, C., and Lehmann, J., 2015, Soft Part Anatomy of Ammonoids: Reconstructing the Animal Based on Exceptionally Preserved Specimens and Actualistic Comparisons. In: Klug, C., Korn, D., De Baets, K., Kruta, I., Mapes, R.H., (eds.) Ammonoid paleobiology, volume I: from anatomy to ecology. Topics in geobiology, v. 43. Springer, Dordrecht. p. 515–538.

Klug, C., Zatoń, M., Parent, H., Hostettler, B., and Tajika, A., 2015, Mature Modifications and Sexual Dimorphism. In: Klug, C. Korn, D., De Baets, K., Kruta, I., Mapes, R. (eds.) Ammonoid Paleobiology. From anatomy to ecology, Topics in Geobiology, v. 43. Springer, Dordrecht. p. 253–320.

Korn, D., and Klug, C., 2003, Morphological pathways in the evolution of early and middle Devonian ammonoids. Paleobiology, v. 29, p. 329–348.

Kruta, I., Rouget, I., Landman, N.H., Tanabe, K., and Cecca, F., 2009, Aptychi microstructure in Late Cretaceous Ancyloceratina (Ammonoidea). Lethaia, v. 42, p. 312-321.

Kruta, I., Landman, N.H., Rouget, I., Cecca, F., and Tafforeau, P., 2011, The role of ammonites in the Mesozoic marine food web revealed by exceptional jaws preservation. Science, v. 331, p. 365–379.

Kruta, I., Landman, N.H., Rouget, I., Cecca, F., and Tafforeau, P., 2013, The radula of the Late Cretaceous scaphitid ammonite *Rhaeboceras halli* (Meek an d Hayden, 1856). Palaeontology, v. 56(1), p. 9–14.

Landman, N.H. and Cobban, W.A., 2007, Ammonite touch marks in Upper Cretaceous (Cenomanian-Santonian) deposits of the Western Interior Seaway. in: Landman, N.H., Davis, R.A., Mapes, R.H. (eds) Cephalopods Present and Past: new insights and fresh perspectives. Springer, Dordrecht.

Landman, N.H., and Waage, K.M., 1986, Shell abnormalities in scaphitid ammonites. Lethaia, v. 19, p. 211–224.

Landman, N.H., and Waage, K.M., 1993, Scaphitid ammonites of the Upper Cretaceous (Maastrichtian) Fox Hills Formation in South Dakota and Wyoming. Bulletin of the American Museum of Natural History, v. 215, p. 1–257.

Landman, N.H., Kennedy, W.J., Cobban, W.A., and Larson, N.L., 2010, Scaphites of the "nodosus group" from the Upper Cretaceous (Campanian) of the Western Interior of North America. Bulletin of the American Museum of Natural History, v. 342, p. 1–242.

Landman, N.H., Cobban, W.A., and Larson, N.L., 2012a, Mode of life and habit of scaphitid ammonites. Geobios, v. 45, p. 87–98.

Landman, N.H., Cochran, K.J., Larson, N.L., Brezina, J., Garb, M.P., and Harries, P.J., 2012b, Methane seeps as ammonite habitats in the U.S. Western Interior Seaway revealed by isotopic analyses of well-preserved shell material. Geology, v. 40, p. 507–510.

Landman, N.H. Remin, Z., Garb, M.P., and Chamberlain, J.A., 2013, Cephalopods from the Badlands National Park area, South Dakota: Reassessment of the position of the Cretaceous/Paleogene boundary. Cretaceous Research, v. 42, p. 1–27.

Landman, N.H., Slattery, J., and Harries, P., 2016a, Encrustation of inarticulate brachiopods on scaphitid ammonites and inoceramids bivalves from the Upper Cretaceous U.S. Western Interior. Acta Geologica Polonica, v. 66(4), p. 645–662.

Landman, N.H., Kruta, I., Denton, J.S.S., and Cochran, J.K., 2016b, Getting unhooked: comment on the hypothesis that heteromorph ammonites were attached to kelp branches on the sea floor, as proposed by Arkhipkin (2014). Journal of Molluscan Studies, v. 82, p. 351–356.

Larson, N.L., 2003, Predation and pathologies in the Late Cretaceous ammonite family Scaphitidae. Mid-America Paleontology Society, v. 26, p. 1–30.

Larson, N.L., Jorgensen, S.D., Farrar, R.A., Larson, P.L., 1997, Ammonites and the other cephalopods of the Pierre Seaway. Geoscience Press, Tucson, Arizona. 148p.

Lehmann, U., 1981, The ammonites: their life and their world. Cambridge University Press, New York.

Lemanis, R., Zachow, S., Fusseis, F., and Hoffmann, R., 2015, A new approach using high-resolution computed tomography to test the buoyant properties of chambered cephalopod shells. Paleobiology, v. 41, p. 313–329. DOI 10.1017/pab.2014.17

Lemanis, R., Korn, D., Zachow, S., Rybacki, E., and Hoffmann, R., 2016, The evolution and development of cephalopod chambers and their shape. PlosOne, v. 11, p. 1–21.

Linzmeier, B.J., Landman, N.H., Peters, S.E., Kozdon, R., Kitajima, K., Valley, J.W., 2018, Ion microprobe-measured stable isotope evidence for ammonite habitat and life mode during early ontogeny. Paleobiology, v. 44, p. 684-708.

Lucia, L.A., and Rojas, O.J., 2009, The nanoscience and technology of renewable biomaterials. Wiley, Hoboken, New Jersey. 344 p.

Lukeneder, A., 2015, Ammonoid Habitats and Life History. in: Klug, C., Korn, D., De Baets, K., Kruta, I., Mapes, R.H. (eds.) Ammonoid paleobiology, volume I: from anatomy to ecology. Topics in geobiology, v. 43. Dordrecht: Springer, 689–791.

Medina, F.A., Buatois, L., and A. Lopez Angriman., 1992, Estratigrafia del Grupo Gustav en la Isla James Ross, Antarctica. Geologia de la Isla James Ross. p. 167–192.

Monks, N., 2000, Functional morphology, ecology, and evolution of the Scaphitaceae Gill, 1871 (Cephalopoda). Journal of Molluscan Studies, v. 66, p. 205–216.

Morton, S.G., 1842, Description of some new species of organic remains of the Cretaceous group of the United States: with a tabular view of the fossils hitherto discovered in this formation. Journal of the Academy of Natural Sciences of Philadelphia v. 8, p. 207–227.

Naglik, C., Tajika, A., Chamberlain, J., and Klug, C., 2015a, Ammonoid locomotion. in: Klug, C. Korn, D., De Baets, K., Kruta, I., Mapes, R. (eds.) Ammonoid Paleobiology. From anatomy to ecology, Topics in Geobiology, v. 43. Springer, Dordrecht. p. 649–688.

Naglik, C., Monnet, C., Goetz, S., Kolb, C., De Baets, K., Tajika, A., and Klug, C., 2015b, Growth trajectories of some major ammonoid sub-clades revealed by serial grinding tomography data. Lethaia, v. 48, p. 29–46.

Naglik, C., Rikhtegar, F., and Klug, C., 2016, Buoyancy of some Palaeozoic ammonoids and their hydrostatic properties based on empirical 3D-models. Lethaia, v. 49, p. 3–12.

Neil, T.R., Askew, G.N., 2018, Swimming mechanics and propulsive efficiency in the chambered nautilus. Royal Society Open Science, v. 5, p. 170467. http://dx.doi.org/10.1098/rsos.170467.

O'Dor, R.K., Wells, J., and Wells, M.J., 1990, Speed, jet pressure and oxygen consumption relationships in free-swimming *Nautilus*. Journal of Experimental Biology, v. 154, p. 383–396.

Okamoto, T., 1996, Theoretical modeling of ammonoid morphology. in: Landman, N.H., Tanabe, K., Davis, R.A. (eds) Ammonoid Paleobiology. Topics in Geobiology, v. 13, Plenum, New York.

Parent, H., Westermann, G.E.G., and Chamberlain, J.A., 2014, Ammonite aptychi: Functions and role in propulsion. Geobios, v. 47, p. 45–55.

Peterman, D.J., and Barton, C.C., 2019, Power scaling of ammonitic suture patterns from Cretaceous Ancyloceratina: constraints on septal/sutural complexity. Lethaia, v. 52, p. 77–90, doi: 10.1111/let.12291

Peterman, D.J., Barton, C.C., and Yacobucci, M.M., 2019a, The hydrostatics of Paleozoic ectocochleate cephalopods (Nautiloidea and Endoceratoidea) with implications for modes of life and early colonization of the pelagic zone. Palaeontologia Electronica, v. 22.2.27A, p. 1–29. https://doi.org/10.26879/884

Peterman, D.J., Ciampaglio. C., Shell, R.C., and Yacobucci, M.M., 2019b, Mode of life and hydrostatic stability of orthoconic ectocochleate cephalopods: hydrodynamic analyses of restoring moments from 3D-printed, neutrally buoyant models of a

baculite. Acta Palaeontologica Polonica, v. 64(3), p. 441–460. https://doi.org/10.4202/app.00595.2019

Peterman, D.J., Barton, C.C., Ciampaglio, C.N., and Yacobucci, M.M., 2019c, Sexual dimorphism in scaphitid ammonoids: differences in hydrostatic properties revealed by virtual 3D modeling. North American Paleontological Conference Program with Abstracts, PaleoBios, v. 36(0).

Seilacher, A., 1963, Umlagerung und Rolltransport von Cephalopoden-Gehäusen. Neues Jahrbuch für Geologie und Paläontologie, Monatshefte, v. 1963, p. 593–615.

Sessa, J.A., Larina, E., Knoll, K., Garb, M., Cochran, J.K., Huber, B.T., MacLeod, K.G., and Landman, N.H., 2015, Ammonite habitat revealed via isotopic composition and comparisons with co-occurring benthic and planktonic organisms. Proceedings of the National Academy of Sciences of the United States of America, v. 112, p. 15562–15567. https://doi.org/10.1073/pnas.1507554112.

Shapiro, E.A., and Saunders, B., 1987, *Nautilus* shell hydrostatics. In: Saunders, B.W., Landman, N.H., (eds.) *Nautilus*—the biology and paleobiology of a living fossil. Springer, Dordrecht. p. 527–545.

Shigeta, Y., 1993, Post-hatching early life history of Cretaceous Ammonoidea. Lethaia, v. 26, p. 133–146.

Skwarko, S.K., 1966, Cretaceous Stratigraphy and Palaeontology of the Northern Territory. Bureau of Mineral Resources, Geology and Geophysics Bulletin No. 73, 165p.

Tajika, A., Naglik, C., Morimoto, N., Pascual-Cebrian, E., Hennhöfer, D.K., and Klug C., 2015a, Empirical 3D-model of the conch of the Middle Jurassic ammonite microconch *Normannites*, its buoyancy, the physical effects of its mature modifications and speculations on their function. Historical Biology, v. 27, p. 181–191.

Tajika, A., Morimoto, N., Wani, R., Naglik, C., and Klug, C., 2015b, Intraspecific variation of phragmocone chamber volumes throughout ontogeny in the modern nautilid *Nautilus* and the Jurassic ammonite *Normannites*. PeerJ, v. 3, p. 1–28. DOI 10.7717/peerj.1306

Tanabe, K., 1979, Paleoecological analysis of ammonoid assemblages in the Turonian Scaphites facies of Hokkaido, Japan. Palaeontology, v. 22(3), p. 609–630.

Tanabe, K., Fukuda, Y., Kanie, Y., Lehmann, U., 1980, *Rhyncholites* and *conchorhynchs* as calcified jaw elements in some Late Cretaceous ammonites. Lethaia, v. 13, p. 157–168.

Tanabe, K., Kruta, I., and Landman, N.H., 2015, Ammonoid Buccal Mass and Jaw Apparatus. in: Klug, C., Korn, D., De Baets, K., Kruta, I., Mapes, R. (eds.)

Ammonoid Paleobiology. From anatomy to ecology, Topics in Geobiology, v. 43. Springer, Dordrecht. P. 429–484.

Trueman, A.E., 1940, The ammonite body-chamber, with special reference to the buoyancy and mode of life of the living ammonite. Quarterly Journal of the Geological Society, v. 384, p. 339–383.

Tsujita, C.J., and Westermann, G.E.G., 1998, Ammonoid habitats and habits in the Western Interior Seaway: a case study from the Upper Cretaceous Bearpaw Formation of southern Alberta, Canada. Palaeogeography, Palaeoclimatology, and Palaeoecology, v. 144, p. 135–160.

Vermeij, G.J., 1993, A natural history of shells. Princeton University Press, Princeton, New Jersey.

Ward, P.D., 1979, Cameral liquid in *Nautilus* and ammonites. Paleobiology, v. 5, p. 40–49.

Ward, P.D. and Greenwald, L., 1982, Chamber refilling in *Nautilus*. Journal of the Marine Biological Association of the United Kingdom, 62, p. 469–475.

Ward, P.D., and Westermann, G.E.G., 1977, Notes on animal weight, cameral fluids, swimming speed, and color polymorphism of the cephalopod *Nautilus pompilius* in the Fiji Islands. Paleobiology, v. 3, p. 377–388.

Wells, M.J., and O'Dor, R.K., 1991, Jet propulsion and the evolution of the cephalopods. Bulletin of Marine Science, v. 49(1-2), p. 419–432.

Westermann, G.E.G., 1996, Ammonoid life and habitat. in: Landman, N.H., Tanabe, K., and Davis, R.A. (eds). Ammonoid Paleobiology, Plenum, New York. p. 607–707.

Westermann, G.E.G., 2013, Hydrostatics, propulsion and life-habits of the Cretaceous ammonoid *Baculites*. Revue de Paleobiologie, v. 32, p. 249-265.

Westermann, G.E.G., and Tsujita, C.J., 1999, Life habits of ammonoids. in: Savazzi, E. (ed). Functional Morphology of the Invertebrate Skeleton. Wiley, Chichester. p. 299–325.

Wright, C.W., 1996, Treatise on invertebrate paleontology: Mollusca 4, Cephalopoda: Ammonoidea. Geological Society of America, Boulder, Colorado.

6.0 CONCLUSIONS

The morphology of ectocochleate cephalopod shells is shaped, in part, by constructional constraints and their phylogenetic history (Seilacher and Gishlick, 2015). However, these shells are also shaped by strict biological functions, specifically, the modification of the shell as a hydrostatic device. Shelled cephalopods, especially heteromorphs, experienced many evolutionary tradeoffs. Ammonoid heteromorphs underwent a series of morphological changes during their evolutionary history that resulted in relatively poor swimming abilities (Ward, 1986; Ward and Bandel, 1987; Westermann, 1996; Monks and Young, 1998; Mikhailova and Baraboshkin, 2009; Peterman et al., 2019a, 2020a, 2020b). Yet these modifications actually represent interesting and unique strategies for the adjustment of life habit and modes of life, compared to their planispiral counterparts (Peterman et al., 2019, 2020a, 2020b). Each of the examined heteromorphs has the capacity for neutral buoyancy (Peterman et al., 2019, 2020a, 2020b), which suggests that their coiling schemes are not merely a result of a liberation from the evolutionary stresses specifically imposed on quasi-planktic or nektic organisms (for contrasting benthic interpretations, see Ebel, 1992; Kakabadzé and Sharikadzé, 1993; Higashiura and Okamoto, 2012). Furthermore, uncoiling of the shell results in a shift in the total mass distribution, increasing stability. In general, U-shaped mature body chambers seem to adjust the position of the hyponome relative to the center of rotation, which allows for an efficient transmission of jet thrust into horizontal backwards movement with little rocking. This property may reflect a relatively common

selective solution for locomotion in heteromorphs, given the abundance of distantly related taxa with this particular adult modification (Kaplan, 2002).

The morphology of marginally-frilled ammonoid septa is genetically controlled and also subjected to constraints at the lower-scale limits (relatively low complexity during early ontogeny). There are also constructional constraints regarding maximum complexity at maturity, as evidenced by the positive relationship between the fractal dimension of hemisutures and terminal whorl height (Peterman and Barton, 2019). An upper-scale limit on complexity may be explained by the retention of cameral liquid in the higher order frills of the septum. This biological function is also influenced by scaling. The fractal-like corrugations of the septum may have been shaped to function over multiple scales, retaining more cameral liquid at larger sizes. More complex frills would have retained more cameral liquid that could have been used as liquid ballasts to reduce buoyancy in a positively buoyant shell, served as liquid reserves to facilitate larger ranges of slow, passive buoyancy adjustment (Kulicki, 1979; Kulicki and Mutvei, 1988; Saunders, 1995), or immobilized cameral liquid to prevent sloshing during locomotion (Klug and Hoffmann, 2015). More data should be acquired to truly understand the functional relationship between septal complexity and cameral liquid retention in ammonoids.

Orthoconic cephalopods without cameral or endosiphuncular deposits were remarkably stable during life, while assuming a vertical orientation in the water column (Peterman et al., 2019). This morphotype probably represents the endmember of high hydrostatic stability due to the optimal separation of the centers of buoyancy and mass. Neither the spatial distribution of cameral liquid in the phragmocone or slight shell

curvature permit a non-vertical static orientation. Furthermore, in a dynamic setting, the living cephalopod would not have been able to significantly rotate away from this vertical posture, suggesting that orthocones with similar morphologies to the studied baculite were primarily vertical migrants that assumed low energy lifestyles (Westermann, 1996; Peterman et al., 2019).

The seemingly aberrant coiling of nostoceratids suggests that they underwent significant changes in their syn vivo hydrostatic properties throughout ontogeny. These changes in coiling represent possible differences in life habit throughout the growth of an individual (Peterman et al., 2020a). Most nostoceratids are characterized by having variable juvenile stages, helical intermediate stages, and an upward-facing U-shaped hook that reflects the attainment of maturity. The three examined species of *Didymoceras* exhibit similar hydrostatic properties throughout ontogeny. The helical stage moves the center of thrust (the location of the hyponome) away from the axis passing through the centers of buoyancy and mass. Therefore, the helical stage would be poorly suited to horizontal movement, but would excel at a rotational movement about some vertical axis (pirouetting). Only two stages during life are well-suited for horizontal movement: 1, during the formation of the first elbow in the juvenile stage, and 2, during adulthood when the body chamber terminates into a recurved, U-shaped hook. These relative increases in horizontal movement could have increased juvenile dispersal potential and facilitated the location of a mate at adulthood (Peterman et al., 2020a).

Similar to the nostoceratids, the U-shaped hook of mature scaphitids would have increased hydrostatic stability while simultaneously adjusting the mass distribution so that thrust energy is efficiently transmitted into horizontal backwards movement

(Peterman et al., 2020a, 2020b). Inflated scaphitids have poorer stability and slower relative swimming velocities than compressed taxa. Shell compression would have been favored in higher energy environments, while inflated morphs would be released from such stresses in lower energy environments. The fossil distributions of these two morphs supports such hydrodynamic constraints, with compressed taxa generally found in more proximal paleoenvironments than inflated taxa (Jacobs et al., 1994). Shell ornamentation does not significantly influence drag or lift for the examined specimen (*Hoploscaphites crassus* microconch). However, the overall shape of the shell imparts lift, which may be involved in controlling height above the seafloor as a nektobenthon. The hydrostatic and hydrodynamic properties of these scaphitids suggest that the mature, U-shaped hook does not impede locomotion.

While heteromorphs are no longer regarded as a genetically senescent group of ammonoids approaching their inevitable extinction, the stigma associated with this typolysis concept has persisted (Wiedmann, 1969). That is, a presumption still exists that these strange cephalopods we not well adapted to anything in particular and only served as bizarre evolutionary experiments. These ammonoids were, in fact, very successful (Mikhailova & Baraboshkin, 2009; Seilacher, 2013) and in several cases are among the few ammonoid species that briefly persisted beyond the Cretaceous-Paleogene extinction event (Landman et al., 2015). Furthermore, their morphologies imposed specific constraints on their syn vivo physical properties, suggesting that these properties served as significant selection mechanisms for heteromorphy in ammonoids.

The virtual and physical modeling techniques of this dissertation offer novel approaches to reconstruct extinct animals. Such models allow the investigation of syn

vivo physical properties that are vital to understand the modes of life, life habits, dispersal potential, paleoecology, and selective pressures that governed the morphology of organisms whose remains are now merely fossils. This dissertation represents my best attempt at bringing such wonderfully enigmatic creatures back to life.

6.1 REFERENCES

Ebel, K., 1992, Mode of life and soft body shape of heteromorph ammonites. Lethaia, v. 25, p. 179-193.

Higashiura, K., and Okamoto, T., 2012, Life orientation of heteromorph ammonites under the negatively buoyant condition: a case study on the *Eubostrychoceras muramotoi* Matsumoto. Fossils, v. 91, p. 19-30.

Jacobs, D.K., Landman, N.H., and Chamberlain Jr., J.A., 1994, Ammonite shell shape covaries with facies and hydrodynamics: iterative evolution as a response to changes in basinal environment. Geology, v. 22, p. 905-908.

Kakabadzé, M.V., and Sharikadzé, M.Z., 1993, On the modes of life of heteromorph ammonites (heterocone, ancylocone, ptychocone). Geobios, v. 15, p. 209-215.

Kaplan, P., 2002, Biomechanics as a test of the functional plausibility: testing the adaptive value of terminal-countdown heteromorphy in Cretaceous ammonoids. Abhandlungen der Geologischen Bundesanstalt, v. 57, p. 181-197.

Klug, C. and Hoffmann, R., 2015, Ammonoid Septa and Sutures. *In* Klug, C., Korn, D., De Baets, K., Kruta, I. & Mapes, R.H. (eds.): Ammonoid paleobiology, Volume I: from anatomy to ecology. Topics in Geobiology, v. 43, p. 45–90, Springer, Dordrecht.

Kulicki, C., 1979, The ammonite shell, its structure, development and biological significance. Palaeontologia Polonica, no. 39, p. 97–142.

Kulicki, C., Mutvei, H., 1988, Functional interpretation of ammonoids septa. In: Wiedmann, J., Kullmann, J. (eds) Cephalopods-present and past. Schweitzerbart, Stuttgart.

Landman, N.H., Goolaerts, S., Jagt, J.W.M, Jagt-Yazykova, E.A. and Machalski, M., 2015, Chapter 19: Ammonites on the brink of extinction: diversity, abundance, and ecology of the Order Ammonoidea at the Cretaceous-Paleogene (K/Pg) boundary. In Klug, C., Korn, D., De Baets, K., Kruta, I. and Mapes, R.H., (eds.) Ammonoid Paleobiology: From macroevolution to paleogeography. Topics in Geobiology, v. 44, p. 497−553.

Mikhailova, I.A., and Baraboshkin, E.Y., 2009, The Evolution of the Heteromorph and Monomorph Early Cretaceous Ammonites of the Suborder Ancyloceratina Wiedmann. Paleontological Journal, v. 43(5), p. 527–536.

Monks, N., and Young, J.R., 1998, Body position and the functional morphology of Cretaceous heteromorph ammonites. Palaeontologia Electronica, v. 1(1), doi 10.26879/98001

Peterman, D.J., and Barton, C.C., 2019, Power scaling of ammonitic suture patterns from Cretaceous Ancyloceratina: constraints on septal/sutural complexity. Lethaia, v. 52, p. 77–90, doi: 10.1111/let.12291

Peterman, D.J., Ciampaglio. C., Shell, R.C., and Yacobucci, M.M., 2019, Mode of life and hydrostatic stability of orthoconic ectocochleate cephalopods: hydrodynamic analyses of restoring moments from 3D-printed, neutrally buoyant models. Acta Palaeontologica Polonica, v. 64(3), p. 441–460. https://doi.org/10.4202/app.00595.2019

Peterman, D.J., Yacobucci, M.M., Larson, N.L, Ciampaglio, C.N., and Linn, T., 2020a, A method to the madness: ontogenetic changes in the hydrostatic properties of *Didymoceras* (Nostoceratidae, Ammonoidea). Paleobiology, forthcoming. DOI: 10.1017/pab.2020.14.

Peterman, D.J., Hebdon, N., Ciampaglio, C.N., Yacobucci, M.M., Landman, N.H., and Linn, T., 2020b, Syn vivo hydrostatic and hydrodynamic properties of scaphitid ammonoids from the U.S. Western Interior. Geobios, forthcoming.

Saunders, W.B., 1995, The ammonoid suture problem: relationships between shell and septum thickness and suture complexity in Paleozoic ammonoids. Paleobiology, v. 21, p. 343–355.

Seilacher, A, 2013, Patterns of macroevolution through the Phanerozoic. Palaeontology, v. 56, p. 1273−1283.

Seilacher, A. and Gishlick, A., 2015, Morphodynamics. Boca Raton, FL.

Ward, P.D., 1986, Cretaceous ammonite shell shapes. Malacologia, v. 27, p. 3-28.

Ward, P.D., and Bandel, K., 1987, Life history strategies in fossil cephalopods. In: Boyle, P.R. (ed.), Cephalopod life cycles, v. II, Academic Press, London, p. 329-350.

Westermann, G.E.G., 1996, Ammonoid life and habitat. In: Landman, N.H., Tanabe, K., Davis, R.A. (eds.), Ammonoid paleobiology, Plenum, New York.

Wiedmann, J., 1969, The Heteromorphs and the ammonoid extinction. Biological Reviews, v. 44, p. 463−602.